KATHOLIEKE UNIVERSITEIT LEUVEN
FACULTY OF ENGINEERING
DEPARTMENT OF ELECTRICAL ENGINEERING (ESAT)
CENTRE FOR PROCESSING SPEECH AND IMAGES (PSI)
Kasteelpark Arenberg 10, B-3001 Leuven-Heverlee (Belgium)

KATHOLIEKE UNIVERSITEIT LEUVEN
FACULTY OF MEDICINE
DEPARTMENT OF MEDICAL DIAGNOSTIC SCIENCES
NUCLEAR MEDICINE
Herestraat 49, B-3000 Leuven (Belgium)

PREDICTION OF IMAGE QUALITY IN EMISSION TOMOGRAPHY

Examination board:

Prof. dr. ir. A. Haegemans, chair
Prof. dr. ir. J. Nuyts, promotor
Prof. dr. ir. P. Suetens, promotor
Prof. dr. ir. D. Vandermeulen, assessor
Dr. ir. D. Loeckx, assessor
Prof. MD. dr. ir. L. Mortelmans
Prof. dr. ir. S. Van Huffel
Prof. dr. sc. M. Defrise, assessor
(Vrije Universiteit Brussel)

Dissertation presented in partial fulfilment of the requirements for the degree of Doctor in Engineering

by

Lin ZHOU

January 2012

© Katholieke Universiteit Leuven – Faculteit Ingenieurswetenschappen
Arenbergkasteel, B-3001 Heverlee (Belgium)

Alle rechten voorbehouden. Niets uit deze uitgave mag worden vermenigvuldigd en/of openbaar gemaakt worden door middel van druk, fotokopie, microfilm, elektronisch of op welke andere wijze ook, zonder voorafgaande schriftelijke toestemming van de uitgever.

All rights reserved. No part of this publication may be reproduced in any form by print, photoprint, microfilm or any other means without written permission from the publisher.

D/2012/7515/1
ISBN 978-94-6018-401-7

Acknowledgement

This thesis would not have been possible without the guidance and the support from many individuals. I would like to take this opportunity to acknowledge everyone who helped me in one way or another for this accomplishment.

First of all, I own my deep gratitude to Prof. Patrick Dupont who was my thesis supervisor during my Master program of medical imaging in 2006. He enlightened me with the first glance of research in the world of medical imaging, and kept me motivated since then. His constant encouragements and supports made my first year of study in Belgium really delightful and motivated me to further study in this area. It was also for his recommendation that made this possible.

It is an honor for me to convey my sincere gratitude to my promoters, Prof. Johan Nuyts and Prof. Paul Suetens, who granted me the opportunity to start my PhD study in the field of nuclear medicine in September 2007. It was a pleasant four-year period pursuing research under their supervisions. Particularly, I would like to express my deepest appreciation to Johan, who has always been there answering my questions, helping me solve problems and clearing the obstacles that I encountered. The joy and enthusiasm that he has for scientific research are motivational and contagious. As an open-minded supervisor, he shows great respect to my research interests and provides with sufficient freedom to my development as a researcher that I want to be. I could not have imagined having a better promoter for my PhD study.

I am grateful to all people from Vrije Universiteit Brussel (VUB) and Universiteit Gent (UGent) who are in collaboration with our group within the framework of Fonds Wetenschappelijk Onderzoek (FWO) project. I have learnt a lot from discussions in the regular project meetings. Particularly, I am very much indebted to Prof. Michel Defrise from VUB. I have benefited a lot from his critical comments on my papers. His illustration of our results from a mathematical point of view is really fascinating and gave me great inspiration for further investigation.

My sincere thanks go to all my jury members for their precious time in evaluating the thesis manuscript. Their critical comments and constructive suggestions have led to significant improvements on my thesis.

I appreciate the inspirational and interdisciplinary atmosphere created by all the colleagues in the medical imaging research center (MIRC). It was a great pleasure working in such a friendly and scientifically active environment. My gratitude also

goes to Dominique Delaere, Bart De Dobbelaer, Stefaan Vleugels, Francine Reniers and Peter Vermaelen who provide daily technical and administrative supports for either MIRC or nuclear medicine.

My research experience is enriched by performing preclinical SPECT scans for Marijke De Saint-Hubert, Kristof Prinsen, Esther Wolfs, Matthias Bauwens and the research group led by Prof. Yicheng Ni. I would like to thank all of the colleagues in the department of nuclear medicine who provide supports for these experiments, especially Bert Vanbilloen for preparing the phantoms and the radioactive markers that are essential for the pinhole SPECT imaging, and Kristof Baete for the training of Symbia (SPECT/CT) and his occasional technical assistance for evening scans.

A special thank goes to Kathleen Vunckx, for her persistent daily support, her time and effort devoted to my papers, and so many valuable suggestions and interesting discussions between us. I would also acknowledge my direct colleagues: Catherine Lemmens, Katrien Van Slambrouck, Selmin Eren, Ahmadreza Rezaei, Koen Michielsen and Ameya Atre. I really enjoyed working with them. They are always being friendly to me, showing me diverse cultures from all over the world and bringing me a lot of joy in the past four years.

I am also grateful to all of my Chinese friends in Leuven: Hang Gao, Ling Tong, Ming Wu, Kai Liu, Di Mo, Junfeng Fan, Meng Deng, Yunan Cheng, Yuanbo Feng, Limin Li, Yan Huang, Xiaolan Deng, Sayuan Liang, Xiang Li, as well as many Chinese imecers and their families. No matter where you are, all the cheerful time that we spent together would never fade away from my memory. We share happiness and sadness, encouraging each other during tough times. Friendships are the most valuable treasure that I have in here.

Last but not least, I would like to convey my sincere thanks to my family. I deeply appreciate my parents and parents-in-law for their constant understanding, support and trust. No word can express my gratitude to my husband Chang. Being always optimistic towards life, he is my source of strength and making my life full of sunshine. With his unconditional love and support, I could not be happier and more satisfied. I am also thankful to my little boy Mu, thank you for bringing us so many delightful moments and thank you for opening the door to a brand new world to me.

Lin

Abstracts

Prediction of image quality in emission tomography

In the field of medical imaging, the choice of the imaging system geometry usually greatly influences the quality of the output image. To guarantee adequate image quality, it is important to estimate which system geometry is most suitable for the given imaging task, and to tune the geometrical parameters to yield the best system performance. In addition, for artifact-free image reconstruction of the acquired data, an accurate description of the system and its geometrical parameters is required. For the analysis, efficient and effective approaches are demanded to predict and assess the image quality, as a function of both the system geometry and the accuracy of the system model.

Focused on image quality prediction and evaluation in emission tomography, this PhD work consists of two studies. In the first one, the noise properties were investigated as a function of the system geometry. Two types of collimator systems, namely the parallel hole and the rotating slat collimator system, were optimized and compared with each other using the optimized parameters. The idea of system optimization was to find the combination of geometrical parameters which yields the minimal variance in the reconstruction with a predefined spatial resolution. The optimization and the comparison of the two systems was mainly performed by two analytical methods. The first one was applied only to the central point of uniform objects with simplified system models, yielding closed-form expressions for the minimal variance, as well as for the relation between the optimized parameters and the target resolution for each collimator system. The second method is more general and can be applied to arbitrary objects with sophisticated system models. With these methods, the relative performance of the two systems was assessed and evaluated using various figures of merit.

In the second study, procedures that determine the geometrical parameters of pinhole SPECT systems were evaluated and optimized. These procedures are typically called (geometrical) calibration procedures. In this study, different sources of error that influence the accuracy of the calibration procedure of a multi-pinhole SPECT system were investigated, and a new approach which stabilizes the calibration result was proposed. The analysis was mainly performed using an analytical linear model, with which the calibration protocol was optimized, reducing the time

and the complexity of the calibration procedure, without compromising the accuracy in the reconstruction. The theoretical results were verified by simulations and supported by reconstructions from real phantom measurements.

Voorspelling van de beeldkwaliteit in emissietomografie

In medische beeldvorming beïnvloedt de geometrie van het beeldvormingsysteem meestal in grote mate de kwaliteit van het uiteindelijke beeld. Om een geschikte beeldkwaliteit te kunnen garanderen, is het belangrijk om in te schatten welke systeemgeometrie het meest aangewezen is voor een gegeven beeldvormingstaak, en de geometrische parameters zo af te regelen dat ze de beste performantie van het systeem opleveren. Bovendien is voor een artefactvrije beeldreconstructie van de gemeten data een accurate beschrijving van het systeem en zijn geometrische parameters vereist. Voor de analyse zijn efficiënte en effectieve methodes nodig voor de voorspelling en bepaling van de beeldkwaliteit als functie van zowel de systeemgeometrie als de nauwkeurigheid van het systeemmodel.

Dit doctoraatswerk, gefocusseerd op de voorspelling en de evaluatie van de beeldkwaliteit in emissietomografie, bestaat uit twee studies. In de eerste studie werden de ruiseigenschappen als functie van de systeemgeometrie onderzocht. Twee types van collimatiesystemen, namelijk het parallelle gaten en het roterende vlakken collimatiesysteem, werden geoptimaliseerd en met elkaar vergeleken, gebruikmakend van de geoptimaliseerde parameters. Voor de systeemoptimalisatie werd gezocht naar de combinatie van geometrische parameters die het gereconstrueerde beeld met minimale variantie oplevert, bij een vooraf gekozen spatiale resolutie. De optimalisatie en de vergelijking van de twee systemen gebeurde voornamelijk met behulp van twee analytische methodes. De eerste werd enkel op het centrale punt van uniforme objecten met vereenvoudigde systeemmodellen toegepast, wat uitdrukkingen in gesloten vorm opleverde voor de minimale variantie, alsook voor de relatie tussen de geoptimaliseerde parameters en de doelresolutie voor elk collimatorsysteem. De tweede methode is meer algemeen en kan toegepast worden op willekeurige objecten met ingewikkelde systeemmodellen. Met deze methodes werd de relatieve performantie van de twee systemen bepaald en geëvalueerd met behulp van verscheidene kwaliteitsmaten.

In de tweede studie werden procedures voor het bepalen van de geometrische parameters van pinhole SPECT systemen geëvalueerd en geoptimaliseerd. Deze procedures worden typisch (geometrische) calibratieprocedures genoemd. In deze studie werden verschillende bronnen van fouten onderzocht die de nauwkeurigheid beïnvloeden van de calibratieprocedure voor een multipinhole SPECT systeem. Er werd ook een nieuwe aanpak voorgesteld die het resultaat van de calibratie stabiliseert. De analyse werd voornamelijk uitgevoerd via een analytisch lineair model, waarmee het calibratieprotocol geoptimaliseerd werd, zodat de tijd en de complexiteit van de calibratieprocedure kon verminderd worden zonder in te leveren op

de nauwkeurigheid van de reconstructie. De theoretische resultaten werden gecontroleerd met simulaties en gestaafd met reconstructies van echte fantoommetingen.

List of acronyms

i-D	i-dimensional
A-MAP	anatomy based maximum-a-posteriori
AOR	axis of rotation
AUC	area under the ROC-curve
CHO	channelized Hotelling observer
CNR	contrast-to-noise ratio
CoR	center of rotation
CRC	contrast recovery coefficient
CSRC	cold spot recovery coefficient
CT	computed tomography
CZT	cadmium-zinc-telluride
DoF	degree of freedom
DoG	difference-of-gaussian
EM	expectation maximization
FBP	filtered backprojection
FIM	Fisher information-based method
FN	false negative
FOM	figure of merit
FOV	field of view
FP	false positive
FPR	false positive rate
FWHM	full width at half maximum
HSRC	hot spot recovery coefficient
ID	image deformation
LIR	local impulse response
LLIR	linearized local impulse response
LS	least squares
MAP	maximum a posteriori
ML	maximum likelihood
MLEM	maximum likelihood expectation maximization
MRI	magnetic resonance imaging
MSE	mean squared error
MTF	modulation transfer function
NaI(Tl)	sodium iodide doped with thallium

NPW	non-prewhitening
OSEM	ordered subsets expectation maximization
OSL	one-step late
PET	positron emission tomography
PMT	photomultiplier tube
PH	parallel hole
PS	point source
PSF	point spread function
PW	prewhitening
RBI-EM	rescaled block-iterative expectation maximization
RE	reconstruction error
RL	resolution loss
RMSD	root mean squared deviation
RMSE	root mean squared error
ROC	receiver operating characteristic
ROI	region of interest
RS	rotating slat
SNR	signal-to-noise ratio
SPECT	single photon emission computed tomography
SVD	singular value decomposition
TOF	time-of-flight
TN	true negative
TP	true positive
TPR	true positive rate
WLS	weighted least squares
WPID	worst possible image deformation
WPRE	worst possible reconstruction error
WPRL	worst possible resolution loss

List of symbols

$\approx$	is approximately equal to
$\propto$	is proportional to
∞	infinity
*	complex conjugate
$^{-1}$	matrix inverse
^{T}	matrix transpose
$\langle\cdot\rangle$	expectation
$\lVert\cdot\rVert$	Euclidean norm
$\Re(\cdot)$	real part
∇^{20}	second partial derivative in the first parameter
∇^{11}	first partial derivative in the first and second parameter
∇	row gradient operator
$\otimes$	convolution
$\triangleq$	is by definition equal to
$\mathcal{R}_i$	i-dimension Radon transform
$\mathcal{R}_i^{-1}$	i-dimension inverse Radon transform
$\mathcal{R}_i^\dagger$	adjoint of $\mathcal{R}_i$
$\mathcal{F}_i$	i-dimension Fourier transform
$\mathcal{F}_i^{-1}$	i-dimension inverse Fourier transform
$\mathbb{R}$	real number domain

a	diameter of pinhole aperture
a_{ij}	probability that a photon emitted from image pixel j is detected in detector bin i
A, A^T	projection and backprojection operator
Atten$(\cdot)$	probability that a photon is not attenuated
$A_{uiq}, B_{uiq}, A_{viq}, B_{viq}, A_q, B_q$	matrices with accurate geometric parameters
$A'_{uiq}, B'_{uiq}, A'_{viq}, B'_{viq}, A'_q, B'_q$	matrices with inaccurate geometric parameters
C_Y	covariance matrix of noiseless measurement Y
C_Q	covariance matrix of measurement Q
Cov	covariance matrix
Cov^j	covariance image correlated to pixel j
d, d_c	diameter of collimator hole
d_p	hole width of parallel hole collimator

d_r	distance between two adjacent septa of rotating slat collimator
d_D	distance between the center of rotation and the detector
$\det(\cdot)$	matrix determinant
D	distance between the image center and the detector
$D(\vec{x})$	distance between the point at $\vec{x}$ and the detector
$D[.]$	diagonal matrix
diameter	diameter of disk/sphere object
d_{1i}, d_{2i}, d_{3i}	distances between point sources or pinhole apertures
e^j	j-th unit vector
e_u, e_v	electrical shifts
$\mathrm{erf}(\cdot)$	error function
E_c^{cb}	geometric efficiency of cone-beam collimator
E_c^{fb}	geometric efficiency of fan-beam collimator
E_c^{parh}, E_p	geometric efficiency of parallel hole collimator
E_c^{spin}	geometric efficiency of single pinhole collimator
E_c^{mpin}	geometric efficiency of multi-pinhole collimator
E_c^{rs}, E_r	geometric efficiency of rotating slat collimator
f	vector of region of interest
f	focus height of a converging collimator
f_i	focus length of the i-th pinhole
$\bar{f}_l$	expectation of lesion profile
F	gain in geometric efficiency (RS versus PH)
F_{uviq}, F_{pq}	notations of all matrices used to calculate reconstruction accuracy
$\boldsymbol{F}$	Fisher information matrix
$\boldsymbol{F}^j$	shift-invariant approximation of the Fisher information matrix $\boldsymbol{F}$
$\mathbf{F}^j$	Fourier transform of $\boldsymbol{F}^j$
$\boldsymbol{F}_{dc}^j$	DC-value of $\boldsymbol{F}^j$
FWHM_c	FWHM of P_c
FWHM_t	FWHM of P_t
G_i	i-dimensional isotropic Gaussian function
$\boldsymbol{G}$	pseudoinverse of the Fisher information matrix $\boldsymbol{F}$
$\boldsymbol{G}^j$	pseudoinverse of $\boldsymbol{F}^j$
$\mathbf{G}^j$	Fourier transform of $\boldsymbol{G}^j$
h, h_c	collimator septa height
$h(s)$	filter used in FBP reconstruction
h_p	septa height of PH collimator
h_p	filter used in FBP reconstruction with PH collimator
$\tilde{h}_p$	Fourier transform of filter h_p
h_r	septa height of RS collimator
h_r	filter used in FBP reconstruction with RS collimator
$\tilde{h}_r$	Fourier transform of filter h_r
H_k $(k = 0, 1)$	hypothesis representing lesion absent/present
H_1, H_2	detector head 1 and 2
i	index of pixel in detector space
i	index of pinhole aperture
I	number of detector pixels

I	number of pinhole aperture
$\overline{\text{ID}}_{\text{est}}$	mean image deformation due to ΔP_0^{est}
ID_{noise}	image deformation due to data noise
j	index of pixel in the image space
j	index of point source
J	number of image pixels
J	number of calibration point sources
k_δ	index of degree of freedom
k_θ	index of acquisition angle
K	covariance matrix of channel outputs
K_N	covariance matrix of internal noise
l_0^j	(linearized) local impulse response of pixel j before post-smoothing
l^j	(linearized) local impulse response of pixel j
L	logarithm of the likelihood
$\mathbf{L}_0^j$	Fourier transform of l_0^j
$\vec{l}_z$	vector of axis of rotation
m	magnification factor
m_i, n_i	mechanical offsets of the i-th pinhole
n	channel noise
M	logarithm of the prior
M	matrix containing first-order derivatives
N	number of noise realizations
N_R	number of pixels in the ROI
N_θ	number of acquisition angles
$p(\cdot)$	probability
$p(\cdot\|\cdot)$	conditional probability
pd	distance between the central pinhole and the center of the image
P	geometrical parameters to be estimated
P_0	true value of geometric parameters without systematic deviations
P_c	point spread function with a collimator system
P_p	point spread function with PH collimator
P_r	point spread function with RS collimator
P_t	point spread function of target resolution
P_T	true values of geometrical parameters
$\boldsymbol{P}$	post-smooth filter
$\boldsymbol{P}^j$	j-dependent post-smooth filter
$\mathbf{P}^j$	Fourier transform of $\boldsymbol{P}^j$
$\mathbf{P}_t$	Fourier transform of P_t
PS_s^α	location of a point source, with s off-center shift and α angular position
q_i	measured number of photons at detector bin i
$\bar{q}_i$	measured number of photons in detector pixel i without noise
Q	measurement of tracer distribution Λ
$Q^{(n)}$	n-th measurement of tracer distribution Λ
$\bar{Q}$	noiseless data
$\boldsymbol{Q}_L^j, \boldsymbol{Q}_C^j$	self-defined filters
$\boldsymbol{R}$	Hessian of the log-prior M

R_c	collimator resolution
R_c^{parh}	parallel hole collimator resolution
R_c^{pinh}	pinhole collimator resolution
R_c^{fb}	fan-beam collimator resolution
R_d	intrinsic detector resolution
R_s	system resolution
$\overline{\mathrm{RE}}$	mean reconstruction error
$\overline{\mathrm{RL}}_{\mathrm{est}}$	mean resolution loss due to $\Delta P_0^{\mathrm{est}}$
$\mathrm{RL}_{\mathrm{noise}}$	resolution loss due to data noise
s	template of numerical observer
s	distance between the slat interval and spinning axis
s_i	scatter and crosstalk at detector bin i
s_N^2	biased estimate of sample variance
s_{N-1}^2	unbiased estimate of sample variance
S	scatter and crosstalk in the measurement
S^2	unit sphere
S_{iq}	measure for resolution loss
$\hat{S}_{iq}$	S_{iq} calculated from repeated simulations
t	septa thickness
t_m, t_f, t_n	3 translation coordinates describing pinhole configuration
t_x, t_y, t_z	3 translation coordinates describing point configuration
T_{pq}	measure for image deformation
T	total acquisition time
T_p	acquisition time per angular position with PH collimator
T_r	acquisition time per angular position with RS collimator
$\hat{T}_{pq}$	T_{pq} calculated from repeated simulations
$\vec{u}_p$	unit vector perpendicular to the integration line in a slice
$\vec{u}_r$	unit vector perpendicular to the slat septa
$\vec{u}_v, \vec{u}_z$	orthogonal unit vectors in the detector plane (PH)
$\vec{u}_\theta$	unit vector perpendicular to the detector plane
$\vec{u}_\phi, \vec{u}_\phi^\perp$	orthogonal unit vectors in the detector plane (RS)
U	frequency-selective channels
U	actual projection of point sources
U^g	actual projection of the grid of point sources
U_0	ideal projection of point sources
U_0^g	ideal projection of the grid of point sources
u, v	orthogonal coordinates in the detector space (pinhole collimator)
u_{ij}, v_{ij}	projection coordinates of point source j through pinhole aperture i
v, z	orthogonal coordinates in the detector space (PH)
Var	variance
Var^j	variance in the reconstructed image pixel j
W	detector width of RS collimator
$W(k_\delta)$	amplitude of the impulsed deviation for the k_δ-th degree of freedom
$\overline{\mathrm{WPID}}$	mean on WPID
$\overline{\mathrm{WPRL}}$	mean on WPRL
x	observation of a single variate θ

$x^{(n)}$	dataset of the n-th observation
$\vec{x}$	vector of a point in the image space
X	observation of multivariate Θ
X_q	point source q on the grid
X_q^R	reconstructed point source q on the grid
x, y, z	cartesian coordinates in the image space
x_j, y_j, z_j	coordinates of j-th point source
$\tilde{x}_j, \tilde{y}_j, \tilde{z}_j$	coordinates of j-th point source after rotation
y	noiseless measurement
$\tilde{y}$	Fourier transform of y
y_p	measurement with PH collimator
$\tilde{y}_p$	Fourier transform of y_p
y_{p0}	unblurred measurement with PH collimator
$\tilde{y}_{p0}$	Fourier transform of y_{p0}
y_r	measurement with RS collimator
$\tilde{y}_r$	Fourier transform of y_r
y_{r0}	unblurred measurement with RS collimator
$\tilde{y}_{r0}$	Fourier transform of y_{r0}
y_i	expected number of photons detected at detector bin i
Y	expectation of measurement
z	lesion profile

α, γ	coordinates of a point on a plane centered between two adjacent slats
β	regularization parameter
β	oblique incident angle
δ	Dirac impulse function
$\delta d, \delta u, \delta v$	3 translations of systematic deviations
$\delta\Phi, \delta\Psi, \delta\Theta$	3 rotations of systematic deviations
ΔP	errors on estimated geometrical parameters
$\Delta P_0^{\mathrm{est}}$	realistic systematic deviations
$\Delta P_0^{im,k}$	impulsed systematic deviation at k-th projection angle
$\Delta P_0^{\mathrm{WPID}}$	systematic deviations yielding WPID
$\Delta P_0^{\mathrm{WPRL}}$	systematic deviations yielding WPRL
ΔP_B	bias on estimated geometrical parameters
$\Delta P_B^{\mathrm{est}}$	ΔP_B in the presence of $\Delta P_0^{\mathrm{est}}$
$\Delta P_B^{im,k}$	ΔP_B in the presence of $\Delta P_0^{im,k}$
ΔP_D	estimated systematic deviations
ΔP_N	standard deviation on estimated geometric parameters
ΔP_0	original systematic deviations
ΔU	difference between U and U_0
ΔU_D	ΔU due to systematic deviations
ΔU_N	ΔU due to random data noise
η	scale test statistic of numerical observer
θ	projection angle
θ	true value of a variate

$\hat{\theta}$	estimated value of a variate by an estimator
Θ	a set of unknown parameters
λ	activity in uniform phantom
$\lambda(\vec{x})$	tracer distribution in the image space
λ_b	activity in background
λ_c	activity in cold region
λ_h	activity in hot region
λ_j	activity in image pixel j
$\hat{\lambda}_j$	estimated activity in image pixel j
$\lambda_j^{(n)}$	estimated activity in image pixel j after n-th iterations
λ_{tp}	ideal PH reconstruction with target resolution
λ_{tr}	ideal RS reconstruction with target resolution
Λ	original tracer distribution
$\hat{\Lambda}$	reconstruction image
$\check{\Lambda}$	reconstruction image based on noiseless data
$\Lambda^{(n)}$	reconstruction image after n-th iterations
$\hat{\mu}$	sample mean
μ	linear attenuation coefficient
ν	frequency conjugate to s
ν, ν_z	frequency conjugate to v, z
$\vec{\nu}$	frequency conjugate to $\vec{x}$
ρ_1, ρ_2, ρ_3	3 rotation angles describing point/pinhole configuration
σ	standard deviation
σ^2	variance
σ_c	collimator aperture w.r.t. the image center
$\sigma_c(\vec{x})$	collimator aperture w.r.t. $\vec{x}$
σ_d	intrinsic detector resolution
σ_i^2	variance in detector bin i with Gaussian noise model
σ_p	PH collimator aperture w.r.t. the image center
σ_r	RS collimator aperture w.r.t. the image center
σ_t	target resolution
σ_p^{opt}	optimal aperture of PH collimator
σ_r^{opt}	optimal aperture of RS collimator
ϕ	spinning angle
Φ	detector tilt
Φ	objective function
Ψ	detector twist
Ω_W	effective detector width of RS collimator

Contents

Acknowledgement **i**

Abstracts **iii**

List of acronyms **vii**

List of symbols **ix**

1 Introduction **1**

- 1.1 Positioning 1
- 1.2 Aim 3
- 1.3 Main contributions 4
- 1.4 Outline 4

2 SPECT Imaging **7**

- 2.1 Basic background 7
  - 2.1.1 Data acquisition 7
  - 2.1.2 Data interpretation 10
  - 2.1.3 Sensitivity and resolution 11
- 2.2 Collimator design 12
  - 2.2.1 Parallel hole collimator 13
  - 2.2.2 Fan-beam and cone-beam collimator 14
  - 2.2.3 Pinhole collimator 15
  - 2.2.4 Rotating slat collimator 16
  - 2.2.5 Hybrid Collimators 16
  - 2.2.6 General guideline for collimator choice 17
- 2.3 Acquisition model 17

2.3.1 Idealized geometry modeling 17
2.3.2 Realistic system response 19
2.3.3 Scatter 19
2.3.4 Attenuation 20
2.4 Image reconstruction 20
2.4.1 Analytical reconstruction 20
2.4.2 Iterative reconstruction 24
2.5 Conclusion 33

3 Image quality evaluation 35
3.1 Data collection 35
3.1.1 Measurements 35
3.1.2 Simulation 36
3.2 Data analysis 36
3.2.1 Estimate quantification 37
3.2.2 Image quantification 38
3.2.3 Image quality evaluation 41
3.3 Analytical evaluation methods 46
3.3.1 Key concepts 46
3.3.2 Fisher information-based method 49
3.4 Application: determination of system geometry 57
3.5 Conclusion 59

4 Optimization and comparison: parallel hole and rotating slat collimation systems 61
4.1 Introduction 62
4.2 Methods 65
4.2.1 System description 65
4.2.2 Acquisition model and reconstruction 67
4.2.3 Performance measure 70
4.2.4 Analytical methods 70
4.2.5 Collimator aperture optimization 72
4.3 Numerical studies 73
4.3.1 Optimal collimator aperture 74
4.3.2 Optimized CNR gain 74

4.3.3 Ellipsoid phantom 74
4.3.4 Variable contrast phantom 76
4.4 FBP: analytical results 78
4.4.1 Optimal collimator aperture 78
4.4.2 Optimized CNR gain 78
4.5 FIM: numerical results 80
4.5.1 Optimal collimator aperture 80
4.5.2 Optimized CNR gain 81
4.5.3 Ellipsoid phantom 85
4.5.4 Variable contrast phantom 85
4.6 Discussion 89
4.7 Conclusion 92

5 Multi-pinhole SPECT calibration **95**
5.1 Introduction 96
5.2 Outline of the study 98
5.3 Methods 101
5.3.1 Principle of calibration 101
5.3.2 Calibration accuracy 104
5.3.3 Reconstruction accuracy 105
5.3.4 Validation with repeated simulations 108
5.3.5 Truncation modeling 109
5.3.6 Two types of systematic deviations 110
5.4 Study I 112
5.4.1 Analytical evaluation 114
5.4.2 Jaszczak phantom reconstruction 115
5.5 Results I 116
5.5.1 Analytical evaluation 116
5.5.2 Jaszczak phantom reconstruction 121
5.6 Conclusion I 125
5.7 Study II 125
5.7.1 Point source selection 125
5.7.2 Phantom experiment 128
5.8 Results II 129
5.8.1 Point source selection 129

5.8.2 Phantom experiment . . . 131
5.9 Conclusion II . . . 132
5.10 Discussion . . . 132

6 General conclusion 139
6.1 Main contribution . . . 139
6.1.1 System optimization and comparison . . . 139
6.1.2 Multi-pinhole SPECT calibration . . . 140
6.2 Suggestions for future work . . . 142
6.2.1 Improvement of Fisher information-based method . . . 142
6.2.2 Further improvement of multi-pinhole calibration . . . 143

A Effective Detector Width 145

B Geometric Efficiency 147

C FBP Calculation for Planar Imaging 149
C.1 Parallel hole collimator . . . 149
C.2 Rotating slat collimator . . . 152
C.3 Comparison between PH and RS . . . 154

D FBP Calculation for Volume Imaging 157
D.1 Parallel hole collimator . . . 157
D.2 Rotating slat collimator . . . 160
D.3 Comparison between PH and RS . . . 163

E Point-to-line distance 165

F Independent noise components 167

Bibliography 167

List of publications 179

Curriculum Vitae 183

Chapter 1

Introduction

1.1 Positioning

Nuclear medicine plays an important role in the field of medical imaging. Different from the image modalities such as computed tomography (CT) or magnetic resonance imaging (MRI) which acquire detailed anatomical information from the target of imaging, nuclear medicine focuses on molecular imaging, which helps to detect and diagnose functional abnormalities in the human body.

The core of nuclear medicine imaging is gamma radiation, emitted by radionuclides. The radionuclides can be categorized into two classes. The first class are the single photon emitters which emit gamma ray photons that can be detected directly by the gamma camera. The second one are the positron emitters which emit positrons that annihilate with electrons up to a few millimeters away from their origins, generating two gamma photons emitted in opposite directions. The nuclear medicine techniques, which exploit the property of these two types of radionuclides, are single photon emission computed tomography (SPECT) and positron emission tomography (PET), respectively.

The procedure of nuclear medicine imaging can be briefly summarized as follows. First, a particular molecule is selected based on its affinity for participating in the biochemical process of interest. The radioactive tracer is prepared by labeling the chosen molecule with a particular radionuclide. Then, the radioactive tracer is administrated to the patient. The tracer will be distributed inside the body and typically be concentrated in the targeted tissue of interest. Next, the patient is positioned in the field of view of the SPECT/PET camera and scanned with the pre-set acquisition protocol. The emitted gamma photons are measured by the SPECT/PET camera during the acquisition. The acquired data are reconstructed into one or more interpretable images using a reconstruction algorithm with an accurate system model, incorporating both geometrical and physical properties of the acquisition system.

A medical diagnosis is given based on the final reconstruction image. That diagnosis may involve visualization of lesions, or quantification of tracer uptake, or even statistical analysis in a small animal study. An image has better quality if the medical doctor or the researcher is more likely to make a better diagnosis with it. Therefore, adequate image quality is very important for clinical and pre-clinical studies. In fact, there are many factors that affect the image quality, among which the choice of the system geometry plays a key role. To guarantee adequate and reliable images, we need to decide which system geometry is most suitable for the given imaging assignment prior to acquisition. If possible, we should also adjust the geometrical parameters of the system such that an acceptable signal-to-noise ratio or lesion detectability can be achieved in the reconstruction image.

Actually, there are general guidelines for the choice of system geometry for different applications. For example, in SPECT imaging, if we want to perform small animal imaging, generally a pinhole collimator system will be used since it has high spatial resolution and focused field of view. For patient imaging, most of the time we use a parallel hole collimator system, and sometimes apply a fan-beam, a cone-beam or a pinhole system for the examination of the head or of small organs of interest. However, when a novel system design is proposed, it is often not straightforward to see for which imaging tasks it will perform best, how to tune the parameters in order to achieve the optimal performance for that design, and whether or not this design is superior to the existing designs for a given assignment. The performance of the newly proposed system thus needs to be evaluated using figures of merit that quantify the quality of the reconstructed image. In this sense, prediction of the image quality in emission tomography is very important.

This PhD work focuses on the prediction of the reconstruction image quality associated with the system geometry in SPECT imaging. This includes both the choice of the camera geometry and the accuracy of the geometric model used during the reconstruction. The former is about the comparison and optimization of different SPECT systems. The latter is basically an error propagation analysis, i.e., once the optimal geometry configuration is determined and applied, we are interested to see the influence of the geometric modeling error (i.e., the difference between the expected system geometry and the actually modeled system geometry) on the reconstruction image quality. We investigated how these errors are propagated into the reconstruction and degrade the reconstruction image quality, and how these errors can be minimized.

In order to predict the image quality in the reconstruction, one needs to simulate the projection process which involves the geometrical and physical properties of the acquisition procedure. With this model, a common procedure is to apply a digitized tracer activity distribution as the input of this model and perform a forward projection operation to simulate the procedure of a real acquisition. This yields the simulated projection data, with which the image quality can be evaluated in two different ways. The first one is to do image reconstruction using the simulated data in the same way as we reconstruct the camera-based data. Since the ground truth (i.e., the input digital distribution) is known, the reconstruction can be directly compared with the original image, and the image quality can be easily quantified using various figures of merit. With this approach, one needs to do many simulations and reconstructions to study noise propagation. It is very time consuming, especially if we want to evaluate a large number of system designs with various parameters. The other way is to directly estimate the image quality based on the simulated projection data through analytical methods which approximately linearize the reconstruction procedure. With a linearized model, the figures of merit can be calculated faster with well-known mathematical operations, eliminating the need of doing repeated simulations and reconstructions. This type of approach is called the *analytical method* throughout the text. Normally, an analytical method involves several assumptions and approximations, therefore it needs to be validated by repeated simulations before it is applied for data analysis.

1.2 Aim

The basic idea of this PhD work is to evaluate and optimize the design of tomographic systems by computing figures of merit from the reconstructed images they produce. This quality assessment should be efficient, because optimization involves the evaluation of a large number of possible designs. The work consists of two studies in emission tomography: the first study investigates the error propagation as a function of the system geometry, the second one evaluates and optimizes procedures to determine the system matrix in pinhole SPECT.

The first study was about the comparison of two different SPECT systems, namely the conventional parallel hole collimation system and the rotating slat collimation system. This study was motivated by our collaborative research with the group in the University of Gent who developed a prototype rotating slat system. Due to a different way of photon accumulation, the geometric efficiency of a rotating slat system is much higher than that of the parallel hole system. However, an extra reconstruction step is needed for the rotating slat system, which encourages the noise propagation in the reconstruction procedure. Therefore, it is difficult to judge which collimation system provides better image quality. The focus of this study was to thoroughly investigate the tradeoff between the resolution and the sensitivity for each system, and to evaluate their relative performance fairly and efficiently.

The second study aimed at reducing the time and complexity of the calibration procedure for our small animal SPECT system without compromising the image quality. For a small animal imaging system, accurate description of the system geometry is essential for high resolution reconstruction. To this end, for each animal scan, a separate scan of radioactive point sources, which is referred to as calibration scan, is always demanded for the estimation of the geometric parameters of the system. This costs extra scanning time. Moreover, variations in the system behavior could induce errors, because we are combining the information from two different scans (the animal scan and the calibration scan). Since the accuracy of the parameter estimation is one of the dominating factors that affect the reconstruction image quality, we needed to explore the sources of error during calibration, and how these errors propagate during the reconstruction procedure into the final tomographic images. The main focus of this study was to investigate the feasibility of a simultaneous animal/calibration scan, as well as to determine the corresponding optimal configuration of point sources based on the error analysis.

1.3 Main contributions

The main contributions of this PhD work are as follows. For the study of comparison of the two collimation systems, first, a novel idea for system optimization was proposed. It was found that for a fixed spatial resolution in the reconstruction, there exists an optimal value of the collimator aperture which corresponds to minimal variance in the reconstructed image. The relation between the target resolution and the optimal collimator aperture was derived mathematically. The optimal apertures are different for the two collimator systems, and the ratio of the optimal collimator resolution values was found to be $\sqrt{2}$. Second, the comparison of the two systems was done using the optimized collimator apertures. Based on the theory of filtered back-projection reconstruction, mathematical expressions were derived to evaluate the relative performance of the two collimator systems. The results were supported by an existing validated analytical method using various figures of merit.

For the study of small animal SPECT calibration, first, a new approach was proposed to stabilize the calibration result. This approach was evaluated in comparison with the previously used method. Second, besides the random noise on the data, another source of error, i.e., the small deviations between the expected camera orbit and the actual camera orbit during the acquisition, was explored. These deviations bias the calibration result and degrade the image quality in the reconstruction. The influence of these deviations on the calibration accuracy and reconstruction accuracy were studied theoretically and verified with real phantom measurements. The theoretical study has been done using an analytical method, which is able to rapidly estimate the effect of the calibration on the final reconstruction, given a certain calibration protocol. Using the analytical method, a good calibration protocol was selected and applied in a real phantom measurement. It was proven that it is feasible to perform simultaneous animal/calibration scans with the proper choice of calibration protocol, which reduces the acquisition time for each experiment without compromising accuracy of the calibration and reconstruction results.

1.4 Outline

Chapter 2 provides background information about SPECT imaging which is essential for the understanding of the subsequent chapters. The basic principle of SPECT imaging is briefly explained, followed by the introduction of typical collimator designs used for SPECT systems. Then, the acquisition model of SPECT is described, and the basic ideas of image reconstruction are explained for the most commonly used analytical and iterative algorithms, respectively.

Chapter 3 focuses on how to predict the image quality in the reconstruction using both repeated simulations and analytical methods. First, the most common figures of merit used for image quality evaluation are listed. Second, an analytical method is introduced for fast estimation of these figures of merit. The key concepts and the basic mathematical derivations of this method are described, and the applications of the proposed method used in this PhD thesis are explained generally.

Chapter 4 presents the work about the comparison between the parallel hole and the rotating slat collimator systems. First, the values and the limitations of previous comparative studies are discussed. Then, two different analytical evaluation methods used in our study are explained. Mathematical expressions that describe the relative performance of the two collimator systems are derived as functions of various geometric parameters. Details and results of both analytical and simulation studies are given at the end.

Chapter 5 explores the feasibility of a simultaneous animal/calibration scan with a multi-pinhole SPECT system. First, an analytical linear model which is used to analyze the error propagation in the calibration and reconstruction procedure is proposed in detail. With that analytical method, the influences of two sources of error are investigated individually. Then, the principle about how to select a calibration configuration for simultaneous animal/calibration scans is explained. Both theoretical and experimental results are presented in detail.

Chapter 6 highlights the main contributions of this PhD work, draws general conclusions and gives some suggestions for future work.

Chapter 2

SPECT Imaging

2.1 Basic background

2.1.1 Data acquisition

In SPECT imaging, the radioactive tracer which is labeled by the *radionuclide* distributes over the patient body and yields the gamma photons that may be emitted along any direction. The photons that go through the *collimator* will be detected by the *gamma camera*. In this way, the continuous tracer distribution is measured and the data are typically stored in a 2-D or 3-D[1] matrix. Based on the *acquisition mode*, the data can either be directly used or be reconstructed for further analysis.

Radionuclide

The most conventional radionuclide used in SPECT imaging is 99m-technetium (^{99m}Tc), which has a main photopeak at 140 kev and a half life of 6.01 hours. Another common SPECT radionuclide is 123-iodine (^{123}I) which gives gamma radiation mostly around 159 kev with a half life of 13.2 hours.

Usually we only use a single radionuclide for a SPECT examination. However, sometimes it is desirable to track more than one biochemical process individually, or to exclusively label external markers used for particular purpose (for example, the attached point sources used for calibration, see chapter 5). In these cases, the application of multiple radionuclides within one acquisition is preferable. The data of different radionuclides are distinguished by their corresponding energy windows (see Fig. 2.1(b)), and the image will be reconstructed individually for each radioisotope. The advantage of using multiple isotopes simultaneously is that the images representing the distribution of different radioactive tracers are inherently registered both spatially and temporally.

---

[1] In case of dynamic imaging, the third dimension indicates the time frame.

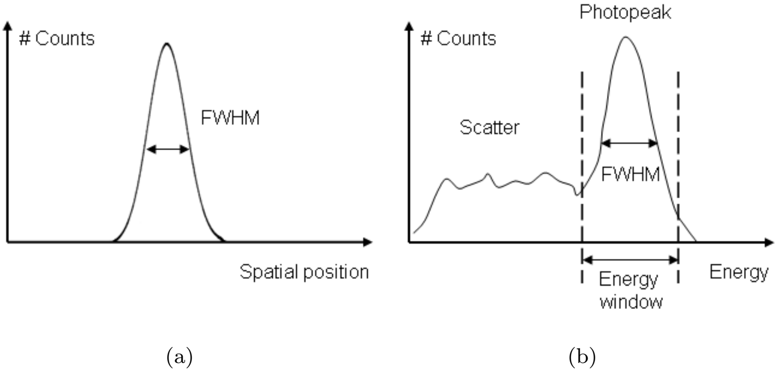

Figure 2.1: (a) Intrinsic resolution of the gamma camera. (b) Energy spectrum and energy window.

Gamma camera

A general SPECT gamma camera mainly consists of two components: scintillation crystal and photo multiplier tube (PMT). The scintillation crystal transforms the incident photon into a light flash. The detection of this flash is realized by the PMT, which is directly attached to the crystal.

The spatial location and the energy of a single scintillation event can only be measured with limited precision, which can be approximately described as Gaussian distributions [56, 116, 153]. Normally, we use the full width at half maximum (FWHM) of the Gaussian to specify the precision. The spatial resolution of a gamma camera (Fig. 2.1(a)) is referred to as *intrinsic resolution*, which typically has a FWHM of 4-5 mm for a scintillation detector. The energy resolution (Fig. 2.1(b)) depends on the material of the scintillation crystal. For the most commonly used crystal in SPECT, i.e., sodium iodide doped with thallium (NaI(Tl)), the energy resolution is around 10% FWHM at 140 kev. An interesting alternative material is cadmium zinc telluride (CZT) which has higher energy resolution (3-6%) at 140 kev. CZT has great potential in the development of new SPECT cameras [26, 122], the current limitation is the high price.

The filtering of the wanted/unwanted photons is realized by applying an *energy window* centered around the photopeak of a certain radionuclide (Fig. 2.1(b)). All photons with energy outside the energy window are rejected with no contribution to the data. With current gamma cameras, multiple energy windows can be applied simultaneously, which allows us to use more than one radioactive tracer (whose photopeaks are distinguishable) at the same time.

For a fixed camera position, the photons counted by the two-dimensional gamma detector are typically stored in a 2-D matrix which can be considered as an image projected from the 3-D tracer distribution to the detection plane of the gamma camera. Therefore, the acquisition procedure is often called *(forward) projection*

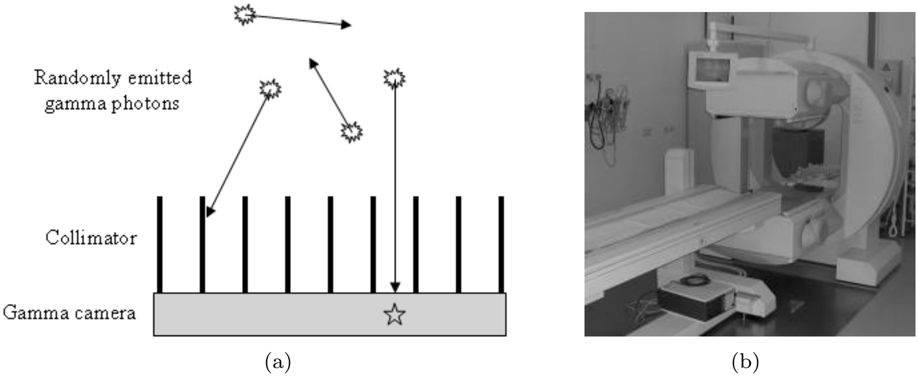

(a) (b)

Figure 2.2: (a) Mounting a collimator in front of the gamma camera. (b) A clinical dual-head SPECT system: E.cam, Fixed 180°, Siemens Medical Solutions.

and the acquired data is referred to as *projection image* or *projection data.*

Collimator

For single photon emitter, the trajectories and the origins of the emitted gamma photons are unpredictable. In order to facilitate the interpretation of the data, mechanical collimation is needed to identify photons coming from certain directions. It is realized by mounting a collimator in front of the gamma camera (Fig. 2.2(a)). The collimator consists of a set of septa which are made of high-attenuating material such as lead or tungsten, so it can efficiently stop the photons whose trajectories are oblique to the septa. Only the photons that can go through the collimator can reach the gamma camera. The design of the collimator determines the geometric efficiency and the geometric resolution of a SPECT system, thus it is one of the key factors influencing the system performance.

A SPECT system may have one or multiple detector heads, with each head consisting of a gamma camera and a collimator (Fig. 2.2(b)). Using the projection data from multiple heads generally improves the image quality of the reconstruction due to the increased detection sensitivity. However, the data of each head can also be processed individually whenever it is necessary.

Acquisition mode

With a SPECT system, basically there are two acquisition modes: *planar imaging* and *tomographic imaging.*

In the mode of planar imaging, single 2-D projection images are acquired at each detector head without the rotation of the gamma camera. One example is the whole-body bone scan (Fig. 2.3) with two detector heads in the front/back of the

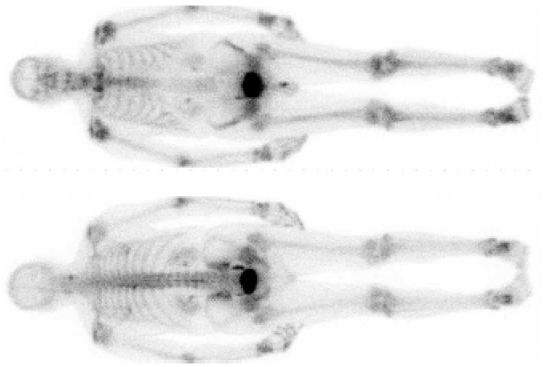

Figure 2.3: Example of planar imaging: anterior and posterior images from a bone scan with the patient bed shifted slowly with respect to the detector heads during the acquisition.

patient. To achieve a large field of view, either the patient bed stays static and the detector heads shift along the bed, or vice versa.

The tomographic imaging (also called *volume imaging*) is used when it is desirable to have the 3-D representation of the tracer distribution within the patient. To this end, the detector heads need to rotate around the patient to obtain projection image from different angles. The 2-D projection images acquired at different angles are piled up yielding a 3-D array which is typically referred to as a *sinogram.* This sinogram data however cannot be interpreted directly and one needs to apply a reconstruction algorithm to reconstruct a 3-D image from the sinogram.

2.1.2 Data interpretation

After data acquisition, we obtain (a series of) 2-D projection image(s). With planar imaging, we can directly analyze the projection data as an image. With tomographic scan, we first need to derive a 3-D image from the projection data acquired from different angular positions, this procedure is called *reconstruction.* After reconstruction we have interpretable images which can be used for further analysis.

Usually, the tracer activity administered to the patient is relatively low in order to avoid unnecessary radioactive exposure. Due to the Poisson nature of the measurement and the noise propagation during the reconstruction, the reconstructed images are often very noisy. In this case, post-processing is necessary. One example is to apply a low-pass filter which suppresses the high frequency noise in the reconstruction. This improves the visualization of the image but meanwhile discards details due to the smoothing effect of low-pass filtering.

A popular tendency is to combine the SPECT images with images acquired from other imaging modalities such as CT or MRI, in order to take advantage of both functional and anatomical information. One way to combine them is to use the information extracted from CT or MRI image as anatomical prior and apply them during the reconstruction [7, 9, 24, 25, 51, 110, 115]. This approach has great potential to improve the spatial resolution of the reconstructed SPECT image. The other way is to simply take the anatomical image as a reference image to better localize the abnormalities that are observed in the SPECT image [7, 11, 111].

For image analysis, sometimes one needs to quantify the activity within a region of interest (ROI), or to see the contrast between different ROIs, or to detect hot or cold lesions based on the image. To guarantee adequate image quality, the properties of a SPECT camera (mainly the sensitivity and the resolution) need to be well-tuned for a given imaging task and the purpose of imaging analysis.

2.1.3 Sensitivity and resolution

Detection sensitivity

For a certain radioisotope, the detection sensitivity of a SPECT system is determined by two factors: the detection efficiency of the gamma camera and the geometric efficiency of the collimator.

The detection efficiency of the gamma camera is the number of photons that are actually detected divided by the total number of photons that reach the crystal.

The geometric efficiency of a collimator is the fraction of the photons emitted from a point in the field of view that will reach the crystal if the photons are not attenuated within the imaging object. Since the collimator stops a large fraction of incident photons, the geometric efficiency of a SPECT system is usually very low. For most of the collimator designs, the geometric efficiency is position-dependent. One exception is with the parallel hole collimator whose geometric efficiency is (nearly) constant throughout the image space.

System resolution

The resolution of a SPECT system is determined by the intrinsic resolution of the gamma camera (see 2.1.1 and Fig. 2.1(a)) and the collimator resolution.

The collimator resolution is a measure of the blurring effect caused by the collimator geometry. As shown in Fig. 2.4(a), if we put a radioactive point source in front of the collimator, the measured photons will be distributed over the detector rather than concentrate at a single projection point due to the finite length of the collimator septa. The collimator resolution can be defined in two different ways. The first one is based on the detector response to the given point source (Fig. 2.4(a)), which is normally referred to as the point spread function (PSF). The other one is based on the single (detector) pixel response to the object plane where the point of interest is placed (see Fig. 2.4(b)). In both cases, the profile of the point/pixel response is typically approximated by a Gaussian. The collimator resolution is then defined as the FWHM of that Gaussian, which is determined by the

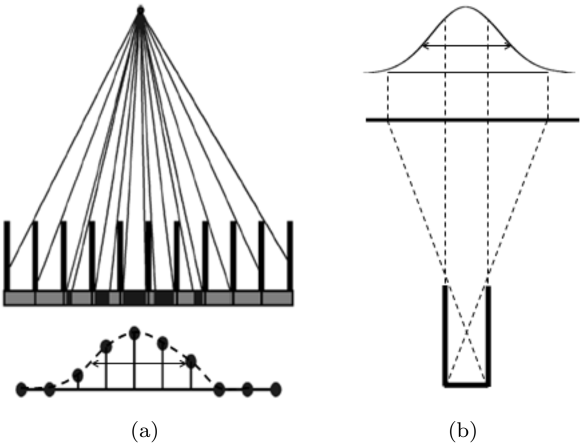

Figure 2.4: Collimator resolution defined based on (a) point spread function, (b) pixel response function [145].

collimator geometry as well as the distance between the location of the point source and the gamma detector. In our context, the latter definition is used for collimator resolution.

Combining the intrinsic detector resolution (R_d) and the collimator resolution (R_c) yields the system resolution (R_s):

$$R_s = \sqrt{R_c^2 + (\frac{R_d}{m})^2} \tag{2.1}$$

where m is a magnification factor determined by the geometric configuration of the collimator[2]. The expression of m will be given individually for each collimator design introduced in the next section.

Tradeoff between sensitivity and resolution

In general, the geometrical efficiency and the collimator resolution (i.e., the FWHM of the collimator response) are both monotonously increased with the opening of the collimator aperture and decreased with the septa height of the collimator. Therefore, there is no straightforward way to improve these two properties simultaneously by adjusting the collimator geometry (see 2.2 for more details).

2.2 Collimator design

In this section, the geometric efficiency and the collimator resolution are discussed for the most commonly used collimator geometries. As a reference, a detailed

---

[2] If $m = 1$, the collimator resolutions yielded by the two definitions are equal.

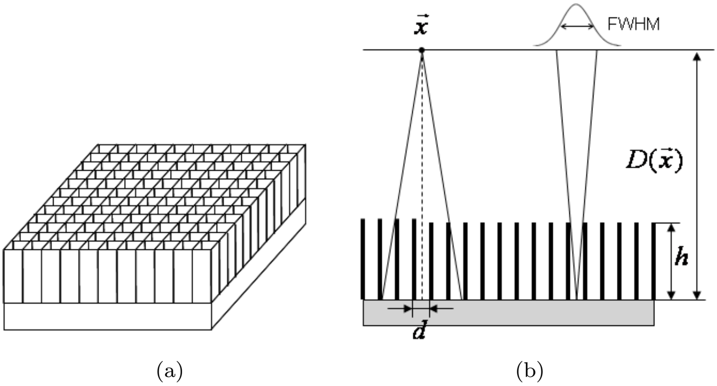

Figure 2.5: (a) Schematic structure and (b) cross-section of a parallel hole collimator.

overview of various collimator designs is provided in [145].

2.2.1 Parallel hole collimator

The parallel hole collimator (Fig. 2.5) is the most conventional collimator used for clinical SPECT and planar imaging. It consists of a series of long, parallel holes closely arranged in a 2-D matrix. The shape of the holes can be circular, square or hexagonal. This geometric configuration only allows the detection of the gamma photons whose trajectories are (nearly) parallel to these holes. Other photons will be stopped by the collimator septa which are highly attenuating.

For a point in the field of view (denoted by $\vec{x}$), the collimator resolution of the parallel hole collimator is [6]:

$$R_c^{parh}(\vec{x}) = \frac{D(\vec{x}) \times d}{h} \tag{2.2}$$

where d is the hole diameter, h is the height of the collimator septa, and $D(\vec{x})$ is the distance between the point $\vec{x}$ and the detector surface. The geometric efficiency of the parallel hole collimator is given by [73, 90, 145]:

$$E_c^{parh} = \frac{d^2}{4\pi h^2} \tag{2.3}$$

Note that in (2.2) and (2.3), the influence of the shape of the holes and the thickness of the collimator septa are neglected.

With the parallel hole collimator, the accumulation of the photons can be approximately considered as line integrals along the direction parallel to the holes. The projection image is non-scaled with respect to the size of the object and the magnification factor of this collimator is $m = 1$.

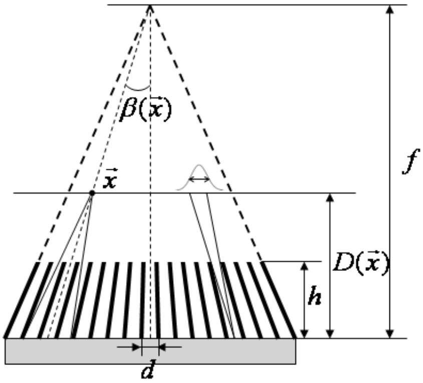

Figure 2.6: Cross-section of a fan-beam/cone-beam collimator.

2.2.2 Fan-beam and cone-beam collimator

The geometry of a fan-beam collimator is similar to that of a parallel hole collimator, but in one direction its septa are not parallel with each other but converging to a line (Fig. 2.6). This geometry increases the geometric efficiency at the expense of reduced field of view.

For a point in the field of view ($\vec{x}$), its oblique incident angle $\beta(\vec{x})$ is defined with respect to the norm of the detector plane. The geometric efficiency of fan-beam collimator is [125]

$$E_c^{fb}(\vec{x}) = \frac{d^2}{4\pi h^2} m(\vec{x}) \cos^3 \beta(\vec{x}) \tag{2.4}$$

with

$$m(\vec{x}) = f/(f - D(\vec{x})) \tag{2.5}$$

where h is the depth of the collimator measured along the norm of the detector plane, f is the focus height of the collimator septa, and $\cos^3 \beta$ is applied as a normalized angular factor. With the fan-beam collimator, we have $m > 1$ which means that the projection is magnified by a factor of m with respect to the original dimension of the object.

The collimator resolution measured along the non-focused direction is the same as (2.2), and the one along the focused direction is [89]:

$$R_c^{fb}(\vec{x}) = \frac{D(\vec{x}) \times d}{h} \frac{f - h}{f} \tag{2.6}$$

Compared with the fan-beam collimator, a cone-beam collimator has even higher geometric efficiency by converging the collimator septa both axially and trans-axially, with [66, 89]

$$E_c^{cb}(\vec{x}) = \frac{d^2}{4\pi h^2} m(\vec{x})^2 \cos^3 \beta(\vec{x}) \tag{2.7}$$

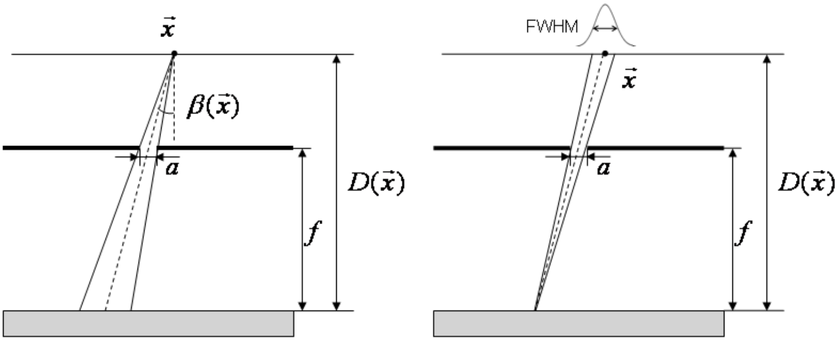

Figure 2.7: Cross-section of a pinhole collimator.

and the collimator resolutions in both direction are the same as (2.6).

2.2.3 Pinhole collimator

Pinhole collimators consist of one or several small holes drilled in a highly attenuating plate or cylindrical tube (Fig. 2.7). Compared to the fan-beam/cone-beam collimator which have the focal point and the detector on the opposite side of the object, the focus of the pinhole collimator is between the object and the detector, which results in a stronger magnification effect when the object is close to the pinhole collimator. This highly converged geometry offers high resolution beyond the intrinsic detector resolution with focused field of view, which makes pinhole collimators ideal for small animal SPECT imaging for pre-clinical experiments.

Based on the number of pinhole apertures, there are single pinhole and multi-pinhole collimators. Compared with single pinhole collimator, multi-pinhole designs make better use of the efficient detection area, increasing the detection sensitivity and therefore enhance the signal-to-noise ratio in the reconstruction image.

The geometric efficiency of a single pinhole collimator can be approximately calculated as

$$E_c^{spin}(\vec{x}) = \frac{a^2}{4\pi f^2} m(\vec{x})^2 \cos^3 \beta(\vec{x}) \tag{2.8}$$

with a the diameter of the pinhole aperture, and

$$m(\vec{x}) = f/(D(\vec{x}) - f) \tag{2.9}$$

where f represents the focus height of the pinhole, i.e., the distance between the collimator plate and the detector. For a multi-pinhole collimator system which has I pinholes, the geometric efficiency is

$$E_c^{mpin}(\vec{x}) = \sum_{i=1}^{I} E_c^{spin,i}(\vec{x}) \tag{2.10}$$

with $E_c^{spin,i}$ the geometric efficiency corresponding to the i-th pinhole aperture. The collimator resolution is approximately

$$R_c^{pinh}(\vec{x}) = \frac{D(\vec{x}) \times a}{f} \tag{2.11}$$

For more accurate expressions for the geometric efficiency and the collimator resolution of pinhole collimators, which take into account the penetration effect of realistic pinhole apertures, one can refer to [2,85,86,114].

2.2.4 Rotating slat collimator

A rotating slat collimator consists of a series of long, thin, rectangular slat septa parallel with each other (Fig. 2.8). Different from the collimators described above, the rotating slat collimator needs to spin around its own axis in order to acquire tomographic projection data. With this collimator, the photons are accumulated as plane integral rather than line integral. Suppose the width of the slat septa is W, the geometric efficiency at point $\vec{x}$ is calculated as the integration along the longer side of the slat septa:

$$E_c^{rs} = \int_{-W/2}^{+W/2} \frac{d}{4\pi D(\vec{x})h} \cos^3 \beta(l, \vec{x}) dl \tag{2.12}$$

with l the distance measure along the septa with respect to the spinning axis, and d the distance between the adjacent parallel slats. The collimator resolution measured perpendicular to the slat septa is the same as (2.2) and the one along the septa is infinite. The magnification factor m equals to 1. A thorough discussion about the geometric properties of the rotating slat collimator is given in [126]. Details about the comparison between this collimator and the conventional parallel hole collimator (see 2.2.1) are presented in chapter 4 and appendix-B.

2.2.5 Hybrid Collimators

Besides the collimator geometries described above, there are hybrid collimators which are designed in concept as a combination of two of these collimators in order to benefit from certain properties of each collimator. For example, combining axial parallel slats with a slit parallel to the axis of rotation results in a slit-slat collimator, which is axially equivalent to a parallel hole collimator and trans-axially similar as a pinhole collimator [78,95,150]. It provides high resolution in trans-axial direction and high geometric efficiency close to the slit due to the magnification geometry along this direction. Meanwhile it also offers extended field of view in the axial direction compared to an ordinary pinhole collimator. The axial resolution of a slit-slat collimator can be improved by slightly converging the slats, which will result in a fan-beam slit collimator [3].

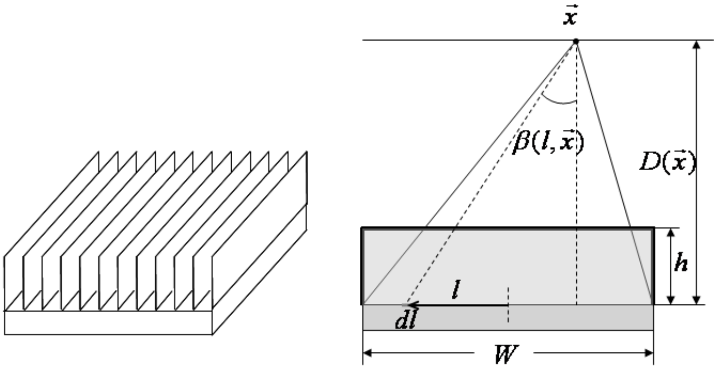

(a) (b)

Figure 2.8: (a) Schematic structure and (b) cross-section of a rotating slat collimator.

2.2.6 General guideline for collimator choice

The designs of the SPECT collimator can be categorized into either stationary (remaining still at each camera position) and rotating (with self-spinning) collimators, or non-converging ($m = 1$) and converging ($m > 1$) collimators. The collimator designs used in commercial SPECT cameras are mainly stationary collimators. Usually, the parallel hole collimator is a good choice when a large field of view (for example whole body imaging) is needed. The converging collimators are more applicable for imaging small objects of interest, for instance the fan-beam and the cone-beam collimator are often used for the examination of heart and brain. For even smaller imaging targets such as thyroid, the pinhole collimator is preferable. The pinhole collimators are also particularly suitable for preclinical small animal imaging. The slit-slat collimator is situated in between the parallel-beam or fan-beam collimation and the pinhole collimation, it can be used for brain, cardiac imaging as well as small animal imaging.

2.3 Acquisition model

The acquisition model describes a mapping from the target of imaging (tracer distribution) to the measured data (sinogram), which can be subdivided into idealized geometry modeling, realistic system response, scatter and attenuation.

2.3.1 Idealized geometry modeling

Idealized geometry modeling describes the schematic geometry mapping from the image space to the detection space, which assumes

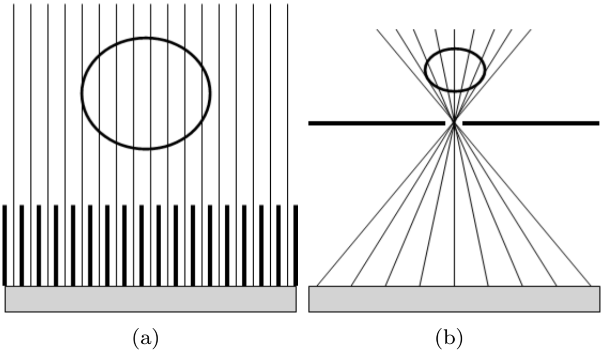

Figure 2.9: Idealized geometry modeling with (a) a parallel hole collimator, (b) a pinhole collimator.

- ideal collimation, i.e., the collimation with the best possible spatial resolution,
- no position-dependent geometric efficiency,
- and no interaction between the photons and the matters encountered between the origins of the photons and the detector.

For instance, with static/rotating collimators, it means that the projection data can be simply modeled as perfect (unweighted) line/plane integrals of the object (Fig. 2.9). In order to establish such an idealized model, the basic geometric parameters are required. For example, with a parallel hole collimator, we need to know the electronic shifts of the detector, which represent the offsets of the center of the detector in the directions orthogonal and parallel to the center of rotation (CoR) [30]. With a single pinhole collimator, besides the electrical detector shifts, we also need the exact values for the location of the pinhole with respect to the CoR, the focus height of the pinhole, the distance between the CoR and the detection surface, etc [20]. To get these parameters, one can either trust the values provided by the manufacturer or estimate them through a specially designed measurement. The latter is called *geometric calibration*. The geometric calibration is important especially for high resolution imaging with converging collimators. The reason is that the errors in the geometric parameters will be amplified in the projection due to the magnification effect of the converged collimator geometry. Using an acquisition model based on inaccurate parameters in the reconstruction will introduce artifacts or degrade the quality in the reconstructed image.

With a non-converging collimator, the estimation of the electrical shifts is usually called the center of rotation measurement, which can be done by measuring a single radioactive point source in front of the collimator [30]. The calibration of converging SPECT systems with fan-beam, cone-beam or pinhole collimator is more complex. In general the calibration procedure of these systems can be summarized as follows [54, 72, 94, 109, 139]:

1. Acquire projection data of one or multiple radioactive point sources placed in the field of view of the system.

2. Establish the geometric mapping from the position of the point sources to the projection locations, which are expressed as a function of all parameters that need to be estimated.

3. Estimate all geometric parameters involved by fitting the estimated projections to the centroids of the measured projections.

The number of the point sources depends on the complexity of the collimator geometry and the prior information that is used to constrain the fitting solution. For example, for single pinhole collimator, it has been proven that at least 3 point sources are needed, and that one needs to know at least two of the distances between the point sources, in order to have unique solution [20]. With a proper fitting algorithm (for example the iterative least squares fitting [20] or the singular value decomposition (SVD) [36]), we can estimate the geometrical parameters with acceptable accuracy to establish the idealized geometry model of the acquisition system.

2.3.2 Realistic system response

With the idealized geometry model, the system response of a SPECT system is assumed to be a perfect delta function throughout the image space. However, the realistic system response, which incorporates the position-dependent system resolution and detection sensitivity, is rather shift-variant. One approach to estimate the realistic system response is using Monte Carlo simulations, which are numerical calculation methods based on random variable sampling [27,116,117,154]. The system response can also be calculated analytically, either using approximated expressions such as those given in 2.2, or using exact but more complex expressions which are verified by real measurements [85,124,126].

2.3.3 Scatter

In light materials such as water or human tissue, a fraction of the emitted photons undergo elastic collisions with electrons. This phenomenon is called *Compton scatter* and changes the trajectories and the energies of these photons. After collision, the photons lose part of their energies, making the energy spectrum even broader (see Fig. 2.1(b)). The scatter degrades the quantification accuracy and the spatial resolution of the reconstruction. The amount of the scatter can be estimated and its effect can be compensated either by Monte Carlo simulations [17,74,75] or by analyzing the energy spectrum of real measurements [65,68,100].

2.3.4 Attenuation

Due to the interaction with the matter, a fraction of emitted photons will either get absorbed or deviate into another direction, which is generally called *attenuation*. Photons are attenuated by all the matters encountered between their origins and the detector, thus the amount of photons gradually decreases when they are traveling through the matter. The *linear attenuation coefficient* μ represents the probability of interaction per unit length. If we have $N(s_1)$ photons emitted at location $s = s_1$ traveling along the $s-$axis, the expected number of photons $N(s_2)$ that arrive at the detector position $s = s_2$ is given by

$$N(s_2) = N(s_1)e^{-\int_{s_1}^{s_2} \mu(s)ds} \tag{2.13}$$

The effect of attenuation can be corrected for in the reconstruction if the distribution of attenuation coefficients within the object is known. An approximate approach is to assume uniform attenuation coefficient within the boundary of the object. A more accurate estimate is to acquire the attenuation map based on transmission data, for example a CT image which is well-registered with the SPECT image. Since the attenuation coefficient is energy-dependent, the values acquired from the transmission scan need to be converted into the values corresponding to the energy level of the emission scan before they are used for attenuation correction.

2.4 Image reconstruction

Based on the acquired data, we can restore a 2-D or 3-D representation of the tracer distribution by using an appropriate reconstruction algorithm with the established acquisition model. Before or during reconstruction, the data needs to be processed with necessary corrections, e.g., *decay correction* due to the finite half-life of injected radionuclide, *scatter correction* due to unexpected Compton scatter, *crosstalk correction* due to the use of dual radionuclides whose energy windows are close to each other, etc. Details about these corrections will not be discussed since they are not actually relevant to the work presented in this thesis.

The reconstruction algorithms can be classified into analytical methods and iterative methods. As a key to understanding these methods, the two basic operations involved in each reconstruction algorithm are *projection* (mapping from image space to detector space) and *backprojection* (mapping from detector space to the image space). Below we will introduce the most representative reconstruction algorithms used in SPECT imaging.

2.4.1 Analytical reconstruction

The most widely used analytical reconstruction algorithm is filtered back-projection (FBP). In this section we will explain the principle of 2-D and 3-D FBP reconstruction [14], which will be used in the comparative study of the parallel hole and the rotating slat collimator systems in chapter 4.

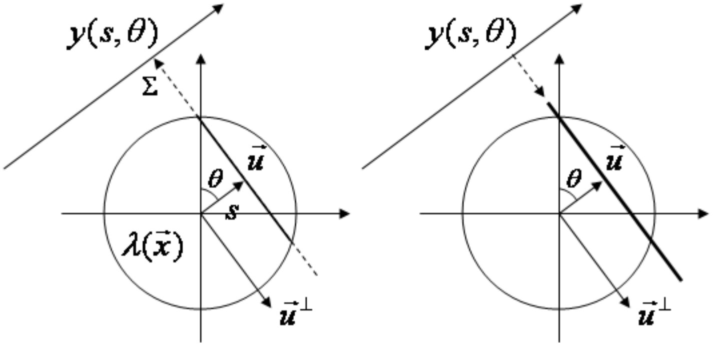

(a) 2-D projection (b) 2-D backprojection

Figure 2.10: Illustration of 2-D projection and backprojection.

2-D filtered back-projection

We take the idealized model of parallel beam acquisition to explain the 2-D FBP algorithm. Suppose we have a 2-D tracer distribution $\lambda(\vec{x})$, with $\vec{x}$ the vector in the image space. During the acquisition, the detector rotates around the object. A unit vector $\vec{u} = (\sin\theta, \cos\theta)$ is defined orthogonal to the projection line at the rotation angle θ (Fig. 2.10). The distance between this projection line and the center of rotation is s. The line integral projection data can be expressed as

$$y(s,\theta) = \int d\vec{x}\lambda(\vec{x})\delta(\vec{x}\cdot\vec{u} - s) \tag{2.14}$$

where $\delta(\cdot)$ is the Kronecker delta function. Mathematically, (2.14) is the definition of 2-D *Radon transform* (denoted by $\mathcal{R}_2$) of the tracer distribution $\lambda(\vec{x})$:

$$\mathcal{R}_2(\lambda(\vec{x})) = y(s,\theta) \tag{2.15}$$

The adjoint of $\mathcal{R}_2$ (see [14], page 17), denoted by $\mathcal{R}_2^{\dagger}$, is given by

$$[\mathcal{R}_2^{\dagger}(y)](\vec{x}) = \int_0^{\pi} d\theta \; y(s,\theta)\Big|_{s=\vec{x}\cdot\vec{u}} = \int_0^{\pi} y(\vec{x}\cdot\vec{u},\theta)d\theta \tag{2.16}$$

Note that $\mathcal{R}_2$ and $\mathcal{R}_2^{\dagger}$ are actually the projection and the backprojection operator, respectively.

Take the 1-D Fourier transform ($\mathcal{F}_1$) of the data $y(s,\theta)$ with respect to s and define $\imath = \sqrt{-1}$, we have

$$\begin{aligned}
\tilde{y}(\nu,\theta) &= [\mathcal{F}_1(y(s,\theta))](\nu) \\
&= \int_{-\infty}^{\infty} ds\, e^{-2\pi\imath\nu s} \int_{\infty} d\vec{x}\lambda(\vec{x})\delta(\vec{x}\cdot\vec{u}-s) \\
&= \int_{\infty} d\vec{x}\lambda(\vec{x}) \int_{\infty} ds\, e^{-2\pi\imath\nu s}\delta(\vec{x}\cdot\vec{u}-s) \\
&= \int_{\infty} d\vec{x}\lambda(\vec{x})e^{-2\pi\imath\nu(\vec{x}\cdot\vec{u})} \\
&= [\mathcal{F}_2(\lambda(\vec{x}))](\vec{\nu})\Big|_{\vec{\nu}=\nu\vec{u}} \qquad (2.17)
\end{aligned}$$

where ν and $\vec{\nu}$ are the frequency conjugates to the variable s and $\vec{x}$, respectively. (2.17) is called *central-slice theorem*, which means that the 1-D Fourier transform of the projection $y(s,\theta)$ is equal to the 2-D Fourier transform of the original function $\lambda(\vec{x})$ evaluated along the line defined by $\vec{\nu} = \nu\vec{u}$ going through the origin of the frequency domain of $\lambda(\vec{x})$. In this case, the central-slice theorem can also be denoted as

$$\mathcal{F}_2 = \mathcal{F}_1\mathcal{R}_2 \qquad (2.18)$$

with which the 2-D Radon transform and its inverse are expressed as

$$\begin{aligned}
\mathcal{R}_2 &= \mathcal{F}_1^{-1}\mathcal{F}_2 \qquad (2.19) \\
\mathcal{R}_2^{-1} &= \mathcal{F}_2^{-1}\mathcal{F}_1 \qquad (2.20)
\end{aligned}$$

The original tracer distribution $\lambda(\vec{x})$ can be computed by calculating the inverse of 2-D Radon transform ($\mathcal{R}_2^{-1}$). With the polar transform $d\vec{\rho} = \nu d\nu d\theta$, the reconstruction image is

$$\begin{aligned}
\lambda(\vec{x}) &= \mathcal{R}_2^{-1}(y(s,\theta)) \\
&= \int_0^{\pi} d\theta \int_{-\infty}^{\infty} |\nu| d\nu e^{2\pi\imath\nu(\vec{x}\cdot\vec{u})} \int_{-\infty}^{\infty} ds\, y(s,\theta)e^{-2\pi\imath\nu s} \\
&= \int_0^{\pi} d\theta \int_{-\infty}^{\infty} d\nu|\nu|\tilde{y}(\nu,\theta)e^{2\pi\imath\nu(\vec{x}\cdot\vec{u})} \\
&= [\mathcal{R}_2^{\dagger}(\int_{-\infty}^{\infty} d\nu|\nu|\tilde{y}(\nu,\theta)e^{2\pi\imath\nu(\vec{x}\cdot\vec{u})})](\vec{x}) \qquad (2.21)
\end{aligned}$$

(2.21) gives the basic principle of 2-D FBP. The whole procedure consists of filtering the projection data in the frequency domain by $|\nu|$, which is typically called *ramp filter*, then taking the 1-D inverse Fourier transform and back-projecting the result. The ramp filter $|\nu|$ functions as a high pass filter which compensates the blurring effect of the back-projection.

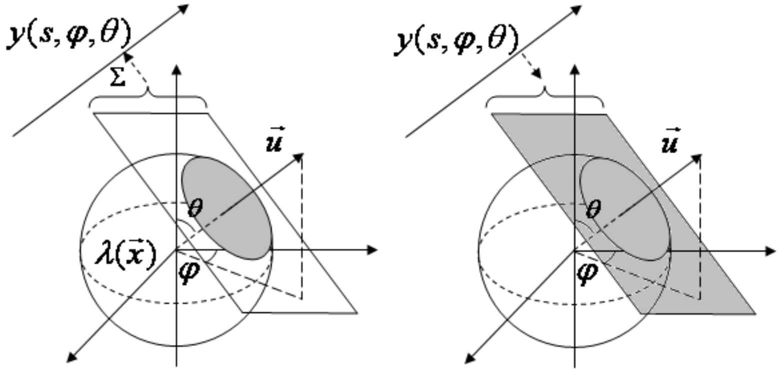

(a) 3-D projection (b) 3-D backprojection

Figure 2.11: Illustration of 3-D projection and backprojection.

Since the multiplication of two functions in the frequency domain is equal to their convolution in the spatial domain, (2.21) can also be written as

$$\lambda(\vec{x}) = \mathcal{R}_2^\dagger(y(s,\theta) \otimes h(s))\Big|_{s=\vec{x}\cdot\vec{u}} \tag{2.22}$$

with

$$h(s) = \int_{-\infty}^{\infty} d\nu |\nu| e^{2\pi\imath\nu s} \tag{2.23}$$

which is the ramp filter in spatial domain.

3-D filtered back-projection

If the projection data can be modeled as plane integrals (for example with rotating slat collimator), we need 3-D FBP algorithm to reconstruct the data. An explanation of 3-D projection and backprojection is shown in Fig. 2.11. In this case, the vector orthogonal to the projection plane can be uniquely defined by two rotation angles ϕ and θ. The acquired data is given by

$$y(s,\phi,\theta) = \int \lambda(\vec{x})\delta(\vec{x}\cdot\vec{u}(\theta) - s)d\vec{x} \tag{2.24}$$

with $\vec{u} = (-\sin\phi\cos\theta, -\sin\phi\sin\theta, \cos\phi)$ the unit vector orthogonal to the projection plane. (2.24) is the definition of 3-D Radon transform:

$$\mathcal{R}_3(\lambda(\vec{x})) = y(s,\phi,\theta) \tag{2.25}$$

The 2-D central-slice theorem (2.17) can be extended to 3-D case, i.e.,

$$\mathcal{F}_3 = \mathcal{F}_1\mathcal{R}_3 \tag{2.26}$$

$$\mathcal{R}_3 = \mathcal{F}_1^{-1}\mathcal{F}_3 \tag{2.27}$$

$$\mathcal{R}_3^{-1} = \mathcal{F}_3^{-1}\mathcal{F}_1 \tag{2.28}$$

The reconstruction image is then calculated as

$$\begin{aligned}
\lambda(\vec{x}) &= \mathcal{R}_3^{-1}(y(s,\phi,\theta)) \\
&= \int_{\frac{1}{2}S^2} d\vec{u} \int_{-\infty}^{\infty} |\nu|^2 d\nu e^{2\pi\imath\nu(\vec{x}\cdot\vec{u})} \int_{-\infty}^{\infty} ds\, y(s,\phi,\theta) e^{-2\pi\imath\nu s} \\
&= \int_{\frac{1}{2}S^2} d\vec{u} \int_{-\infty}^{\infty} d\nu |\nu|^2 \tilde{y}(\nu,\phi,\theta) e^{2\pi\imath\nu(\vec{x}\cdot\vec{u})} \qquad (2.29)
\end{aligned}$$

where S^2 is the unit sphere. It can be seen that the filter used in 3-D FBP is $\tilde{h}(\nu) = |\nu|^2$, with the corresponding expression in the spatial domain

$$h(s) = \frac{-1}{4\pi^2} \frac{\partial^2 \delta(s)}{\partial s^2} \qquad (2.30)$$

with which the reconstructed tracer distribution is

$$\lambda(\vec{x}) = \frac{-1}{4\pi^2} \int_{\frac{1}{2}S^2} d\vec{u} \left(\frac{\partial^2 y(s,\phi,\theta)}{\partial s^2} \right) \Big|_{s=\vec{x}\cdot\vec{u}} \qquad (2.31)$$

The FBP reconstruction explained in this section works on the data acquired by non-converging collimator systems with idealized geometric modeling. It works linearly on the projection data assuming shift-invariant system response, which is not true for SPECT imaging. Many studies focus on how to correct for the depth-dependent collimator blurring and the attenuation in an analytical way. One of the feasible solutions is to pre-process the sinogram in the Fourier space prior to the FBP reconstruction [41, 52, 148]. In order to incorporate the position-dependent geometric efficiency for the plane integral data, adaptations need to be made based on the basic FBP algorithm [155, 156]. Furthermore, special analytic algorithms were developed to reconstruct the data acquired with converging collimator systems [34, 55, 71, 137]. In the framework of this PhD, we do not consider sophisticated acquisition models with analytical reconstruction methods, therefore further details will not be discussed.

In general, the basic FBP can be considered as an unweighted least squares method (see 2.4.2) since the same weight is applied for all rotating angles. A major limitation of FBP reconstruction is that it cannot take the Poisson nature of the data into consideration. As a result, the reconstruction of noisy data using FBP will suffer from streak-like artifacts. This limitation can be overcome by using statistic iterative reconstruction algorithms discussed in the next section.

2.4.2 Iterative reconstruction

The advantage of iterative reconstruction algorithms is that they can easily involve realistic physical effects during the acquisition. To illustrate the principle of different iterative algorithms, we start with the introduction of basic notations. Suppose the original tracer distribution in the image space is digitized into pixels, where λ_j is the actual tracer activity in image pixel j, the data in detector unit i is given by

$$y_i = \sum_{j=1}^{J} a_{ij}\lambda_j + s_i \approx q_i, i = 1, \ldots, I \tag{2.32}$$

where a_{ij} representing the probability that photons emitted from pixel j will be detected in detector unit i, s_i accounts for the presence of scatter (and possibly crosstalk from other radionuclide), y_i is the expected number of photons detected at the detector unit i and q_i is the actually measured number of photons at i which is corrupted by noise. I and J are the total number of elements in the detector space and image space, respectively. As indicated at the beginning of 2.4, the influence of scatter and crosstalk will not be discussed. Therefore we drop s_i in (2.32) and the equation becomes

$$y_i = \sum_{j=1}^{J} a_{ij}\lambda_j \approx q_i \tag{2.33}$$

As a mapping from the image pixel j to detection pixel i, (2.33) performs a projection operation. Likewise, the corresponding back-projection operation is given by:

$$b_j = \sum_{i} a_{ij} f_i \tag{2.34}$$

where b_j is the value back-projected to pixel j, and f_i represents the data that needs to be back-projected.

The matrix notation of (2.33) is

$$Y = A\Lambda \approx Q \tag{2.35}$$

By definition, the matrix $A = \{a_{ij}\}$ is the projection operator and its transpose A^T is the back-projection operator. In emission tomography, A is typically called *system matrix* which is the matrix format of the acquisition model.

The aim of reconstruction is to estimate Λ given the acquired data Q. A good estimate can be achieved by using various iterative algorithms, among which the most representative ones will be briefly explained.

Least-square solution

In order to obtain a reasonable estimate of Λ with noisy data Q, the simplest way is to minimize the objective function:

$$\begin{aligned}\Phi(\Lambda) &= \|Q - A\Lambda\|^2 = (Q - A\Lambda)^T(Q - A\Lambda) \\ &= \|Q\|^2 + \Lambda^T A^T A\Lambda - 2\Lambda^T A^T Q\end{aligned} \tag{2.36}$$

with $\| \cdot \|$ the Euclidean norm of the column matrix. The minima of $\Phi(\Lambda)$ can be found by setting the partial derivative of $\Phi(\Lambda)$ with respect to Λ to zero:

$$\frac{\partial \Phi(\Lambda)}{\partial \lambda} = 0 \Rightarrow A^T A \Lambda - A^T Q = 0 \Rightarrow \Lambda = (A^T A)^{-1} A^T Q \tag{2.37}$$

(2.37) gives the normal solution of the least-square (LS) problem. However, since the dimension of the system matrix in emission tomography is usually very large, it is impractical to directly compute λ using (2.37). Alternatively, this solution can be iteratively approached using Landweber algorithm:

$$\Lambda^{(n+1)} = \Lambda^{(n)} + cA^T(Q - A\Lambda^{(n)}) \tag{2.38}$$

with

$$0 < c < \frac{2}{\|A\|^2} \tag{2.39}$$

where $\|A\|$ is the square root of the largest eigenvalue of $A^T A$. (2.39) guarantees the convergence of (2.38).

Weighted least-square solution

If we consider a simple Gaussian model of the data, the data q_i is a Gaussian random variable with mean value $y_i = \sum_j a_{ij}\lambda_j$ and variance σ_i^2. The probability of measuring q_i photons if y_i photons are expected, which is also called the *likelihood*, is given by

$$p(q_i|y_i) = \frac{1}{\sqrt{2\pi}\sigma_i} e^{-(q_i - y_i)^2 / 2\sigma_i^2} \tag{2.40}$$

Assume that the detection of one photon is independent from that of other photons, then the probabilities can be simply multiplied:

$$p(Q|Y) = \prod_i \frac{1}{\sqrt{2\pi}\sigma_i} e^{-(q_i - y_i)^2 / 2\sigma_i^2} \tag{2.41}$$

Denote the covariance matrix of the data as C_Q, which is a diagonal matrix $C_Q = diag\{\sigma_1^2, \sigma_2^2, \ldots, \sigma_I^2\}$ with the determinant $\det(C_Q)$, the likelihood with Gaussian noise model is

$$p(Q|Y) = (2\pi)^{-I/2} (\det(C_Q))^{-1/2} e^{-(1/2)(Q-Y)^T C_Q^{-1} (Q-Y)} \tag{2.42}$$

We aim to maximize the likelihood $p(Q|Y)$, which is equivalent to minimize

$$\Phi(\Lambda) = (Q - Y)^T C_Q^{-1} (Q - Y) = (Q - A\Lambda)^T C_Q^{-1} (Q - A\Lambda) \tag{2.43}$$

The normal solution of (2.43) is

$$\Lambda = (A^T C_Q^{-1} A)^{-1} A^T C_Q^{-1} Q \tag{2.44}$$

Similar as the LS method, the weighted least-square (WLS) solution can be iteratively approached by

$$\Lambda^{(n+1)} = \Lambda^{(n)} + cA^T C_Q^{-1}(Q - A\Lambda^{(n)}) \tag{2.45}$$

with

$$0 < c < \frac{2}{\|C_Q^{-1/2}A\|^2} \tag{2.46}$$

Maximum likelihood expectation maximization

The Gaussian noise model is fairly accurate if we have a large number of measured photons. However, the number of counts are usually very low and the noise in emission tomography is better characterized by the Poisson distribution. The reason is that the probability of radioactive decay is independent of time, and that randomly selected events from a Poisson distribution preserve the Poisson character. The likelihood with the Poisson model is

$$p(q_i|y_i) = \frac{e^{-y_i} y_i^{q_i}}{q_i!} \tag{2.47}$$

with the multiplication of the probabilities

$$p(Q|Y) = \prod_i \frac{e^{-y_i} y_i^{q_i}}{q_i!} \tag{2.48}$$

In SPECT imaging, the most popular iterative reconstruction method is *maximum likelihood expectation maximization* (MLEM) algorithm [113]. This name consists of two parts, ML and EM. The first part is the maximization of the likelihood function (ML) which is the goal of this algorithm, and the second part is the expectation maximization (EM) which is the specific algorithm used to find this maximum.

In order to simplify the calculation, we maximize the logarithm of the likelihood (*log-likelihood*) rather than the likelihood with MLEM algorithm. Since the logarithm function is monotonically increasing, maximizing the log-likelihood is equivalent to the maximization of the likelihood function. The log-likelihood with Poisson noise model is given by

$$\begin{aligned} L(Q|\Lambda) &= \sum_i q_i \ln(y_i) - y_i \\ &= \sum_i q_i \ln(\sum_j a_{ij}\lambda_j) - \sum_j a_{ij}\lambda_j \end{aligned} \tag{2.49}$$

Note that the element $\ln(q_i!)$ is dropped because it is independent of λ_j, thus it is a fixed value during the reconstruction. The maximization is realized by setting the partial derivative of $L(Q|\Lambda)$ with respect to λ_j equal to zero:

$$\frac{\partial L}{\partial \lambda_j} = \sum_i a_{ij}(\frac{q_i}{\sum_j a_{ij}\lambda_j} - 1) = 0 \tag{2.50}$$

(2.50) is a non-linear function thus it cannot be solved directly. The solution of (2.50) can be approached using the EM algorithm, which is a simple and reliable algorithm that guarantees the convergence of the estimate.

With the EM approach, first we introduce a "complete" dataset $X = \{x_{ij}\}$, with x_{ij} the number of photons that have been emitted from pixel j and detected at the detector unit i. This complete data is actually not observable, however it is assumed to be known. The expectation of x_{ij}, given Λ is

$$\langle x_{ij}|\Lambda\rangle = a_{ij}\lambda_j \tag{2.51}$$

where $\langle\cdot\rangle$ represents expectation. Same as Q, X is also Poisson distributed. Similar to (2.50), we can calculate the log-likelihood for this complete data X:

$$L_x(X, \Lambda) = \sum_i \sum_j (x_{ij} \ln(a_{ij}\lambda_j) - a_{ij}\lambda_j) \tag{2.52}$$

Since the value of x_{ij} is not known, it is impossible to calculate $L_x(X, \Lambda)$. However, with the current estimate of Λ, we can compute the expectation of $L_x(X, \Lambda)$, which is

$$\begin{aligned} \left\langle L_x(X, \Lambda)|Q, \Lambda^{(n)}\right\rangle &= \sum_i \sum_j (n_{ij} \ln(a_{ij}\lambda_j) - a_{ij}\lambda_j) && (2.53) \\ n_{ij} &= a_{ij}\lambda_j^{(n)} \frac{q_i}{\sum_k a_{ik}\lambda_k^{(n)}} && (2.54) \end{aligned}$$

with $\lambda_j^{(n)}$ the current estimate of λ_j after n-th iteration. (2.53) is maximized by setting the partial derivative with respect to λ_j to zero:

$$\frac{\partial}{\partial \lambda_j} \left\langle L_x(X, \Lambda)|Q, \Lambda^{(n)}\right\rangle = \sum_i (\frac{n_{ij}}{\lambda_j} - a_{ij}) = 0 \tag{2.55}$$

which leads to

$$\lambda_j = \frac{\sum_i n_{ij}}{\sum_i a_{ij}} \tag{2.56}$$

Combining (2.54) and (2.56) yields the complete MLEM algorithm:

$$\lambda_j^{(n+1)} = \frac{\lambda_j^{(n)}}{\sum_i a_{ij}} \sum_i a_{ij} \frac{q_i}{\sum_{j'} a_{ij'}\lambda_{j'}^{(n)}} \tag{2.57}$$

Based on (2.50) and (2.57), the MLEM algorithm can also be considered as a *gradient ascent method*, i.e.,

$$\lambda_j^{(n+1)} = \lambda_j^{(n)} + \frac{\lambda_j^{(n)}}{\sum_i a_{ij}} \frac{\partial L}{\partial \lambda_j}\bigg|_{\Lambda^{(n)}} \tag{2.58}$$

Similar as a majority of iterative algorithms, MLEM has the property that high frequencies converge more slowly than low frequencies. Running MLEM with a large number of iterations will introduce substantial high frequency noise in the reconstructed image. One approach to noise reduction is to stop the iteration earlier before the noise starts to accumulate. However, the reconstructed image generated in this way cannot accurately represent the tracer distribution. A better solution is to run MLEM algorithm until convergence, then post-smooth the image to suppress the high frequency noise. This approach is called *post-smoothed MLEM*, which provides reconstruction images with (nearly) uniform resolution, but requires longer computation time. The convergence speed of EM method can be greatly improved by applying alternative algorithms, for example the ordered subset expectation maximization (OSEM) [64], the enhanced complete-data ordered subset expectation maximization (E-COSEM) [62], the rescaled block-iterative expectation maximization (RBI-EM) [28], etc. As one of the most commonly used algorithms, the principle of OSEM will be explained in the next section.

Ordered subset expectation maximization

The basic idea of the *ordered subset expectation maximization* [64] is to divide the projection data into groups (subsets), with each subset containing a few of projection images. Like MLEM, the goal of OSEM is to maximize the likelihood, but the estimate is updated using projections in one subset rather than the whole projection dataset. For each subset, the current estimate obtained from the previous subset will be applied as the initial value in the EM iteration. Suppose the projection data is divided into subsets $S_1, S_2, \ldots, S_K$, with K the total number of subsets, the OSEM estimate updated using the data contained in subset S_k is given by

$$\lambda_j^{(n+1)}(S_k) = \frac{\lambda_j^{(n)}}{\sum_{i \in S_k} a_{ij}} \sum_{i \in S_k} a_{ij} \frac{q_i}{\sum_{j'} a_{ij'} \lambda_{j'}^{(n)}} \tag{2.59}$$

A *(global) iteration* of OSEM is defined as a single pass through all subsets. Each OSEM iteration costs similar computation time compared to one standard EM iteration, however it accelerates the convergence by approximately a factor of K.

In SPECT, the subsets naturally correspond to groups of projections at different rotation angles. It is recommended to select the subsets in a balanced and exhaustive way, such that each subset can contribute equally to the reconstruction. For example, for a 360° tomographic acquisition with 64 acquisition angles, the subsets may be defined in such a way that every subset contains projections separated by 45° ($K = 8$ with 8 projections in each subset) or 90° ($K = 16$ with 4 projections in each subset). In addition, the number of projections in each subset should not be too small, especially with low number of counts. In other words, every subset should contain sufficient data in order to obtain better likelihood values.

An example of the global iteration of OSEM is shown in Fig. 2.12. The two figures in the upper left are the original image and the corresponding noisy projection, respectively. The projections are acquired with 64 projection angles equally

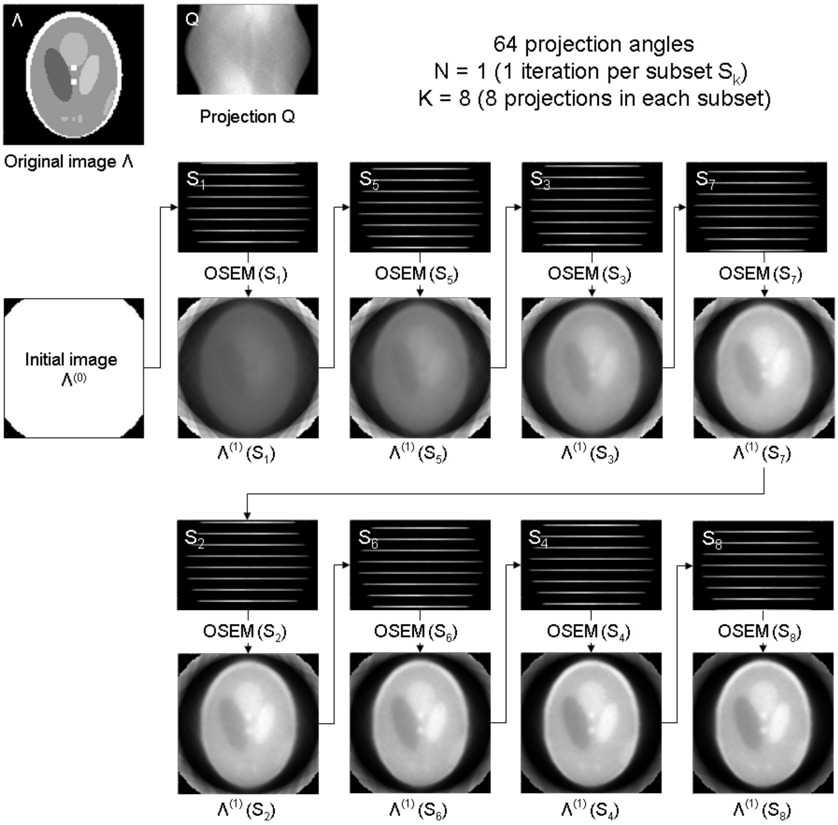
Λ
Original image Λ
Q
Projection Q
64 projection angles
N = 1 (1 iteration per subset S_k)
K = 8 (8 projections in each subset)
Initial image
$\Lambda^{(0)}$
S_1
OSEM (S_1)
$\Lambda^{(1)}(S_1)$
S_5
OSEM (S_5)
$\Lambda^{(1)}(S_5)$
S_3
OSEM (S_3)
$\Lambda^{(1)}(S_3)$
S_7
OSEM (S_7)
$\Lambda^{(1)}(S_7)$
S_2
OSEM (S_2)
$\Lambda^{(1)}(S_2)$
S_6
OSEM (S_6)
$\Lambda^{(1)}(S_6)$
S_4
OSEM (S_4)
$\Lambda^{(1)}(S_4)$
S_8
OSEM (S_8)
$\Lambda^{(1)}(S_8)$

Figure 2.12: Example of one global iteration with OSEM.

distributed over 360°. A uniform image is used as the initial image of the whole reconstruction. For each iteration, the image is updated by (2.59) using the projection data of the current subset (S_k). The updated image is then applied as the initial image of the subsequent iteration which uses the data of the next subset. OSEM converges better with large angular difference between subsequent subsets, therefore a sequence of subset (S_1, S_5, S_3, S_7, S_2, S_6, S_4, S_8) is chosen in Fig. 2.12.

Actually, OSEM does not converge to the ML solution in the presence of noise. The convergence of OSEM can be improved by using a sequence of reducing number of subsets, which ends up with a standard MLEM which uses all projections within one iteration. We denote this sequence as $N_1 \times K_1, N_2 \times K_2, \ldots, N_n \times K_n$ (number of global iterations × number of subsets), with $K_1 > K_2 > \ldots > K_n = 1$. An example of such a sequence is shown in Fig. 2.13. The scheme is set to be $1\times 8, 1\times 4, 1\times 2, 1\times 1$. Note that the left column in Fig. 2.13 actually corresponds to the global iteration explained in Fig. 2.12. The image reconstructed with the setting of $N_1 \times K_1$ is applied as the initial image of the next setting $N_2 \times K_2$, and so on.

The scheme of the reducing number of subsets is applied to do most image

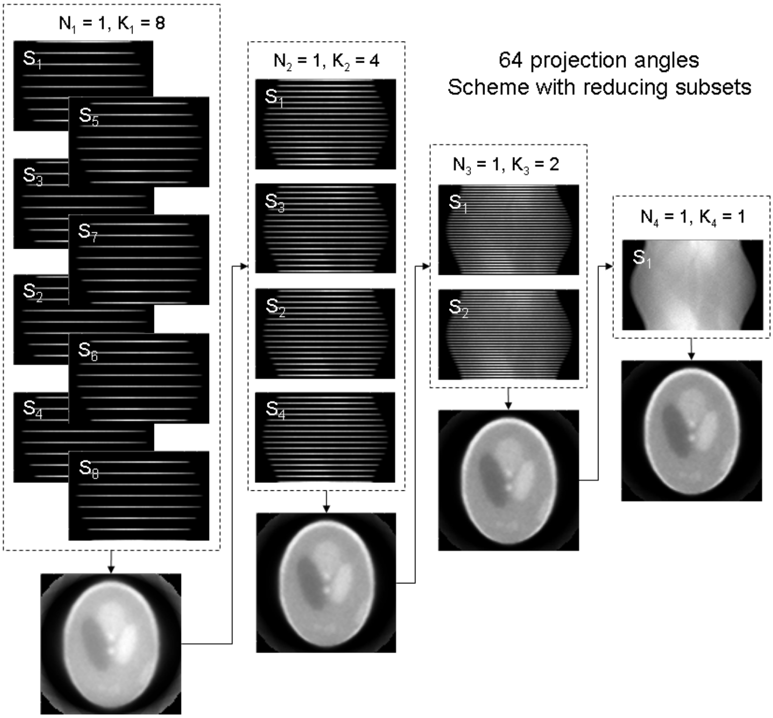

Figure 2.13: Example of an OSEM scheme with reducing subsets.

reconstructions in the subsequent chapters.

Maximum a posteriori

With the conditional and marginal probabilities of the tracer distribution Λ and the measurement Q, the rule of Bayes states that

$$p(\Lambda|Q) = \frac{p(Q|\Lambda)p(\Lambda)}{p(Q)} \tag{2.60}$$

where the *likelihood* $p(Q|\Lambda)$ is the probability of obtaining the measurement Q given the tracer distribution Λ. The *prior* $p(\Lambda)$ is the probability of having Λ without considering the measurement. The *posterior* $p(\Lambda|Q)$ is the probability of having the tracer distribution Λ with the acquired data Q. The probability $p(Q)$ is a fixed value for the given measurement, which remains constant during the reconstruction.

Actually, the goal of statistic iterative reconstruction is to find an estimate of Λ such that the posterior $p(\Lambda|Q)$ is maximal. With MLEM algorithm, we actually assume that the prior probability $p(\Lambda)$ is constant for all Λ estimates, thus maximizing the likelihood $p(Q|\Lambda)$ is equivalent to maximizing the posterior $p(\Lambda|Q)$.

With a proper choice of prior $p(\Lambda)$, Λ can be estimated by the *maximum a posteriori* (MAP) approach which maximizes $p(\Lambda|Q)$. The objective function that will be maximized in MAP is given by

$$\Phi(\Lambda, Q) = L(Q|\Lambda) - \beta M(\Lambda) \tag{2.61}$$

where $M(\Lambda)$ is the logarithm of the prior $p(\Lambda)$, and β is the regularization parameter or weight given to $M(\Lambda)$. If we apply the EM algorithm to find the maximum of $\Phi(\Lambda, Q)$, similar as (2.55), we need to solve

$$\frac{\partial}{\partial \lambda_j} \langle L_x(X, \Lambda) - \beta M(\Lambda) \rangle = \frac{\sum_i n_{ij}}{\lambda_j} - \sum_i a_{ij} - \beta \frac{\partial M(\lambda_j)}{\partial \lambda_j} = 0 \tag{2.62}$$

The direct solution of (2.62) is impractical. An alternative solution was proposed in [53] and is called the *one-step late* (OSL) algorithm. It makes use of gradients of the previous iteration step. The formula for OSL is given by

$$\lambda_j^{(n+1)} = \frac{\lambda_j^{(n)}}{\sum_i a_{ij} + \beta \frac{\partial M}{\partial \lambda_j}\big|_{\Lambda^{(n)}}} \sum_i a_{ij} \frac{q_i}{\sum_{j'} a_{ij'} \lambda_{j'}^{(n)}} \tag{2.63}$$

With (2.63), the denominator may be very small with a large β, which causes numerical problems. To improve the stability of the computation, it is better to consider MAP as a gradient ascent algorithm. Following the idea in [97], we have

$$\lambda_j^{(n+1)} = \lambda_j^{(n)} + \lambda_j^{(n)} \frac{\frac{\partial L}{\partial \lambda_j}\big|_{\Lambda^{(n)}} - \beta \frac{\partial M}{\partial \lambda_j}\big|_{\Lambda^{(n)}}}{\sum_i a_{ij} + 2\lambda_j^{(n)} \beta \frac{\partial^2 M}{\partial \lambda_j^2}\big|_{\Lambda^{(n)}}} \tag{2.64}$$

where the factor of 2 in the denominator comes from the curvature of the surrogate function for $M(\Lambda)$ [42, 70].

For MAP reconstruction, there exists various types of prior $p(\Lambda)$ which are designed to restore different features embedded in the original tracer distribution. The choice of prior depends on the application. To obtain an image with local smoothness, one can choose Gibbs-Markov priors [49], among which the most commonly used ones are the quadratic prior [91], the Huber prior [91], the median root prior [4], etc. With multi-modality imaging techniques, anatomical information acquired from CT or MRI images can be used as anatomical priors which helps to enhance the spatial resolution in the emission imaging. Examples include the A-prior used in anatomy based maximum-a-posterior (A-MAP) which requires accurate segmentation of the anatomical image [9], as well as the Bowsher prior [8, 25, 132], the mutual information-based [115] and the joint entropy-based [96] priors with which the explicit segmentation can be avoided.

By properly tuning the regularization parameter β, it is feasible to achieve (nearly) uniform spatial resolution in the reconstruction [45, 118, 119]. In that case, the resolution and the noise properties of MAP reconstruction is very similar to those of post-smoothed MLEM reconstruction [98, 119], and therefore they can be analyzed in the same way (see 3.3.2).

More details about MAP reconstruction are omitted here because they are irrelevant to the PhD work presented in this thesis.

2.5 Conclusion

In this chapter, we introduce the basic concepts in SPECT imaging from data acquisition to data interpretation. To explain the tradeoff between the resolution and the sensitivity, a brief overview of various collimator designs is provided. Issues with regard to how to establish an acquisition model are briefly discussed and the most representative reconstruction algorithms used in SPECT imaging are explained in general.

Chapter 3

Image quality evaluation

Imaging quality assessment is an important branch in medical imaging research field. There are several goals of quality assessment. First, it helps us to optimize the acquisition protocol, which includes injected dose, the duration of the acquisition, the width of the energy window and so on. Second, since the performance of the SPECT system depends on for example the size of the object, the distribution of the tracer, the energy of the radionuclide, etc, the image quality is really application-based or task-based. By quality assessment we can know which imaging system is most suitable for a given imaging task, as well as how to adjust the system parameters to achieve the best performance.

There are various figures of merit (FOMs) that can be applied to evaluate the system performance for different imaging tasks. As explained in 3.1, the FOMs can be either estimated from real measurements, or calculated based on the data acquired from computer-based simulations. The most commonly used FOMs are explained in 3.2. An analytical approach which can be applied to efficiently calculate these FOMs is introduced in 3.3. The applications of the proposed analytical method in this PhD work are summarized in 3.4.

3.1 Data collection

The data used for image quality assessment in emission tomography are typically collected in two ways, either by *real measurements* or by *numerical simulations*.

3.1.1 Measurements

The most straightforward way to evaluate the image quality is by doing real measurements of specially designed phantoms. The investigation of different FOMs requires different types of phantoms. For example, phantoms consisting of line sources or hot rods with varying diameters are typically used for the resolution study (e.g., the Jaszczak phantom used in chapter 5). Contrast recovery can be evaluated by measuring a phantom with hot or cold spots on a warm background. Homogeneous phantoms are often used to examine for instance the quantification accuracy or the inhomogeneity of the image.

3.1.2 Simulation

Although the data acquired from the measurements are very representative and realistic, doing measurements normally involves many procedures which make it very tedious and time-consuming. For image quality assessment, we prefer an efficient alternative, i.e., computer-based numerical simulations. With simulations, the acquisition procedure of the emission imaging is modeled with sufficient accuracy. A typical example is the Monte Carlo-based method with which millions of photons are simulated and tracked from their origins, incorporating their elaborate interactions with the tissues and materials encountered along their paths. Using Monte Carlo methods, one can implement a very realistic system matrix, but these methods require extremely high computing power. More often, we perform simulations just using simplified forward projectors, which model the procedure of photon accumulation as for example the weighted line/plane integration. This projector-based simulation is less realistic than the Monte Carlo-based method, but much faster and usually sufficiently accurate for our purpose.

The advantages of projector-based simulation are that the ground truth is exactly known, and that it is easy to generate both noiseless data and data with multiple noise realizations. The latter is realized by adding random noise in every simulated dataset and repeating the simulations for a number of times. For convenience, we call this *repeated simulations* in the remainder of the text. With repeated simulations, it is convenient to study the noise characteristics of the images produced by a certain system whose performance needs to be quantified or evaluated.

With the data yielded from repeated simulations and the corresponding (reconstruction) images, we can calculate the most relevant FOMs related to the system performance for a given imaging task (see 3.2). However, using an analytical method with which the noise characteristics are considered, it is possible to estimate the FOMs using only the noiseless data without doing reconstruction (see 3.3), which is certainly more appealing. The analytical method can be validated by repeated simulations.

In this PhD work, we mainly use projector-based simulated data for image quality evaluation.

3.2 Data analysis

Before explaining the most common figures of merit, we introduce the concept of *estimator*. Statistically, an estimator is a rule for computing the estimate of a given quantity based on the observed data, which is either the measured or the simulated data in emission tomography. A reconstruction algorithm is actually an estimator, which estimates the tracer distribution based on the acquired data. The geometric calibration procedure (see 2.3.1 and chapter 5) can also be considered as an estimator, which estimates the geometric parameters of the camera based on the point source projections.

In this section, we will first introduce general measures that quantify the parameters estimated by an estimator, and then illustrate some FOMs that are particularly relevant to the quantification and the quality evaluation of the (reconstruction) image.

3.2.1 Estimate quantification

Suppose we are interested in estimating an unknown parameter θ with a certain estimator based on the observed data x which are corrupted by noise or other errors during the data observation. The estimated value is denoted by $\hat{\theta}$. With repeated observations of θ, every time we get a different dataset x due to the random noise. The n-th observation and the corresponding estimate are denoted as $x^{(n)}$ and $\hat{\theta}(x^{(n)})$, respectively. The sample mean $\hat{\mu}(\theta)$ is then calculated as

$$\hat{\mu}(\theta) = \frac{1}{N}\sum_{n=1}^{N}\hat{\theta}(x^{(n)}) \tag{3.1}$$

$\hat{\mu}(\theta)$ is considered as a good estimate of the expectation value $\langle\hat{\theta}\rangle$. The performance of the estimator can be qualified by the following figures of merit.

Bias

The bias is defined as the difference between the expectation of the estimate and the true value of the parameter to be estimated, i.e.,

$$\mathrm{Bias}(\hat{\theta}) = \left\langle\hat{\theta}\right\rangle - \theta \tag{3.2}$$

An estimator with zero bias is *unbiased*, otherwise it is *biased*. A biased estimator will systematically over- or underestimate the real value of the parameter with positive and negative bias, respectively.

Variance

The variance is used to quantify the noise in the data. The variance of a variate θ is often symbolized by the square of the standard deviation (σ^2), which is calculated by

$$\sigma^2 = \mathrm{Var}(\hat{\theta}) = \left\langle(\hat{\theta} - \left\langle\hat{\theta}\right\rangle)^2\right\rangle \tag{3.3}$$

With repeated observations, the sample variance is given by

$$s_N^2 = \frac{1}{N} \sum_{n=1}^{N} \left(\hat{\theta}(x^{(n)}) - \hat{\mu}(\theta) \right)^2 \tag{3.4}$$

(3.4) is a biased estimate of the population variance. The unbiased estimate is

$$s_{N-1}^2 = \frac{1}{N-1} \sum_{n=1}^{N} \left(\hat{\theta}(x^{(n)}) - \hat{\mu}(\theta) \right)^2 \tag{3.5}$$

Mean squared error

The mean squared error (MSE) is the expectation of the squared errors:

$$\mathrm{MSE}(\hat{\theta}) = \left\langle (\hat{\theta} - \theta)^2 \right\rangle \tag{3.6}$$

The MSE, the bias and the variance is related by

$$\mathrm{MSE}(\hat{\theta}) = \mathrm{Var}(\hat{\theta}) + \mathrm{Bias}(\hat{\theta})^2 \tag{3.7}$$

For an unbiased estimator, the variance equals the MSE.

Covariance

If multiple variates are estimated, we can calculate the correlation between these variates, which is called covariance. Suppose we have two variates θ_j and θ_k, the covariance between them is

$$\mathrm{Cov}(\hat{\theta}_j, \hat{\theta}_k) = \left\langle (\hat{\theta}_j - \left\langle \hat{\theta}_j \right\rangle)(\hat{\theta}_k - \left\langle \hat{\theta}_k \right\rangle) \right\rangle \tag{3.8}$$

With repeated observations, the estimate of the population covariance is

$$\mathrm{Cov}(\hat{\theta}_j, \hat{\theta}_k) = \frac{1}{N-1} \sum_{n=1}^{N} \left(\hat{\theta}_j(x^{(n)}) - \hat{\mu}(\theta_j) \right) \left(\hat{\theta}_k(x^{(n)}) - \hat{\mu}(\theta_k) \right) \tag{3.9}$$

A square matrix whose (j,k)-th element equals to $\mathrm{Cov}(\theta_j, \theta_k)$ is the *covariance matrix*. The j-th element on the diagonal of the covariance matrix is the variance of θ_j.

3.2.2 Image quantification

Recall from chapter 2 that, for a tracer distribution $\Lambda = [\lambda_1, \lambda_2, \cdots, \lambda_J]^T$ and a given acquisition system with the system matrix A, the expected data is $Y = A\Lambda + S$, where S represents the presence of scatter (and possibly also crosstalk) in the data. The actually acquired data is $Q(\Lambda) = [q_1, q_2, \cdots, q_I]^T$. The tracer distribution can be estimated based on the measured data $Q(\Lambda)$ using a reconstruction algorithm. The estimated image is denoted as $\hat{\Lambda} = [\hat{\lambda}_1, \hat{\lambda}_2, \cdots, \hat{\lambda}_J]^T$. For later reference, we denote $\bar{Q} \triangleq Y$ as the noiseless data and $\check{\Lambda} \triangleq \hat{\Lambda}(\bar{Q})$ as the corresponding estimated image.

Similar to (3.1), the mean of the estimate $\hat{\mu}(\Lambda)$ can be calculated based on N times repeated simulations with the same tracer distribution Λ:

$$\hat{\mu}(\Lambda) = \frac{1}{N} \sum_{n=1}^{N} \hat{\Lambda}(Q^{(n)}) \tag{3.10}$$

where $Q^{(n)}$ is the n-th measurement of Λ.

Measures for pixel

Each pixel in the reconstruction image can be considered as a single variate. Therefore for each pixel we can calculate the bias and the variance, as well as the covariance between this pixel and all the other pixels in the reconstruction image. The calculation is the same as explained in 3.2.1, i.e., the variance in pixel j and the covariance between pixel j and k are computed as

$$\mathrm{Var}^j = \frac{1}{N-1} \sum_{n=1}^{N} \left(\hat{\lambda}_j(Q^{(n)}) - \hat{\mu}(\lambda_j) \right)^2 \tag{3.11}$$

$$\mathrm{Cov}(\hat{\lambda}_j, \hat{\lambda}_k) = \frac{1}{N-1} \sum_{n=1}^{N} \left(\hat{\lambda}_j(Q^{(n)}) - \hat{\mu}(\lambda_j) \right) \left(\hat{\lambda}_k(Q^{(n)}) - \hat{\mu}(\lambda_k) \right) \tag{3.12}$$

The covariance matrix of the reconstruction image is a $J \times J$ matrix, whose (j,k)-th element is

$$[\mathrm{Cov}(\hat{\Lambda})]_{j,k} = \mathrm{Cov}(\hat{\lambda}_j, \hat{\lambda}_k) \tag{3.13}$$

Given the relatively large number of image pixels in emission tomography, this matrix tends to be huge for realistic systems, making it impractical to compute the entire covariance matrix in practice.

Measures for ROI

Sometimes we are interested in ROIs rather than pixels. In this case, estimation of the mean and the variance in a given ROI is important. The mean of the ROI (Mean(ROI)) and the variance on this mean (Var(ROI)) in the reconstruction image are calculated as

$$\mathrm{Mean(ROI)} = \frac{1}{N} \sum_{n=1}^{N} \left(\frac{1}{N_R} \sum_{j \in \mathrm{ROI}} \hat{\lambda}_j(Q^{(n)}) \right) = \frac{1}{N_R} \sum_{j \in \mathrm{ROI}} \hat{\mu}(\lambda_j) \tag{3.14}$$

$$\mathrm{Var(ROI)} = \frac{1}{N-1}\sum_{n=1}^{N}\left[\frac{1}{N_R}\sum_{j\in\mathrm{ROI}}\hat{\lambda}_j(Q^{(n)}) - \mathrm{Mean(ROI)}\right]^2 \tag{3.15}$$

where N_R is the total number of pixels in the ROI. Var(ROI) can also be calculated from the covariance matrix, i.e.,

$$\mathrm{Var(ROI)} = \sum_{j\in\mathrm{ROI}}\sum_{k\in\mathrm{ROI}}\mathrm{Cov}(\hat{\lambda}_j, \hat{\lambda}_k) \tag{3.16}$$

In the simulation where the ground true Λ is known, we can calculate the MSE for a ROI:

$$\mathrm{MSE(ROI)} = \sum_{j\in\mathrm{ROI}}\left(\hat{\lambda}_j - \lambda_j\right)^2 \tag{3.17}$$

Another commonly used measure is root mean squared error (RMSE), sometime also called root mean square deviation (RMSD), defined as

$$\mathrm{RMSE(ROI)} = \sqrt{\mathrm{MSE(ROI)}} = \sqrt{\sum_{j\in\mathrm{ROI}}\left(\hat{\lambda}_j - \lambda_j\right)^2} \tag{3.18}$$

Measures for lesion

For evaluation of lesion detection and quantification, one often considers simplified lesions, consisting of a uniform increased (hot) or decreased (cold) tracer uptake compared to the surrounding tissue. In [58] and [67], three measures for lesion detection in a reconstruction image were proposed: hot spot recovery coefficient (HSRC, hot lesions in a cold background), cold spot recovery coefficient (CSRC, cold lesion in hot background) and the contrast recovery coefficient (CRC, the contrast in the reconstruction image divided by the contrast in the original tracer distribution). These measures are defined as

$$\mathrm{HSRC} = \frac{\mathrm{Mean(lesion)}}{\mathrm{True(lesion)}} \tag{3.19}$$

$$\mathrm{CSRC} = \frac{\mathrm{Mean(lesion)}}{\mathrm{Mean(background)}} \tag{3.20}$$

$$\mathrm{CRC} = \frac{\left(\mathrm{Mean(lesion)} - \mathrm{Mean(background)}\right)/\mathrm{Mean(background)}}{\left(\mathrm{True(lesion)} - \mathrm{True(background)}\right)/\mathrm{True(background)}} \tag{3.21}$$

where lesion and background refer to ROIs in the lesion and the background, respectively, and True(ROI) is the true of the mean value in the assigned ROI, given by

$$\mathrm{True(ROI)} = \frac{1}{N_R}\sum_{j\in\mathrm{ROI}}\lambda_j \tag{3.22}$$

Note that CRC has another definition which is correlated to the concept of the impulse response and the resolution in the reconstruction image rather than to the lesion detection [107]. That definition will be introduced in 3.2.3 and will be actually applied as a measure of the resolution in the post-smoothed MLEM reconstructions in the subsequent chapters.

3.2.3 Image quality evaluation

Impulse response

For an imaging system, usually we use the point spread function (PSF) or the modulation transfer function (MTF) to describe the system response to a point input in spatial domain or frequency domain, respectively [14]. In emission tomography, there are two types of PSF. The first one is the response to a point source which is purely determined by the system itself (see 2.1.3). The second one is the response to a point source which is defined in the reconstruction image. As a simple illustration, if we scan a single point source, the acquired data and the reconstructed image can be described by the first and the second PSF, respectively. To avoid confusion, a more general term *impulse response* is used to refer to the second definition.

In emission tomography, the impulse response is usually shift-variant due to the system geometry and the properties of the reconstruction algorithm, meaning that different locations in the field of view correspond to different impulse responses [46]. This shift-variant property precludes the use of global PSF or MTF for analysis. If we add one single impulse δ at location j in the object Λ, the measured data is $Q(\Lambda + \delta e^j)$ instead of $Q(\Lambda)$, with e^j the j-th unit vector. The impulse response is defined by

$$l^j(\hat{\Lambda}) \quad = \quad \lim_{\delta \to 0} \frac{\left\langle \hat{\Lambda}(Q(\Lambda + \delta e^j)) \right\rangle - \left\langle \hat{\Lambda}(Q(\Lambda)) \right\rangle}{\delta} \tag{3.23}$$

With repeated simulations, the impulse response at the pixel location j can be approximated as

$$l^j(\hat{\Lambda}) \approx \frac{\hat{\mu}(\Lambda + \delta e^j) - \hat{\mu}(\Lambda)}{\delta} \tag{3.24}$$

Due to the shift-variant property and the large number of pixels in the image, the impulse response is often studied locally in emission tomography.

Resolution

An important measure about image quality is the spatial resolution in the reconstruction image. Note that the resolution discussed here is not the same as the system resolution mentioned in chapter 2, but closely related to the impulse response. If the impulse response is Gaussian, the resolution refers to the FWHM of the Gaussian profile. In general, the resolution in the reconstruction is determined by the following factors:

- The system response to a single point source (the blurring effect due to finite system resolution),
- the acquisition model used for reconstruction (whether or not the blurring effects are incorporated in the acquisition model),
- the choice and the setting of the reconstruction method (the properties of the filter used for the analytical algorithm, or the iteration scheme and the regularization used for iterative algorithms)
- and the post-processing of the reconstructed image.

Contrast recovery coefficient

As mentioned before, the contrast recovery coefficient (CRC) has two different definitions. One is a measure of how much contrast is recovered in the reconstructed image (see (3.21)). The other definition is the j-th element of the impulse response at pixel j [107], i.e.,

$$\mathrm{CRC}^j = l_j^j(\hat{\Lambda}) \tag{3.25}$$

By this definition, the CRC is actually the peak value of the impulse response. It means that a larger CRC corresponds to a narrower impulse response which has a smaller FWHM. Therefore the CRC is closely related to the resolution in the reconstruction, and vice versa[1]. In the scope of this PhD work, we use (3.25) rather than (3.21) as the definition of CRC since we apply the post-smoothed MLEM which always requires a target resolution in reconstruction.

Contrast-to-noise ratio

Usually there is a trade-off between the quantification accuracy and the noise in the reconstruction image. Therefore these two properties are often combined as one figure of merit. One example is the contrast-to-noise ratio (CNR) which is defined as follows:

$$\mathrm{CNR} = \frac{\mathrm{CRC}}{\sqrt{\mathrm{Var}}} \tag{3.26}$$

If two reconstruction images are forced to have the same spatial resolution, they have the same pixel CRCs. If we compare the two systems in this case, the ratio of the CNR values is actually the ratio of the squared root of the variances.

---

[1] This holds in most of the cases, especially when the impulse response is Gaussian-shaped. However, one should note that if the profile of the impulse response is very non-Gaussian, the relation between the CRC and the resolution might be different.

Signal-to-noise ratio

Another commonly used figure of merit is the signal-to-noise ratio (SNR) which is

$$\mathrm{SNR} = \frac{\mathrm{Signal}}{\sqrt{\mathrm{Var}}} \tag{3.27}$$

The SNR can be calculated for a single pixel or a ROI in the reconstruction image, with Signal defined as the pixel value or the mean value on the ROI, respectively.

Application of observers

Based on the reconstruction image, very often we need to decide whether there is a lesion or not, which is a *classification* problem [12,13]. To evaluate the system performance in classification tasks, we can apply an *observer* to the image [84,120,121]. The observer can be a human who is trained to make a diagnosis, or a mathematical model or a computer algorithm. A standard method to study the lesion detectability is the receiver operating characteristic (ROC) study, which compares the true positive versus false positive rates for human observers [84, 120, 121]. Since the human observer is very time-consuming and requires a large number of images, numerical observers were developed, which greatly reduce the time for ROC analysis. The objective of the mathematical model is to simulate the performance of human observers.

Given a reconstruction image $\hat{\Lambda}$, a linear numerical observer calculates a scalar test statistic by

$$\eta(\hat{\Lambda}) = s^T \hat{\Lambda} \tag{3.28}$$

with s the observer template. For a binary classification problem, we compare this statistic to a predefined threshold to decide whether or not there is a lesion present. If $\eta(\hat{\Lambda})$ exceeds the decision threshold then $\hat{\Lambda}$ is determined to have a lesion (positive), otherwise there is no lesion (negative). If there is really a lesion present, the positive and the negative decision is called a true positive (TP) and a false negative (FN), and if there is actually no lesion, the corresponding decision is called a false positive (FP) and a true negative (TN), respectively.

For binary classification tests, the performance of the observer can be evaluated by two statistical measures, namely the sensitivity and the specificity:

$$\mathrm{sensitivity} = \frac{\mathrm{TP}}{\mathrm{TP+FN}} \tag{3.29}$$

$$\mathrm{specificity} = \frac{\mathrm{TN}}{\mathrm{TN+FP}} \tag{3.30}$$

The tradeoff between the sensitivity and the specificity is often analyzed with a ROC curve (see Fig. 3.1), which is a plot of true positive rate (TPR, = sensitivity) versus false positive rate (FPR, = 1-specificity). The area under the ROC curve

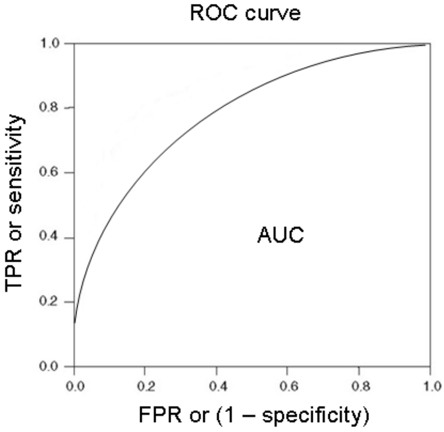

Figure 3.1: Example of a ROC curve.

(AUC) is often used to measure the lesion detectability. AUC ranges from 0.5 which indicates a worthless test to 1.0 which corresponds to a perfect one.

The detection performance can also be quantified by the SNR of $\eta(\hat{\Lambda})$ [84, 120, 121], which sometimes is also called detectability index. It is defined by

$$\mathrm{SNR}^2(\hat{\Lambda}) = \frac{\left(\left\langle \eta(\hat{\Lambda})|H_1 \right\rangle - \left\langle \eta(\hat{\Lambda})|H_0 \right\rangle\right)^2}{\left(\mathrm{Var}(\eta(\hat{\Lambda})|H_1) + \mathrm{Var}(\eta(\hat{\Lambda})|H_0)\right)/2} \tag{3.31}$$

where H_0 is the null hypothesis representing lesion absent and H_1 is the hypothesis representing lesion present. If $\eta(\hat{\Lambda})$ obeys a Gaussian distribution, the SNR is related to the AUC by

$$\mathrm{AUC} = \frac{1}{2}\left[1 + \mathrm{erf}\left(\frac{\mathrm{SNR}}{2}\right)\right] \tag{3.32}$$

where $\mathrm{erf}(\cdot)$ is the error function.

There exist various types of numerical observers. The difference between them is the calculation of the test statistic $\eta(\hat{\Lambda})$. For better illustration, first we define the profile of the lesion as

$$z \equiv \left\langle \hat{\Lambda}|H_1 \right\rangle - \left\langle \hat{\Lambda}|H_0 \right\rangle \tag{3.33}$$

where $\left\langle \hat{\Lambda}|H_1 \right\rangle$ and $\left\langle \hat{\Lambda}|H_0 \right\rangle$ are the expectations of $\hat{\Lambda}$ with and without the lesion, respectively.

To detect a nonrandom signal in white Gaussian noise, the optimal choice is a nonprewhitening (NPW) observer, which applies a simple matched filter to calculate $\eta(\hat{\Lambda})$ [16, 81, 123]:

$$\eta_{\mathrm{NPW}}(\hat{\Lambda}) = z^T \hat{\Lambda} \tag{3.34}$$

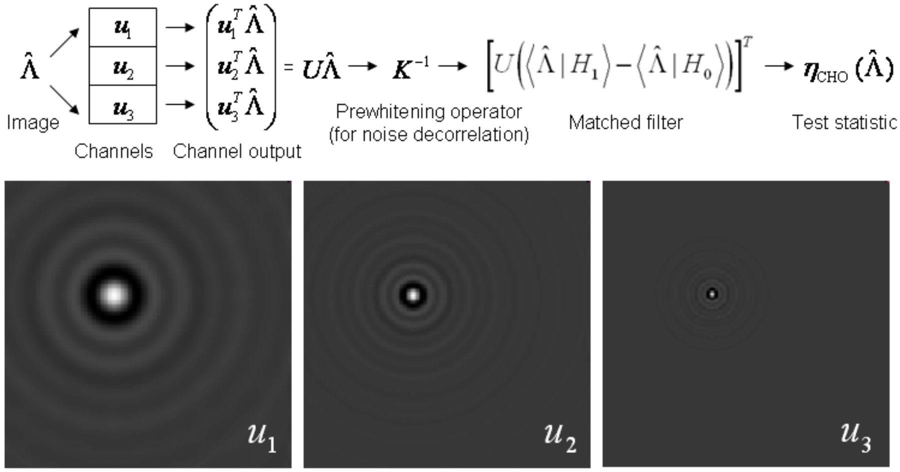
$\hat{\Lambda}$
Image
u_1
u_2
u_3
Channels
$u_1^T\hat{\Lambda}$
$u_2^T\hat{\Lambda}$
$u_3^T\hat{\Lambda}$
Channel output
$= U\hat{\Lambda}$
K^{-1}
Prewhitening operator (for noise decorrelation)
$\left[U\left(\langle\hat{\Lambda}|H_1\rangle - \langle\hat{\Lambda}|H_0\rangle\right)\right]^T$
Matched filter
$\eta_{\mathrm{CHO}}(\hat{\Lambda})$
Test statistic
u_1
u_2
u_3

Figure 3.2: Upper row: flow chart about the calculation of $\eta_{\mathrm{CHO}}(\hat{\Lambda})$ [50] using three channels. Lower row: DOG channel templates, the frequency is increased from left to right.

If the noise is Gaussian but correlated, it is better to apply the prewhitening (PW) observer which incorporates a prewhitening operation in the calculation of the $\eta(\hat{\Lambda})$ [16, 123]:

$$\eta_{\mathrm{PW}}(\hat{\Lambda}) = z^T[\mathrm{Cov}(\hat{\Lambda})]^{-1}\hat{\Lambda} \tag{3.35}$$

with $\mathrm{Cov}(\hat{\Lambda})$ the covariance matrix of $\hat{\Lambda}$.

The most popular observers are the channelized Hotelling observers (CHOs) because they have a good correlation with human performance [50, 92, 93, 147]. This correlation is influenced by the lesion properties and the choice of the channel functions. The test statistic of CHO is

$$\eta_{\mathrm{CHO}}(\hat{\Lambda}) = z^T U^T K^{-1}(U\hat{\Lambda} + n) \tag{3.36}$$

where U represents a set of frequency-selective channels which mimic the human visual system, n is the channel noise which models the uncertainty in the human detection process. K is the covariance matrix of the channel outputs, which is

$$K = \frac{1}{2}U\left(\mathrm{Cov}(\hat{\Lambda}|H_1) + \mathrm{Cov}(\hat{\Lambda}|H_0)\right)U^T + K_N \tag{3.37}$$

where K_N is the covariance of the internal noise. $\mathrm{SNR}_{\mathrm{CHO}}$ can be written as:

$$\mathrm{SNR}_{\mathrm{CHO}} = \sqrt{z^T U^T K^{-1} U z} \tag{3.38}$$

A simple example for the calculation of $\eta_{\mathrm{CHO}}(\hat{\Lambda})$ using a difference-of-gaussian (DoG) model [1] with three channels is given in Fig. 3.2.

3.3 Analytical evaluation methods

As explained before, the figures of merit proposed in 3.2 can be calculated with repeated simulations. However, to achieve accurate estimates, a large number of noise realizations are required, which makes the simulation-based methods very time-consuming. A more efficient alternative is to calculate the figures of merit in an analytical way. In [15], analytical expressions for the mean and the variance were given as a function of iteration number for MLEM reconstruction. The idea was extended and applied for OSL-MAP EM algorithm in [140]. This approach is useful for the evaluation of the system performance with reconstructions stopped at early iterations, however it can only be applied to the algorithms with explicit update equations with certain approximations.

As a complementary approach, Fessler et al. proposed a method which analyzes the resolution, the mean and the covariance matrix for iterative reconstruction at the point of convergence [43, 46]. The properties of the noise and the resolution were studied by computing partial derivatives of the objective function and truncated Taylor expansion approximations. This method is consistent with the one proposed in [15] when the algorithm iterates till convergence [101, 103]. The advantage of this method is that it does not require explicit expressions for the objective function, and that it can be easily extended for the calculation of other FOMs. In [107, 108], it was extended to derive the simplified expressions for the local impulse response and the covariance matrix using Fourier transform. Later, this method was applied for the estimation of the bias and the variance in regions of interest [106], as well as the evaluation of the systems in lesion detectability with numerical observers [102, 104, 149, 151, 152]. Other interesting extensions include [63, 69, 82, 138, 158]. Since this approach incorporates the computation of the *Fisher information matrix*, it is referred to as *Fisher information-based methods* in the remainder of the text.

In this section, we focus on how to analytically calculate the most relevant FOMs with the Fisher information-based method. We first introduce the basic concepts in 3.3.1, and then explain how to derive the analytical expressions for the FOMs in 3.3.2. Based on the basic equations which can be applied to any objective function, the expressions for the local impulse response, the covariance matrix, the measures for the ROI and the SNR for the channelized Hotelling observer were first derived for the converged MAP reconstruction and were then adapted for the post-smoothed MLEM reconstruction.

3.3.1 Key concepts

Fisher information matrix

The Fisher information is an important concept in the theory of statistical inference. It measures the amount of information that an observable random variable X carries about an unknown parameter θ [57, 79, 123].

Definition. The Fisher information is defined in a following way: given an observation X and a vector $\Theta = [\theta_1, \cdots, \theta_K]^T$ as the unknown parameters, the Fisher

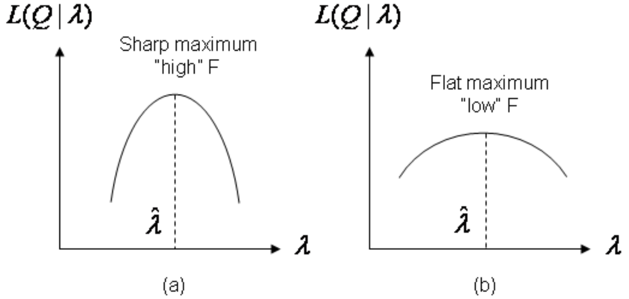

Figure 3.3: Plot of log-likelihood. (a) curve with sharp maximum. (b) curve with flat maximum.

information matrix $F(\Theta)$ is a $K \times K$ symmetric matrix whose (j,k)-th element is the covariance between first partial derivatives of the log-likelihood:

$$[F(\Theta)]_{j,k} = \mathrm{Cov}\left[\frac{\partial \ln p(X|\Theta)}{\partial \theta_j}, \frac{\partial \ln p(X|\Theta)}{\partial \theta_k}\right] \tag{3.39}$$

An alternative but equivalent definition is based on the expected values of the second partial derivatives

$$[F(\Theta)]_{j,k} = -\left\langle \frac{\partial^2 \ln p(X|\Theta)}{\partial \theta_j \partial \theta_k} \right\rangle \tag{3.40}$$

where $p(X|\Theta)$ is the conditional probability density function of the data. Note that the Fisher information matrix depends on the parameters to be estimated. Therefore, one should specify which Fisher information is used for the data analysis.

In emission tomography, the observable variable and the parameter to be estimate are the acquired data Q and the original tracer distribution Λ, respectively. Using the notations defined in chapter 2, the (j,k)-th element of the Fisher information matrix of the reconstruction image is given by

$$[F(\Lambda)]_{j,k} = -\left\langle \frac{\partial^2 L(Q|\Lambda)}{\partial \lambda_j \partial \lambda_k} \right\rangle \tag{3.41}$$

It can be considered as a measure of the sharpness of the peak of the log-likelihood curve [Fig. 3.3]. A sharp maximum represents the problem is well-posed, and a flat maximum corresponds to an ill-posed case.

Cramér-Rao bound. If Λ is estimated by an unbiased estimator and if $F(\Lambda)$ is nonsingular, an important inequality is given by

$$\mathrm{Var}(\hat{\lambda}_j) \geq [F^{-1}(\Lambda)]_{jj} \tag{3.42}$$

which gives the lower bound of the variance on the estimate $\hat{\lambda}_j$, called *Cramér-Rao bound* [33, 57, 79, 123]. An estimator which achieves this lower bound is called *efficient.* To be general, a bound can be placed on the covariance matrix of the estimate, which is given by

$$\mathrm{Cov}(\hat{\Lambda}) \geq [F^{-1}(\Lambda)] \tag{3.43}$$

which means that $\mathrm{Cov}(\hat{\lambda}) - [F^{-1}(\Lambda)]$ is positive semidefinite. For an efficient and unbiased estimator, the inequality in (3.43) becomes an equality, where the covariance matrix is the inverse of the Fisher information matrix. Since the covariance is a measure of the uncertainty, the Fisher information matrix is actually a measure of certainty. This explains why it is involved in the analytical expressions of many FOMs that are closely related to the system performance [13].

Gaussian noise model. If we assume that the data in the measurement follow a Gaussian distribution, with the expressions given in (2.32) the likelihood is

$$p(Q|\Lambda) = \prod_i \frac{1}{\sqrt{2\pi}\sigma_i} e^{-(q_i - \sum_j a_{ij}\lambda_j - s_i)^2/(2\sigma_i^2)} \tag{3.44}$$

and the log-likelihood is

$$L(Q|\Lambda) = -\frac{1}{2}\sum_i (q_i - \sum_j a_{ij}\lambda_j - s_i)^2/\sigma_i^2 \tag{3.45}$$

The first and the second derivatives are calculated as

$$\begin{aligned} \frac{\partial L}{\partial \lambda_j} &= \sum_i \frac{q_i a_{ij} - a_{ij}\sum_k a_{ik}\lambda_k - s_i a_{ij}}{\sigma_i^2} \\ \frac{\partial^2 L}{\partial \lambda_j^2} &= -\sum_i \frac{a_{ij}^2}{\sigma_i^2} \\ \frac{\partial^2 L}{\partial \lambda_j \partial \lambda_k} &= -\sum_i \frac{a_{ij}a_{ik}}{\sigma_i^2} \end{aligned} \tag{3.46}$$

By definition, the Fisher information matrix is

$$F(\Lambda) = A^T C_Q^{-1} A \tag{3.47}$$

where $C_Q \triangleq \mathrm{Cov}(Q) = D[\sigma_i^2]$ is the covariance matrix of the acquired data, with $D[\cdot]$ representing the diagonal matrix.

Poisson noise model. With the Poisson noise model, the likelihood is given by

$$p(Q|\Lambda) = \prod_i \frac{e^{-(\sum_j a_{ij}\lambda_j + s_i)}(\sum_j a_{ij}\lambda_j + s_i)^{q_i}}{q_i!} \tag{3.48}$$

with the log-likelihood

$$L(Q|\Lambda) = \sum_i \left(q_i \ln(\sum_j a_{ij}\lambda_j + s_i) - \sum_j a_{ij}\lambda_j - s_i - \ln q_i! \right)$$

The partial derivatives are

$$\begin{aligned}
\frac{\partial L}{\partial \lambda_j} &= -\sum_i a_{ij}\left(\frac{q_i}{\sum_j a_{ij}\lambda_j + s_i} - 1\right) \\
\frac{\partial^2 L}{\partial \lambda_j \partial \lambda_k} &= -\sum_i \frac{a_{ij}a_{ik}q_i}{(\sum_j a_{ij}\lambda_j + s_i)^2} = -\sum_i \frac{a_{ij}a_{ik}q_i}{y_i^2}
\end{aligned} \tag{3.49}$$

Using $\bar{q}_i(\Lambda)$ to denote the noiseless data y_i, the (j,k)-th element of the Fisher information matrix is calculated as

$$[F(\Lambda)]_{j,k} = -\left\langle \frac{\partial^2 L}{\partial \lambda_j \partial \lambda_k} \right\rangle = \sum_i a_{ij}\left[\frac{\langle q_i \rangle}{\bar{q}_i^2(\Lambda)}\right] a_{ik} = \sum_i a_{ij}\left[\frac{1}{\bar{q}_i(\Lambda)}\right] a_{ik} \tag{3.50}$$

The last equal sign is due to $\langle q_i \rangle = \bar{q}_i(\Lambda)$ [13].

The matrix format of (3.50) is given by

$$F(\Lambda) = A^T D\left[\frac{1}{\bar{q}_i(\Lambda)}\right] A \tag{3.51}$$

Linearization

In order to analyze the performance of the nonlinear imaging system, we assume that the system is locally linear. With this assumption, the behavior of the system near a given point can be approximately described by a linear function. We call this *linearization*. For the function $y = f(x)$, the equation of linearization at the point of interest $x = x_0$ is given by

$$y = f(x_0) + \left.\frac{\partial f}{\partial x}\right|_{x_0} (x - x_0) \tag{3.52}$$

which is actually the first-order Taylor expansion of the function.

For a multi-variable function Y = f(X), we have

$$Y = f(X_0) + \nabla f \Big|_{X_0} (X - X_0) \tag{3.53}$$

where X is the vector of variables, X_0 is the linearization point of interest, ∇ is a row gradient operator, and ∇f is a matrix consisting of the first-order derivatives of f with respect to each single variable in the vector X.

3.3.2 Fisher information-based method

In this section we will briefly explain how to estimate the linear impulse response, the covariance matrix of the reconstruction image and some other figures of merit based on the calculation of the Fisher information matrix.

Basic derivations

In emission tomography, many estimators are implicitly defined as the maximizers of a certain objective function, which is either the likelihood or the posterior:

$$\hat{\Lambda} = \hat{\Lambda}(Q) = \arg\max_{\lambda \geq 0} \Phi(\Lambda, Q) \tag{3.54}$$

There is no analytical solution for such an estimator, therefore iterative algorithms are often applied. If we ignore the non-negativity constraint, the maximum of Φ satisfies:

$$\tfrac{\partial}{\partial \lambda_j} \Phi(\Lambda, Q)\big|_{\Lambda=\hat{\Lambda}} = 0 \quad (j = 1, \cdots, J) \tag{3.55}$$

We want to compute how the solution $\hat{\Lambda}$ changes as a function of small variations in Q. To this end, we take the derivative with respect to q_i at $\Lambda = \hat{\Lambda}$, with the chain rule it yields

$$\sum_k \frac{\partial^2}{\partial \lambda_j \partial \lambda_k} \Phi(\hat{\Lambda}, Q) \frac{\partial}{\partial q_i} \hat{\lambda}_k(Q) + \frac{\partial^2}{\partial \lambda_j \partial q_i} \Phi(\hat{\Lambda}, Q) = 0 \tag{3.56}$$

The matrix notation of (3.56) is denoted as

$$\nabla^{20} \Phi(\hat{\Lambda}, Q) \nabla_q \hat{\Lambda}(Q) + \nabla^{11} \Phi(\hat{\Lambda}, Q) = 0 \tag{3.57}$$

where the (j, k)th elements of ∇^{20} is $\partial^2/\partial\lambda_j\partial\lambda_k$, the (j, i)th element of ∇^{11} is $\partial^2/\partial\lambda_j\partial q_i$, and ∇_q is the row gradient operator. If $-\nabla^{20}\Phi(\hat{\Lambda}, Q)$ is positive definite, we can solve $\nabla_q\hat{\Lambda}(Q)$ by

$$\nabla_q \hat{\Lambda}(Q) = [-\nabla^{20} \Phi(\hat{\Lambda}(Q), Q)]^{-1} \nabla^{11} \Phi(\hat{\Lambda}(Q), Q) \tag{3.58}$$

(3.58) is used to derive the expressions for the linear impulse response and the covariance matrix of the reconstruction image.

Mean value. Previous studies state that, with a likelihood-based estimator, the expectation of the estimate is approximately equal to the value that one obtains by estimating the noiseless data $\bar{Q}$ [15, 29, 146]:

$$\left\langle \hat{\Lambda}(Q) \right\rangle \approx \hat{\Lambda}(\bar{Q}) \triangleq \check{\Lambda} \tag{3.59}$$

Linearized local impulse response. Recall from 3.2.3 that the local impulse response is defined by (3.23), i.e.,

$$l^j(\hat{\Lambda}) = \lim_{\delta \to 0} \frac{\left\langle \hat{\Lambda}(Q(\Lambda + \delta e^j)) \right\rangle - \left\langle \hat{\Lambda}(Q(\Lambda)) \right\rangle}{\delta}$$

The assumption of (3.59) is equivalent to assuming that the estimator is locally linear [46]. Substituting (3.59) into (3.23) yields the definition of the *linearized* *local impulse response* (LLIR):

$$\begin{aligned} l^j(\Lambda) &\approx \lim_{\delta\to 0} \frac{\hat{\Lambda}(\bar{Q}(\Lambda+\delta e^j)) - \hat{\Lambda}(\bar{Q}(\Lambda))}{\delta} \\ &= \frac{\partial}{\partial\lambda_j}\hat{\Lambda}(\bar{Q}) \end{aligned} \tag{3.60}$$

Applying the chain rule to (3.60), it yields

$$\begin{aligned} l^j(\hat{\Lambda}) &\approx \nabla_q \hat{\Lambda}(\bar{Q}(\Lambda)) \frac{\partial}{\partial\lambda_j}\bar{Q}(\Lambda) \\ &= [-\nabla^{20}\Phi(\hat{\Lambda}(\bar{Q}),\bar{Q})]^{-1}\nabla^{11}\Phi(\hat{\Lambda}(\bar{Q}),\bar{Q})\frac{\partial}{\partial\lambda_j}\bar{Q}(\Lambda) \end{aligned} \tag{3.61}$$

Covariance matrix. In order to find a good approximation for the covariance matrix of the reconstruction, the estimate $\hat{\Lambda}(Q)$ is linearized near the point $Q = \bar{Q}$ using (3.53):

$$\hat{\Lambda}(Q) \approx \hat{\Lambda}(\bar{Q}) + \nabla_q\hat{\Lambda}(\bar{Q})\bigg|_{Q=\bar{Q}} (Q-\bar{Q}) \tag{3.62}$$

Taking the covariance of both sides yields

$$\mathrm{Cov}(\hat{\Lambda}(Q)) \approx \nabla_q\hat{\Lambda}(\bar{Q}) \cdot \mathrm{Cov}(Q) \cdot [\nabla_q\hat{\Lambda}(\bar{Q})]^T \tag{3.63}$$

Combining (3.63) and (3.58), we have the general approximation for the covariance matrix of the estimator:

$$\begin{aligned} \mathrm{Cov}(\hat{\Lambda}(Q)) \approx [-\nabla^{20}\Phi(\hat{\Lambda}(\bar{Q}),\bar{Q})]^{-1} \cdot \nabla^{11}\Phi(\hat{\Lambda}(\bar{Q}),\bar{Q}) \cdot \mathrm{Cov}(\bar{Q}) \\ \cdot[\nabla^{11}\Phi(\hat{\Lambda}(\bar{Q}),\bar{Q})]^T \cdot [-\nabla^{20}\Phi(\hat{\Lambda}(\bar{Q}),\bar{Q})]^{-1} \end{aligned} \tag{3.64}$$

Prediction for MAP reconstruction

Based on the basic equations (3.61) and (3.64), analytical expressions for the LLIR and the covariance matrix were proposed for converged MAP reconstructions [43, 46].

As discussed in chapter 2, the objective function that is maximized with the MAP reconstruction has the form of

$$\Phi(\Lambda, Q) = L(Q|\Lambda) - \beta M(\Lambda) \tag{3.65}$$

where $L(Q|\Lambda)$ is the log-likelihood, β is the regularization parameter and $M(\Lambda)$ is the log-prior. With a Poisson noise model, the derivatives of the log-likelihood are

$$-\nabla^{20}L(Q|\Lambda) = A^T D\left[\frac{q_i}{\bar{q}_i^2(\Lambda)}\right] A \tag{3.66}$$

$$\nabla^{11}L(Q|\Lambda) = A^T D\left[\frac{1}{\bar{q}_i(\Lambda)}\right] \tag{3.67}$$

with which we have

$$-\nabla^{20}\Phi(\Lambda,Q) = A^T D\left[\frac{q_i}{\bar{q}_i^2(\Lambda)}\right]A+\beta\boldsymbol{R}(\Lambda) \tag{3.68}$$

$$\nabla^{11}\Phi(\Lambda,Q) = A^T D\left[\frac{1}{\bar{q}_i(\Lambda)}\right] \tag{3.69}$$

where $\boldsymbol{R}(\Lambda)$ is the Hessian matrix of the log-prior, i.e., a square matrix containing the second-order partial derivatives of $M(\Lambda)$.

Linearized local impulse response. Substituting (3.68) and (3.69) into (3.61) with $Q=\bar{Q}$ and $\Lambda=\check{\Lambda}$, and note that $(\partial/\partial\lambda_j)\bar{Q}(\Lambda)=Ae^j$, it yields

$$l^j(\hat{\Lambda}) \approx [A^T D\left[\frac{\bar{q}_i(\Lambda)}{\bar{q}_i^2(\check{\Lambda})}\right]A+\beta\boldsymbol{R}(\check{\Lambda})]^{-1}A^T D\left[\frac{1}{\bar{q}_i(\check{\Lambda})}\right]Ae^j \tag{3.70}$$

Since the projection is a smoothing operation, $\bar{q}_i(\check{\Lambda})$ and $\bar{q}_i(\Lambda)$ is very similar [46]. Therefore the LLIR approximation of MAP estimator can be simplified by

$$l^j(\hat{\Lambda}) \approx [\boldsymbol{F}+\beta\boldsymbol{R}(\check{\Lambda})]^{-1}\boldsymbol{F}e^j \tag{3.71}$$

with the Fisher information matrix

$$\boldsymbol{F}=A^T D\left[\frac{1}{\bar{q}_i(\check{\Lambda})}\right]A \tag{3.72}$$

The j-th diagonal element of the diagonal matrix in (3.72) is the reciprocal of the variance of q_i under Poisson statistics.

Covariance matrix. Applying (3.68) and (3.69) to (3.64), and assuming that $\bar{q}_i(\Lambda)\approx\bar{q}_i(\check{\Lambda})$, we have

$$\mathrm{Cov}(\hat{\Lambda}) \approx [\boldsymbol{F}+\beta\boldsymbol{R}(\check{\Lambda})]^{-1}\boldsymbol{F}[\boldsymbol{F}+\beta\boldsymbol{R}(\check{\Lambda})]^{-1} \tag{3.73}$$

ROI quantification. Following the idea proposed in [106], we can evaluate the system performance based on ROI quantification. Let the total activity inside the ROI be

$$\lambda_{\mathrm{ROI}}=f^T\Lambda \tag{3.74}$$

where f is the vector of the ROI with $f[j]$ equal to 1 if the pixel j is inside the ROI, and 0 otherwise. In general, the bias and the variance of this ROI are

$$\mathrm{Bias}(\lambda_{\mathrm{ROI}}) = f^T\left\langle\hat{\Lambda}\right\rangle-f^T\Lambda \tag{3.75}$$

$$\mathrm{Var}(\lambda_{\mathrm{ROI}}) = f^T\mathrm{Cov}(\hat{\Lambda})f \tag{3.76}$$

For the analysis of a ROI surrounded by uniform background, we use Λ_0 to denote a reference image where the activity inside the ROI is equal to the uniform background. Let $\Delta_{\mathrm{ROI}}=\Lambda-\Lambda_0$ which represents the activity inside the ROI above the background. One approximation is that the reconstruction of the uniform background is unbiased inside the ROI, i.e.,

$$f^T\langle\hat{\Lambda}_0\rangle - f^T\Lambda_0 \approx 0 \tag{3.77}$$

Applying (3.77) to (3.75), we have

$$\begin{aligned}\mathrm{Bias}(\lambda_{\mathrm{ROI}}) &\approx f^T\left\langle\hat{\Lambda}\right\rangle - f^T\Lambda + f^T\Lambda_0 - f^T\left\langle\hat{\Lambda}_0\right\rangle \\ &\approx f^T\check{\Lambda} - f^T\Lambda + f^T\Lambda_0 - f^T\check{\Lambda}_0 \\ &= f^T(\check{\Lambda}-\check{\Lambda}_0) - f^T(\Lambda-\Lambda_0)\end{aligned} \tag{3.78}$$

Using the first-order Taylor expansion, it yields

$$\mathrm{Bias}(\lambda_{\mathrm{ROI}}) \approx -\nabla_q(\hat{\Lambda}(\bar{Q}))\Delta_{\mathrm{ROI}} - f^T\Delta_{\mathrm{ROI}} \tag{3.79}$$

Applying the expression for $-\nabla_q(\hat{\Lambda}(\bar{Q}))$, we have

$$\mathrm{Bias}(\lambda_{\mathrm{ROI}}) \approx f^T[\boldsymbol{F} + \beta\boldsymbol{R}(\check{\Lambda})]^{-1}\boldsymbol{F}\Delta_{\mathrm{ROI}} \tag{3.80}$$

The expression for the variance on λ_{ROI} can be directly derived as

$$\mathrm{Var}(\lambda_{\mathrm{ROI}}) \approx f^T[\boldsymbol{F} + \beta\boldsymbol{R}(\check{\Lambda})]^{-1}\boldsymbol{F}[\boldsymbol{F} + \beta\boldsymbol{R}(\check{\Lambda})]^{-1}f \tag{3.81}$$

We denote the bias on the mean activity in the ROI and the variance on that mean by Bias(ROI) and Var(ROI), respectively. If the total number of image pixels in the ROI is N_R, these two measures are

$$\mathrm{Bias(ROI)} \approx \frac{1}{N_R}f^T[\boldsymbol{F} + \beta\boldsymbol{R}(\check{\Lambda})]^{-1}\boldsymbol{F}\Delta_{\mathrm{ROI}} \tag{3.82}$$

$$\mathrm{Var(ROI)} \approx \frac{1}{N_R^2}f^T[\boldsymbol{F} + \beta\boldsymbol{R}(\check{\Lambda})]^{-1}\boldsymbol{F}[\boldsymbol{F} + \beta\boldsymbol{R}(\check{\Lambda})]^{-1}f \tag{3.83}$$

The derivations above are valid in the simplest case for ROI quantification. More sophisticated cases, such as with random activity or variable contrast in the ROI, are discussed in [106].

CHO Signal-to-noise ratio. In [102], the analytical expressions for the SNR of channelized Hotelling observer was derived for converged MAP reconstruction. In order to compute SNR for this observer (see 3.38), one needs the expressions for z and the covariance matrices of the reconstruction $\mathrm{Cov}(\hat{\Lambda}|H_k)$ $(k = 0, 1)$.

In the case of small lesion and low noise, we can apply the first-order Taylor series expansion to (3.33), resulting in

$$z \equiv \left\langle\hat{\Lambda}|H_1\right\rangle - \left\langle\hat{\Lambda}|H_0\right\rangle \approx \nabla_q\hat{\Lambda}(\bar{Q})A\bar{f}_l \tag{3.84}$$

with $\bar{f}_l \equiv \langle\Lambda|H_1\rangle - \langle\Lambda|H_0\rangle$ the expectation of the lesion profile. Applying the expressions for $\nabla_q\hat{\Lambda}(\bar{Q})$, we have

$$z \approx [\boldsymbol{F} + \beta\boldsymbol{R}(\check{\Lambda})]^{-1}\boldsymbol{F}\bar{f}_l \tag{3.85}$$

For the covariance matrix of the MAP reconstruction $\mathrm{Cov}(\hat{\Lambda}|H_k)$, it is reasonable to assume that the presence of a small lesion hardly affects the Poisson noise in the data. Ignoring the object variation, we have the following approximation:

$$\mathrm{Cov}(\hat{\Lambda}|H_k) \approx \mathrm{Cov}(\hat{\Lambda}) \approx [\boldsymbol{F} + \beta \boldsymbol{R}(\check{\Lambda})]^{-1} \boldsymbol{F} [\boldsymbol{F} + \beta \boldsymbol{R}(\check{\Lambda})]^{-1} \tag{3.86}$$

The covariance of the channel output is thus

$$K \approx U[\boldsymbol{F} + \beta \boldsymbol{R}(\check{\Lambda})]^{-1} \boldsymbol{F} [\boldsymbol{F} + \beta \boldsymbol{R}(\check{\Lambda})]^{-1} U^T + K_N \tag{3.87}$$

Substituting (3.84) and (3.87) into (3.38), we can calculate $\mathrm{SNR}_{\mathrm{CHO}}$.

Here we only explain how to calculate the SNR for the channelized Hotelling observer. To calculate the SNR for other numerical observers, with the variations in the object and the background taken into consideration, one can refer to [102, 104, 149, 151, 152].

Local shift-invariance approximation. It can be seen that the key equations in this analytical approach are (3.71) for the LLIR and (3.73) for the covariance matrix. All the other figures of merit can be derived based on these two equations. The computation of (3.71) and (3.73) involve the inversion of $J \times J$ matrices $\boldsymbol{F}$ and $[\boldsymbol{F} + \beta \boldsymbol{R}(\check{\Lambda})]$, where J is the total number of image pixels. Since the number of image pixels are relatively high in emission tomography, solving (3.71) and (3.73) is not practically feasible.

To avoid this problem, an approximate computation was proposed in [107, 108]. The idea was to assume local shift-invariance of the system. If we consider the elements of the j-th column of the Fisher information matrix $\boldsymbol{F}$ as an image associated with the j-th pixel (denoted as $\boldsymbol{F}^j$), these Fisher information images vary smoothly as we move to the columns of $\boldsymbol{F}$ associated with neighboring pixels. In addition, the Fisher information image was assumed to have local support, implying that the resolution and variance at pixel j are mainly determined by the j-th column of $\boldsymbol{F}$. With these assumptions, the LLIR and the covariance matrix associated with pixel j can be approximately calculated using $\boldsymbol{F}^j$ instead of $\boldsymbol{F}$, with approximated expressions

$$\begin{aligned} l^j(\hat{\Lambda}) &\approx [\boldsymbol{F}^j + \beta \boldsymbol{R}^j(\check{\Lambda})]^{-1} \boldsymbol{F}^j e^j & (3.88) \\ \mathrm{Cov}^j(\hat{\Lambda}) &\approx [\boldsymbol{F}^j + \beta \boldsymbol{R}^j(\check{\Lambda})]^{-1} \boldsymbol{F}^j [\boldsymbol{F}^j + \beta \boldsymbol{R}^j(\check{\Lambda})]^{-1} e^j & (3.89) \end{aligned}$$

where $\boldsymbol{F}^j$ and $\boldsymbol{R}^j$ are approximated as symmetrical Toeplitz matrices. In this case, they become shift-invariant filters. $l^j(\hat{\Lambda})$ and $\mathrm{Cov}^j(\hat{\Lambda})$ can be then computed by matrix multiplications in the Fourier domain, which is more efficient and practical.

For MAP reconstruction with regularization, the spatial resolution in the reconstruction image is often non-uniform and shift-variant [46]. In [45, 118, 119], the regularization parameters are determined by fitting the impulse response to a symmetrical target function, which yields nearly perfect shift-invariant impulse response. As shown in [98, 119], MAP reconstruction and post-smoothed MLEM reconstruction have similar noise properties if the resolution is carefully matched. Therefore, it is reasonable to adapt the Fisher information-based approach to estimate the figures of merit for post-smoothed MLEM, which yields nearly uniform resolution in the reconstructed image.

Prediction for post-smoothed MLEM reconstruction

To enable the comparison between different systems at equal uniform spatial resolution, the analytical expressions derived for MAP reconstruction were adapted and extended to approximate the postsmoothed MLEM with a fixed target resolution [130, 135, 160].

LLIR and covariance matrix. With the post-smoothed MLEM reconstruction, the regularization parameter β is set to zero, and a post-smooth filter $\boldsymbol{P}$ is used to impose isotropic Gaussian impulse response. Since the Fisher information matrix $\boldsymbol{F}$ may not be invertible without the regularization of the prior, an approximate pseudoinverse $\boldsymbol{G}$ was introduced [130]. With these adaptations, the expressions for the LLIR of a certain pixel j and the covariance matrix of the reconstruction image become:

$$
\begin{aligned}
l^j(\hat{\Lambda}) &\approx \boldsymbol{PGF}e^j &(3.90)\\
\mathrm{Cov}(\hat{\Lambda}) &\approx \boldsymbol{PGFG}^T\boldsymbol{P}^T &(3.91)
\end{aligned}
$$

For matched resolution in the reconstruction, (3.90) and (3.91) are equivalent to (3.71) and (3.73).

Since we are only interested in local properties of pixel j, it is reasonable to assume that locally $\hat{\Lambda}$ can be considered as shift-invariant [107, 108]. With this approximation, $\boldsymbol{F}$ can be turned into a circulant matrix $\boldsymbol{F}^j$. Accordingly, $\boldsymbol{G}$ and $\boldsymbol{P}$ also become j-dependent. The expressions for the LLIR and the covariance matrix for pixel j are turned into

$$
\begin{aligned}
l^j(\hat{\Lambda}) &\approx \boldsymbol{P}^j\boldsymbol{G}^j\boldsymbol{F}^j e^j &(3.92)\\
\mathrm{Cov}^j(\hat{\Lambda}) &\approx \boldsymbol{P}^j\boldsymbol{G}^j\boldsymbol{F}^j\boldsymbol{G}^{jT}\boldsymbol{P}^{jT} e^j &(3.93)
\end{aligned}
$$

with

$$
\mathbf{G}^j = \frac{\mathbf{F}^{j*}\max(\Re(\mathbf{F}^j), 0)}{\mathbf{F}^{j*}\mathbf{F}^j\max(\Re(\mathbf{F}^j), 0) + \epsilon} \tag{3.94}
$$

where $\mathbf{G}^j$ and $\mathbf{F}^j$ are the Fourier transform of $\boldsymbol{G}^j$ and $\boldsymbol{F}^j$. respectively, * represents the complex conjugate, $\Re(\mathbf{F}^j)$ is the real part of $\mathbf{F}^j$ and $\epsilon = 10^{-10}|\mathbf{F}^j_{dc}|^3$ with $\mathbf{F}^j_{dc}$ the dc-value of $\boldsymbol{F}^j$ in the Fourier domain [130]. The advantage of (3.92) and (3.93) is that they can be efficiently calculated in the Fourier domain [108, 130].

To simplify the expressions below, we define a set of filters:

$$
\begin{aligned}
\boldsymbol{Q}^j_L &= \boldsymbol{P}^j\boldsymbol{G}^j\boldsymbol{F}^j &(3.95)\\
\boldsymbol{Q}^j_C &= \boldsymbol{P}^j\boldsymbol{G}^j\boldsymbol{F}^j\boldsymbol{G}^{jT}\boldsymbol{P}^{jT} &(3.96)
\end{aligned}
$$

with which the LLIR and the covariance matrix correlated to pixel j can be written as

$$
\begin{aligned}
l^j(\hat{\Lambda}) &\approx \boldsymbol{Q}^j_L e^j &(3.97)\\
\mathrm{Cov}^j(\hat{\Lambda}) &\approx \boldsymbol{Q}^j_C e^j &(3.98)
\end{aligned}
$$

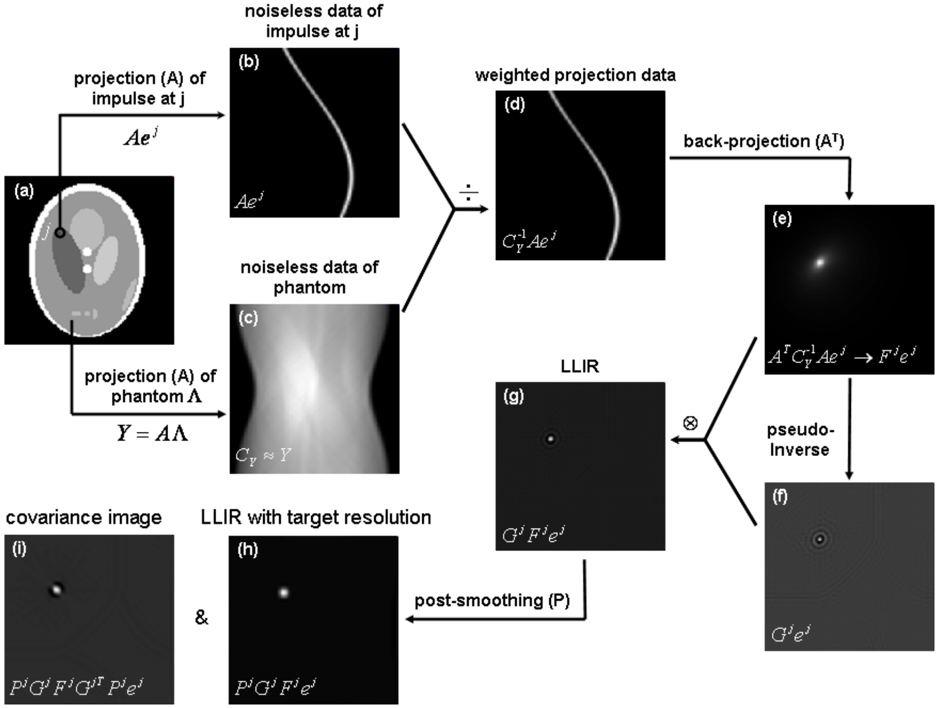
noiseless data of impulse at j
projection (A) of impulse at j
Ae^j
(b)
Ae^j
weighted projection data
(d)
$C_Y^{-1}Ae^j$
÷
back-projection (A^T)
(a)
j
(e)
$A^TC_Y^{-1}Ae^j \rightarrow F^je^j$
noiseless data of phantom
(c)
$C_Y \approx Y$
projection (A) of phantom Λ
$Y = A\Lambda$
LLIR
(g)
$G^jF^je^j$
⊗
pseudo-Inverse
(f)
G^je^j
covariance image
(i)
$P^jG^jF^jG^{jT}P^je^j$
&
LLIR with target resolution
(h)
$P^jG^jF^je^j$
post-smoothing (P)

Figure 3.4: Explanation about how to calculate the LLIR and the covariance matrix correlated with a certain pixel of interest j. (a) the phantom and the pixel of interest j. (b) noiseless projection of an impulse at j. (c) noiseless projection of the phantom. (d) projection of the impulse at j weighted by (c). (e) back-projection of (d). (f) pseudoinverse of (e). (g) LLIR without post-smoothing. (h) and (i) LLIR and covariance matrix at target resolution after post-smoothing.

For better understanding, Fig. 3.4 provides an explanation about the calculation of the LLIR and the covariance image for a certain pixel in a 2-D digitized phantom. Due to the Poisson nature of the data, the variance image of the projection data (denoted as C_Y) equals the noiseless projection Y. The phantom and the pixel of interest are shown in Fig. 3.4(a). Based on (3.72), the Fisher information image $\boldsymbol{F}^j$ is basically calculated by a forward projection A of an impulse at pixel j (Fig. 3.4(b)), weighted by the inverse of the variance distribution of Y (Fig. 3.4(c) and (d)), and followed by a backprojection A^T (Fig. 3.4 (e)). Based on $\boldsymbol{F}^j$ we can calculate the pseudoinverse $\boldsymbol{G}^j$ (Fig. 3.4(f)). Multiplying Fig. 3.4(e) and (f) in the Fourier domain yields the LLIR without post-smoothing (Fig. 3.4(g)). Based on this LLIR, we can derive a proper post-smoothing filter $\boldsymbol{P}^j$ to impose an isotropic resolution with Gaussian profile, yielding the LLIR (Fig. 3.4(h)) and the covariance matrix (Fig. 3.4(i)) at the target resolution.

Pixel contrast-to-noise ratio. By definition, the CRC and the variance of pixel j are the j-th elements of $l^j(\hat{\Lambda})$ and $\mathrm{Cov}^j(\hat{\Lambda})$, respectively. The pixel contrast-to-noise ratio is then calculated as

$$\begin{aligned}\mathrm{CNR}^j &= \mathrm{CRC}^j/\sqrt{\mathrm{Var}^j} \\ &\simeq e^{jT}\boldsymbol{Q}_L^j e^j/\sqrt{e^{jT}\boldsymbol{Q}_C^j e^j}\end{aligned} \tag{3.99}$$

ROI contrast-to-noise ratio. Assuming local shift-invariance, it is valid to apply $\boldsymbol{Q}_L^j$ and $\boldsymbol{Q}_C^j$, which are derived for the particular pixel of interest j, to a small ROI centered at j [135]. Here we are interested in the mean in the ROI response (Mean(ROI)) rather than the bias on that ROI (Bias(ROI)). Suppose the ROI is centered at pixel j and is defined by a vector of f, the mean in this ROI and the variance on this mean can be approximated as

$$\mathrm{Mean(ROI)} \approx \frac{1}{N_R} f^T \boldsymbol{Q}_L^j f \tag{3.100}$$

$$\mathrm{Var(ROI)} \approx \frac{1}{N_R^2} f^T \boldsymbol{Q}_C^j f \tag{3.101}$$

The ROI contrast-to-noise ratio is

$$\mathrm{CNR(ROI)} = \mathrm{Mean(ROI)}/\sqrt{\mathrm{Var(ROI)}} \tag{3.102}$$

CHO Signal-to-noise ratio. For a lesion located near pixel j, the following approximations for z and K can be derived based on (3.84) and (3.87) for post-smoothed MLEM reconstruction:

$$z \approx \boldsymbol{Q}_L^j \bar{f}_l \tag{3.103}$$

$$K \approx U \boldsymbol{Q}_C^j U^T \tag{3.104}$$

Note that in (3.104) the internal noise K_N is ignored. With these two expressions we can calculate $\mathrm{SNR}_{\mathrm{CHO}}$ using (3.38).

Validation. The approximations for the LLIR (3.92) and the pixel variance calculated based on the covariance matrix (3.93) have been validated for shift-variant single and multi-pinhole SPECT systems [130] and for a time-of-flight(TOF) PET system [135]. The CNR for the ROIs (3.102) and the SNR of CHO were applied as the figures of merit in the comparative study between the parallel hole and the rotating slat collimators at a fixed target resolution. The analytical expressions for these two measures were verified in [160] with the validation results presented in chapter 4.

3.4 Application: determination of system geometry

The ideas and the methods introduced in this chapter were applied as the main analysis tools in this PhD work. The Fisher information-based method, which predicts the image quality for post-smoothed MLEM reconstruction, was used to optimize and compare different SPECT collimation systems. The idea of model linearization was applied to investigate the calibration problem of a multi-pinhole SPECT system.

System optimization and comparison

In the first part of this PhD work (**chapter 4**), we took advantage of the analytical methods to evaluate the relative performance of a parallel hole collimator and a rotating slat collimator. We imposed a target resolution which is larger than the geometric resolution of each collimator, and applied i) the theory of the FBP reconstruction explained in chapter 2, and ii) the Fisher information-based method which was adapted for the post-smoothed MLEM reconstruction. As the same target resolution was imposed in the reconstruction, we only need to compare the variance in the reconstruction. The collimator systems were first optimized and then compared with each other using their optimal configurations. Both pixel variance and ROI variance were computed and compared. In addition, the lesion detectability of these two systems were also evaluated by calculating the SNR for the channelized Hotelling observer.

Geometrical parameters estimation

In the second part of this PhD work (**chapter 5**), we extended the linearization model to study the noise propagation properties in the calibration procedure of a multi-pinhole system, whose configuration was optimized by the Fisher information-based method [133]. The errors on the estimated parameters and their influence on the reconstruction accuracy were fully explored in an analytical way.

As briefly discussed in chapter 2, the calibration of multi-pinhole SPECT is performed by measuring several point sources in the FOV, and comparing the measured projections with the estimated projections to estimate all geometric parameters. Let P and U be the geometric parameters to be estimated and the projections of the point sources, respectively. Obviously U is a function of P. Assuming a linear relation between the small variation in the parameters (ΔP) and the deviations in the projection data (ΔU), we have

$$U = U_0 + M(P - P_0) \tag{3.105}$$

where P_0 is the real value of P, U_0 is the original projection data calculated using P_0, and M is a matrix containing the first-order derivatives of the projection coordinates U to each parameter of P, calculated at the point P_0. For convenience, (3.105) can also be written as

$$\Delta U = M \Delta P \tag{3.106}$$

with $\Delta U = U - U_0$ and $\Delta P = P - P_0$. The least squares solution of (3.106) is given by

$$\Delta P = (M^T M)^{-1} M^T \Delta U \tag{3.107}$$

and the covariance matrix of the estimated parameters is

$$\mathrm{Cov}(P) = (M^T M)^{-1} M^T \mathrm{Cov}(U) M (M^T M)^{-1} \tag{3.108}$$

The equations (3.106)-(3.108) are essential for the further analysis of the calibration problem which is discussed in detail in chapter 5.

3.5 Conclusion

In this chapter, we explain the commonly used figures of merit for image quality evaluation, as well as how to calculate these FOMs by numerical simulations and by an analytical Fisher information-based method. The analytical method is first illustrated for converged MAP reconstruction and then for post-smoothed MLEM reconstruction. In the end, the applications of the proposed analytical method in this PhD work presented in the next two chapters are indicated.

Chapter 4

Optimization and comparison: parallel hole and rotating slat collimation systems

In a previous study of our group, a method was proposed to compare different tomographic systems. It assumes that each system acquires a tomographic scan of a certain tracer distribution in the same acquisition time. From this scan, each system is forced to reconstruct an image with a predefined spatial resolution. The system that can perform this task with the "most favorable" noise propagation is considered as the best system. The variance on pixel values is used to assess the noise in the reconstructed image. In this work, we extend this idea to compare the performance of the parallel hole (PH) and the rotating slat (RS) collimator systems.

In order to compare the two systems fairly, we first optimized the configuration of each collimator at a predefined target resolution, yielding the *optimal collimator aperture* which gives the minimal pixel variance in the reconstruction, and then compared the performance of the two collimator systems with their own optimal collimator apertures.

Two different analytical approaches were used for analysis. The first method is based on the FBP theory (see 2.4.1) which was applied to the central point of a uniform symmetrical phantom. Due to the symmetry, this method is also relevant to MLEM/WLS reconstruction. It yields analytical expressions for the optimal collimator aperture and the corresponding variance of the reconstructed pixel values, but it can only be applied to highly symmetrical configurations. The second method is the Fisher information-based method which was adapted for the post-smoothed MLEM reconstruction (see 3.3.2). It provides numerical results, and it is more general and can be applied to non-symmetrical objects and shift-variant tomographic systems. With the Fisher information-based method, we calculated the CNRs in pixels of interest, the CNRs in regions of interest, as well as the SNR for channelized Hotelling observer with each collimator system.

The comparative study of the two collimator systems were done for both planar imaging and volume imaging. The main results are: 1) For cases where both methods are valid, they are in excellent agreement. 2a) The optimal collimator aperture varies linearly with the target resolution. 2b) For a fixed target resolution, the optimal collimator aperture depends on the collimator type and the imaging mode (planar or volume). 2c) The optimal aperture of PH is a factor of $\sqrt{2}$ larger than that of RS, regardless of the figure of merit in use. 3a) The relative performance of the two collimators is determined by the object size, the object-to-detector distance and the spot-to-background contrast. 3b) Different figures of merit yield very similar relative performance for RS versus PH.

4.1 Introduction

In SPECT imaging, image quality is limited by the tradeoff between the spatial resolution and the geometric efficiency. For the conventional parallel hole (PH) collimator (Fig. 4.1(a)), the geometric efficiency is always very low for a reasonable spatial resolution since PH only detects photons whose trajectories are parallel to the collimator holes. In contrast to PH, a rotating slat (RS) collimator (Fig. 4.1(b)) can achieve a much higher geometric efficiency without any resolution loss due to its capability of in-plane photons collection [48, 59, 60, 76, 77, 126, 141, 143, 144, 157]. However, in order to interpret the plane integral data acquired by RS, even for planar imaging, an extra reconstruction step is needed, which results in increased noise propagation. It is not obvious whether or not a higher geometric efficiency will lead to improved image quality. The goal of our study is to compare the PH and the RS collimators with different analytical noise propagation models, investigating which collimator provides better image quality in the reconstructions.

To compare different tomographic systems, it is important to state clearly which FOM will be used and for which kind of imaging task the comparison will be performed. Indeed, there are various FOMs and tasks that can be applied to the system comparison, e.g., the SNR of a human observer for a lesion detection task, or the mean and the variance of an estimator in an estimation task [13]. In our previous studies, we used the estimate of the variance on the value of the reconstructed pixel or on the mean value of a ROI to evaluate the noise propagation characteristics of different tomographic systems. For fair comparison, we assume that each system acquires a tomographic scan of the same tracer distribution in the same acquisition time and we tune the reconstruction algorithm for each system in such a way that all reconstructed images have the same predefined spatial resolution. The system that yields the lowest variance can then be considered as the best system. This approach was used in [133] for the selection of the best design among various multipinhole configurations. In this chapter, we extend this idea to compare the PH and the RS collimators.

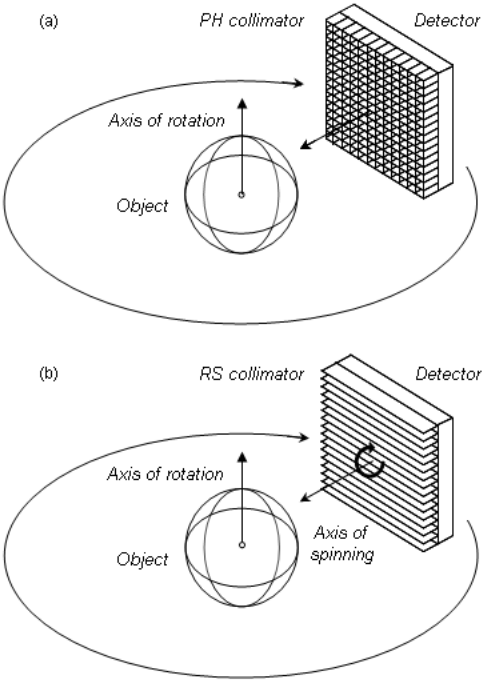

Figure 4.1: (a) Geometry of a parallel hole (PH) collimator system. (b) Geometry of a rotating slat (RS) collimator system.

Comparative studies between these two collimator systems have already been presented in several papers [59, 60, 76, 77, 141, 157]. In [76] and [77], a specific expression of the SNR gain (RS versus PH) at the center of a uniform disk/sphere of activity was derived for planar and volume imaging, respectively. The comparison was based on the noise propagation behavior of FBP reconstruction. It was found that RS outperformed PH only for small objects. Effort has been made in [77] to achieve an isotropic point spread function for each collimator, but the final spatial resolutions yielded by the two systems were not really identical. Zhang and Zeng [157] compare these two collimators using the same figure of merit and the same type of phantom as in [77] for the iterative least squares (LS) reconstruction, yielding similar results as [77]. In that study, the variation of the geometric efficiency within the FOV and the distance-dependent detector response were not taken into consideration. In [59, 60], the PH and the RS systems were compared using MLEM reconstruction with the system model derived from Monte Carlo simulations. The contrast-to-noise for cold and hot spots with varying sizes was investigated at different iterations. It was found that the PH collimator only outperforms RS for low contrast lesions in very large warm background. The results are reliable because they were derived based on accurate system models. However, the analysis was done with fixed object-to-detector distances. Since the geometric efficiency of the RS collimator is position-dependent while that of PH is constant, changing the detector distance may have a significant influence on the outcome of the collimator comparison. Wang et al [141] performed a real lesion phantom study. The data were reconstructed using the rescaled block-iterative expectation maximization (RBI-EM) algorithm. The contrast-to-noise analysis (similar as in [59, 60]) showed that RS leads to a better contrast recovery than PH for the same background noise level. Since different detectors were used for the two collimator systems (NaI for PH and CZT for RS), it was not clear how much of the improvement was due to the high geometric efficiency of RS and how much was due to the better energy resolution of the CZT detector.

Besides the points discussed above, the tradeoff between the collimator resolution and the noise has not yet been fully explored in previous works. For the same predefined spatial resolution (called *target resolution* in the remainder of the text), the variance of the reconstructed image varies with the collimator resolution, in a way that is specific to each type of collimator. The main innovation in the present work is the investigation of the relation between the variance and the collimator resolution for the PH and RS collimators and the comparison of these two types of systems using for each the collimator resolution that yields the minimal pixel/ROI variance at fixed target resolution. To avoid the confusion between the resolution in the reconstruction and the collimator resolution, we introduce the term of *collimator aperture* to denote the collimator resolution. The collimator aperture which corresponds to the minimal variance is thus defined as the *optimal collimator aperture* of a certain collimator system.

The purpose of this study is therefore to make a fair comparison between the PH and the RS systems. The word "fair" in this context refers to the following:

- The two systems are equipped with the same type of detector with the same detection area,
- the object-to-detector distance is the same,
- the acquisition is done for the same tracer distribution in the same amount of time,
- the reconstructions have the same spatial target resolution,
- and as mentioned above we use the collimator aperture that is optimized individually for each system.

We used two analytical approaches in this study. The first one is based on the theory of FBP reconstruction and is similar to the work in [76, 77]. The FBP-based method uses a simplified system model and closed form expressions can only be obtained for highly symmetrical configurations. The second approach is the Fisher information-based method (FIM), which gives fast predictions of the linearized local impulse response and of the covariance image [43, 46, 107, 130, 135] for iterative reconstructions. In this study, the FIM was used to estimate the noise properties of the post-smoothed MLEM reconstruction. Compared with the FBP-based method, one of the advantages of FIM is that it allows the implementation of more accurate physical models. Practical considerations, such as the attenuation within the phantom, the position dependence of the geometric efficiency as well as the effect of the collimator blurring, can be conveniently included in the system model. Therefore FIM was used to generalize and extend the results yielded by the FBP-based calculation.

We applied these two methods to uniform symmetrical phantoms and contrast phantoms, investigating for each type of collimator the relation between the optimal collimator aperture and the target resolution. With the optimal collimator apertures corresponding to a certain target resolution, the figures of merit obtained with the two systems, i.e., the variance of the reconstructed pixel/ROI values and the SNR for channelized Hotelling observer, were compared as functions of the phantom size, the object-to-detector distance and the spot-to-background contrast. The study was done for both planar imaging and volume imaging and the results were verified with repeated simulations.

This chapter is organized as follows. In 4.2.1, the geometry of the PH and the RS systems, the concept of the collimator aperture and the geometric efficiency are described. In 4.2.2, we give general descriptions about the data acquisition and the reconstruction with the target resolution. The figures of merit used for system comparison are introduced in 4.2.3 and the two proposed methods (FBP and FIM) are briefly described in 4.2.4. In 4.2.5 we explain how to optimize the collimator aperture. Details about the numerical experiments are given in 4.3. The results obtained from the two methods are presented in 4.4 and 4.5, respectively. The results are further discussed in 4.6 and our conclusions are given in 4.7. Details of all the mathematical derivations are presented in appendices.

4.2 Methods

4.2.1 System description

Collimator geometry

We consider a PH collimator consisting of a 2-D array of long narrow square holes with width d_p and height h_p (Fig. 4.1(a)). The RS collimator is modeled as a series of long thin slat septa positioned parallel with each other and perpendicular to the detector surface (Fig. 4.1(b)). The slat septa have a width W and a height h_r. The distance between two adjacent slat septa is d_r. Both the PH and the RS collimators were equipped with a square detector array with size $W \times W$. In this study we assume that there is no penetration through the septa, that the thickness of the septa is negligible, and that the detectors have a perfect absorption efficiency and a perfect intrinsic detector resolution. The distance D between the center of the image space and the detector surface is constant during the tomographic acquisitions[1].

---

[1] A discussion about the influence of these assumptions is presented in 4.6.

For the RS system, the collimator and the detector need to spin around a spinning axis in order to acquire complete data. This axis is perpendicular to the detector surface, connecting the center of the detector array and the center of the image space. For tomographic scans, both the PH and the RS collimators rotate around the object. The axis of rotation (AOR) is the line parallel to the detector surface through the center of the image space.

Collimator aperture

The collimator aperture (which denotes the collimator resolution) is a measure of the response of a collimator system to a point source in the object plane, characterized by the PSF. The PSF[2] is here denoted as P_c and is modeled by a Gaussian with standard deviation of σ_c, where the subscript c represents "collimator" and can be substituted by either p or r to refer to the PH or the RS collimator, respectively (the same convention will be used for other quantities below). The collimator aperture can be expressed by either the full width at half maximum (FWHM_c) of the PSF or by its standard deviation, which for a Gaussian PSF is given by

$$\sigma_c = \frac{\mathrm{FWHM}_c}{2\sqrt{2\ln 2}} \tag{4.1}$$

Generally speaking, the collimator response is depth-dependent. For the proposed collimator geometries we have at a location $\vec{x}$ in the image space, [145]

$$\mathrm{FWHM}_c(\vec{x}) = D(\vec{x})d_c/h_c \tag{4.2}$$

where $D(\vec{x})$ is the distance between $\vec{x}$ and the detector plane. Combining (4.1) and (4.2) yields

$$\sigma_c(\vec{x}) = \frac{D(\vec{x})d_c}{2\sqrt{2\ln 2}h_c} \tag{4.3}$$

We use the symbol σ_c or FWHM_c (without argument $\vec{x}$) to denote the collimator aperture that corresponds to the center of the image space, i.e.

$$\sigma_c = \frac{Dd_c}{2\sqrt{2\ln 2}h_c} \tag{4.4}$$

Geometric efficiency

The geometric efficiency of a collimation system (E_c) is the fraction of the photons emitted from a point in the object that will be detected if there is no attenuation. The geometric efficiency is closely related to the collimator aperture. Generally, E_p is proportional to σ_p^2, and E_r is proportional to σ_r. In addition, E_r also depends on the detector width W, because a wider detector spans a larger solid angle. However, the detection efficiency decreases with increasing incidence angle, and therefore we introduce an *effective detector width* Ω_W which takes a normalized angular factor into account. Appendix-A gives the specific definition of Ω_W. With this definition, E_r is proportional to Ω_W, which leads to concise expressions.

---

[2] For the RS system, it only refers to the PSF profile along the dimension perpendicular to the collimator septa.

Due to the collimator geometry, E_r is position-dependent while E_p is not. Expressions of E_p and E_r can be found in appendix-B.

4.2.2 Acquisition model and reconstruction

Acquisition Model

The tracer distribution is denoted as $\lambda(\vec{x})$, with $\vec{x}$ the vector in the image space. It is nonnegative, and $\lambda(\vec{x}) = 0$ for $\vec{x} \notin S$, with S the finite support of $\lambda(\vec{x})$. Schematic drawings describing the notations used below are shown in Fig. 4.2.

For planar imaging, $\lambda(\vec{x})$ represents a 2-D distribution[3] ($\vec{x} \in \mathbb{R}^2$) in a plane parallel to the detector surface. During the acquisition, the PH collimator is stationary and the RS collimator spins around the spinning axis. The acquired data for the PH system is here modeled as

$$y_p(\vec{x}) = T_p E_p \int_{\mathbb{R}^2} P_p(\|\vec{x} - \vec{\xi}\|)\lambda(\vec{\xi})d\vec{\xi} \tag{4.5}$$

where T_p is the acquisition time, E_p is the geometric efficiency, P_p is the PSF which models the collimator blurring, and $\|\cdot\|$ represents the Euclidean norm. As discussed above, P_p is a 2-D isotropic Gaussian with standard deviation of σ_p.

The planar RS acquisition is modeled as

$$y_r(s, \phi) = T_r \int_{-W/2}^{+W/2} dl \int_{\mathbb{R}^2} E_r(\alpha - l, D)P_r(|s - \beta|)\lambda(\vec{\xi})d\alpha d\beta \tag{4.6}$$

with

$$\vec{\xi} = \alpha\vec{u}_\phi^\perp + \beta\vec{u}_\phi \tag{4.7}$$

where s is the distance between the slat interval and the spinning axis, ϕ is the spinning angle, $\vec{u}_\phi$ and $\vec{u}_\phi^\perp$ are two orthogonal unit vectors in the detector plane, with $\vec{u}_\phi = (-\sin\phi, \cos\phi)$ orthogonal to the slat septa. Note that for this 2-D imaging configuration, the distance D between the source and the detector plane is fixed and the geometric efficiency E_r (see (B.2) in appendix-B) only varies along $\vec{u}_\phi^\perp$. P_r is the 1-D PSF spread along $\vec{u}_\phi$. Assuming equal acquisition time for both collimator systems, we have

$$T_r = T_p/\pi \tag{4.8}$$

because RS spins over π during the acquisition.

---

[3] To simplify the problem, we use a 2-D tracer distribution rather than a 3-D tracer distribution for planar imaging.

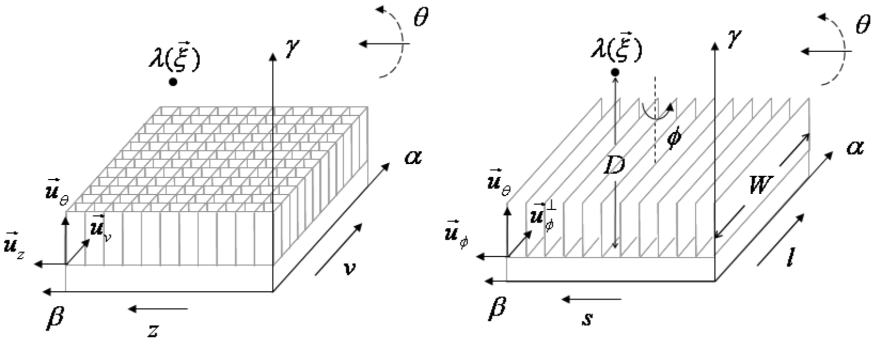

(a) PH collimator

(b) RS collimator

Figure 4.2: Notations used for acquisition model of (a) parallel hole collimator, (b) rotating slat collimator.

For volume imaging, $\lambda(\vec{x})$ represents a 3-D distribution ($\vec{x} \in \mathbb{R}^3$). For both collimator systems, the collimator and the detector rotate around the AOR. The acquired data of the PH system is modeled as

$$y_p(v,\theta,z) = T_p E_p \int_{\mathbb{R}^3} P_p(\sqrt{(v-\alpha)^2+(z-\beta)^2},\gamma)\text{Atten}(\vec{\xi})\lambda(\vec{\xi})d\alpha d\beta d\gamma \quad (4.9)$$

with

$$\vec{\xi} = \alpha\vec{u}_v + \beta\vec{u}_z + \gamma\vec{u}_\theta \quad (4.10)$$

where θ is the acquisition angle with respect to the AOR, and v and z are the 2-D orthogonal coordinates in the detector array, defined by unit vectors $\vec{u}_v$, $\vec{u}_z$, respectively, with $\vec{u}_z$ parallel to the AOR. The third unit vector $\vec{u}_\theta = (-\sin\theta, \cos\theta, 0)$ is orthogonal to the detector plane. Atten($\vec{\xi}$) represents the probability that a photon, emitted from $\vec{\xi}$ and traveling parallel to $\vec{u}_\theta$, is not attenuated.

The data acquired by the tomographic RS system is modeled as

$$\begin{aligned} y_r(s,\phi,\theta) = T_r \int_{-W/2}^{+W/2} dl \int_{\mathbb{R}^3} & E_r(\alpha-l,\gamma)P_r(|s-\beta|,\gamma) \\ & \times \text{Atten}(\vec{\xi},l)\lambda(\vec{\xi})d\alpha d\beta d\gamma \quad (4.11) \end{aligned}$$

where

$$\vec{\xi} = \alpha\vec{u}_\phi^\perp + \beta\vec{u}_\phi + \gamma\vec{u}_\theta \quad (4.12)$$

with $\vec{u}_\phi^\perp = (\cos\phi\cos\theta, \cos\phi\sin\theta, \sin\phi)$ and $\vec{u}_\phi = (-\sin\phi\cos\theta, -\sin\phi\sin\theta, \cos\phi)$. In (4.11), Atten($\vec{\xi}, l$) has a similar meaning as Atten($\vec{\xi}$) in (4.9), with trajectory of the photon from $\vec{\xi}$ to the detector position l.

Note that in (4.9) and (4.11), the PSF $P_c(\cdot, \gamma)$ models a depth(γ)-dependent collimator response, representing a Gaussian with standard deviation of $\sigma_c(\gamma)$ given by (4.3).

The decay of the tracer during the acquisition and the photon scattering are not included in our model, and the data is assumed to be Poisson distributed.

Reconstruction with Target Resolution

From y_p and y_r we reconstruct the image using either FBP or MLEM, with a spatial resolution equal to the predefined target resolution. The reconstruction is achieved by making an initial (nearly) unbiased reconstruction, which is then smoothed with a post-processing filter to impose the target PSF (P_t), in our case an isotropic Gaussian with target standard deviation σ_t.

To ensure that the initial reconstruction is nearly unbiased, the blurring due to the finite collimator aperture needs to be compensated during the reconstruction. With FBP, this is done by deconvolving the acquired data for the collimator PSF. With MLEM, the effect of the collimator blurring is included in the system model. It was assumed that a nearly unbiased reconstruction is achieved by iterating MLEM until convergence.

To estimate the resolution and the noise properties in post-smoothed MLEM reconstructions, we use the Fisher information-based method introduced in 3.3.2, which applies to a discrete model of the acquisition. With the discrete model, both the image space and the detection space are digitized into pixels with finite size. The LLIR (l^j) and the covariance image (Cov^j) correlated to a particular pixel j in the reconstruction are used to describe the resolution and the noise properties, respectively.

In this study, we choose $\sigma_t > \sigma_c$, such that post-smoothing is always needed to achieve the target resolution. The post-smoothing filter is designed based on the deviation between the LLIR l^j of the nearly-unbiased initial reconstruction and the target PSF P_t. Applying this filter to the nearly-unbiased initial reconstruction then ensures that the final l^j equals P_t.

Compared to FIM which needs the discrete model, the FBP-based method uses the continuous data acquisition model and the variance is calculated for a point rather than for a pixel with finite size. The difference is only apparent however because the variance is calculated in both cases for a smoothed image with a prescribed target resolution σ_t. As long as the pixel size is sufficiently small compared to the target resolution (which is the case in our study), the effect of the discretization is small and can be considered negligible. The calculated variance actually corresponds to the detection of a (non-uniform) ROI with a Gaussian profile with standard deviation σ_t.

Details about the two methods are presented in 4.2.4.

4.2.3 Performance measure

The relative performance of the two systems was mainly compared using the ratio (gain) between the CNR of a reconstructed point/pixel obtained with the RS and PH collimators. Based on the definition of CNR given by (3.26), we have

$$\mathrm{Gain}_{\mathrm{CNR}} = \frac{\mathrm{CNR}_r}{\mathrm{CNR}_p} = \frac{\mathrm{CRC}/\sqrt{\mathrm{Var}_r}}{\mathrm{CRC}/\sqrt{\mathrm{Var}_p}} = \sqrt{\frac{\mathrm{Var}_p}{\mathrm{Var}_r}} \tag{4.13}$$

Note that CRC is canceled out because it is the same for both collimator systems as we impose equal target resolution (see 3.2.3).

(4.13) is computed using both proposed methods. With the Fisher information-based method, we also calculate the gains of the CNRs in the regions of interest ($\mathrm{CNR}_{\mathrm{ROI}}$) and of the SNR for a channelized Hotelling observer ($\mathrm{SNR}_{\mathrm{CHO}}$):

$$\mathrm{Gain}_{\mathrm{CNR}}(\mathrm{ROI}) = \frac{\mathrm{CNR}_{\mathrm{ROI},r}}{\mathrm{CNR}_{\mathrm{ROI},p}} \tag{4.14}$$

$$\mathrm{Gain}_{\mathrm{SNR}}(\mathrm{CHO}) = \frac{\mathrm{SNR}_{\mathrm{CHO},r}}{\mathrm{SNR}_{\mathrm{CHO},p}} \tag{4.15}$$

with more details presented in 4.2.4.

4.2.4 Analytical methods

FBP-based calculation

The first method used for the comparative study between the PH and the RS collimator systems is based on the theory of FBP reconstruction explained in 2.4.1. The main principle is as follows. The object $\lambda(\vec{x})$ is a uniform disk or a uniform sphere for planar and volume imaging, respectively. The center of $\lambda(\vec{x})$ coincides with the center of the image space. To simplify the calculation, the following approximations are made in (4.5), (4.6), (4.9) and (4.11): 1) There is no attenuation within the object, i.e. $\mathrm{Atten}(\vec{\xi}) = 1$, and 2) The position-dependence of the geometric efficiency and of the collimator response is ignored, i.e., γ is replaced by D (distance between the center of the image space and the detector) in the second argument of E_r, P_p, and P_r. Thus, the effect of the collimator smoothing is modeled by a single convolution between the data and a Gaussian with standard deviation σ_c. In addition, when calculating the variance at the center of the object, the variance of the data acquired at the center of the detector is used to approximate the variance of the data of all the other detectors.

To reconstruct the data, the conventional way is to apply a ramp filter (for 2-D RS or 3-D PH imaging) or a second derivative filter [14] (for 3-D RS imaging) to the acquired data, and then perform back-projection. To impose the target resolution σ_t, an extra filter which corresponds to a Gaussian kernel with a standard deviation of $\sqrt{\sigma_t^2 - \sigma_c^2}$ is applied together with the reconstruction filters before the back-projection, which is equivalent to post-smooth the initial unbiased reconstruction.

Based on the reconstruction formula, the variance of the central point of the reconstructed image is derived as a function of the collimator aperture σ_p (PH) or σ_r (RS). This variance is further minimized by choosing an optimal value for the collimator aperture (see 4.2.5). The minimal variance for each collimator system is used in (4.13) to evaluate of the relative performance of the two collimator systems.

This method is only valid for the central point of a uniform symmetrical object. Detailed calculations can be found in appendix-C and appendix-D.

Fisher information-based method

The second approach is the Fisher information-based method introduced in 3.3.2, which was applied to estimate the CNR in pixels of interest, the CNR in regions of interest and the SNR for a channelized Hotelling observer for the post-smoothed MLEM reconstruction with the two collimator systems.

FIM assumes discrete data and is most conveniently presented in matrix notation, and the matrices are calculated based on noiseless projection. As explained before, the activity distribution and the acquired data are denoted by $\Lambda = [\lambda_1, \lambda_2, \cdots, \lambda_J]^T$ and $Y = [y_1, y_2, \cdots, y_I]^T$, respectively. The data is expressed as

$$Y = A\Lambda \tag{4.16}$$

where A is the system matrix. The image estimated by the reconstruction algorithm is denoted by $\hat{\Lambda}$. (4.16) is implemented by discretizing (4.5)-(4.12), with A including the combined effect of the position-dependent geometric efficiency, the depth-dependent collimator response, as well as the attenuation within the object.

For convenience, we re-write the expressions derived in 3.3.2 to illustrate how to estimate CNR, $\mathrm{CNR_{ROI}}$ and $\mathrm{SNR_{CHO}}$ for post-smoothed MLEM by FIM. To simplify the expressions, a set of filters are defined:

$$\begin{aligned} \boldsymbol{Q}_L^j &= \boldsymbol{P}^j \boldsymbol{G}^j \boldsymbol{F}^j && (4.17) \\ \boldsymbol{Q}_C^j &= \boldsymbol{P}^j \boldsymbol{G}^j \boldsymbol{F}^j \boldsymbol{G}^{jT} \boldsymbol{P}^{jT} && (4.18) \end{aligned}$$

where $\boldsymbol{F}^j$ is the Fisher information image, $\boldsymbol{G}^j$ is the approximate pseudoinverse of $\boldsymbol{F}^j$, and $\boldsymbol{P}^j$ is the post-smoothing filter which imposes the target resolution. In this study, $\boldsymbol{P}^j$ is defined in the following way:

$$\mathbf{P}^j[k] = \begin{cases} \mathbf{P}_t[k]/\mathbf{L}_0^j[k] & \text{if } \Re(\mathbf{L}_0[k]) \geqslant 0.005, \\ 0 & \text{if } \Re(\mathbf{L}_0[k]) < 0.005 \end{cases} \tag{4.19}$$

where $\mathbf{P}^j$, $\mathbf{P}_t$, $\mathbf{L}_0^j$ are the Fourier transforms of $\boldsymbol{P}^j$, P_t and l_0^j, with $l_0^j = \boldsymbol{G}^j \boldsymbol{F}^j e^j$ the LLIR before post-smoothing, k is the index of the elements in the Fourier domain, and $\Re(\cdot)$ denotes the real part of a complex number.

Using the filters defined above, the LLIR and the covariance image correlated to pixel j are

$$l^j(\hat{\Lambda}) \approx \boldsymbol{Q}_L^j e^j \tag{4.20}$$

$$\mathrm{Cov}^j(\hat{\Lambda}) \approx \boldsymbol{Q}_C^j e^j \tag{4.21}$$

The CNR in pixel j is

$$\mathrm{CNR} = \mathrm{CRC}^j / \sqrt{\mathrm{Var}^j} \approx e^{jT} \boldsymbol{Q}_L^j e^j / \sqrt{e^{jT} \boldsymbol{Q}_C^j e^j} \tag{4.22}$$

The CNR of a ROI centered at j is

$$\mathrm{CNR}_{\mathrm{ROI}} = \mathrm{Mean(ROI)} / \sqrt{\mathrm{Var(ROI)}} \approx f^T \boldsymbol{Q}_L^j f / \sqrt{f^T \boldsymbol{Q}_C^j f} \tag{4.23}$$

where f is the vector of the ROI with $f[k]$ equal to 1 if the pixel k is inside the ROI, and 0 otherwise. The SNR for channelized Hotelling observer is

$$\mathrm{SNR}_{\mathrm{CHO}} = \sqrt{z^T U^T K^{-1} U z} \tag{4.24}$$

with

$$z \approx \boldsymbol{Q}_L^j \bar{f}_l \tag{4.25}$$

$$K \approx U \boldsymbol{Q}_C^j U^T \tag{4.26}$$

where $\bar{f}_l$ is the expectation of the lesion profile and U represents a series of frequency-selective channels.

As explained in 3.2.3, CRC^j is constant for a given target resolution. The (co)variance in the reconstruction is proportional to the measured activity Y (with $\mathrm{Cov}^j \propto \boldsymbol{F}^{-1}$, $\boldsymbol{F} \propto C_Y^{-1}$ and $C_Y \propto Y$), and inversely proportional to the acquisition time T (with $A \propto T$, $C_Y \propto T$, thus $\boldsymbol{F} \propto T$). As a result, CNR is inversely proportional to $\sqrt{Y}$ and proportional to $\sqrt{T}$.

4.2.5 Collimator aperture optimization

As we impose the target spatial resolution σ_t, the variance in the reconstruction is a function of the collimator aperture σ_c, because the variance is influenced by the geometric efficiency and the effect of collimator blurring, both of which are in turn determined by the collimator aperture. Therefore, it is possible to minimize the variance (or maximize the $\mathrm{CNR}/\mathrm{CNR}_{\mathrm{ROI}}/\mathrm{SNR}_{\mathrm{CHO}}$) by a proper choice of the collimator aperture. Here we use CNR as the figure of merit to explain how to find the minimal variance or maximal CNR with each collimator system.

With the FBP-based calculation, the optimal value of the collimator aperture is derived by calculating the derivative of the denominator of the variance expression with respect to σ_c (see appendix-C and -D). This yields the minimal variance and the optimal collimator apertures σ_c^{opt}.

With FIM, the optimal collimator aperture of a certain system is estimated as follows: 1) Choose a target resolution σ_t and a particular pixel j. 2) Calculate the CNR using different collimator apertures[4]. 3) Plot the CNR curve as a function of the collimator aperture. 4) Interpolate the curve by the least-squares polynomial fitting method. 5) Locate the maximal CNR on the curve. 6) Define the collimator aperture which corresponds to the maximal CNR as the optimal collimator aperture σ_c^{opt} for the chosen target resolution. (This maximal CNR value is thus called *optimized CNR* in the remainder of the text.)

Using either the minimized variance (FBP) or the optimized CNR (FIM) of each collimator system as the input of (4.13) leads to an ultimate measure for the system comparison

$$\mathrm{Gain}_{\mathrm{CNR}}^{\mathrm{opt}} = \frac{\mathrm{CNR}_r^{\mathrm{opt}}}{\mathrm{CNR}_p^{\mathrm{opt}}} = \sqrt{\frac{\mathrm{Var}_p^{min}}{\mathrm{Var}_r^{min}}} \tag{4.27}$$

With FIM, we also found the maximal values for $\mathrm{CNR}_{\mathrm{ROI}}$ and $\mathrm{SNR}_{\mathrm{CHO}}$ with each collimator, yielding

$$\mathrm{Gain}_{\mathrm{CNR}}^{\mathrm{opt}}(\mathrm{ROI}) = \frac{\mathrm{CNR}_{\mathrm{ROI},r}^{\mathrm{opt}}}{\mathrm{CNR}_{\mathrm{ROI},p}^{\mathrm{opt}}} \tag{4.28}$$

$$\mathrm{Gain}_{\mathrm{SNR}}^{\mathrm{opt}}(\mathrm{CHO}) = \frac{\mathrm{SNR}_{\mathrm{CHO},r}^{\mathrm{opt}}}{\mathrm{SNR}_{\mathrm{CHO},p}^{\mathrm{opt}}} \tag{4.29}$$

4.3 Numerical studies

Using the methods proposed in 4.2.4, we determined the optimal aperture for each collimator system, and then evaluated the relative performance of the PH and the RS collimators with their own optimal apertures.

With the FBP-based method, the results were directly obtained from the analytical calculation. With the Fisher information-based method which does not produce closed form solutions, we applied it to particular PH and RS systems with particular objects described by concrete parameters. The latter is called *numerical study*, which will be described in detail in this section. In numerical studies, synthetic noise-free data were computed using digitized versions of (4.5)-(4.12) with specified parameters. Four numerical studies were performed by the Fisher information-based method. The results of the first two studies can be directly compared with those from the FBP-based method since they were both obtained based on uniform phantoms. The other two studies aimed to further generalize and extend the FBP-based results by applying FIM to non-uniform, non-symmetrical phantoms.

---

[4] The collimator aperture σ_c can be varied by changing D, d_c or h_c, or their combinations (see (4.4)). In this study we fix D and d_c and only vary h_c.

The system parameters used in the first three studies are given in table 4.1, and those used for the last one is given in table 4.2. In each study, the acquisition time was 20 minutes for both the PH and the RS collimator systems.

4.3.1 Optimal collimator aperture

First, the relation between the optimal collimator aperture (σ_p^{opt}, σ_r^{opt}) and the target resolution σ_t was derived for planar and volume imaging, respectively. Five different target resolutions were applied. The FWHM of the target resolution ranged from 7.2 mm to 14.4 mm.

The phantom used in planar imaging was a uniform disk with $diameter = 54$ mm and detector distance $D = 100$ mm. The activity within the phantom was $\lambda = 9.344$ kBq/cm^2. The optimal aperture was found for each target resolution and calculated only for the central point of the phantom.

The phantom used in volume imaging was a uniform sphere positioned at the center of the image space, with $diameter = 54$ mm and $D = 300$ mm. The activity of the phantom was 9.344 kBq/cc. We assumed uniform attenuation within the phantom, with the attenuation coefficient $\mu = 0.01505$ mm^{-1}. The optimal collimator aperture was individually calculated for the central point, 6 eccentric points and 2 ROIs. The eccentric points were selected equidistantly on the X-axis or the Z-axis (see Fig. 4.5(a)). The ROIs were spherical and located at the center of the phantom, with the same activity distribution as the phantom, and with diameter of 7.2 mm and 18.0 mm, respectively.

4.3.2 Optimized CNR gain

With the optimal collimator aperture derived in 4.3.1, the optimized CNR gain ($\mathrm{Gain}_{\mathrm{CNR}}^{\mathrm{opt}}$) was calculated for the central point of the phantom, as a function of phantom diameter ($diameter = 20.4 \rightarrow 116.4$ mm) or detector distance ($D = 50 \rightarrow 300$ mm for planar imaging, $D = 120 \rightarrow 300$ mm for volume imaging), with three different target resolutions ($\mathrm{FWHM}_t = 9$ mm/10.8 mm/12.6 mm). The phantom activity and the attenuation coefficient were the same as in 4.3.1.

4.3.3 Ellipsoid phantom

To verify the consistency of the acquisition models and reconstruction procedures, a post-smoothed MLEM reconstruction was performed for a simulated asymmetrical ellipsoidal phantom, with the PH and the RS collimator systems, respectively. As shown in Fig. 4.12(a), this phantom consists of a warm background ($\lambda = 4.823$ kBq/cc, $\mu = 0.0120$ mm^{-1}), a hot spherical region ($\lambda = 9.645$ kBq/cc, μ=0.0120 mm^{-1}) and a cold spherical region (λ=2.411 kBq/cc, μ=0.0045 mm^{-1}). The length of the semi-axes along/perpendicular to the axis of rotation were 36 mm

Table 4.1: System parameters used for uniform phantom and ellipsoid phantom

Parameter	**Planar imaging**	**Volume imaging**
Detector array	97x97	97x97
Image dimension	97x97	97x97x97
Septa space & Pixel size (d_c)	1.2 mm	1.2 mm
Detector width (W)	116.4 mm	116.4 mm
Projection angles (θ, ϕ)	PH: stationary RS: 64 spin angles over 2π	PH: 64 rotation angles over 2π RS: 64 spin / 64 rotation angles over 2π
Raw data dimension	PH: 97x97 RS: 97x64	PH: 97x97x64 RS: 97x64x64

and 27 mm, respectively. The diameter of the two regions was 21.6 mm. The distance between the center of the phantom and the detector was 80 mm. The FWHM of the target resolution was 9 mm.

First, we used FIM to optimize the collimator aperture for the central point of the phantom. Second, for each collimator system, the noiseless sinogram of this phantom with and without an impulse in its center were generated and reconstructed, yielding two reconstruction images. The LLIR was then obtained by subtracting these two reconstructions. Based on the shape of LLIR, the post-smoothing filter was defined by (4.19) and was applied to the reconstruction image.

In order to accelerate the convergence, OSEM algorithm (see 2.4.2) was applied for the reconstruction. The iteration scheme for the PH system was 5×32, 5×16, 5×8, 5×4, 5×2, 5×1 (number of global iterations × number of subsets). For the RS system, the scheme of the subsets was the same and the number of iterations was doubled, because the reconstruction of RS data has a lower convergence speed than that of PH data [59].

4.3.4 Variable contrast phantom

To obtain the ranking of the system performance with different figures of merit in more realistic cases, we used contrast phantoms with variable parameters to calculate the gain and the optimal collimator aperture correlated to CNR, $\mathrm{CNR}_{\mathrm{ROI}}$ and $\mathrm{SNR}_{\mathrm{CHO}}$ with each collimator system, using the Fisher information-based method.

In this study, the contrast phantom used for planar/volume imaging had a very similar structure as the ellipsoid phantom that shown in Fig. 4.12(a), i.e., it consists of an ellipse/ellipsoid and two circles/spheres, representing the background (λ_b), the hot organ (λ_h) and the cold organ (λ_c), respectively. The system parameters and the basic setting of the phantom are given in table 4.2. In both imaging modes, the pixels of interest were the central points of the two organs. Both the ROIs and the lesions were circular and located at the center of the organs. The ROIs had a diameter of 8 pixels and had the same activity as the organ, while the lesions had a diameter of 2 pixels and the lesion-to-organ contrast was 2. The distance between the center of the phantom and the detector was 100 mm.

For the calculation of $\mathrm{SNR}_{\mathrm{CHO}}$, we used a DOG model with 3 channels as the observer model. The channels were defined as the differences of pairs of a set of four 2-D Gaussians. These Gaussians were with means of 0 and standard deviations of $(2d\sqrt{\pi})^{-1}\mathrm{pixel}^{-1}$ where $d = 0.573, 0.995, 1.592$ and 2.653. These parameters were the same as in [50].

Optimal collimator aperture

With the basic setting of the phantom parameters, we first calculated the collimator aperture which yields the maximum value of each figure of merit using the approach explained in 4.2.5. For each FOM, the optimal collimator aperture was found for the central pixel of the phantom, using the PH and the RS collimator system, respectively. This study was only done for planar imaging.

Gain with different FOMs

With the variable setting of the phantom parameters (see table 4.2), the gains in $\mathrm{CNR}/\mathrm{CNR}_{\mathrm{ROI}}/\mathrm{SNR}_{\mathrm{CHO}}$ were computed as functions of phantom size, organ contrast and the organ size, respectively. First, the dimension of the contrast phantom was scaled globally. Second, the contrast in the hot organ with respect to the background (λ_h/λ_b) was varied. Third, the size of the two organs was changed simultaneously. In each case, we only applied the scaling factor to the assigned parameter and kept the other parameters at the same values as given in the basic setting. The FWHM of the target resolution was 4 pixels. The septa heights of the two collimator systems were chosen to yield the minimal variance according to the results of the FBP-based method.

Validation

For each data point with variable parameter settings, the values of CNR, $\mathrm{CNR}_{\mathrm{ROI}}$ and $\mathrm{SNR}_{\mathrm{CHO}}$ estimated by FIM were verified by simulations for planar imaging. The phantom and the system parameters used in the simulation were the same as those used in FIM (see table 4.2).

To calculate the measures related to the noise property, we performed repeated simulations with 100 noise realizations. For each realization, we added random Poisson noise to the noiseless projection data, and used the resultant noisy data to do image reconstruction. Based on all the reconstructions, the measures were computed using the equations given in 3.2. The variance in the pixel (Var^j) and the variance in the ROI (Var(ROI)) were calculated by (3.11) and (3.15), respectively. The covariance matrix of the reconstruction image ($\mathrm{Cov}(\hat{\Lambda}|H_k)$) used in (3.37) to estimate $\mathrm{SNR}_{\mathrm{CHO}}$ was computed based on (3.12).

For measures which are defined as expectation values, we assumed that the expectation of an estimate can be approximated as the value obtained by estimating the noiseless data[5]. For the calculation of the impulse response, instead of using (3.24), we used

$$l^j(\hat{\Lambda}) = \frac{\hat{\Lambda}(Y(\Lambda + \delta e^j)) - \hat{\Lambda}(Y(\Lambda))}{\delta} \tag{4.30}$$

Similarly, the mean in the ROI defined in (3.14) was computed as

$$\mathrm{Mean(ROI)} = \frac{1}{N_R} \sum_{j \in \mathrm{ROI}} \hat{\lambda}_j(Y) \tag{4.31}$$

---

[5] It is the same assumption that we made for FIM (see (3.59)). This assumption holds when the original tracer distribution Λ is with sufficient number of counts, which was the case in our study.

with $\hat{\lambda}_j$ the value in the j-th pixel of $\hat{\Lambda}$. The lesion profile defined in (3.33) was estimated by

$$z = \hat{\Lambda}\left(Y(\Lambda|H_1)\right) - \hat{\Lambda}\left(Y(\Lambda|H_0)\right) \tag{4.32}$$

For the PH system, the image reconstruction was done using standard MLEM algorithm with 100 iterations. For the RS system, an iteration scheme of 20×20, 20×10, 20×5, 20×2, 20×1 was used with the OSEM algorithm (see 2.4.2).

4.4 FBP: analytical results

We first present the results from the FBP-based methods. All the relevant mathematical derivations can be found in appendix-C and appendix-D, for planar and volume imaging, respectively.

4.4.1 Optimal collimator aperture

For the central point of a uniform symmetrical phantom, we obtain a linear relation between the target resolution σ_t and the optimal collimator apertures σ_p^{opt}, σ_r^{opt}. For planar imaging

$$\sigma_p^{opt} = \sigma_t/\sqrt{2} \tag{4.33}$$
$$\sigma_r^{opt} = \sigma_t/2 \tag{4.34}$$

and for volume imaging

$$\sigma_p^{opt} = \sigma_t/\sqrt{3} \tag{4.35}$$
$$\sigma_r^{opt} = \sigma_t/\sqrt{6} \tag{4.36}$$

Note that for both imaging modes the simplified model leads to the remarkable relation

$$\sigma_p^{opt} = \sqrt{2}\sigma_r^{opt} \tag{4.37}$$

4.4.2 Optimized CNR gain

With the above mentioned optimal collimator apertures, the optimized CNR gains (RS versus PH) in the central point of uniform disk/sphere phantoms are

$$\mathrm{Gain}_{\mathrm{CNR}}^{\mathrm{opt}}(\text{2-D}) = 1.116\sqrt{\frac{\Omega_W}{diameter}} \tag{4.38}$$
$$\mathrm{Gain}_{\mathrm{CNR}}^{\mathrm{opt}}(\text{3-D}) = 1.192\sqrt{\frac{\Omega_W}{diameter}} \tag{4.39}$$

Table 4.2: Parameters used for variable contrast phantom

	Planar imaging	**Volume imaging**
System parameters		
Detector array	128x128	64x64
Image dimension	128x128	64x64x64
Septa space & Pixel size (d_c)	1.8 mm	1.8 mm
Detector width (W)	230.4 mm	115.2 mm
Projection angles (θ, ϕ)	PH: stationary RS: 100 spin angles over 2π	PH: 40 rotation angles over 2π RS: 40 spin / 40 rotation angles over 2π
Raw data dimension	PH: 128x128 RS: 128x100	PH: 64x64x40 RS: 64x40x40
Phantom parameters (basic setting)		
Long/short axis of phantom	180/108 mm	108/72 mm
Diameter of hot/cold organ	27 mm	14.4 mm
Distance between two organs	72 mm	54 mm
Background activity	4.823kBq/cc	4.823kBq/cc
Contrast ($\lambda_h : \lambda_b : \lambda_c$)	8:2:1	8:2:1
Phantom parameters (variable setting)		
Scaling factor (phantom size)	0.3-1.2 (step 0.3)	0.6-1.0 (step 0.4)
Scaling factor (spot size)	0.4-1.0 (step 0.2)	0.6-1.6 (step 0.2)
Scaling factor (contrast $\lambda_h : \lambda_b$)	1:16-16:1 (step $\lambda_h \times 2$)	1:16-16:1 (step $\lambda_h \times 2$)

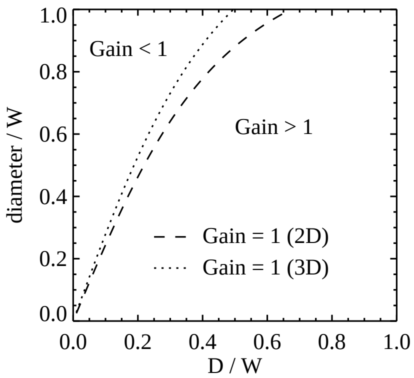

Figure 4.3: Optimized CNR gain: influence of phantom size (*diameter*) and detector distance D with respect to the detector width W. The upper left area is where $\text{Gain}_{\text{CNR}}^{\text{opt}} < 1$, and the lower right area is where $\text{Gain}_{\text{CNR}}^{\text{opt}} > 1$.

for planar (2-D) and volume (3-D) imaging, respectively. Ω_W is the effective detector width that is defined in appendix-A, and *diameter* refers to the diameter of the phantom.

From (4.38) and (4.39), it can be seen that $\text{Gain}_{\text{CNR}}^{\text{opt}}$ is independent of the target resolution σ_t, but depends on the size of the phantom (*diameter*) and the detector distance (D) with respect to the detector width (W). The influence of these factors on the gain is illustrated in Fig. 4.3.

If $D/W >> 1$, we have $\Omega_W \approx W$ (see appendix-A). This implies that in the far-field case, RS is always better than PH as long as the phantom diameter is no larger than the detector width.

4.5 FIM: numerical results

4.5.1 Optimal collimator aperture

Fig. 4.4 shows the optimal collimator aperture of the central point of the 2-D/3-D symmetrical phantom, calculated by both proposed methods. The optimal apertures are plotted as a function of target resolution for both planar imaging (left) and volume imaging (right). For planar imaging, the results of the two methods are in good agreement. For volume imaging, there are small deviations for large target resolutions.

Fig. 4.5 shows the results for all points of interest calculated by FIM in volume imaging. Fig. 4.5(b) plots the optimal aperture for all the points at a target resolution of $\text{FWHM}_t = 9$ mm. The dashed lines plot the values calculated by (4.35) and (4.36) as reference. From these plots we can see that the optimal aperture is

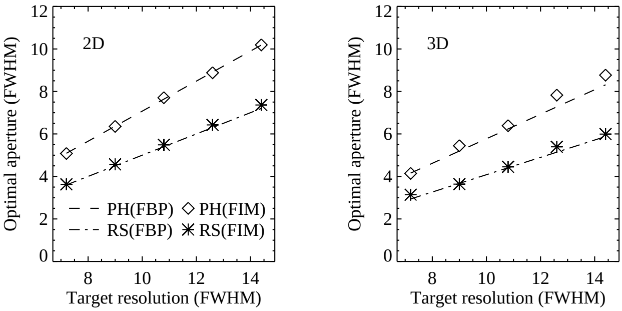

Figure 4.4: Results of central point. The optimal collimator apertures calculated from the two methods are plotted as a function of the target resolution for planar imaging (left) and volume imaging (right), respectively. The unit of the FWHM is mm.

insensitive to the location of the point. Fig. 4.5(c) shows the CNRs of all points of interest, which were calculated using σ_p^{opt} and σ_r^{opt} of the central point of the phantom (point 0). For both PH and RS, the CNR goes up when the point becomes more eccentric.

Fig. 4.6 shows the optimal aperture (left) and the ratio of the optimal apertures (right) of the central ROIs, calculated by FIM in volume imaging. From Fig. 4.6 we can see that: 1) The optimal aperture of the large ROI is always larger than that of the small ROI. 2) For the same target resolution, $\sigma_p^{opt} \approx \sqrt{2}\sigma_r^{opt}$.

4.5.2 Optimized CNR gain

Fig. 4.7 and Fig. 4.8 show the optimized CNR gain at the central point of the phantom, plotted as a function of detector distance D (left) or phantom diameter (right), calculated for planar and volume imaging, respectively. The target resolution is with $\mathrm{FWHM}_t = 9$ mm. For planar imaging, we can see that the results of the two methods (FBP and FIM) are in good agreement for small phantoms or large D. For large phantoms or small D, the gains are slightly underestimated by the FBP-based method (4.38). For volume imaging on the other hand, the gains yielded by FIM are systematically smaller than those from FBP. Generally, the CNR gain increases with increased detector distance or smaller phantom size.

Fig. 4.9 plots the optimized CNR values that yielded the gain in Fig. 4.8. For volume imaging, the CNR acquired by either of the collimator systems increases with decreased detector distance or smaller phantom size.

Fig. 4.10 is similar to Fig. 4.8, with the optimized CNR gains calculated by FIM with different target resolutions. It confirms that CNR gain is not influenced by the choice of the target resolution, as long as the corresponding optimal aperture is used for each collimator system.

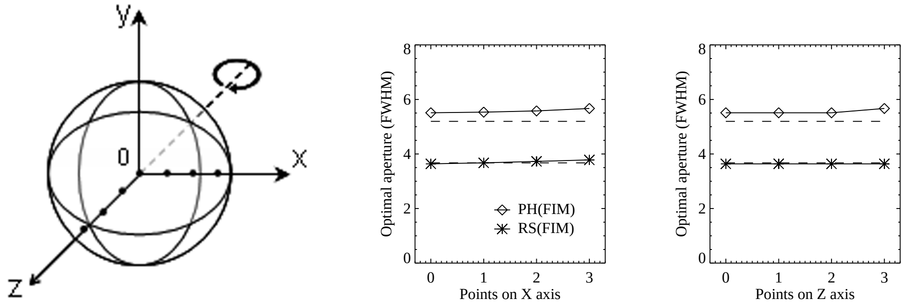

(a) Points of interest

(b) Optimal aperture

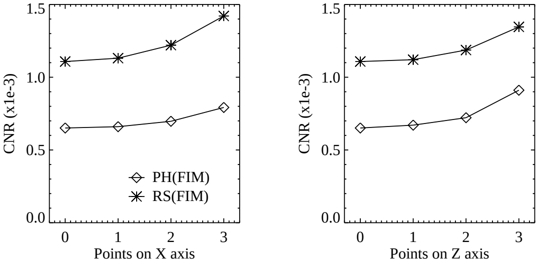

(c) CNR

Figure 4.5: Results of eccentric points. (a) 3-D spherical phantom and points of interest. Z is the axis of rotation, and X is perpendicular to Z. (b) Optimal collimator aperture of all points of interest, calculated for the target resolution with $\mathrm{FWHM}_t = 9$ mm. The dashed lines indicate the values obtained from the FBP calculation, which is only valid for point 0. (c) CNR of all points of interest, calculated using the optimal apertures of point 0, with $\mathrm{FWHM}_t = 9$ mm. The unit of the FWHM is mm.

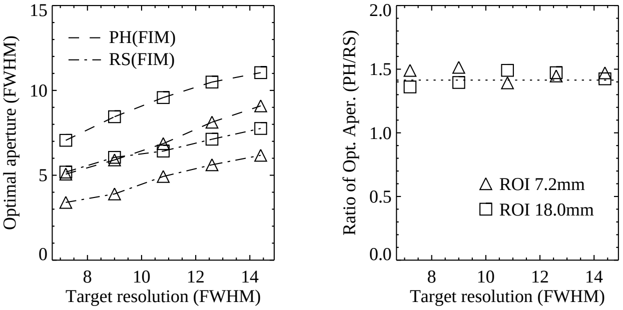

Figure 4.6: Results of central ROIs. Left: Optimal aperture of the ROI as a function of the target resolution. Right: Ratio of the optimal aperture ($\sigma_p^{opt}/\sigma_r^{opt}$). The dotted line indicates the value of $\sqrt{2}$. The unit of the FWHM is mm.

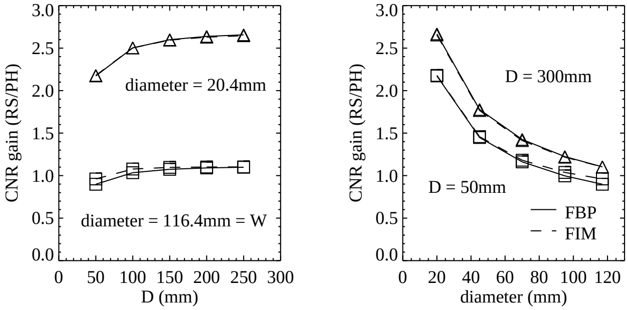

Figure 4.7: Optimized CNR Gain in planar imaging with $\mathrm{FWHM}_t = 9$ mm. Left: Gains plotted as a function of detector distance D for two different phantom sizes (triangle: *diameter* = 20.4 mm, square: *diameter* = W). Right: Gains plotted as a function of phantom diameter at two different detector distances (triangle: $D =$ 300 mm, square: $D = 50$ mm).

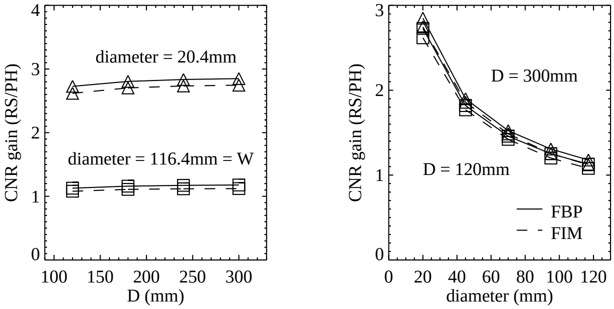

Figure 4.8: Optimized CNR Gain in volume imaging with $\mathrm{FWHM}_t = 9$ mm. Left: Gains plotted as a function of detector distance D for two different phantom sizes (triangle: *diameter* = 20.4 mm, square: *diameter* = W). Right: Gains plotted as a function of phantom diameter at two different detector distances (triangle: $D =$ 300 mm, square: $D = 120$ mm).

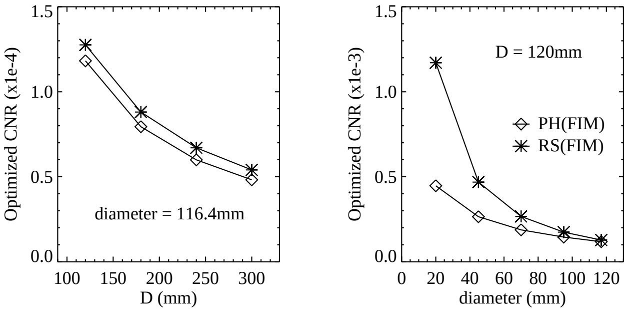

Figure 4.9: Optimized CNR in volume imaging with $\text{FWHM}_t = 9$ mm. Left: CNR plotted as a function of detector distance D for a phantom with $diameter = W$. Right: CNR plotted as a function of phantom diameter with $D = 120$ mm.

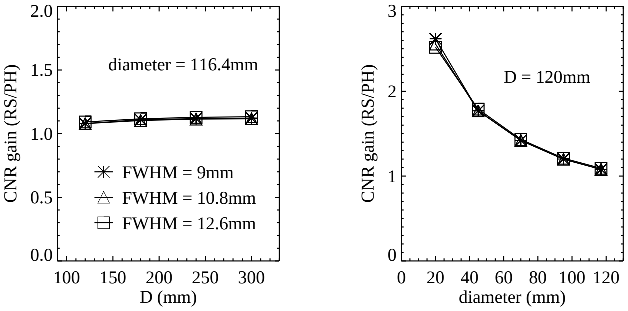

Figure 4.10: Optimized CNR gain in volume imaging with different target resolutions (FWHM_t = 9 mm/10.8 mm/12.6 mm). Left: Gains plotted as a function of detector distance D for a phantom with $diameter = W$. Right: Gains plotted as a function of phantom diameter with $D = 120$ mm.

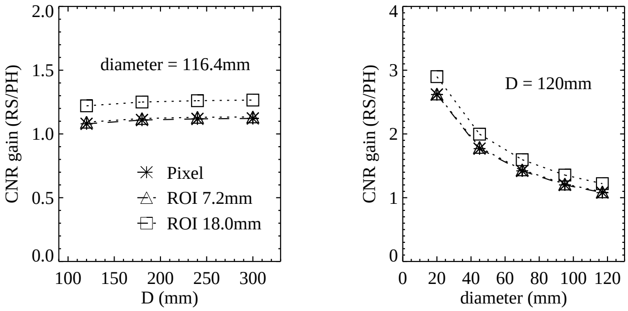

Figure 4.11: CNR Gain of central ROIs in volume imaging with $\mathrm{FWHM}_t = 9$ mm. The gains were calculated for the central ROIs with the optimal apertures minimizing the pixel variance. The asterisk represents the gain in the central pixel which is the same as the dashed line in Fig. 4.8. Left: Gains plotted as a function of detector distance D for a phantom with $diameter = W$. Right: Gains plotted as a function of phantom diameter with $D = 120$ mm.

Fig. 4.11 shows the CNR gains of the central ROIs, calculated with the collimator apertures which minimize the variance in the central pixels. Very similar outcomes of the system comparison are yielded for the central pixel and the central ROIs.

4.5.3 Ellipsoid phantom

For the target resolution of $\mathrm{FWHM}_t = 9$ mm, the optimal apertures for the central point of the ellipsoidal phantom are $\mathrm{FWHM}_p^{opt} = 5.448$ mm, $\mathrm{FWHM}_r^{opt} = 3.638$ mm and $\mathrm{FWHM}_p^{opt}/\mathrm{FWHM}_r^{opt} \approx 1.497$. Fig. 4.12 shows the central sagittal slice of (a) the original phantom, (b) the phantom smoothed by the target resolution, (c)-(d) the PH and the RS MLEM reconstructions of the noiseless sinogram of this phantom, post-smoothed to the target resolution. The reconstructions look quite similar to the smoothed version of the original phantom.

4.5.4 Variable contrast phantom

Optimal aperture

Fig. 4.13 gives the results about the optimal aperture corresponding to the central point of the contrast phantom in planar imaging. We use the symbol of square/triangle/diamond to represent $\mathrm{CNR}/\mathrm{CNR}_{\mathrm{ROI}}/\mathrm{SNR}_{\mathrm{CHO}}$, and use the solid and the dashed lines to indicate PH and RS, respectively. As shown in the left figure in Fig. 4.13, each FOM yields its own optimal aperture sets. Although the optimal apertures are different for different FOMs, the ratio of the optimal apertures ($\sigma_p^{opt}/\sigma_r^{opt}$) is always close to $\sqrt{2}$ (Fig. 4.13, right).

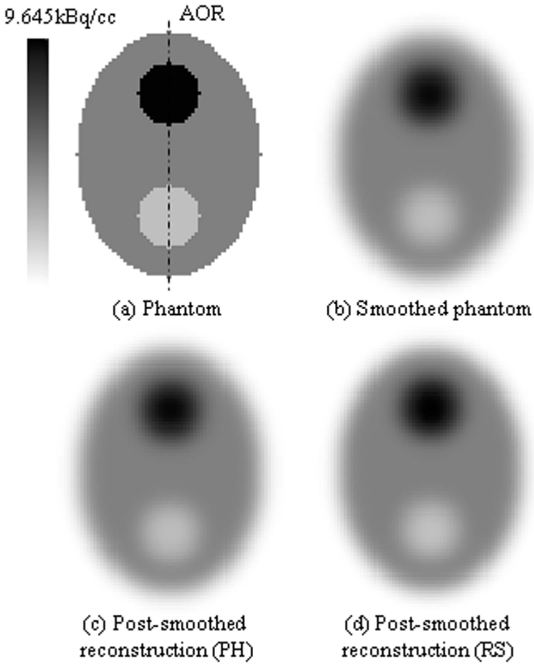
9.645kBq/cc
AOR
(a) Phantom
(b) Smoothed phantom
(c) Post-smoothed reconstruction (PH)
(d) Post-smoothed reconstruction (RS)

Figure 4.12: Central sagittal slice of (a) ellipsoid phantom, (b) phantom smoothed with target resolution ($\mathrm{FWHM}_t = 9$ mm). (c)-(d) PH and RS MLEM reconstructions, calculated using their own optimal collimator apertures, post-smoothed to the target resolution. The dash dot line represents the axis of rotation.

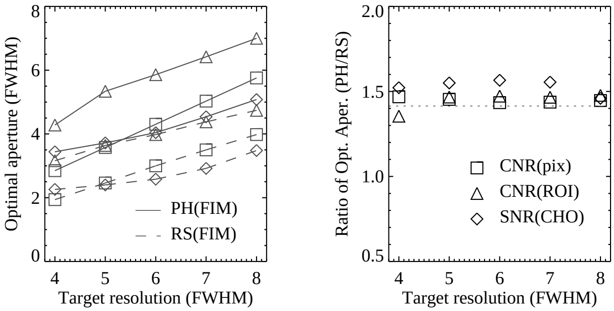

Figure 4.13: Results with contrast phantom in planar imaging. Left: Optimal collimator apertures are plotted as a function of the target resolution. Right: Ratio of the optimal aperture. The dashed line represents the value of $\sqrt{2}$.

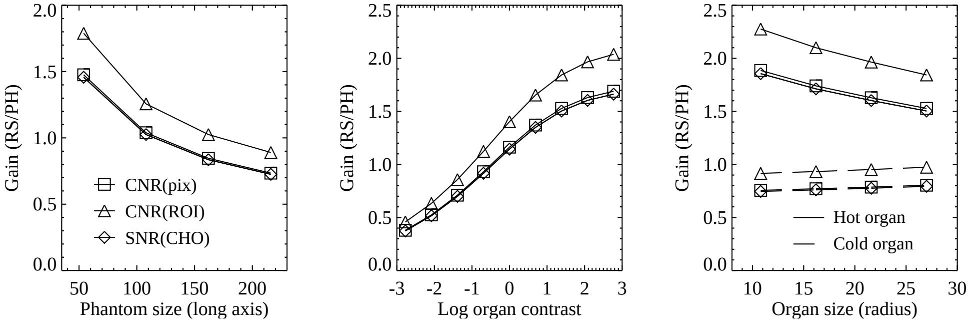

Figure 4.14: Gains (RS/PH) in planar imaging, plotted as a function of phantom size (left), organ-to-background contrast (middle) and organ size (right).

Gain with different FOMs

The comparison results using different FOMs are shown in Fig. 4.14 and Fig. 4.15 for planar and volume imaging, respectively. It can been seen that 1) with increased phantom size, all the gains decrease. 2) The gains go up with increased organ-to-background contrast. For planar imaging, PH has slightly better performance than RS in low contrast cases, while for volume imaging, RS always outperforms PH with the given parameters. 3) For planar imaging, the gains decrease with increasing organ size for the hot organ, while it is the opposite for the cold organ. Overall, RS is better in hot spot imaging (gains > 1) and PH has benefit in cold spot imaging (gains < 1). For volume imaging, again RS yields better results with hot spot, but the two collimator systems behave almost equally well in cold spot imaging. The plots of the gains in both organs are quite flat with respect to the organ size.

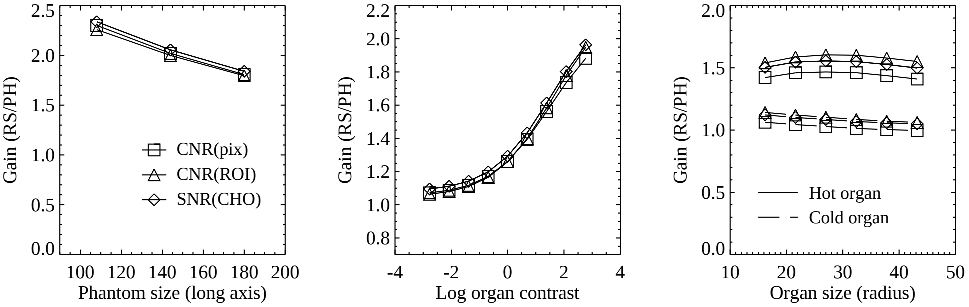

Figure 4.15: Gains (RS/PH) in volume imaging, plotted as a function of phantom size (left), organ-to-background contrast (middle) and organ size (right).

Validation

The validation results for each data point in Fig. 4.14 are shown in Fig. 4.16. The asterisk and triangle represent PH and RS, respectively. The approximated CNR, $\mathrm{CNR_{ROI}}$ and $\mathrm{SNR_{CHO}}$ are in good agreement with their values computed from repeated simulations.

If we plot the $\mathrm{CNR_{ROI}}$ predicted by FIM with respect to the $\mathrm{CNR_{ROI}}$ calculated from the repeated simulations (Fig. 4.16, middle), a slope of 1.04 can be derived using least squares fitting. In addition, 64.7% (resp. 94.1%) of the plotted points are located in the 68.3% (resp. 95.4%) confidence intervals (one and two standard deviations) centered on the identity line, indicating that the $\mathrm{CNR_{ROI}}$ estimated by FIM are in good accordance with those estimated from the repeated simulations.

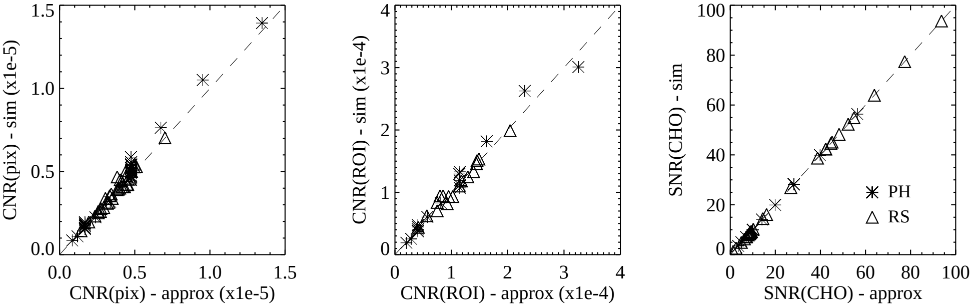

Figure 4.16: Validation results for each data point in Fig. 4.14. Left/middle/right: $\mathrm{CNR/CNR_{ROI}/SNR_{CHO}}$. The dashed lines indicate the perfect agreement.

4.6 Discussion

Previously, the validation of FIM has been performed for various multi-pinhole SPECT system configurations [130], as well as for the TOF-PET system [135]. As for the PH and the RS collimator system, we did the validation based on a 2-D contrast phantom with post-smoothed MLEM reconstruction of 100 noise realizations (Fig. 4.16). Although the validation is only performed for planar imaging, we believe that FIM will be also valid for volume imaging due to its capability of accommodating shift-variant system response [130] and the attenuation within the phantom [135].

For the imaging systems studied here, FBP yields essentially the unweighted least squares (LS) solution. However, for a large symmetrical object, most of the projection values contributing to the reconstruction of a central point have the same expected value. Due to the assumed Poisson distribution, they also have the same variance, which means that LS can be approximately considered as weighted least squares (WLS). On the other hand, the approximate Fisher information-based method yields predictions that are in good agreement with reconstructions produced with MLEM or WLS followed by post-smoothing. Therefore, for the center of a large symmetrical object, post-smoothed LS, WLS and MLEM should all produce nearly the same variance at matched resolution. In our case, although the system models used for FBP and FIM are not identical due to the FBP-specific approximations, the difference is expected to have only minor influence on the variance of the central point of the object, where the modeling of the geometric efficiency and the collimator blurring is always accurate. Consequently, FBP calculation and FIM should agree well for the central points.

It can be seen from the results that the two methods indeed give very similar results for the central point of a uniform object. Although the FBP-based calculation involves some particular approximations, it provides insight into the mechanisms of noise propagation for the two types of collimators, and is expected to be accurate at least for the basic results ((4.33)-(4.37)). FIM was validated for the proposed collimation geometries, and coincides well with the FBP-based method. In addition, FIM is more flexible in the sense that it can be applied to more realistic phantoms and more sophisticated system models, including the attenuation of the phantom and the depth-dependent collimator response in volume imaging, therefore it was used to extend and generalize the results of the FBP-based calculation.

The comparison was performed with several assumptions described in 4.2.1. In fact, these assumptions (the septal penetration, the detector efficiency, etc.) are expected to have minor impact on the outcome of the collimator comparison. A non-negligible septa thickness t will introduce a scale factor of $d_c^2/(d_c+t)^2$ in σ_p and of $d_c/(d_c+t)$ in σ_r. As a result, σ_c^{opt} in (4.33)-(4.37) should also be scaled, and a scale factor of $\sqrt{(d_c+t)/d_c}$ should be applied to the optimized CNR gain in (4.38)-(4.39). For a realistic acquisition system with intrinsic detector resolution $\sigma_d \neq 0$, σ_t should be replaced by $\sqrt{\sigma_t^2-\sigma_d^2}$. With this replacement, our main results (4.33)-(4.39) will still hold for the central point of a symmetrical phantom.

From (4.33)-(4.36), we found that the optimal collimator aperture is proportional to the target resolution that is imposed in the reconstruction. Similar results were presented in a study of pinhole imaging system [44], which claims that in order to minimize the variance of the emission-rate density estimate at a particular spatial resolution, the pinhole size should be proportional to that resolution. Furthermore, for a Gaussian-shaped pinhole aperture, the FWHM of the pinhole aperture that yields the minimal variance in planar imaging equals the desired spatial resolution divided by $\sqrt{2}$. The tradeoff between the spatial resolution and the noise with this Gaussian pinhole collimator is very similar to that with the PH collimator in our study. Therefore, (4.33)-(4.36) could be also considered as a reference for the system optimization of other collimators whose configurations are similar to the proposed collimations in this chapter.

Using the two analytical methods, it was also found that the optimal aperture of a line-integral acquisition system is always $\sqrt{2}$ times larger than that of a plane-integral acquisition system. This relation was first derived with the FBP-based calculation for a central point in an ideal phantom ((4.37)), and was then verified for eccentric points (Fig. 4.5) and central ROIs (Fig. 4.6) by FIM using more sophisticated system models. In addition, a similar ratio was also found for the central point of non-symmetrical, non-uniform phantom (Fig. 4.12) and with different figures of merit (Fig. 4.13). Based on the results above, we propose to compare these two types of systems with their collimator aperture ratio equal to $\sqrt{2}$. The principle of using the optimal collimator aperture could be applied to any system comparison task at equal spatial resolution.

Our results show (Fig. 4.5(c)) that the eccentric pixels have a lower variance and higher CNR than central pixels in the phantom. This well-known observation [5] is explained by the fact that, with the PH(RS) system, some of the lines(planes) through eccentric pixels have a shorter intersection length (or less intersection area) with the phantom and are therefore less multiplexed with neighbouring pixels than the lines(planes) through the central pixels.

The CNR gain ((4.38) and (4.39)) can also be written as a function of the geometric efficiency gain F (with $F = E_r/E_p$). For example, for volume imaging, it yields

$$\mathrm{Gain}_{\mathrm{CNR}}^{\mathrm{opt}} = 1.192\sqrt{\frac{\Omega_W}{diameter}} = 1.653\sqrt{\frac{F\sigma_t}{diameter}} \tag{4.40}$$

This expression is similar to those presented in [77, 157], where the formula was expressed as the gain in SNR rather than in CNR. Since we compared the two systems based on the same activity distribution, the SNR gain is actually equivalent to the CNR gain. The main differences between our approach and [77,157] are that we compared PH and RS at a fixed target resolution, and that we used the optimized aperture for each collimator system.

The mathematical expressions for the optimal aperture and the optimized CNR gain are derived based on uniform symmetrical phantoms, while realistic tracer distributions in human and preclinical imaging are usually very non-uniform. To generalize the basic results, we applied the Fisher information-based method to contrast phantoms with variable parameters, in order to explore the relative performance of the two systems using different figures of merit. To verify the consistency between the projector and back-projector, we also present the reconstruction images of a non-uniform, non-symmetrical ellipsoid phantom using the optimal aperture of its central point calculated by FIM. With the modeling of depth-dependent blurring and the attenuation, the reconstruction in volume imaging is very time-consuming. Therefore we did not consider numerical verification of FIM in this setting.

The relative performance of the two systems for the central point of a uniform symmetrical phantom can be evaluated based on Figs. 4.3, 4.7 and 4.8. Fig. 4.3 explicitly gives the condition under which the RS will outperform PH, and vice versa. Although the "Gain = 1" boundaries depicted in Fig. 4.3 are not accurate due to the FBP-specific approximations, they can be considered as references for the collimator comparison when combined with Figs. 4.7 and 4.8. It can be seen that the comparative result is ultimately determined by the object size and the object-to-detector distance D. Generally, the optimized CNR gain increases with smaller object size (which is in agreement with [59, 76, 77, 157]) or with larger object-to-detector distance. One should note that for tomographic scans the absolute CNR value actually decreases as the detector distance increases, therefore the object should always be positioned as close as possible to the collimator, regardless of the system in use.

The relative performance of the two systems with non-uniform contrast phantoms can be evaluated based on Fig. 4.14 and Fig. 4.15. Using the collimator aperture optimized for pixel variance, the gains in all three figures of merit (CNR, $\mathrm{CNR_{ROI}}$ and $\mathrm{SNR_{CHO}}$) give very similar rankings. PH only yield better results than RS in 2-D cold spot imaging in combination with a large background, while RS outperforms PH in the rest of the cases. These results are in agreement with [59, 60]. However, in [60], it is claimed that the RS collimator is more than 4 times better than PH for 3-D cold spot imaging, while for the same case in our study only slight improvement was found by using the RS system (Fig. 4.15, right). This discrepancy is probably due to the fact that in [60] they applied equal collimator apertures for both systems and that there may not have been a perfect match of the spatial resolution in the reconstructions.

In this study, the projection and the backprojection with the RS collimator treat all the detectors between the neighboring slat septa as one detector element (see (4.6) and (4.11)). This RS projector is called *non-pixellated projector*. If the detector array is pixellated, i.e., each detector pixel participates individually in the projection/backprojection, the RS projector becomes a *pixellated projector*. Obviously, the information carried in the data acquired with a non-pixellated projector is less than that with a pixellated projector. In that case, every pixel is reconstructed with lower certainty, resulting in a higher variance in the reconstruction. However, based on our study [161], the increase of the variance is very small and has no significant influence on the comparative result between the PH and the RS systems. Hence, the non-pixellated RS projector is preferable since it facilitates the algorithm implementation and saves a lot of computation time compared to a pixellated RS projector.

Only objects smaller than the field of view (FOV) of the collimators were considered in this study to avoid the possibly confounding effects of the data truncation problem which is still poorly understood. When an object is larger than the FOV in transaxial direction, both PH and RS systems may suffer from increased variance and artifacts, depending on the amount of data truncation. For axial truncation, however, PH has the advantage because the axial out-of-FOV activity remains undetected and does not create artifacts. In contrast, the RS system will detect a contribution from this activity. This contribution will increase the variance in the reconstruction. Moreover, unless the acquisition can be well modeled as plane integrals, artifact-free reconstruction may be problematic as well. However, only considering objects fitting in the FOV, we already found that for very large objects, the PH collimator should be recommended rather than the RS collimator. Consequently, considering even larger objects which will cause additional problems for RS, will not change that recommendation.

With uniform phantoms, the CNR gains for two different ROI sizes were quantified with the collimator aperture optimized for the pixel variance. Strictly speaking, for optimal quantification of an object of interest, both the collimator aperture and the target resolution should be adjusted to match the size of that object. However, in practice, we usually produce a single image with a fixed aperture size, applying a certain amount of smoothing, and then use that image for all kinds of tasks such as visual inspection, definition of ROIs with different sizes and quantification of the ROI-values. In this sense, it is reasonable to perform the comparative task for a single pixel or the ROIs with different sizes based on the same system parameters. The ranking for the relative system performance is found to be very similar regardless of the object of interest.

4.7 Conclusion

In this study, we compare the PH and the RS collimators using the optimal collimator aperture that yields the minimal pixel variance at a prescribed spatial resolution. Two analytical methods, the FBP-based calculation and the Fisher information-based method, are applied to compute the optimized CNR using a simplified collimator blurring model and a realistic depth-dependent blurring model, respectively. It is shown that the two methods yield very similar results for the central point in a uniform disk or sphere phantom. To generalize the basic results derived from the FBP-based calculation, we also applied FIM to estimate the CNR in eccentric pixels of interest, the CNR in regions of interest, as well as the SNR for channelized Hotelling observer using non-uniform non-symmetrical contrast phantom with variable parameters.

It is found that the variance in the reconstruction image varies with the collimator aperture, and that the optimal collimator aperture is proportional to the target spatial resolution imposed in the reconstruction. For equal spatial resolution in the reconstruction, RS always needs more post-smoothing than PH. Therefore, the optimal collimator aperture of a RS system is always smaller than that of a PH system. Our results suggest that a fair comparison between the performance of the two types of collimators can be achieved using a ratio of $\sqrt{2}$ between the PH and the RS collimator apertures. With the optimal apertures, the expressions of the CNR gain (RS versus PH) are derived in different imaging modes. The three proposed figures of merit yield a very similar ranking for the relative system performance, which is determined by the object size, the object-to-detector distance as well as the spot-to-background contrast. For planar imaging, PH only outperforms RS for cold spot imaging with large objects, while RS gives better results for all the rest of the cases. For volume imaging, RS is almost always better than PH, if the object is not larger than the detector width.

Chapter 5

Multi-pinhole SPECT calibration

For pinhole SPECT, geometric calibration is needed to acquire an accurate description of the geometrical configuration. It is often achieved by putting several radioactive point sources in the field of view, and estimating all the parameters using penalized least squares fitting between the estimated point projections and the mass centers of the measured point projections.

For a single pinhole SPECT system with circular orbit, the geometry can be uniquely determined from a measurement of three point sources, provided that at least two inter-point distances are known. In contrast, it has been shown mathematically that, for a multi-pinhole SPECT system with circular orbit, only two point sources are needed, and the knowledge of the distance between them is not required. In our study, it was found that the conclusion for multi-pinhole SPECT only holds if the motion of the camera is perfectly circular. In reality, the detector heads systematically slightly deviate from the circular orbit, which may introduce non-negligible bias in the estimated parameters and degrade the reconstructed image. These small deviations from the ideal orbit are called *systematic deviations* in the remainder of the text.

To study the error propagation in multi-pinhole SPECT calibration, we extended an analytical linear model and applied it for two purposes: 1) to estimate the influence of both data noise and systematic deviations on the accuracy of the calibration and on the image quality of the reconstruction, using different prior information during calibration, and 2) to determine a point source configuration which yields an accurate and stable calibration result and acceptable reconstruction errors in the presence of systematic deviations.

In this chapter, the details about these two studies are explicitly explained. The theoretical results derived based on the analytical method were verified by (repeated) simulations, and well supported by the results from real experiments using Jaszczak-type resolution phantoms.

5.1 Introduction

For accurate image reconstruction, a good estimate of the system matrix is required. Determining the system matrix is particularly challenging for small animal imaging with multi-pinhole SPECT using a rotating gamma camera. For (multi-) pinhole SPECT, it is convenient to factorize the system matrix into several contributions. These include

- the geometry of the idealized pinhole system, where idealized means that the acquisition is modeled as perfect line integrals,
- the blurring caused by the intrinsic detector resolution and the finite (effective) diameter of the pinholes,
- the position dependent detector sensitivity, caused by the finite aperture angle of the pinholes and the position dependence of the relevant solid angles.

In this work we only study the estimation of the first contribution to the system matrix. Estimating the related geometrical parameters is called *geometrical calibration* or simply *calibration* (see 2.3.1). Once the position of these idealized projection lines is known, the acquisition model can be further improved by modeling the finite resolution (e.g. by replacing the single line with a tube or a set of lines [127]), and by taking into account the calculated or measured detector sensitivities for each pinhole aperture [10].

For a conventional single pinhole SPECT system with circular camera motion, there are 6 degrees of freedom (DoFs) for the gamma camera and 3 DoFs of the pinhole. However, since we can arbitrarily define the position of the pinhole along the axis of rotation and where the projection angle is zero, only 7 parameters are needed to uniquely characterize the geometry of the single pinhole SPECT system [20]. It has been proven mathematically and experimentally that a measurement of 3 point sources, of which at least two inter-point distances are known, is necessary and sufficient to determine these 7 geometrical parameters [20].

Compared with single pinhole SPECT, multi-pinhole SPECT systems attract more attention due to the increase of the detection sensitivity, which results in a higher signal-to-noise ratio in the reconstruction image [18,38,80,112,128,130]. As proven mathematically in [131,142], a rotating multi-pinhole SPECT only requires 2 point sources without any knowledge about their distance with respect to each other. However, our preliminary tests with measured data indicated that if the distance between the point sources is not fixed to its true value, the calibration of the multi-pinhole system can be unstable and the reconstruction may suffer from a large scaling effect (with the reconstructed distances typically smaller than the true ones).

With the mathematical models proposed in [131, 142], a basic assumption is that the acquisition orbit is perfectly circular. In reality, there are always slight deviations between the circular orbit and the actual orbit due to gravity, mechanical imprecisions, or other reasons [36, 88]. Some of the deviations follow a certain pattern (for example a sine-curve) as a function of acquisition angle, and some are more erratic. These systematic deviations will introduce bias on the calibration results if we use a calibration method which assumes perfect camera motion. Since the deviations are expected to be very small, the bias was assumed to be negligible in the previous studies.

The calibration procedure we currently use is described in [99]. The calibration phantom is a rigid plexi plate containing three radioactive point sources. It is positioned in the center of the field of view, and a scan is acquired with the same geometry and protocol as those of the animal scan. From this scan, the geometry is estimated using a two-step procedure based on least squares fitting. For all the geometrical parameters and the point sources locations, we give initial values and calculate the coordinates of the point projections. These parameters and locations are then fitted by comparing the estimated projections to the mass centers of the measured point projections using a least squares fitting procedure. Prior knowledge of the distances between the point sources is typically applied during the fit in order to improve the calibration stability [21]. In the first step of the procedure, the so-called *conventional calibration*, a single value is fitted for each parameter. This problem is over-determined and has a unique solution. The results are used as the input values of the second step, which we refer to as *refined calibration* [36]. With refined calibration, the detector and the pinhole collimator are considered as one rigid object, whose motion can be uniquely described by 3 translation coordinates and 3 rotation angles. These 6 degrees of freedom are determined individually for each projection angle. Here, the number of unknowns is very large and the sum of squared differences has probably many local minima. For that reason, a penalty which discourages large translations and rotations is introduced since all the deviations are expected to be small.

The conventional calibration basically estimates the mean value of each parameter over all angular positions[1]. If the systematic deviations lead to non-negligible bias on these mean values, that bias is not corrected for in the second step, because the refined calibration tends to produce perturbative angle dependent adjustments with (nearly) zero mean. In this work, we show that this bias can degrade the reconstruction image quality, and we propose a method to predict the degradation, which can be used to design robust calibration configurations.

The first goal of this work (study I) is to study the error propagation in multi-pinhole SPECT calibration. To do this, we extended an analytical linear approximation model, which was previously used to estimate the noise propagation property in single pinhole calibration [21], to investigate the influence of both data noise and systematic orbit deviations on multi-pinhole SPECT calibration. This method first estimates the bias and the variance on the estimated parameters (calibration accuracy), and uses these to compute the resolution loss and image deformation in the reconstructed images (reconstruction accuracy). With this method, the stability and accuracy of the calibration/reconstruction results with and without the prior knowledge of the distance were explored. The comprehensive calibration/reconstruction results of a typical point source setup were analyzed both theoretically and with reconstructions of measured data.

---

[1] Each parameter is estimated as a single value, although in reality its true value may vary during rotation. We assumed this estimated value is a useful mean value. Apparently, it is not a true mean because it is biased.

The second goal of this work (study II) is to determine point source configurations which lead to an accurate and stable calibration result for our multi-pinhole SPECT system, particularly in the presence of systematic deviations. The selection was done using the proposed analytical method. In order to reduce the acquisition time for small animal experiments, we were interested in simultaneous animal/calibration scanning. Therefore the candidate point sources were only allowed to be localized on the surface of a cylindrical tube which is assumed to be the animal carrier. The reconstruction errors corresponding to every point combination were calculated and compared. One of the selected point configurations was used in a simultaneous phantom/calibration measurement to support the theoretical result.

5.2 Outline of the study

For better understanding of the following sections, we first introduce the most relevant notations and symbols used in the remainder of the text. In addition, we classify the calibration problems into several cases, which will be discussed explicitly in 5.3.

We define the parameter set P_T as the true geometric parameters consisting of both the camera-specific parameters and the locations of the point sources. We use U_0 to denote the original projection of the point sources without the disturbance of noise or systematic deviations, and the symbol U to represent the projection data which are subject to either random noise or systematic deviations, or both. The difference between this "actual" projection and the original projection is thus $\Delta U = U - U_0$. Applying a calibration procedure to U results in the estimated parameter set P. The difference between the estimated and the true parameters is $\Delta P = P - P_T$.

Ideally, the camera follows a perfectly circular motion. Then P_T are constant for all projection angles, and will be denoted as P_0. However, if the camera slightly deviates from the circular orbit, these parameters need to be adjusted as a function of the projection angle. As mentioned in the introduction, the deviation at each acquisition angle can be described by 6 degrees of freedom (DoFs). We symbolize the amplitude of each DoF by $\Delta P_0(k_\delta, k_\theta)$, with k_δ and k_θ the index of the degree of freedom and the index of the projection angle, respectively. For convenience, we use $\Delta P_0(k_\delta, \cdot)$ to denote the deviation pattern of the k_δ-th DoF as a function of the projection angles, use $\Delta P_0(\cdot, k_\theta)$ to denote the 6 DoFs corresponding to the k_θ-th angle, and use ΔP_0 (with no argument) to denote the systematic deviations in general which involve all 6 DoFs of all acquisition angles.

Since ΔP_0 is not involved in the projection model of conventional calibration, we consider it as a source of error disturbing the projection. To distinguish between the influences of the two error sources, we use ΔU_N and ΔU_D to denote ΔU caused by data noise and systematic orbit deviations, respectively, with ΔU_D a function of ΔP_0.

Assuming that the effects of the two error sources are independent from each other, we discuss the calibration problems in the following cases:

- Case 0: The projection is ideal ($U = U_0$), thus the geometric parameters are perfectly estimated ($P = P_0$).
- Case 1: The projection U is disturbed by measurement noise ($U = U_0 + \Delta U_N$) and the parameter estimation is done with conventional calibration. The noise on the data introduces uncertainty on each estimated parameter, and this uncertainty will be expressed as variance (or standard deviation, denoted as ΔP_N) on the final parameter estimates ($P = P_0(\pm \Delta P_N)$).
- Case 2: The projection U is subject to systematic orbit deviations ($U = U_0 + \Delta U_D$), and the parameter estimation is done with conventional calibration. The orbit deviations will introduce bias (ΔP_B)[2] on the estimated parameters ($P = P_0 + \Delta P_B$).
- Case 3: The projection is the same as in case 2, but the refined calibration is performed after the conventional calibration to estimate the systematic deviations (with element denoted as $\Delta P_D(k_\delta, k_\theta)$[3]). The parameters with this refined adjustment are $P = P_0 + \Delta P_B + \Delta P_D$.

A summary of all these cases can be found in table 5.1.

Real measurements will be subject to both noise and systematic deviations. However, it is assumed that they are independent such that the contributions can be studied separately. Therefore, we only compute the degradation of image quality in the reconstruction due to ΔP in case 1, 2, and 3 using the analytical method, and then compare the results for a general evaluation about the influence of different error sources and of the application of different calibration procedures.

In this study, first, we analyzed the calibration accuracy and reconstruction accuracy in case 1, 2 and 3 based on a typical 3-point calibration phantom (study I). Then, a point source configuration was selected for our multi-pinhole SPECT system in case 3 only (study II).

This chapter is organized as follows. In 5.3.1, the principle of calibration using point sources is briefly explained. The expressions for the projection coordinates U are given as a function of the parameter set P with and without the modeling of systematic deviations. In addition, the use of prior knowledge of distances during the calibration is also described. In 5.3.2 we explain how to apply a linear approximation model to estimate the accuracy on the estimated parameters, such as the

---

[2] It is assumed that the systematic deviation $\Delta P_0(\cdot, k_\theta)$ has (nearly) zero mean, therefore we define ΔP_B as the bias with respect to P_0 rather than $P_0 + \Delta P_0(k_\delta, k_\theta)$.

[3] Note that both $\Delta P_0(k_\delta, k_\theta)$ and $\Delta P_D(k_\delta, k_\theta)$ represent systematic deviations, but the former is the ground truth and the latter is the estimation. The rule of notation for ΔP_0 also holds for ΔP_D.

Table 5.1: Overview of calibration problems

Case	**Error source**	**True param.** P_T	**Proj. data** U	**Calibration procedure**	**Estimated param.** P
0	-	P_0	U_0	conventional	P_0
1	noise	P_0	$U_0 + \Delta U_N$	conventional	$P_0(\pm \Delta P_N)$
2	systematic deviations	$P_0 + \Delta P_0(k_\delta, k_\theta)$	$U_0 + \Delta U_D$	conventional	$P_0 + \Delta P_B$
3	systematic deviations	$P_0 + \Delta P_0(k_\delta, k_\theta)$	$U_0 + \Delta U_D$	conventional + refined	$P_0 + \Delta P_B + \Delta P_D(k_\delta, k_\theta)$

Table 5.2: Camera-specific geometrical parameters

d_D	distance between the image center and the detector plane
f_i	focal length of i-th pinhole aperture
m_i, n_i	mechanical offsets of i-th pinhole aperture in detector column/row direction
e_u, e_v	electrical detector offsets in detector column/row direction
Φ	tilt angle, i.e. angle between the detector plane and the AOR
Ψ	twist angle, i.e., orientation of the detector grid as a rotation around an axis perpendicular to the detector plane

Table 5.3: Unknown calibration parameters per calibration method.

Calibration method	**Camera-specific parameters**	**Point source location parameters**
No distances fixed	d_D, $f_{i=1,\dots,I}$, $m_{i=1,\dots,I}$, $n_{i=1,\dots,I}$, e_u, e_v, Φ, Ψ	$x_{j=1,\dots,J}$, $y_{j=1,\dots,J}$, $z_{j=1,\dots,J}$
Inter-point distance(s) fixed	d_D, $f_{i=1,\dots,I}$, $m_{i=1,\dots,I}$, $n_{i=1,\dots,I}$, e_u, e_v, Φ, Ψ	3 translations, 2 or 3 rotations
Inter-pinhole distance(s) fixed	d_D, 3 translations, 2 or 3 rotations, e_u, e_v, Φ, Ψ	$x_{j=1,\dots,J}$, $y_{j=1,\dots,J}$, $z_{j=1,\dots,J}$
All distances fixed	d_D, 3 translations, 2 or 3 rotations, e_u, e_v, Φ, Ψ	3 translations, 2 or 3 rotations

standard deviation ΔP_N and the bias ΔP_B obtained with conventional calibration. In 5.3.3, the measures for the reconstruction accuracy are proposed as a function of projection coordinates and ΔP, and an efficient approach for computing these measures is described for the above mentioned case 1, 2 and 3, respectively. In 5.3.4, we explain how to verify the proposed analytical method using repeated numerical simulations for each individual case. The data truncation modeling is described in 5.3.5. The deviation patterns used for point configuration selection are explained in 5.3.6. Details, results and the conclusion of the first study are given in 5.4-5.6, and those of the second study are presented in 5.7-5.9, respectively.

5.3 Methods

5.3.1 Principle of calibration

Point Projection with Perfect Circular Orbit

Following the notations in [20], we describe a multi-pinhole SPECT system with circular camera motion using the following parameters: detector distance d_D[4], focal distances $f_1, f_2, \ldots, f_I$, mechanical offsets $m_1, m_2, \ldots, m_I$ and $n_1, n_2, \ldots, n_I$, electrical offsets e_u and e_v, tilt angle Φ, and twist angle Ψ, with I the total number of pinhole apertures. These parameters are briefly described in table 5.2 and illustrated in Fig. 5.1. The projection data is acquired at different rotation angles Θ, indexed by k_θ ($k_\theta = 1, \ldots, N_\theta$, with N_θ the total number of angles). It is assumed that all the parameters are independent of the acquisition angle and remain constant during the acquisition.

Similar to the single pinhole geometry [20], the projection coordinates are expressed as $U = [\ldots, u_{ij}(k_\theta), v_{ij}(k_\theta), \ldots]^T$, where ^{T} denotes the transpose, and the projection coordinates u, v of the calibration point source j (x_j, y_j, z_j) through pinhole aperture i along the k_θ-th projection angle can be written as:

$$u_{ij}(k_\theta) = f_i \frac{m_i - \tilde{x}_j}{d_D - f_i + \tilde{y}_j} + m_i + e_u \qquad (5.1)$$

$$v_{ij}(k_\theta) = f_i \frac{n_i - \tilde{z}_j}{d_D - f_i + \tilde{y}_j} + n_i + e_v \qquad (5.2)$$

in which

$$\begin{bmatrix} \tilde{x}_j \\ \tilde{y}_j \\ \tilde{z}_j \end{bmatrix} = R_3(\Psi) R_2(\Phi) R_1(\theta) \begin{bmatrix} x_j \\ y_j \\ z_j \end{bmatrix} \qquad (5.3)$$

---

[4] It is different from the symbol d used in [20] which represents the distance between the axis of rotation and the pinhole.

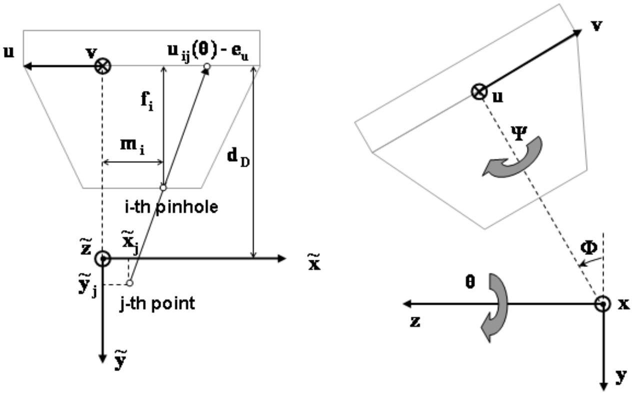

(a) (b)

Figure 5.1: (a) Illustration of the geometry parameters along column direction. (b) Illustration of three rotation angles.

with $\theta = \Theta(k_\theta)$ and

$$R_1(\theta) = \begin{bmatrix} \cos\theta & \sin\theta & 0 \\ -\sin\theta & \cos\theta & 0 \\ 0 & 0 & 1 \end{bmatrix} \tag{5.4}$$

$$R_2(\Phi) = \begin{bmatrix} 1 & 0 & 0 \\ 0 & \cos\Phi & -\sin\Phi \\ 0 & \sin\Phi & \cos\Phi \end{bmatrix} \tag{5.5}$$

$$R_3(\Psi) = \begin{bmatrix} \cos\Psi & 0 & -\sin\Psi \\ 0 & 1 & 0 \\ \sin\Psi & 0 & \cos\Psi \end{bmatrix} \tag{5.6}$$

The parameter set to be estimated (P) consists of both camera-specific parameters (d_D, f_i, m_i, n_i, e_u, e_v, Φ, Ψ) and point source locations (x_j, y_j, z_j). For the conventional calibration, we apply (5.1) and (5.2) to calculate the locations of the point source projection using the initial estimates for all parameters. The estimates are updated by minimizing the sum of the squared differences between the calculated projections and the centroids of the measured projections.

The uniqueness and the stability of the fitting solution is influenced by the choice of the point sources. For multi-pinhole SPECT, two point sources are essential to yield a unique solution, providing that they do not form a line orthogonal to the axis of rotation [131, 142].

Point Projection with Systematic Deviations

If the orbit of the camera slightly deviates from the assumed perfect circle, the actual geometric parameters described in table 5.2 will vary from projection angle to projection angle. For each acquisition position, the ensemble of the detector and the pinhole collimator can be considered as a rigid object with 6 degrees of freedom, i.e., 3 translation coordinates and 3 rotation angles, all assumed to be small [36]. As shown in Fig. 5.1, the v-axis is orthogonal to the u-axis, and the distance d_D is measured along the direction perpendicular to the detector plane uv. Therefore we use δd, δu and δv to denote the 3 translation coordinates and $\delta\Phi$, $\delta\Psi$ and $\delta\Theta$ to denote the 3 rotation angles as a function of the rotation angle. By definition, we have $\Delta P_0 = [\delta d^T, \delta u^T, \delta v^T, \delta\Phi^T, \delta\Psi^T, \delta\Theta^T]^T$. The parameters are adapted as

$$\begin{aligned}
d_D(k_\theta) &= d_D + \delta d(k_\theta) && (5.7)\\
m_i(k_\theta) &= m_i + \delta u(k_\theta) && (5.8)\\
n_i(k_\theta) &= n_i + \delta v(k_\theta) && (5.9)\\
e_u(k_\theta) &= e_u - \delta u(k_\theta) && (5.10)\\
e_v(k_\theta) &= e_v - \delta v(k_\theta) && (5.11)\\
\Phi(k_\theta) &= \Phi + \delta\Phi(k_\theta) && (5.12)\\
\Psi(k_\theta) &= \Psi + \delta\Psi(k_\theta) && (5.13)\\
\Theta'(k_\theta) &= \Theta(k_\theta) + \delta\Theta(k_\theta) && (5.14)
\end{aligned}$$

Applying (5.7)-(5.14) to (5.1)-(5.6), we have the general projection equations:

$$u_{ij}(k_\theta) = f_i \frac{m_i(k_\theta) - \tilde{x}_j(k_\theta)}{d_D(k_\theta) - f_i + \tilde{y}_j(k_\theta)} + m_i(k_\theta) + e_u(k_\theta) \tag{5.15}$$

$$v_{ij}(k_\theta) = f_i \frac{n_i(k_\theta) - \tilde{z}_j(k_\theta)}{d_D(k_\theta) - f_i + \tilde{y}_j(k_\theta)} + n_i(k_\theta) + e_v(k_\theta) \tag{5.16}$$

with

$$\begin{bmatrix} \tilde{x}_j(k_\theta) \\ \tilde{y}_j(k_\theta) \\ \tilde{z}_j(k_\theta) \end{bmatrix} = R_3(\Psi(k_\theta)) R_2(\Phi(k_\theta)) R_1(\Theta'(k_\theta)) \begin{bmatrix} x_j \\ y_j \\ z_j \end{bmatrix} \tag{5.17}$$

For the refined calibration, we used the calibrated values of all parameters yielded by the conventional calibration as inputs of (5.15) and (5.16) to estimate $\Delta P_D(\cdot, k_\theta)$, which consists of the k_θ-th elements of δd, δu, δv, $\delta\Phi$, $\delta\Psi$, $\delta\Theta$, using a penalized least squares fitting method.

Distance as Prior Knowledge

As mentioned in 5.3.1, besides the camera-specific parameters, the positions of the point sources are also estimated during the conventional calibration. In order to acquire extra robustness of the calibration result, we always take advantage of the information about the distances between the point sources. For three point sources, it is achieved by transforming the Cartesian coordinates of the point sources [x_j, y_j, z_j] ($j = 1, 2, 3$) into three translation coordinates (t_x, t_y, t_z), three rotation angles (ρ_1, ρ_2, ρ_3) and three distances (d_{12}, d_{13}, d_{23}) [21]. For two point sources, beside the three translation coordinates, it only yields two rotation angles (ρ_1, ρ_2) and one distance (d_{12}). In our case, the three points are small cavities drilled in a rigid plate (which is our so-called *calibration phantom*), thus the distances between the point sources are fixed. The phantom position is then uniquely described by t_x, t_y, t_z, ρ_1, ρ_2 and ρ_3, and we only need to estimate these 6 parameters to determine the point source positions.

Similar to the calibration phantom, the configuration of our multi-pinhole plate is also rigid. In principle we can use the same strategy. For the $i-$th pinhole aperture, we take $[m_i, f_i, n_i]$ as the Cartesian coordinates to denote the pinhole position. The coordinate transformation will end up with 3 translation coordinates (t_m, t_f, t_n), 3 rotation angles (ρ_1, ρ_2, ρ_3) and $3 \times (I - 2)$ independent distances $(d_{12}, d_{13}, d_{23}, \ldots, d_{1i}, d_{2i}, d_{3i})$[5]. If the distances between the pinhole apertures are known, we can apply the same approach, i.e., using the inter-pinhole distances to stabilize the calibration result and only fitting the 6 parameters which indicate the position of the pinhole plate in the image space.

With conventional calibration, the number of unknown parameters P depends on whether or not the prior knowledge of the distances will be used, and if so, which distances (inter-point or inter-pinhole) will be fixed during the calibration. An overview is provided in table 5.3.

5.3.2 Calibration accuracy

It is assumed that the relation between ΔU and the small variations in the estimates ΔP can be approximately described using the following linear equation:

$$\Delta U = M \Delta P \tag{5.18}$$

where M is a matrix containing the first-order derivatives of the projection coordinates U_0 (see (5.1) and (5.2)) to each parameter of P_0. The least squares solution of the linear system (5.18) yields the variations ΔP induced by small errors in the projection coordinates ΔU:

$$\Delta P = (M^T M)^{-1} M^T \Delta U \tag{5.19}$$

where ^{T} denotes matrix transpose. Note that ΔP in (5.19) has a single value for each parameter and therefore corresponds to the conventional calibration procedure. We will use (5.19) to estimate the variance (or the standard deviation ΔP_N) and the bias (ΔP_B) on the estimated parameter P, due to data noise and systematic deviations, respectively.

---

[5] This only holds for $I \geq 3$. If $I = 2$, it will result in 3 translations, 2 rotations and only 1 distance.

Case 1

If the projection coordinate U is only disturbed by data noise, the noise is better characterized by its covariance matrix $\mathrm{Cov}(U)$ rather than by a single noise realization ΔU_N. The calibration accuracy can then be expressed by the covariance matrix of the estimated parameters P:

$$\mathrm{Cov}(P) = (M^T M)^{-1} M^T \mathrm{Cov}(U) M (M^T M)^{-1} \tag{5.20}$$

The variance on the $j-$th parameter ($\mathrm{Var}(P_j)$) is the $j-$th diagonal element of the covariance matrix:

$$\mathrm{Var}(P_j) = (\sigma(P_j))^2 = [\mathrm{Cov}(P)]_{jj} \tag{5.21}$$

We have $\Delta P_N = [\sigma(P_j)]$ with $\sigma(P_j)$ the standard deviation on the j-th parameter.

Case 2

If the projection U is only subject to systematic deviations, we calculate U using (5.7)-(5.17) and compute $\Delta U_D = U - U_0$. The bias on the estimated parameters is computed by (5.19):

$$\Delta P_B = (M^T M)^{-1} M^T \Delta U_D \tag{5.22}$$

Case 3

The bias ΔP_B on the estimated parameters is calculated in the same way as in case 2. With the analytical linear model, there is no straightforward way to estimate $\Delta P_D(k_\delta, k_\theta)$. However, it is still feasible to approximately estimate the reconstruction accuracy with an alternative approach. That approach will be discussed in detail in 5.3.3.

5.3.3 Reconstruction accuracy

To evaluate the reconstruction accuracy, we use a similar approach as in [21]. Two figures of merit, i.e., the loss of spatial resolution and the deformation in the reconstruction image, are applied to quantify the degradation of the reconstruction accuracy. To this end, a grid of points which is considered sufficiently covering the field of view of the multi-pinhole system is reconstructed analytically. To distinguish between the projection of the calibrating point sources and the projection of this grid of point sources used for reconstruction evaluation, we add the superscript ^{g} in the latter case, with U_0^g and U^g corresponding to the ideal and actual projection coordinates of the point sources on the grid, respectively.

For a point on the grid $X_q = [x_q, y_q, z_q]^T$, the projection ray ((5.1) and (5.2)) that goes through this point and the $i-$th pinhole can be expressed in a general format:

$$a_{uiq}(k_\theta)x_q + b_{uiq}(k_\theta)y_q + c_{uiq}(k_\theta)z_q + d_{uiq}(k_\theta) = 0 \tag{5.23}$$
$$a_{viq}(k_\theta)x_q + b_{viq}(k_\theta)y_q + c_{viq}(k_\theta)z_q + d_{viq}(k_\theta) = 0 \tag{5.24}$$

or in matrix format

$$A_{uiq}(k_\theta)X_q + B_{uiq}(k_\theta) = 0 \tag{5.25}$$
$$A_{viq}(k_\theta)X_q + B_{viq}(k_\theta) = 0 \tag{5.26}$$

with $A_{uiq}(k_\theta) = [a_{uiq}(k_\theta), b_{uiq}(k_\theta), c_{uiq}(k_\theta)]^T$, $B_{uiq}(k_\theta) = d_{uiq}(k_\theta)$, $A_{viq}(k_\theta) = [a_{viq}(k_\theta), b_{viq}(k_\theta), c_{viq}(k_\theta)]^T$ and $B_{viq}(k_\theta) = d_{viq}(k_\theta)$. Combining the matrices in (5.25) and (5.26) of all projection angles, all pinhole apertures and both directions u and v, we have

$$A_qX_q + B_q = 0 \tag{5.27}$$

with $A_q = [A^T_{u1q}(1), A^T_{v1q}(1), \ldots, A^T_{uIq}(N_\theta), A^T_{vIq}(N_\theta)]^T$ and similar for B_q. The dimensions of A_q and B_q are $N_{AB} \times 3$ and $N_{AB} \times 1$, respectively, with $N_{AB} = 2 \times N_\theta \times I$.

If the system is perfectly calibrated, all the parameters get exact values and $X^R_q = [x_q, y_q, z_q]^T$ is the unique solution of (5.27). However, with noise or systematic deviations on the data, the calibration cannot be perfect and will introduce small variations ΔP in the estimated parameters. This yields matrices A'_q and B'_q which are functions of U^g and ΔP. As a result, (5.27) is typically overdetermined. In this case, we calculated the coordinates of the 'reconstructed' point source X^R_q as the least squares solution of the linear equation (5.27):

$$X^R_q = -({A'}^T_q A'_q)^{-1}{A'}^T_q B'_q \tag{5.28}$$

where the arguments U^g and ΔP are dropped for convenience. Using (5.28) we can estimate the resolution loss and the image deformation as reconstruction accuracy.

The loss of spatial resolution is estimated based on the distance (denoted by $S_{iq}(k_\theta)$) between the reconstructed point $X^R_q = [x^R_q, y^R_q, z^R_q]^T$ and the corresponding back-projection ray through the i-th pinhole aperture along the k_θ-th projection angle. The calculation of $S_{iq}(k_\theta)$ can be found in appendix-E. At each projection angle, we decompose S_{iq} in three directions as $S_{iq} = [s^x_{iq}, s^y_{iq}, s^z_{iq}]^T$, and take the longest length among all three dimensions, all acquisition angles and all points on the grid with back-projection rays through all pinhole apertures as the measure of the resolution loss.

$$\text{Res. Loss} = \max_i(\max_q(\max_\theta(\max_\epsilon(\|s^\epsilon_{iq}(k_\theta)\|)))) \tag{5.29}$$

where $\epsilon \in (x, y, z)$ indicates the direction of the measure.

The image deformation is evaluated from the relative difference in distance between any two points on the grid before and after the reconstruction[6]. Let p and q

---

[6] Note that the definition of the image deformation is different from that in [21] in order to facilitate the validation.

be the index of the two points, the corresponding relative difference T_{pq} is defined as

$$T_{pq} = \frac{\|X_p^R - X_q^R\| - \|X_p - X_q\|}{\|X_p - X_q\|} \times 100\% \tag{5.30}$$

We define the maximal value of T_{pq} among all points combinations on the grid as the image deformation.

$$\text{Img. Def.} = \max_p(\max_q(\|T_{pq}\|)) \tag{5.31}$$

Note that $S_{iq}(k_\theta)$ and T_{pq} are two arrays which have $3 \times N_\theta \times N_q \times I$ and $N_q \times (N_q - 1)/2$ number of elements, respectively, with N_q the number of points on the grid.

The matrices A'_q and B'_q which yield X_q^R (and subsequently $S_{iq}(k_\theta)$ and T_{pq}) are calculated differently in the noise study and in the study of the systematic deviations. In order to simplify the expressions that follow, we first introduce symbols $F_{uviq}(U^g, \Delta P, k_\theta)$ and $F_{pq}(U^g, \Delta P)$ to denote the set of matrices involved, i.e.,

$$\begin{aligned} F_{uviq}(U^g, \Delta P, k_\theta) \equiv{} & A'_{uiq}(U^g, \Delta P, k_\theta), B'_{uiq}(U^g, \Delta P, k_\theta), \\ & A'_{viq}(U^g, \Delta P, k_\theta), B'_{viq}(U^g, \Delta P, k_\theta) \\ F_{pq}(U^g, \Delta P) \equiv{} & A'_p(U^g, \Delta P), B'_p(U^g, \Delta P), \\ & A'_q(U^g, \Delta P), B'_q(U^g, \Delta P) \end{aligned}$$

Next, we will discuss how to compute the measures for the resolution loss ($S_{iq}(k_\theta)$) and the image deformation (T_{pq}) in case 1, 2 and 3.

Case 1

If ΔP is only due to data noise, the matrices A' and B' are computed based on U_0^g and the covariance matrix $\text{Cov}(P)$. As explained in [21], $\text{Cov}(P)$ can be decomposed as $\text{Cov}(P) = \Gamma\Gamma^T$. By a linear transformation $\Delta P_N^k = \Gamma e_k$ with $e_k = [0, \ldots, 0, 1, 0, \ldots, 0]^T$ the $k-$th unit vector, it yields parameter estimate errors ΔP_N^1, ΔP_N^2, ..., ΔP_N^K, with K the total number of unknown camera-specific parameters[7]. Since these ΔP_N^k are uncorrelated noise components, it is valid to assume that these errors have an independent effect on the image reconstruction accuracy. Thus they can be added quadratically (see appendix-F):

---

[7] The parameters related to the point source location do not influence the reconstruction, therefore they are not considered here.

$$S_{iq}(k_\theta) = \sqrt{\sum_{k=1}^{K} \|S_{iq}(F_{uviq}(U_0^g, \Delta P_N^k, k_\theta))\|^2} \tag{5.32}$$

$$T_{pq} = \sqrt{\sum_{k=1}^{K} \|T_{pq}(F_{pq}(U_0^g, \Delta P_N^k))\|^2} \tag{5.33}$$

Case 2

If there are only systematic deviations during the acquisition, the matrices A' and B' are computed using $U^g = U_0^g + \Delta U_D^g$ and the bias ΔP_B is generated by (5.19):

$$S_{iq}(k_\theta) = S_{iq}(F_{uviq}(U^g, \Delta P_B, k_\theta)) \tag{5.34}$$

$$T_{pq} = T_{pq}(F_{pq}(U^g, \Delta P_B)) \tag{5.35}$$

Case 3

Although it is not feasible in this case to calculate the calibration accuracy $(\Delta P_B + \Delta P_D(k_\delta, k_\theta))$ with the linear model, we propose an approach to approximate the reconstruction accuracies. Recall that the true systematic deviations and the estimated deviations are ΔP_0 and ΔP_D, respectively. It is assumed that ΔP_0 can be accurately estimated by refined calibration, i.e., $\Delta P_D \approx \Delta P_0$. As a result, the influence of systematic deviations is (almost) compensated in the reconstruction procedure, and we expect the resolution loss and the image deformation in case 3 to be predicted with the following equations:

$$S_{iq}(k_\theta) = S_{iq}(F_{uviq}(U_0^g, \Delta P_B, k_\theta)) \tag{5.36}$$

$$T_{pq} = T_{pq}(F_{pq}(U_0^g, \Delta P_B)) \tag{5.37}$$

Note that, since the effects of the systematic deviations are assumed to be canceled out, they are not included in A' and B'. However, since the bias ΔP_B cannot be corrected for by refined calibration, it will still degrade the reconstruction accuracy, and therefore needs to be incorporated in A' and B' in (5.36) and (5.37). Also note that (5.36) and (5.37) are optimistic estimates. The reconstruction accuracies will be worse if $\|\Delta P_D - \Delta P_0\| > 0$.

5.3.4 Validation with repeated simulations

The calibration accuracy and the reconstruction accuracy can be validated by numerical simulations.

Case 1

For noise propagation, we first calculate the projection U_0 of the calibrating point sources using (5.1) and (5.2), then add Gaussian noise on U_0 and perform conventional calibration. For each calibrated parameter, the variance (or the standard deviation) is derived from multiple noise realizations. The calibration of the n-th noise realization will result in a disturbed parameter set ΔP_N^n. Thus, the error measures can be estimated as

$$\hat{S}_{iq}(k_\theta) = \sqrt{\frac{1}{N_s}\sum_{n=1}^{N_s} \|S_{iq}(F_{uviq}(U_0^g, \Delta P_N^n, k_\theta))\|^2} \tag{5.38}$$

$$\hat{T}_{pq} = \sqrt{\frac{1}{N_s}\sum_{n=1}^{N_s} \|T_{pq}(F_{pq}(U_0^g, \Delta P_N^n))\|^2} \tag{5.39}$$

where N_s is the number of noise realizations.

Case 2

To verify the reconstruction accuracy with systematic deviations, we use (5.15) and (5.16) to generate the calibrating point source projections with deviations but without noise ($U = U_0 + \Delta U_D$), then perform conventional calibration based on the deviated projections. The bias ΔP_B is estimated during the fitting and is used to analytically reconstruct the grid of point sources from U^g. The measures for the resolution loss and the image deformation are calculated in the same way as in 5.3.3 with (5.34) and (5.35).

Case 3

To quantify the reconstruction accuracy corresponding to the two-step calibration procedure, we perform the refined calibration based on $U = U_0 + \Delta U_D$ using the parameters estimated in case 2 ($P_0 + \Delta P_B$) as initial values for the fitting. The refined calibration yields the estimated systematic deviation ΔP_D, with which the computation for the accuracy measures becomes

$$\hat{S}_{iq}(k_\theta) = S_{iq}(F_{uviq}(U^g, \Delta P_B + \Delta P_D, k_\theta)) \tag{5.40}$$

$$\hat{T}_{pq} = T_{pq}(F_{pq}(U^g, \Delta P_B + \Delta P_D)) \tag{5.41}$$

5.3.5 Truncation modeling

In 5.3.1, we give the equations which yield projection coordinates for each point source through each aperture for all projection angles. In reality, a point source will not always be detected through every pinhole aperture at every projection angle. With the analytical method, this data truncation is modeled by only preserving the columns or rows in U, M and $\text{cov}(U)$ ((5.19) and (5.20)) corresponding to those projection points that are located in the field of view (FOV) of the aperture and in the valid detector area. With numerical simulation, the truncated point projections are simply not used for the least squares fitting in the calibration procedure. For each pinhole of our multi-pinhole collimators, we determined the aperture FOV on the detector from long planar scans of a small plane source put in front of each hole.

5.3.6 Two types of systematic deviations

For the selection of point source configuration (study II), we applied two types of systematic deviations. The first one is with the deviation pattern which is estimated by refined calibration based on previously measured calibration data. This is called *realistic systematic deviations* which is particularly relevant to the behavior of our gamma. The second one is with the deviation pattern which yields the *worst possible reconstruction error* (WPRE), and it is correspondingly referred to as *WPRE systematic deviations*.

We aimed to estimate the influence of these systematic deviations on the reconstruction error, as a function of various point configurations. Recall from (5.19) that the difference between the estimated parameters and the true parameters ΔP is

$$\Delta P = (M^T M)^{-1} M^T \Delta U$$

The bias on the parameters is the expectation of this difference, i.e.,

$$\Delta P_B = \langle \Delta P \rangle = \left\langle (M^T M)^{-1} M^T \Delta U \right\rangle \tag{5.42}$$

With real measurements, the projection data is subject to both data noise (ΔU_N) and systematic deviations (ΔU_D). In this case, (5.42) can be further written as

$$\begin{aligned}
\Delta P_B &= \left\langle (M^T M)^{-1} M^T (\Delta U_D + \Delta U_N) \right\rangle \\
&= (M^T M)^{-1} M^T \langle \Delta U_D + \Delta U_N \rangle \\
&= (M^T M)^{-1} M^T \Delta U_D + (M^T M)^{-1} M^T \langle \Delta U_N \rangle
\end{aligned} \tag{5.43}$$

With random noise, $\langle \Delta U_N \rangle$ is expected to be zero. Therefore we have

$$\begin{aligned}
\Delta P_B &= (M^T M)^{-1} M^T \Delta U_D \\
&= (M^T M)^{-1} M^T (U(\Delta P_0) - U_0)
\end{aligned} \tag{5.44}$$

where ΔP_0 represents either the realistic systematic deviations or the WPRE systematic deviations, which will be explained as follows.

Realistic Deviation Pattern

The realistic deviation pattern is denoted by ΔP_0^{est}, and was estimated from previously acquired calibration data. The point source projections U disturbed by ΔP_0^{est}

are written as $U(\Delta P_0^{\mathrm{est}})$. Using (5.44), the bias on the parameters is

$$\Delta P_B^{\mathrm{est}} = (M^T M)^{-1} M^T (U(\Delta P_0^{\mathrm{est}}) - U_0) \tag{5.45}$$

Take case 3 for example, the two reconstruction errors are estimated as

$$\begin{aligned} \mathrm{RL}_{\mathrm{est}} &= \max_{i,q,\epsilon,k_\theta} (|s_{iq}^{\epsilon}(F_{uviq}(U_0^g, \Delta P_B^{\mathrm{est}}, k_\theta))|) && (5.46) \\ \mathrm{ID}_{\mathrm{est}} &= \max_{p,q}(|T_{pq}(F_{pq}(U_0^g, \Delta P_B^{\mathrm{est}}))|) && (5.47) \end{aligned}$$

WPRE Deviation Pattern

The aim of introducing the WPRE deviation pattern is to find a generally good point configuration which gives adequate result regardless of the behavior of camera motion. In principle, it is impossible to simulate all potential systematic deviations of all gamma cameras. The idea we applied here is to calculate the reconstruction errors corresponding to a series of *impulsed deviations* with a constrained amplitude for each degree of freedom. It was assumed that the influence of these impulsed deviations on the reconstruction error are independent. With this assumption, these deviations can be combined linearly to yield a value which is equal to the maximal absolute sum of the reconstruction errors yielded by all these impulsed deviations. This value is so-called the *worst possible reconstruction error*, representing either the worst possible resolution loss (WPRE) or the worst possible image deformation (WPID) according to the figure of merit for which the maximum absolute sum is calculated.

In order to find the WPRL and the WPID values as well as the corresponding deviation patterns, the following approach was used. We apply an *impulse* of a certain deviation at one certain acquisition angle. This impulsed deviation pattern is symbolized by $\Delta P_0^{im,k}(k_\delta, \cdot)$, with the superscript k indicating where the impulse is given. The k_θ-th elements in $\Delta P_0^{im,k}(k_\delta, \cdot)$ are given as

$$\Delta P_0^{im,k}(k_\delta, k_\theta) = \begin{cases} W(k_\delta) & k_\theta = k, \\ -W(k_\delta)/(N_\theta - 1) & k_\theta \neq k \end{cases} \tag{5.48}$$

with $W(k_\delta)$ the amplitude of the impulse, estimated as the maximum amplitude of the corresponding realistic deviation:

$$W(k_\delta) = \max |\Delta P_0^{\mathrm{est}}(k_\delta, \cdot)| \tag{5.49}$$

By the definition given by (5.48), the mean of $\Delta P_0^{im,k}(k_\delta, \cdot)$ across all angles is zero.

The bias on the estimated parameters due to this impulsed deviation is

$$\Delta P_B^{im,k}(k_\delta) = (M^T M)^{-1} M^T (U(\Delta P_0^{im,k}(k_\delta, \cdot)) - U_0) \tag{5.50}$$

To further simplify the expressions, we define

$$\begin{aligned} s_{iq}^{\epsilon}(k, k_\delta, k_\theta) &\equiv s_{iq}^{\epsilon}(F_{uviq}(U_0^g, \Delta P_B^{im,k}(k_\delta), k_\theta)) && (5.51) \\ T_{pq}(k, k_\delta) &\equiv T_{pq}(F_{pq}(U_0^g, \Delta P_B^{im,k}(k_\delta))) && (5.52) \end{aligned}$$

and introduce a sign function (Sgn(x)):

$$\mathrm{Sgn}(x) = \begin{cases} 1 & \text{if } x \geq 0, \\ -1 & \text{if } x < 0 \end{cases} \tag{5.53}$$

Assuming these impulses have independent influence on the image quality[8], the WPRL and the WPID is defined as

$$\mathrm{WPRL} = \max_{i,q,\epsilon,k_\theta} \sum_{k_\delta=1}^{6} \sum_{k=1}^{N_\theta} |s_{iq}^{\epsilon}(k, k_\delta, k_\theta)| \tag{5.54}$$

$$\mathrm{WPID} = \max_{p,q} \sum_{k_\delta=1}^{6} \sum_{k=1}^{N_\theta} |T_{pq}(k, k_\delta)| \tag{5.55}$$

The corresponding deviation patterns are

$$\Delta P_0^{\mathrm{WPRL}}(k_\delta, \cdot) = \sum_{k=1}^{N_\theta} \left(\Delta P_0^{im,k}(k_\delta, \cdot) \times \mathrm{Sgn}(s_{\tilde{i}\tilde{q}}^{\tilde{\epsilon}}(k, k_\delta, \tilde{k_\theta})) \right) \tag{5.56}$$

$$\Delta P_0^{\mathrm{WPID}}(k_\delta, \cdot) = \sum_{k=1}^{N_\theta} \left(\Delta P_0^{im,k}(k_\delta, \cdot) \times \mathrm{Sgn}(T_{\tilde{p}\tilde{q}}(k, k_\delta)) \right) \tag{5.57}$$

where $\tilde{i}, \tilde{q}, \tilde{\epsilon}, \tilde{k_\theta}$ and $\tilde{p}, \tilde{q}$ are the values satisfying (5.54) and (5.55), respectively.

An example demonstrating how to calculate WPRL and $\Delta P_0^{\mathrm{WPRL}}$ ((5.48)-(5.56)) in a simplified case is demonstrated in Fig. 5.2.

5.4 Study I

In the first study, we investigated the influence of data noise and systematic deviations on the reconstruction accuracy with both the proposed analytical method and a real measurement. The studies were based on our self-designed 7-pinhole collimators for a typical acquisition setting with dual-head gamma camera. Each designed multi-pinhole plate consists of a central aperture with 6 surrounding apertures located on a circle with a radius of 20 mm. A detailed description, as well as the technical drawing of this pinhole design, can be found in [133]. The calibration phantom in use was a Bequé phantom [21] which consists of three radioactive point sources with 1 mm diameter (Fig. 5.3(a)). The data were acquired using both detector heads and with 64 projection angles equally spread over 360°. Detector 1 and detector 2 started at the top and the bottom of the gantry respectively and rotated clockwise during the acquisition.

One of the aims is to investigate the influence of applying the prior knowledge about inter-point and inter-pinhole distances on the calibration/reconstruction accuracy. To this end, four different calibration methods were applied to the same data:

---

[8] In fact, there are $N_\theta - 1$ rather than N_θ independent impulses, because $\sum_{k=1}^{N_\theta} \Delta P_0^k(k_\delta, \cdot) = 0$.

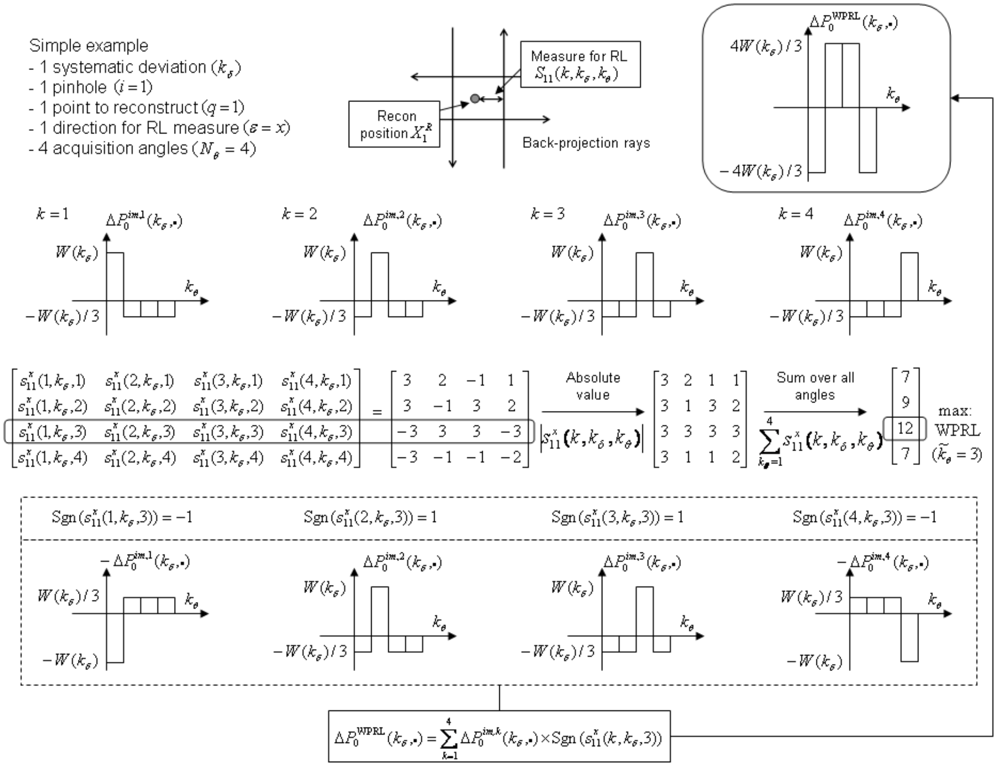
Simple example
- 1 systematic deviation (k_δ)
- 1 pinhole ($i=1$)
- 1 point to reconstruct ($q=1$)
- 1 direction for RL measure ($\varepsilon = x$)
- 4 acquisition angles ($N_\theta = 4$)
Recon position X_1^R
Measure for RL $S_{11}(k, k_\delta, k_\theta)$
Back-projection rays
$\Delta P_0^{\mathrm{WPRL}}(k_\delta, \bullet)$
$4W(k_\delta)/3$
$-4W(k_\delta)/3$
k_θ
$k=1$
$\Delta P_0^{im,1}(k_\delta, \bullet)$
$k=2$
$\Delta P_0^{im,2}(k_\delta, \bullet)$
$k=3$
$\Delta P_0^{im,3}(k_\delta, \bullet)$
$k=4$
$\Delta P_0^{im,4}(k_\delta, \bullet)$
$W(k_\delta)$
$-W(k_\delta)/3$
$\begin{bmatrix} s_{11}^x(1,k_\delta,1) & s_{11}^x(2,k_\delta,1) & s_{11}^x(3,k_\delta,1) & s_{11}^x(4,k_\delta,1) \\ s_{11}^x(1,k_\delta,2) & s_{11}^x(2,k_\delta,2) & s_{11}^x(3,k_\delta,2) & s_{11}^x(4,k_\delta,2) \\ s_{11}^x(1,k_\delta,3) & s_{11}^x(2,k_\delta,3) & s_{11}^x(3,k_\delta,3) & s_{11}^x(4,k_\delta,3) \\ s_{11}^x(1,k_\delta,4) & s_{11}^x(2,k_\delta,4) & s_{11}^x(3,k_\delta,4) & s_{11}^x(4,k_\delta,4) \end{bmatrix} = \begin{bmatrix} 3 & 2 & -1 & 1 \\ 3 & -1 & 3 & 2 \\ -3 & 3 & 3 & -3 \\ -3 & -1 & -1 & -2 \end{bmatrix}$
Absolute value
$|s_{11}^x(k, k_\delta, k_\theta)|$
$\begin{bmatrix} 3 & 2 & 1 & 1 \\ 3 & 1 & 3 & 2 \\ 3 & 3 & 3 & 3 \\ 3 & 1 & 1 & 2 \end{bmatrix}$
Sum over all angles
$\sum_{k_\theta=1}^{4} s_{11}^x(k, k_\delta, k_\theta)$
$\begin{bmatrix} 7 \\ 9 \\ 12 \\ 7 \end{bmatrix}$
max: WPRL ($\tilde{k}_\theta = 3$)
$\mathrm{Sgn}(s_{11}^x(1,k_\delta,3)) = -1$
$\mathrm{Sgn}(s_{11}^x(2,k_\delta,3)) = 1$
$\mathrm{Sgn}(s_{11}^x(3,k_\delta,3)) = 1$
$\mathrm{Sgn}(s_{11}^x(4,k_\delta,3)) = -1$
$-\Delta P_0^{im,1}(k_\delta, \bullet)$
$\Delta P_0^{im,2}(k_\delta, \bullet)$
$\Delta P_0^{im,3}(k_\delta, \bullet)$
$-\Delta P_0^{im,4}(k_\delta, \bullet)$
$W(k_\delta)/3$
$-W(k_\delta)$
$\Delta P_0^{\mathrm{WPRL}}(k_\delta, \bullet) = \sum_{k=1}^{4} \Delta P_0^{im,k}(k_\delta, \bullet) \times \mathrm{Sgn}(s_{11}^x(k, k_\delta, 3))$

Figure 5.2: Demonstration of the calculation of WPRL and the corresponding deviation pattern ($\Delta P_0^{\mathrm{WPRL}}$) in a simplified case. Note that the numbers given in the matrix are only illustrative.

- fitting all parameters, including all distances,
- fixing only the inter-point distance(s),
- fixing only the inter-pinhole distances,
- fixing both the inter-point and inter-pinhole distances.

The resolution loss and the image deformation yielded by all these methods are compared.

The other purpose is to find out whether it is enough to use only 2 point sources to do the calibration with adequate accuracy, even in the presence of systematic deviations. As a preliminary test, we separated the projections of the 3 point sources, and performed the calibration with

- projection data of all 3 point sources,
- projection data of the 1st and the 2nd point source,
- projection data of the 1st and the 3rd point source

which are referred to as *3PS*, *2PS-sub12* and *2PS-sub13* in the remainder of the text, respectively. The calibration results and the reconstruction accuracies of 2PS-sub12 and 2PS-sub13 were compared with those of 3PS for each detector head individually.

5.4.1 Analytical evaluation

For the analytical study, typical values were used for P_0. The detector distance (d_D) and the focal length of the pinhole collimator (f) were chosen to be 206 mm and 176 mm, respectively. The mechanical offsets of the pinhole apertures were the same as the designed values [133]. The electrical shifts (e_u, e_v), tilt angle (Φ) and twist angle (Ψ) were expected to be zero. The calibration phantom was positioned in the center of the field of view, and was parallel to the two detector planes at the beginning of the acquisition. The inter-point distances d_{12}, d_{13} and d_{23} were 26 mm, 19 mm and 26 mm, respectively.

The analytical linear model described in 5.3 was applied to evaluate the reconstruction accuracy of different calibration methods combined with different point source settings (3PS, 2PS-sub12 and 2PS-sub13). For the noise propagation study, we modeled the error (ΔU_N) on the determination of the centroid of the projection points due to data noise by a Gaussian distribution with realistic standard deviation of 0.6 mm. For the influence of systematic deviations, we used the deviations estimated from a previous refined calibration procedure with dual-head data as ΔP_0. All 6 degrees of freedom in ΔP_0 are plotted in Fig. 5.4 as a function of k_θ. The two detector heads have very different deviation patterns.

The calibration accuracies, i.e., the variance and the bias on each parameter to be estimated, were calculated by (5.21) and (5.22), respectively. The corresponding

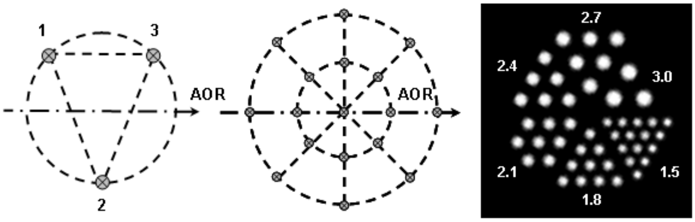

(a) Bequé phantom **(b) Point source grid** **(c) Jaszczak phantom**

Figure 5.3: (a) Configuration of the Bequé calibration phantom. (b) Cross section of the grid of points used to evaluate the reconstruction accuracy. The point sources are positioned on two circles with a radius of 10mm/20mm. (c) Trans-axial slice of the Jaszczak phantom with 40 mm diameter used in study I. The diameters of the hollow rods are given in the unit of millimeter.

reconstruction accuracies were calculated as explained in 5.3.3. The grid of points that was used to generate U_0^g and U^g had a cross section shown in Fig. 5.3(b). The radius of the two circles were 10 mm and 20 mm, respectively. The complete grid was obtained by rotating the displayed grid by 0° and 90° around the axis of rotation.

The analytical evaluation was done with both non-truncated and truncated point projections. The results were verified by numerical simulations with 100 noise realizations (see 5.3.4).

5.4.2 Jaszczak phantom reconstruction

In order to visually inspect the degradation of the reconstruction quality, we reconstructed a Jaszczak-type phantom using the parameters estimated from different calibration approaches. The Jaszczak-type phantom (Fig. 5.3(c)) consists of a plastic cylinder with an outer diameter of 40 mm and 6 wedge-shaped sections with multiple hollow rods having a diameter ranging from 1.5 mm to 3.0 mm in steps of 0.3 mm. This configuration facilitates us to closely examine the resolution and the image deformation of the reconstruction image.

We scanned the Jaszczak-type phantom on a clinical dual-head gamma camera (E.cam, Fixed 180°, Siemens Medical Solutions) equipped with the self-designed 7-pinhole collimators. For the Jaszczak phantom, we filled the hollow rods with 37 MBq ^{99m}Tc, and scanned the phantom with 30 seconds/view in step-and-shoot mode. The calibration data were acquired immediately after the phantom scan. The three point sources on the calibration phantom were filled with 1.85 MBq ^{99m}Tc each and were scanned using the same geometry but with 10 seconds/view acquisition. The diameter of each point source was 1 mm.

For each calibration approach, the data were reconstructed twice. First, the parameters were estimated based on the conventional calibration procedure which assumes perfect circular camera motion. Second, the parameters adapted by the

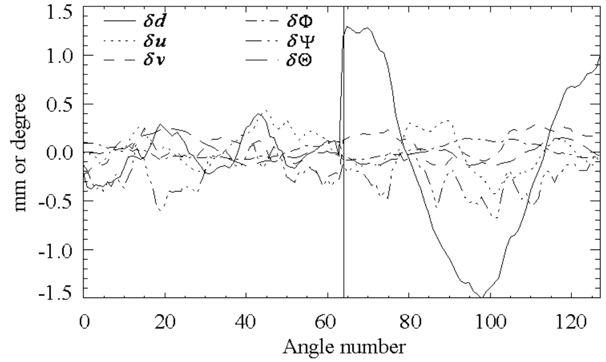

Figure 5.4: Plot of the systematic deviation ΔP_0 acquired from a previous refined calibration as a function of angular position k_θ. Different line types represent different degrees of freedom. Angles with number 0-63 and 64-127 are for detector head 1 and head 2, respectively. The translations are expressed in mm, the rotations in degrees.

refined calibration were used. To show the effect of the very different systematic deviation patterns (Fig. 5.4), the reconstruction was performed for each head separately.

For the reconstruction, the activity distribution of the phantom was reconstructed in a $72 \times 72 \times 88$ image space with 0.6^3 mm^3 voxels. The OSEM algorithm (see 2.4.2) was used for reconstruction with the following iteration scheme: 5×16, 5×8, 5×4, 5×2, 5×1 (global iteration × number of subsets). Corrections for decay and scatter were applied. Due to the small size of the phantom, the influence of the attenuation was expected to be negligible. Therefore the attenuation within the phantom was ignored during the reconstruction.

5.5 Results I

5.5.1 Analytical evaluation

As an example of calibration accuracy, the results of both detector heads with truncation modeling are given in Fig. 5.5 and Fig. 5.6. In the left column the standard deviations ΔP_N on the camera-specific parameters[9] due to noise propagation are plotted. In the right column, the bias on the same parameters (ΔP_B) are shown for the given systematic deviations (Fig. 5.4). It can be seen that ΔP_N are very small (all less than 0.3 mm or degree), whereas ΔP_B on the same parameters (for example the focus heights f_i) are much more pronounced. The three point settings

---

[9] Because of the large number of camera-specific parameters, we only present the errors on m_i, f_i and n_i for the second, the fourth and sixth pinhole aperture.

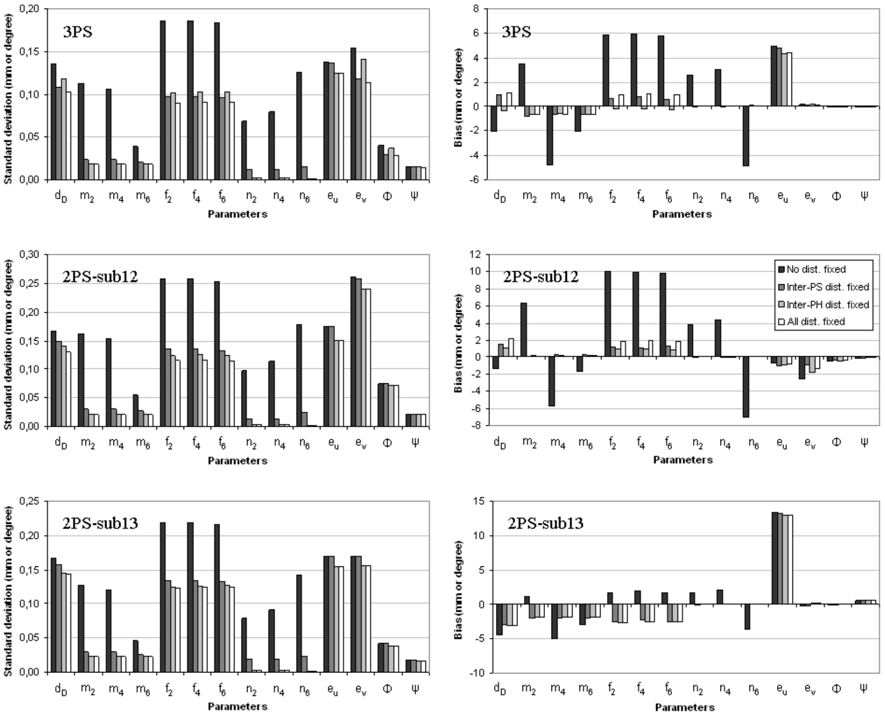

Figure 5.5: Calibration accuracies of a subset of the parameters with detector head 1, yielded with different calibration point settings and with truncated point projections. Top / middle / bottom row: 3PS / 2PS-sub12 / 2PS-sub13. Left / right column: standard deviation (ΔP_N) / bias (ΔP_B) on each parameter. Results of four calibration methods are plotted in cluster. The unit of error is either in mm or in degrees.

(3PS, 2PS-sub12 and 2PS-sub13) in combination of two detector heads yield similar noise properties but very different bias on the estimated parameters.

It is not obvious from Fig. 5.5 and Fig. 5.6 which point source setting will result in better reconstruction accuracy. In table 5.4, table 5.5 and table 5.6 we give specific values for resolution loss and image deformation for case 1, 2 and 3, respectively. The figures between the brackets are the corresponding values acquired from numerical simulations presented for validation purpose. The results are shown for both detector heads. Mostly the reconstruction accuracies predicted by our linear approximation model are in good agreement with those obtained from simulations.

There are several points worth noticing in these tables. First, the degradation of the reconstruction quality due to noise is almost the same for the two detector heads, but the degradation due to bias is quite different because of the different systematic deviations. Second, with the given systematic deviations, the recon-

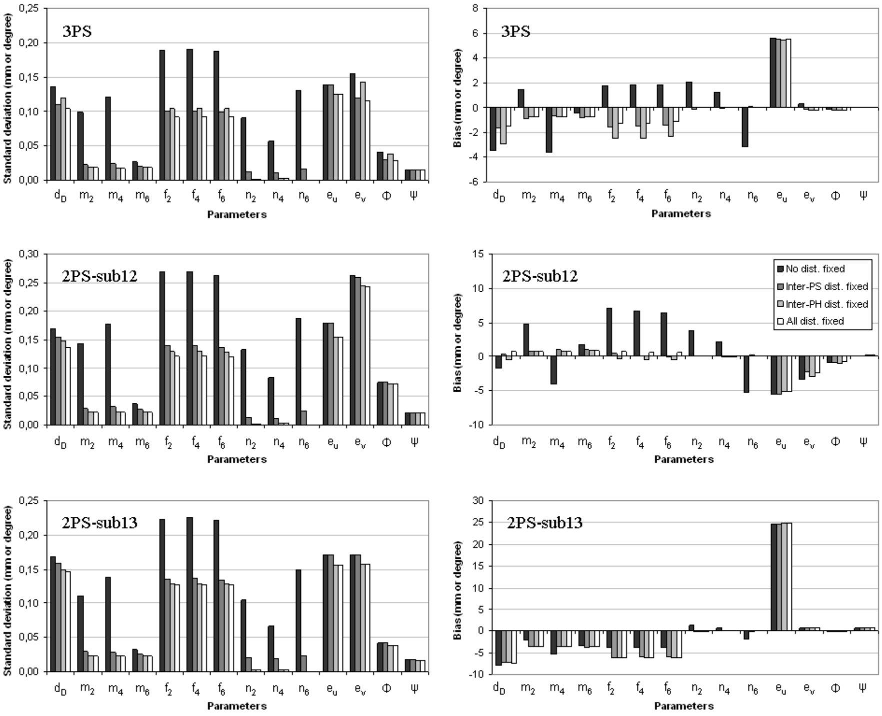

Figure 5.6: Calibration accuracies of a subset of the parameters with detector head 2, yielded with different calibration point settings and with truncated point projections. Top / middle / bottom row: 3PS / 2PS-sub12 / 2PS-sub13. Left / right column: standard deviation (ΔP_N) / bias (ΔP_B) on each parameter. Results of four calibration methods are plotted in cluster. The unit of error is either in mm or in degrees.

Table 5.4: Reconstruction accuracy in case 1 with truncated projections. Values in brackets are calculated from simulations.

	3PS		**2PS-sub12**		**2PS-sub13**	
Head 1	**Res. Loss**	**Img. Def.**	**Res. Loss**	**Img. Def.**	**Res. Loss**	**Img. Def.**
No dist. fixed	0.023 (0.024)	0.761% (0.821%)	0.026 (0.027)	1.103% (1.108%)	0.039 (0.035)	0.859% (0.890%)
Inter-PS dist. fixed	0.023 (0.023)	0.052% (0.058%)	0.025 (0.025)	0.132% (0.118%)	0.038 (0.033)	0.084% (0.083%)
Inter-PH dist. fixed	0.009 (0.010)	0.055% (0.059%)	0.018 (0.017)	0.112% (0.105%)	0.011 (0.012)	0.057% (0.053%)
All dist. fixed	0.009 (0.009)	0.041% (0.041%)	0.018 (0.018)	0.112% (0.112%)	0.011 (0.011)	0.056% (0.057%)
Head 2	**Res. Loss**	**Img. Def.**	**Res. Loss**	**Img. Def.**	**Res. Loss**	**Img. Def.**
No dist. fixed	0.021 (0.023)	0.772% (0.822%)	0.027 (0.027)	1.129% (1.105%)	0.038 (0.035)	0.873% (0.920%)
Inter-PS dist. fixed	0.021 (0.021)	0.054% (0.056%)	0.026 (0.027)	0.133% (0.122%)	0.037 (0.039)	0.086% (0.081%)
Inter-PH dist. fixed	0.010 (0.011)	0.056% (0.061%)	0.018 (0.017)	0.113% (0.103%)	0.011 (0.011)	0.058% (0.057%)
All dist. fixed	0.009 (0.009)	0.042% (0.042%)	0.018 (0.019)	0.113% (0.112%)	0.011 (0.011)	0.057% (0.055%)

Table 5.5: Reconstruction accuracy in case 2 with truncated projections. Values in brackets are calculated from simulations.

	3PS		**2PS-sub12**		**2PS-sub13**	
Head 1	**Res. Loss**	**Img. Def.**	**Res. Loss**	**Img. Def.**	**Res. Loss**	**Img. Def.**
No dist. fixed	0.90 (0.78)	-28.8% (-30.8%)	0.80 (0.72)	-41.1% (-42.1%)	1.39 (1.04)	-22.0% (-22.3%)
Inter-PS dist. fixed	0.99 (1.00)	1.74% (1.81%)	0.95 (0.97)	1.94% (2.02%)	1.39 (1.38)	-1.61% (-1.67%)
Inter-PH dist. fixed	0.97 (0.96)	-0.91% (-0.83%)	0.87 (0.89)	1.09% (1.19%)	1.35 (1.36)	-1.72% (-1.80%)
All dist. fixed	0.92 (0.93)	1.24% (1.31%)	0.90 (0.92)	1.53% (1.63%)	1.35 (1.36)	-1.72% (-1.81%)
Head 2	**Res. Loss**	**Img. Def.**	**Res. Loss**	**Img. Def.**	**Res. Loss**	**Img. Def.**
No dist. fixed	1.44 (1.32)	-19.2% (-17.7%)	1.35 (1.21)	-30.9% (-28.5%)	2.36 (2.07)	-14.4% (-14.2%)
Inter-PS dist. fixed	1.56 (1.55)	2.88% (2.76%)	1.52 (1.45)	3.51% (3.32%)	2.39 (2.32)	-3.99% (-4.40%)
Inter-PH dist. fixed	1.49 (1.48)	-2.70% (-2.88%)	1.28 (1.27)	2.18% (-2.25%)	2.34 (2.28)	-4.09% (-4.52%)
All distances fixed	1.47 (1.45)	-2.10% (-2.19%)	1.28 (1.26)	2.70% (2.49%)	2.34 (2.28)	-4.09% (-4.52%)

Table 5.6: Reconstruction accuracy in case 3 with truncated projections. Values in brackets are calculated from simulations.

	3PS		**2PS-sub12**		**2PS-sub13**	
Head 1	**Res. Loss**	**Img. Def.**	**Res. Loss**	**Img. Def.**	**Res. Loss**	**Img. Def.**
No dist. fixed	0.55 (0.48)	-28.7% (-30.8%)	0.44 (0.60)	-41.2% (-41.9%)	1.09 (1.00)	-21.8% (-22.3%)
Inter-PS dist. fixed	0.39 (0.54)	0.86% (0.87%)	0.23 (0.42)	1.14% (1.03%)	0.80 (1.19)	-1.03% (-1.81%)
Inter-PH dist. fixed	0.24 (0.42)	-0.34% (-0.44%)	0.16 (0.47)	-0.95% (-0.29%)	0.69 (1.10)	-1.12% (-1.94%)
All dist. fixed	0.26 (0.37)	0.32% (0.34%)	0.18 (0.38)	0.71% (0.69%)	0.69 (1.10)	-1.12% (-1.94%)
Head 2	**Res. Loss**	**Img. Def.**	**Res. Loss**	**Img. Def.**	**Res. Loss**	**Img. Def.**
No dist. fixed	0.80 (0.80)	-18.2% (-16.5%)	0.86 (0.60)	-31.1% (-28.1%)	1.66 (1.90)	-13.2% (-14.1%)
Inter-PS dist. fixed	0.66 (0.78)	0.87% (1.43%)	0.55 (0.71)	1.98% (1.44%)	1.37 (2.09)	-2.48% (-4.35%)
Inter-PH dist. fixed	0.39 (0.55)	-1.05% (-1.28%)	0.41 (0.50)	-1.57% (-0.61%)	1.31 (2.05)	-2.58% (-4.46%)
All dist. fixed	0.34 (0.47)	-0.45% (-0.55%)	0.42 (0.45)	-1.20% (0.40%)	1.31 (2.05)	-2.58% (-4.47%)

struction errors due to noise are negligible compared with those due to bias, even for detector head 1 whose deviations are not pronounced. Third, regardless of the cause of the error, the reconstruction accuracy (especially the image deformation) improved if we applied the prior knowledge of either the inter-point or inter-pinhole distances during the calibration. However the gain hardly increased when we fixed all distances. Fourth, the negative relative deformation values in table 5.5 and 5.6 predict that the reconstructed object will be up to 40% smaller than the true object, if no distance information is used during calibration. Fifth, since detector head 2 suffers from more severe systematic deviations than head 1, the corresponding accuracies are much worse. Sixth, with the given point source position, the 2PS-sub12 leads to similar resolution properties as 3PS, whereas 2PS-sub13 results in very bad resolution in the reconstruction. Seventh, comparing table 5.5 with table 5.6, it can be seen that the refined calibration significantly improves the resolution in the reconstruction. However, it hardly affects the scaling effect in the image dimension, especially if no distances were fixed.

Note that all the results presented in this section are calculated based on truncated projections.

5.5.2 Jaszczak phantom reconstruction

Fig. 5.7 and Fig. 5.8 shows trans-axial slices of 24 reconstruction images (4 calibration methods × 2 calibration procedures (conventional / refined) × 3 point settings) reconstructed using the data of detector head 1 and head 2, respectively.

Before comparing the reconstructions with the analytical predictions, recall that the influence of data noise is negligible compared to that of systematic deviations based on the theoretical analysis. Therefore we expect that table 5.5 (case 2) and table 5.6 (case 3) approximately predict the degradation of the image quality in the reconstructions which correspond to the conventional / refined calibration.

Take Fig. 5.8 for example, we can see that if no distance is fixed during the calibration, the reconstruction image is obviously scaled, with scaling factor 2PS-sub12 > 3PS > 2PS-sub13. However, once we fix either inter-point or inter-pinhole distances, the deformation becomes negligible. In all cases, the refined calibration improves the image resolution, but hardly affects the image deformation. The resolution with 2PS-sub12 is comparable with, and sometimes even better than that of 3PS. For instance, the rods with diameter of 2.1 mm are more clear and circular-shaped with 2PS-sub12 rather than with 3PS. The resolution with 2PS-sub13 is however much worse even with refined calibration. These findings are all in accordance with table 5.5 and table 5.6.

Fig. 5.9 and Fig. 5.10 show maximum intensity projections of the reconstructions with the three calibration settings, reconstructed using the data of each head with refined calibration. It can be seen that the image deformation in the axial direction is very similar to that in the trans-axial direction (Fig. 5.7 and Fig. 5.8). The axial resolution is however difficult to compare since the phantom has little variation along the axis of rotation.

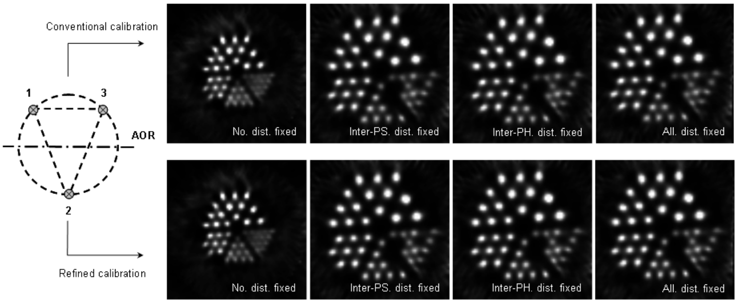
Conventional calibration
1
3
AOR
2
Refined calibration
No. dist. fixed
Inter-PS. dist. fixed
Inter-PH. dist. fixed
All. dist. fixed

(a) Reconstructions with parameters estimated from the projection of 3 point sources (3PS)

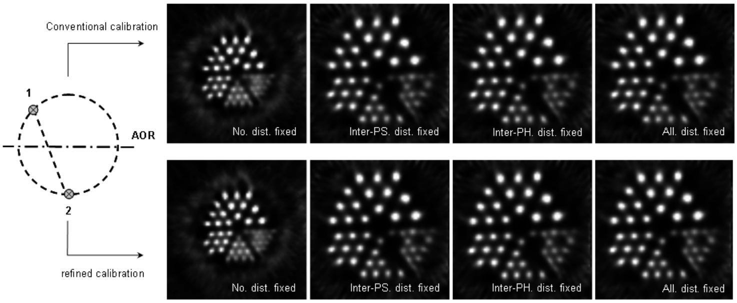
Conventional calibration
1
AOR
2
refined calibration
No. dist. fixed
Inter-PS. dist. fixed
Inter-PH. dist. fixed
All. dist. fixed

(b) Reconstructions with parameters estimated from the projection of 2 point sources (2PS-sub12)

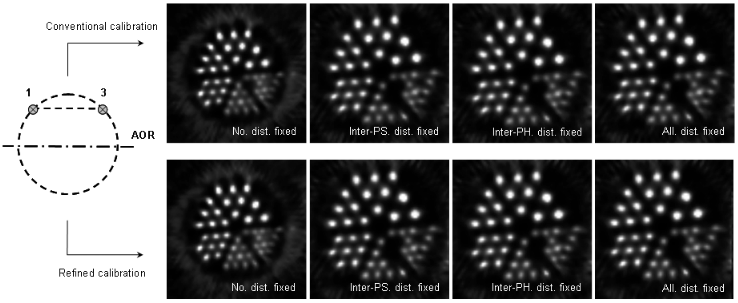
Conventional calibration
1
3
AOR
Refined calibration
No. dist. fixed
Inter-PS. dist. fixed
Inter-PH. dist. fixed
All. dist. fixed

(c) Reconstructions with parameters estimated from the projection of 2 point sources (2PS-sub13)

Figure 5.7: Trans-axial slices of Jaszczak phantom reconstructions, using the data from detector head 1. Top / middle / bottom group: with 3PS / 2PS-sub12 / 2PS-sub13 calibration setting. Upper / lower row in each group: reconstruction image with conventional / refined calibration. Left to right in each group: with four different calibration methods (No distance fixed, inter-point distance(s) fixed, inter-pinhole distances fixed and all distances fixed).

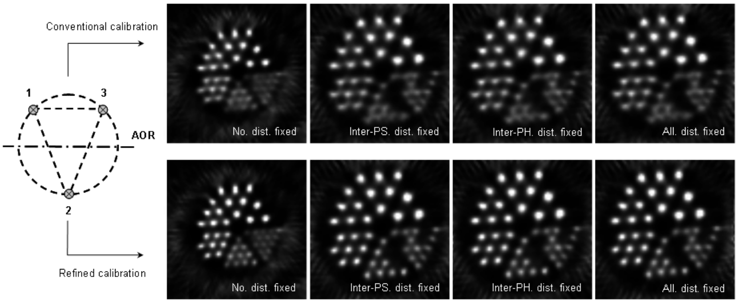
Conventional calibration
1
3
AOR
2
Refined calibration
No. dist. fixed
Inter-PS. dist. fixed
Inter-PH. dist. fixed
All. dist. fixed
No. dist. fixed
Inter-PS. dist. fixed
Inter-PH. dist. fixed
All. dist. fixed

(a) Reconstructions with parameters estimated from the projection of 3 point sources (3PS)

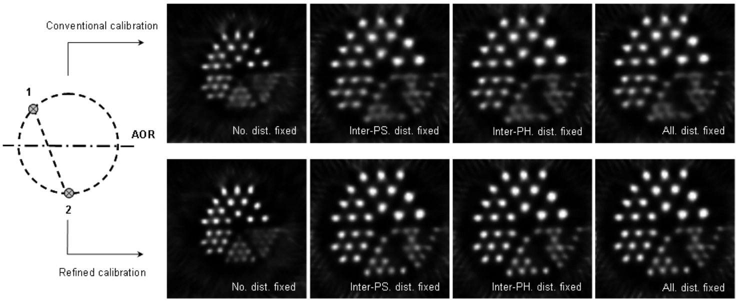
Conventional calibration
1
AOR
2
Refined calibration
No. dist. fixed
Inter-PS. dist. fixed
Inter-PH. dist. fixed
All. dist. fixed
No. dist. fixed
Inter-PS. dist. fixed
Inter-PH. dist. fixed
All. dist. fixed

(b) Reconstructions with parameters estimated from the projection of 2 point sources (2PS-sub12)

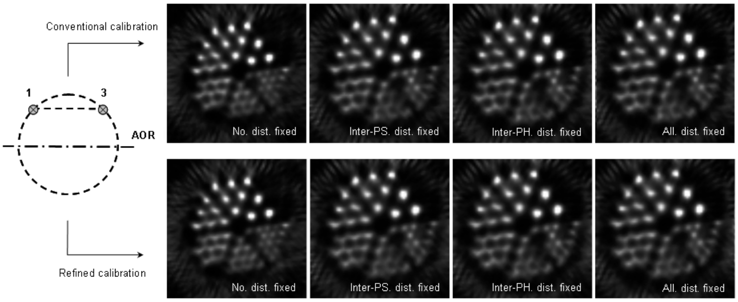
Conventional calibration
1
3
AOR
Refined calibration
No. dist. fixed
Inter-PS. dist. fixed
Inter-PH. dist. fixed
All. dist. fixed
No. dist. fixed
Inter-PS. dist. fixed
Inter-PH. dist. fixed
All. dist. fixed

(c) Reconstructions with parameters estimated from the projection of 2 point sources (2PS-sub13)

Figure 5.8: Trans-axial slices of Jaszczak phantom reconstructions, using the data from detector head 2. Top / middle / bottom group: with 3PS / 2PS-sub12 / 2PS-sub13 calibration setting. Upper / lower row in each group: reconstruction image with conventional / refined calibration. Left to right in each group: with four different calibration methods (No distance fixed, inter-point distance(s) fixed, inter-pinhole distances fixed and all distances fixed).

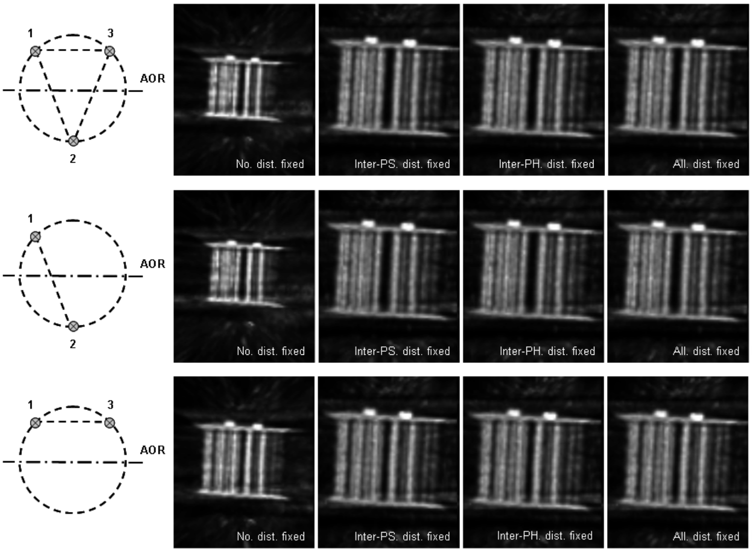
1
3
AOR
2
No. dist. fixed
Inter-PS. dist. fixed
Inter-PH. dist. fixed
All. dist. fixed

Figure 5.9: Maximum intensity projections of Jaszczak phantom reconstructions. Top / middle / bottom: with 3ps / 2PS-sub12 / 2PS-sub13 calibration setting, using the data from detector head 1. Parameters were estimated by refined calibration.

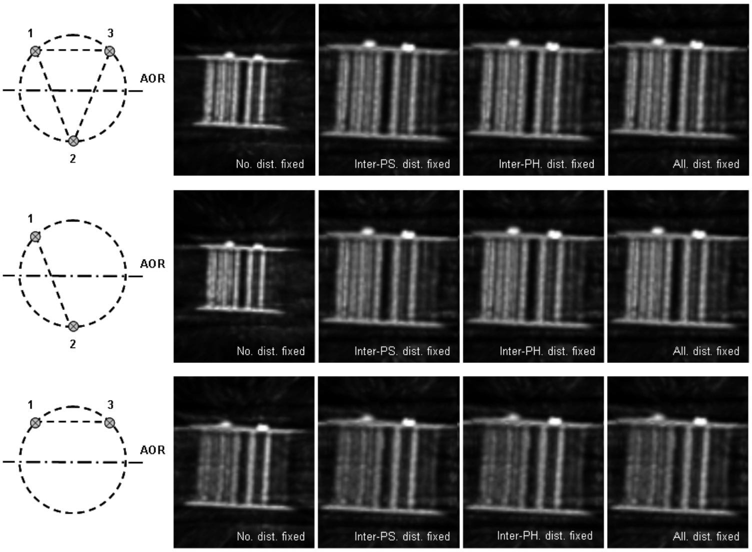
1
3
AOR
2
No. dist. fixed
Inter-PS. dist. fixed
Inter-PH. dist. fixed
All. dist. fixed

Figure 5.10: Maximum intensity projections of Jaszczak phantom reconstructions. Top / middle / bottom: with 3ps / 2PS-sub12 / 2PS-sub13 calibration setting, using the data from detector head 2. Parameters were estimated by refined calibration.

5.6 Conclusion I

In this part, the bias and variance on each geometrical parameter (calibration accuracy), as well as the resolution loss and image deformation in the reconstructed image (reconstruction accuracy) were estimated using the proposed analytical method. Results show that small systematic deviations may introduce non-negligible bias on the estimated parameters, and that the reconstruction errors are dominated by this bias rather than by noise on the estimated coordinates of the point source projections. It is also shown that if no prior knowledge about any distance is applied, the dimension of the reconstruction image may be considerably scaled due to biased parameters. The two presented distance-fixing methods, i.e., fixing the inter-point source or inter-pinhole aperture distances, yield similar, improved reconstruction accuracy, however the latter is preferable since it facilitates simultaneous animal-calibration data acquisition. In addition, the reconstruction errors can be significantly reduced by carefully positioning the calibrating point sources.

5.7 Study II

In the second study, we selected the point source configuration, which facilitates simultaneous animal-calibration scan without compromising the reconstruction image quality, for our 7-pinhole collimator system. Based on the conclusion from the first study, the influence of the data noise can be ignored compared to that of the systematic deviations. Since we always use the two-step calibration procedure for real measurements, we only considered case 3 for the theoretical analysis of the point sources selection. First, we picked out good point configurations with the proposed two types of systematic deviations, then applied the chosen 2-point configuration to a real phantom measurement. The data were acquired using both detector heads and at 64 projection angles equally spread over 360°. To stabilize the calibration result, the distances between the pinhole apertures were used as prior information during the calibration.

5.7.1 Point source selection

System Parameters

We used typical values for the geometrical parameters of the multi-pinhole SPECT system. The focal length of the pinhole collimator (f_i, with $i = 1, \ldots, 7$) was 176 mm. The mechanical offsets of the pinhole apertures (m_i, n_i) were the same as the designed values [133]. The electrical shifts (e_u, e_v), tilt angle (Φ) and twist angle (Ψ) were set to zero. For convenience, we used the distance between the central pinhole and the center of the image (pd), instead of the detector distance dd, to indicate how close the object is to the pinhole collimators. The choice of pd depends on the specific purpose of the scan: to image a small region of interest, the detector head should be as close as possible to the object. In this case, the value of *pd* should be small but still larger than the radius of the animal carrier (which is about 20 mm in our case). On the other hand, imaging a large part of the object needs a large *pd* to increase the field of view. In order to find good point configurations in general, three typical *pd* values (25, 30 and 35 mm) were used for investigation.

To model the system deviations, we used the datasets from previous calibration scans, estimating in total 23 individual sets of systematic deviations. These deviation data were used either directly as realistic deviations (ΔP_0^{est}) or to obtain $W(k_\delta)$ to generate WPRE deviation patterns.

Point Source Candidates

To facilitate the simultaneous animal/calibration scan, we only allowed point sources to be attached to the animal carrier, which in most cases is a cylindrical tube. In our case, the cylindrical tube has a radius of 20 mm, a length of 30 mm and its central axis coincides with the AOR. Sampling the surface of the cylinder, we have 28 locations for the point source candidates (Fig. 5.11(a)). These point candidates were equally distributed over 7 circles, which are perpendicular to the AOR and -15, -10, -5, 0, 5, 10 and 15 mm off-center with respect to the central pinhole aperture. Here we use $\text{PS}_\text{s}^\alpha$ to explicitly describe the location of a point source, where s is the off-center shift and α indicates the angular position of the point on the circle. By definition, we have $\text{s} = -15, -10, -5, 0, 5, 10$ and 15 mm and $\alpha = 0, \pi/2, \pi$ and $3\pi/2$. Fig. 5.11(b) shows the locations of these points with respect to the initial position of the two detector heads at the beginning of the acquisition. The figure assumes we stand in front of the gamma camera and face the gantry. The initial angular position of detector head 1 and 2 corresponds to $\alpha = 0$ and $\alpha = \pi$, respectively. The value of α was increased clockwise, same as the rotation angle θ.

We selected both 2-point and 3-point configurations, which are expressed in the format of $\text{PS}_{\text{s}_1}^{\alpha_1}$–$\text{PS}_{\text{s}_2}^{\alpha_2}$ and $\text{PS}_{\text{s}_1}^{\alpha_1}$–$\text{PS}_{\text{s}_2}^{\alpha_2}$–$\text{PS}_{\text{s}_3}^{\alpha_3}$, respectively. The reconstruction errors corresponding to any 2-point and 3-point configurations were calculated using the proposed analytical method. The results were compared across all point combinations and good configurations were determined based on the principle explained below.

Principle of Selection

Since the pinhole designs of the two detector heads are not identical and the behaviors of the two heads are quite different from each other (see Fig. 5.4 for example), we calculated the reconstruction errors individually for each head. For each point combination, the measure used to quantify the reconstruction error (RE) was calculated averaging over all three *pd* values and both detector heads:

$$\text{RE} = \sqrt{\frac{1}{2}[(\frac{\text{RE}_{H1}^{25} + \text{RE}_{H1}^{30} + \text{RE}_{H1}^{35}}{3})^2 + (\frac{\text{RE}_{H2}^{25} + \text{RE}_{H2}^{30} + \text{RE}_{H2}^{35}}{3})^2]} \tag{5.58}$$

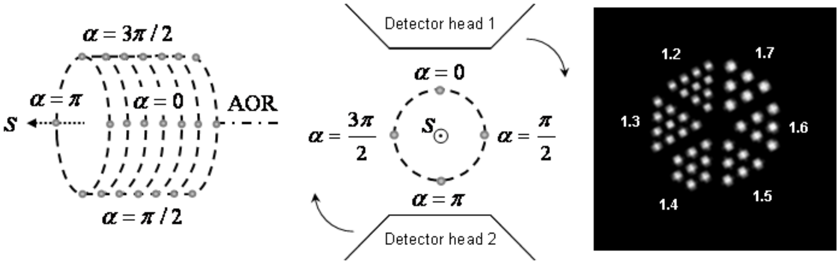

(a) (b) (c)

Figure 5.11: (a) Point source candidates on the cylindrical surface. (b) Point source locations with respect to the initial position of the detector heads. (c) Trans-axial slice of the Jaszczak phantom with 30 mm diameter used in study II. The diameters of the hollow rods are given in the unit of millimeter.

With realistic deviation patterns, RE stands for $\mathrm{RL}_{\mathrm{est}}$ or $\mathrm{ID}_{\mathrm{est}}$. With WPRE deviations, RE represents either WPRL or WPID. The mean and the standard deviation of RE were calculated over all 23 files, indicated by $\overline{\mathrm{RE}}$ and $\sigma(\mathrm{RE})$, respectively. $\sigma(\mathrm{RE})$ was used as a reference to see how sensitive the results are to the possibly non-consistent systematic deviations. In addition, we also calculated the reconstruction errors when the projection data are only subject to random noise[10]. The corresponding RE was denoted by $\mathrm{RL}_{\mathrm{noise}}$ or $\mathrm{ID}_{\mathrm{noise}}$, respectively.

For high resolution small animal imaging, we are concerned more about the spatial resolution than the image deformation in the reconstruction. Therefore the resolution loss was considered as the main figure of merit for the selection of the point configurations. With realistic deviations, we first pick out point configurations which yield $\overline{\mathrm{ID}}_{\mathrm{est}} < 2\%$, and then select the one which results in the minimal $\overline{\mathrm{RL}}_{\mathrm{est}}$. With WPRE deviation patterns, we first choose point combinations with $\overline{\mathrm{WPID}} < 10\%$, and then select the one which yields the minimal $\overline{\mathrm{WPRL}}$.

In this study, truncation effects due to the limited field of view of the pinhole apertures and the limited area of the detector were taken into consideration. The former was modeled by generating masks based on the measured sensitivities of the pinhole apertures.

Robustness Test

For practical reasons, we prefer to use the inter-pinhole aperture distances rather than the inter-point source distance(s), as the prior knowledge during the calibration. To avoid extra efforts on placing the point sources at exact positions, we expected that the selected point configuration is robust to small shift(s) of the point source locations, i.e., the reconstruction errors are insensitive to the deviation between the expected point source location and the actual point source location. To test this, we calculated the reconstruction errors related to point sources slightly shifted with respect to the expected position for certain point configurations. Every time we shift either a single point or all the points along one of the three axes (x-, y- and z-) by -2 mm or 2 mm. For each shifted configuration we calculated $\overline{\mathrm{RL}}_{\mathrm{est}}$ and $\overline{\mathrm{ID}}_{\mathrm{est}}$ to see how these results are influenced due to the shift(s) of the points locations. Three point configurations were tested, i.e., the winners of the 2-point and 3-point combinations selected with realistic deviation patterns, as well as the Bequé calibration phantom which was optimized for a single pinhole system [21] and was typically used in our animal experiments.

---

[10] To model the noise, the errors on the determination of the centroids of the point projections were considered to be Gaussian distributed with a standard deviation of 0.6 mm, same as in Study I

5.7.2 Phantom experiment

To visually inspect the performance of the selected point source configuration, we reconstructed a Jaszczak-type phantom using parameters estimated with different calibration point configurations. The Jaszczak-type phantom consists of a plastic cylinder with an outer diameter of 30 mm and 6 wedge-shaped sections with multiple hollow rods having a diameter ranging from 1.2 mm to 1.7 mm in steps of 0.1 mm. It allows us to closely examine the resolution and the image deformation of the reconstruction image.

We filled the hollow rods of the Jaszczak phantom with 37 MBq ^{99m}Tc and put the phantom on the animal carrier. The phantom was positioned in the center of the field of view, and was scanned with 30 seconds/view in step-and-shoot mode on a clinical dual head gamma camera (E.cam, Fixed 180°, Siemens Medical Solutions) equipped with the self-designed 7-pinhole collimators.

Two different point configurations were applied for calibration purpose. The first one was the selected 2-point configuration attached directly to the animal tube and was scanned simultaneously with the phantom. In order to distinguish the projections of the point sources and the phantom, each point source was filled with 1.85 MBq ^{123}I rather than ^{99m}Tc. The second one is the 3-point Bequé phantom which needs to be positioned in the center of the field of view. Each of the three point sources on the Bequé phantom was filled with 1.85 MBq ^{99m}Tc. As a separate scan, the calibration data were acquired immediately after the phantom scan using the same geometry but with 10 seconds/view acquisition.

In each case, the data were reconstructed twice. The first time was with the geometric parameters estimated from conventional calibration. The second time was with the parameters that were adapted by the refined calibration. The activity distribution of the phantom was reconstructed using dual head data. The image space was 72 × 72 × 88 with (0.6 mm)^3 voxels. The OSEM algorithm (see 2.4.2) was used for reconstruction with the following iteration scheme: 5×16, 5×8, 5×4, 5×2, 5×1 (global iterations × number of subsets). No corrections for decay, scatter and attenuation were applied.

5.8 Results II

5.8.1 Point source selection

Fig. 5.12 plots the relations between the proposed figures of merit for all 2-point configurations. In Fig. 5.12(a) - 5.12(d), it can be seen that if a point configuration results in small resolution loss ($\overline{\mathrm{RL}}_{\mathrm{est}}$ or $\overline{\mathrm{WPRL}}$), in general it also yields small image deformation ($\overline{\mathrm{ID}}_{\mathrm{est}}$ or $\overline{\mathrm{WPID}}$) and small standard deviation on resolution loss ($\sigma(\mathrm{RL}_{\mathrm{est}})$ or $\sigma(\mathrm{WPRL})$), indicating that it is insensitive to the variation in systematic deviations. Fig. 5.12(e) plots the resolution loss calculated using two types of systematic deviations ($\overline{\mathrm{RL}}_{\mathrm{est}}$ versus $\overline{\mathrm{WPRL}}$). Fig. 5.12(f) gives the relation between $\overline{\mathrm{RL}}_{\mathrm{est}}$ and $\mathrm{RL}_{\mathrm{noise}}$. It can be seen that the influence of data noise is negligible compared with that of systematic deviations, and that the point configurations which generate the same $\mathrm{RL}_{\mathrm{noise}}$ may yield very different $\overline{\mathrm{RL}}_{\mathrm{est}}$, indicating that the rule for positioning the point sources is more strict when we take systematic deviations into consideration. The relation between $\overline{\mathrm{WPRL}}$ and $\mathrm{RL}_{\mathrm{noise}}$ is shown in Fig. 5.12(g). It seems that these two measures have an approximated linear relation in most of the cases, and that the point configuration which generates the minimal $\overline{\mathrm{WPRL}}$ also yields the lowest $\mathrm{RL}_{\mathrm{noise}}$.

The point configurations selected by the principles explained in 5.7.1 are listed in table 5.7 and table 5.8 for the two types of systematic deviations, respectively. The point configurations which yield the minimal $\mathrm{RL}_{\mathrm{noise}}$ are shown in table 5.9. The figures in bold are the ones used for selection. Note that the point configurations which yield the same results with WPRE are not equivalent with realistic deviations for different α, and that the point configurations which yield the lowest $\overline{\mathrm{WPRL}}$ are actually a subset of those yielding the lowest $\mathrm{RL}_{\mathrm{noise}}$.

Table 5.7: Point configuration selected with realistic deviations

	$\overline{\mathrm{RL}}_{\mathrm{est}}$	$\overline{\mathrm{ID}}_{\mathrm{est}}$	$\overline{\mathrm{WPRL}}$	$\overline{\mathrm{WPID}}$	$\mathrm{RL}_{\mathrm{noise}}$	$\mathrm{ID}_{\mathrm{noise}}$
$\mathrm{PS}^{\pi/2}_{-10}$–$\mathrm{PS}^{3\pi/2}_{10}$	**0.35**	1.16%	1.89	9.73%	0.015	0.073%
$\mathrm{PS}^{\pi/2}_{-5}$–$\mathrm{PS}^{3\pi/2}_{0}$–$\mathrm{PS}^{\pi/2}_{15}$	**0.29**	1.05%	1.71	9.62%	0.015	0.085%

Table 5.8: Point configuration selected with WPRE deviations

	α	$\overline{\mathrm{RL}}_{\mathrm{est}}$	$\overline{\mathrm{ID}}_{\mathrm{est}}$	$\overline{\mathrm{WPRL}}$	$\overline{\mathrm{WPID}}$	$\mathrm{RL}_{\mathrm{noise}}$	$\mathrm{ID}_{\mathrm{noise}}$
$\mathrm{PS}^{\alpha}_{-15}$–$\mathrm{PS}^{\alpha+\pi}_{10}$	0	0.61	1.48%	**1.83**	8.89%	0.015	0.072%
	$\pi/2$	0.43	1.22%				
	π	0.62	2.11%				
	$3\pi/2$	0.38	1.30%				
$\mathrm{PS}^{\alpha}_{-15}$–$\mathrm{PS}^{\alpha-\pi/2}_{0}$ –$\mathrm{PS}^{\alpha+\pi/2}_{10}$	0	0.45	1.64%	**1.52**	8.06%	0.012	0.066%
	$\pi/2$	0.41	1.18%				
	π	0.38	1.55%				
	$3\pi/2$	0.44	1.11%				

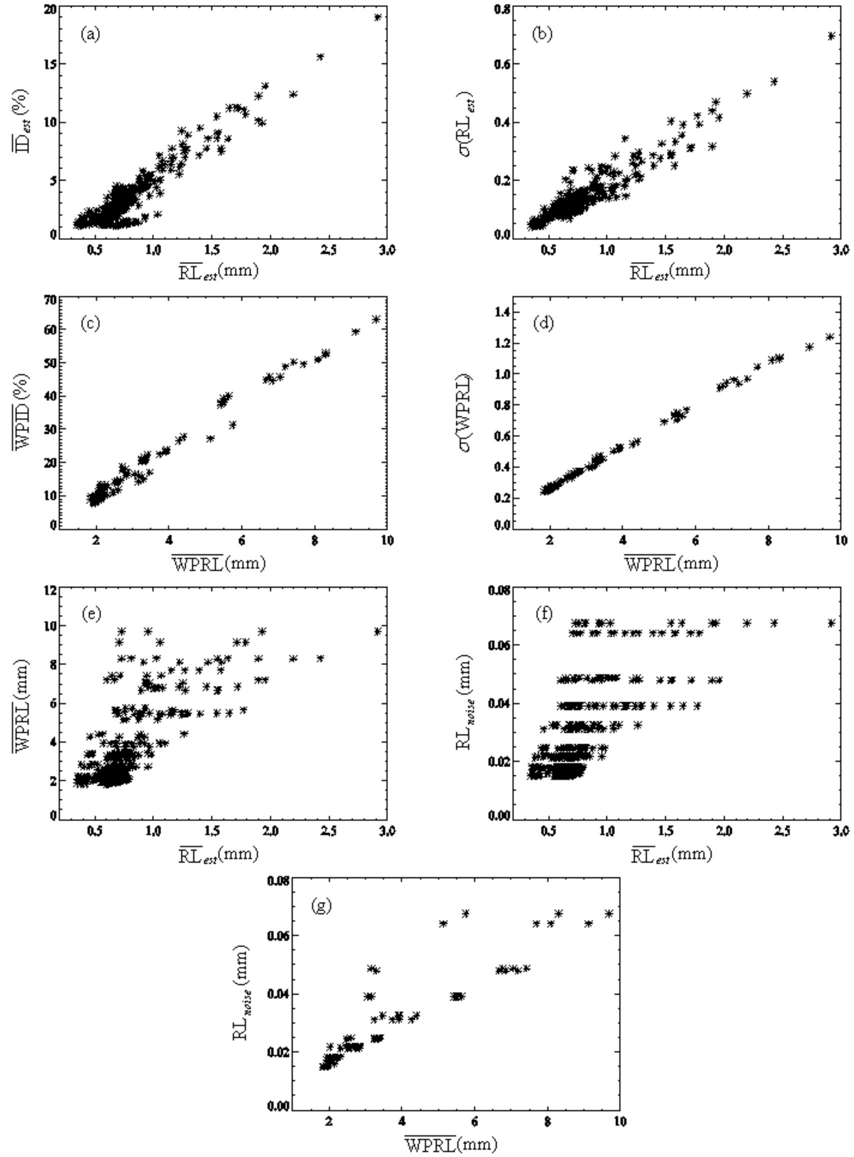

Figure 5.12: Reconstruction errors of all 2-point configurations. Plots of (a) $\overline{\mathrm{RL}}_{\mathrm{est}}$ vs $\overline{\mathrm{ID}}_{\mathrm{est}}$. (b) $\overline{\mathrm{RL}}_{\mathrm{est}}$ vs $\sigma(\mathrm{RL}_{\mathrm{est}})$. (c) $\overline{\mathrm{WPRL}}$ vs $\overline{\mathrm{WPID}}$. (d) $\overline{\mathrm{WPRL}}$ vs $\sigma(\mathrm{WPRL})$. (e) $\overline{\mathrm{RL}}_{\mathrm{est}}$ vs $\overline{\mathrm{WPRL}}$. (f) $\overline{\mathrm{RL}}_{\mathrm{est}}$ vs $\mathrm{RL}_{\mathrm{noise}}$. (g) $\overline{\mathrm{WPRL}}$ vs $\mathrm{RL}_{\mathrm{noise}}$.

Table 5.9: Point configuration selected with noisy projections

		$\overline{\text{RL}}_{\text{est}}$	$\overline{\text{ID}}_{\text{est}}$	$\overline{\text{WPRL}}$	$\overline{\text{WPID}}$	RL_{noise}	ID_{noise}
$\text{PS}^{\alpha_1}_{-15}$–$\text{PS}^{\alpha_2}_{10}$	min	0.38	1.18%	1.83	7.91%	**0.015**	0.072%
	max	0.71	3.10%	1.96	8.89%		
$\text{PS}^{\alpha_1}_{-15}$–$\text{PS}^{\alpha_2}_{0}$	min	0.33	0.89%	1.52	6.96%	**0.012**	0.066%
–$\text{PS}^{\alpha_3}_{10}$	max	0.70	3.03%	1.82	9.08%		
α_1, α_2 and α_3 can be any angle $\in$ [0, $\pi/2$, π, $3\pi/2$]							

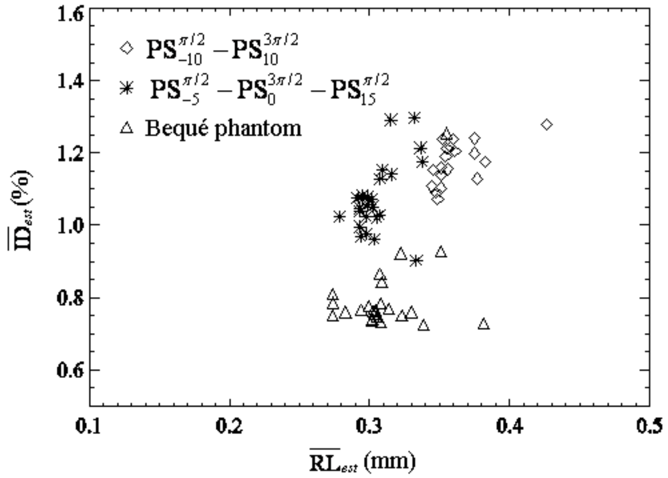

Figure 5.13: Robustness test for the selected point configurations. The diamond/asterisk symbol represents the 2-point/3-point configurations selected with realistic deviation patterns. The triangle symbol represents the typical Bequé calibration phantom.

The result for the robustness test is shown in Fig. 5.13. The three symbols represent the two chosen point configurations and the Bequé calibration phantom. For each point configuration, most of the data points concentrate within a range of 0.1 mm for the resolution loss. Therefore these configurations are considered robust enough to be used for the measurement in practice.

5.8.2 Phantom experiment

Fig. 5.14 shows the trans-axial slices of the reconstruction images of the Jaszczak-type phantom. It can be seen that the resolution in the image reconstructed using the parameters estimated with the projection of the selected 2-point configuration is very similar to that of the typical Bequé calibration phantom. The resolution in the reconstruction image is slightly better when we applied refined calibration to correct for systematic deviations.

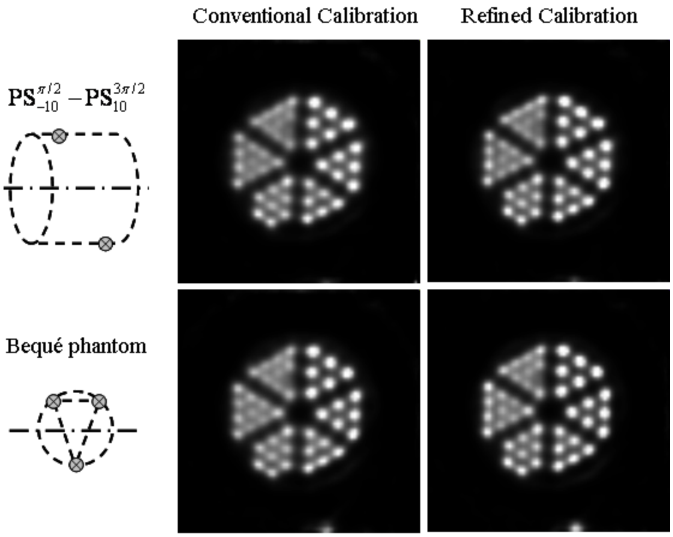

Figure 5.14: Trans-axial slices of reconstruction images of Jaszczak phantom. Top/bottom: reconstruction with parameters estimated from projection of different point configurations. Left/right: reconstruction with parameters estimated by conventional/refined calibration procedure.

5.9 Conclusion II

In this part, we selected the calibration point configuration which yields accurate and stable calibration results using the proposed analytical linear model. Two different types of systematic deviations, the realistic deviations and the WPRE deviations, were used for the selection. The winner of the 2-point configuration was applied in a simultaneous phantom/calibration scan. The results showed that the chosen point combination leads to satisfying resolution in the reconstruction image, and that it is feasible to replace the typical Bequé calibration phantom to perform a simultaneous animal/phantom data acquisition.

5.10 Discussion

In the first study, we considered two sources of error in multi-pinhole SPECT calibration: random measurement noise and systematic orbit deviations. For fast estimation, we analyzed the error sources individually using an analytical linear model. Two measures, i.e., resolution loss and image deformation, are proposed as figures of merit to quantify the degradation of the image quality in the reconstruction image due to each of the disturbing factors. The theoretical results show that the presence of systematic deviations plays a key role in the degradation of the reconstruction quality, whereas the data noise has a hardly observable effect on the accuracies of the reconstructed images.

In Fig. 5.5 and Fig. 5.6, not all the camera-specific parameters are given due to the limited space in the figure. For the pinhole locations, we only plot the results corresponding to the 2nd, 4th and 6th pinhole aperture. Actually, the results of the 3rd, 5th and 7th pinhole are somehow similar to those of the 6th, 2nd and 4th pinhole since their configurations are approximately symmetrical. In addition, one should note that the offset of the first pinhole n_1 was not fitted during the calibration but calculated from $n_1 = m_1 \tan \Psi$ [20]. This was done to determine the location of the origin of the coordinate system along the axis of rotation [87].

In table 5.4 and table 5.5, the reconstruction errors predicted by the analytical method are always in good agreement with those calculated from simulations. In table 5.6, the predictions almost everywhere underestimate the image degradation when compared to the numerical simulations. This may indicate that the refined calibration did not completely eliminate the angular dependence of the parameters, as assumed in (5.36) and (5.37).

The refined calibration was initialized with the result of the conventional calibration and produced similar deformation and better resolution in all distance-fixing cases. As suggested in the introduction, we think that the refined calibration does not find an exact solution, but rather a nearby local minimum, and therefore suffers from very similar bias on the mean values of the (angle dependent) geometrical parameters. Although the refinement improves the reconstruction quality, it does not eliminate the problems due to this bias.

For the analytical study, we used a standard deviation of 0.6 mm to model the Gaussian noise. This value is derived based on the calibration results of real measurements. If we ignore the bias on the parameters, it is valid to assume that the difference between the measured projection and the refined-calibrated projection is only due to the noise in the measurement. The standard deviation on the difference between the measured and the estimated refined projection coordinates was around 0.6 mm in both $u-$ and $v-$ directions. Taking the bias into consideration will yield more accurate estimated projections, leading to an even smaller standard deviation. Therefore 0.6 mm is probably a pessimistic estimate for the noise. Nevertheless, as shown in the results, the influence of data noise is already negligible compared to that of systematic deviations.

The bias on the estimated parameters is determined by the given systematic deviations. Both the shape and the amplitude of the deviations greatly influence the result. In reality, the real pattern of the deviations is always unknown and can only be approximately estimated from previous refined calibrations. For the analytical study we only present the results with one set of typical systematic deviations. In fact, with all the calibration scans we ever performed, we have in total 23 different sets of systematic deviations. We applied these deviations to 3PS and repeated the analysis for detector head 2. For each calibration method, the standard deviation of 23 resolution loss values is about 0.2 mm for both case 2 and case 3. It means that the motion of the gamma camera cannot be precisely reproduced every time, and that the variation in the camera motion between the animal scan and the calibration scan may introduce extra resolution loss in the reconstruction. Therefore, if possible, it is preferable to acquire the animal data and the calibration data within one single acquisition.

Our method is general and applicable to any multi-pinhole system based on a circularly rotating detector. Since orbit deviations are very camera-specific and greatly influence the image quality, representative deviations need to be used when applying the method to another system.

Based on both the analytical results and the phantom experiment, we found that if no distance information is applied, the reconstruction may be remarkably scaled, both trans-axially and axially, with respect to the original size due to the lack of information about the pinhole magnification. Therefore we strongly recommend to use either the inter-point or inter-pinhole distances as prior knowledge during calibration. For the point sources, there are two typical approaches to fix their distances. The first one is to drill small holes on a rigid plate and fill them with radioactivity. The disadvantage is that it usually restricts the shape of the phantom, which compromises its use during the animal scan. This was the case with our Bequé phantom, therefore a separate calibration scan is demanded. The second approach is to attach the point sources to, e.g., the animal bed as separate markers, where special procedures are required to guarantee accurately known fixed distances between them [40]. Individual markers make it possible to perform a simultaneous animal-calibration scan, but it requires extra effort to guarantee the accurate inter-point distances. By contrast, fixing the inter-pinhole distances is more straightforward. Typically multiple apertures are drilled or eroded with high precision in a single rigid plate [112,128,133] or cylinder [18,39]. Once the distances are accurately determined, they will be known for every scan with the same pinhole collimator. Combining this calibration approach with the individual point source markers (distance information is then not required) facilitates us to do simultaneous animal-calibration data acquisitions.

To determine the inter-pinhole distances accurately, one could either trust the specifications provided by the manufacturer, or acquire a large number of calibration scans, e.g., using a calibration phantom with point sources at accurately known distances, and then derive the distances between the apertures by averaging over all calibrations. We tried both approaches. Based on the difference between the fitted projection and the measured projection, we conclude that the averaged values derived from repeated calibrations are more reliable than the values provided by the manufacturer.

To facilitate discrimination between point source and animal projections, the use of two isotopes with sufficiently different energies is recommended. DiFilippo et al. suggested the use of Gadolinium-153 (^{153}Gd), which emits among others gammas of 97 keV and 103 keV (no higher-energy emissions) [40]. These energies can easily be discriminated from the photopeak energies of the most commonly used SPECT isotopes ($^{99\mathrm{m}}$Tc: 140 keV, ^{123}I: 159 keV). Additional advantages of using two distinct isotopes are the lower dose required to discern the point sources and the fact that a long-living isotope can be chosen, e.g., ^{153}Gd with a half-life of 242 days, such that the point sources do not need to be refilled for every calibration scan.

Usually one would expect that using more point sources for the calibration should always produce better results. This is true if the projection data is only disturbed by random noise. Indeed, in table 5.4, 3PS always results in better reconstruction accuracy than 2PS-sub12 and 2PS-sub13. However, it is not the same with the systematic deviation. In table 5.5 and 5.6, 3PS outperforms 2PS-sub13, but has slightly worse resolution than 2PS-sub12. We assume that if one uses projection data suffering from systematic deviations to do conventional calibration assuming perfect camera motion, the projection data actually carries "inaccurate" information. If the additional point source carries less accurate information than the other two, it might make the results slightly worse.

The same principle also applies when we compare the results with and without truncation modeling (the analytical results related to the non-truncated case are not shown in this thesis). With noise in the data, the reconstruction errors with truncated projections are always inferior to those with non-truncated projections due to the increase of uncertainty. However, when the projection data are subject to systematic deviations, most of the time we have slightly better results with truncated projections.

In agreement with the analytical prediction, the reconstruction images show that 2PS-sub13 yields larger reconstruction errors than 2PS-sub12, indicating that the position of the point sources strongly influences the calibration result. Hence it is of great interest to optimize the location of the point sources in order to minimize both the variance and the bias on the calibration parameters. In a previous study where only data noise was considered [136], it was found that the distance between the point sources, measured along the axis of rotation, should be as large as possible. The current study adds that the point sources should not be put on a line parallel to the rotation axis. Details about the optimization of the point source locations are presented in study II.

A phantom only provides anecdotal evidence, and since this particular phantom has very little variation in axial direction, it only verified the predictions in two of the three dimensions. Nevertheless, the good agreement between the analytical predictions and the observed reconstruction quality of the Jaszczak phantom is encouraging.

In the second study, we applied two types of systematic deviations for the selection of the point source configuration. The realistic deviation patterns were estimated from previous calibration data, therefore they were most relevant to the behavior of our clinical gamma camera. With realistic deviations, a 2-point and a 3-point configuration were selected particularly for the calibration of our multi-pinhole system. However, another gamma camera may be subject to totally different systematic deviations. Therefore we also tried to find point configurations which are expected to provide acceptable reconstruction error with any possible deviation pattern. It was studied by introducing a concept of worst possible reconstruction error and selecting the point source configuration with the smallest WPRE. Based on Fig. 5.12(f), it can be seen that a small WPRL generally corresponds to a small $\overline{\mathrm{RL}}_{\mathrm{est}}$ as well. Therefore, although the minimal achievable WPRE is still unacceptable (about 1.5-1.8 mm for resolution loss and 9% for image deformation), one should keep in mind that it is actually over-pessimistic and the reconstruction in reality will be much better. Therefore, very probably the corresponding point configuration is adequate to be used in practice.

For the selection of the 2-point configuration, although $\mathrm{PS}^{\alpha}_{-15}$–$\mathrm{PS}^{\alpha+\pi}_{10}$($\alpha = 0, \pi/2, \pi$ and $3\pi/2$) all behave equally well with WPRE deviations, PS^{0}_{-15}–PS^{π}_{10} and PS^{π}_{-15}–PS^{0}_{10} are inferior to $\mathrm{PS}^{\pi/2}_{-15}$–$\mathrm{PS}^{3\pi/2}_{10}$ and $\mathrm{PS}^{3\pi/2}_{-15}$–$\mathrm{PS}^{\pi/2}_{10}$ for spatial resolution calculated with realistic deviations. It can be interpreted as follows. With our camera, the second detector head is subject to more severe systematic deviations than the first head, thus it dominates the result. The maximum deviations of this detector head always occur when it is at the top ($\alpha = 0$) and the bottom ($\alpha = \pi$) position due to the effect of gravity. Hence, the latter two point configuration are less sensitive to systematic deviations caused by gravity, i.e., their projections are less distorted in the presence of our realistic deviations, and they yield better resolution with realistic camera motion. We expect that it is a common phenomenon for most gamma cameras, therefore we suggest that the point sources should be placed on a horizontal plane crossing the axis of rotation rather than on a plane perpendicular to the floor.

Intuitively, it seems that in order to obtain a good estimate of systematic deviations by refined calibration, one should use the point sources sensitive to the deviations rather than those insensitive to the deviations. This is contradictory to what we proposed in the last paragraph. However, one should note that with the refined calibration, it is impossible to correct all parameters for the bias yielded by the conventional parameters, because some of those parameters are fixed during refined calibration. For example, small deviations produce bias on the focus height of the pinhole (f_i) in the conventional calibration (see Fig. 5.5 and Fig. 5.6). Since the focus height remains fixed in the refined calibration, the bias remains even if the refined calibration would correctly estimate the small deviations that cause this bias. Using point sources insensitive to systematic deviations is actually recommended to improve the accuracy of the conventional calibration rather than that of the refined calibration. For further improvement, a possible solution is to modify the calibration procedure, such that it can estimate all parameters in a single fitting procedure, rather than with the current two-step procedure. Another potential solution is to iterate between the current two calibration steps, which allows interactions between all estimated parameters. With these approaches, a point configuration sensitive to systematic deviations will be more appropriate than the one that is insensitive to those deviations.

Based on the presented results, we propose some common rules for positioning the calibration point sources, First, at least two point sources should be put apart with respect to each other not only in the axial direction (which is what we found with noise propagation theory [136]), but also in the trans-axial direction. Second, to calibrate a multi-pinhole system with unknown systematic deviations, either use two point sources placed in the horizontal plane, or use three point sources located at different angular positions (α). The latter one is recommended because it can provide more information if one wants to estimate systematic deviations of the gamma camera using the principle of refined calibration.

We use the word "selection" rather than "optimization" for two reasons. First, the choice of the point source combination is influenced by the principle of selection. In our case, we focus more on the resolution loss and less on the image deformation. There is no real optimal solution for both figures of merit. Second, the point source space is only limited to the surface of a coaxial cylinder due to our special purpose. Nevertheless, we expect that the selected point configurations are adequate for most rotating multi-pinhole SPECT systems.

Chapter 6

General conclusion

6.1 Main contribution

This PhD work consists of two parts, i.e., a study about system optimization and comparison and a study about multi-pinhole calibration. The main contributions in each study are summarized here.

6.1.1 System optimization and comparison

We compared two types of collimator systems, namely the parallel hole (PH) and the rotating slat (RS) collimation systems. First, the geometric configurations of these two systems were optimized to yield the minimal variance in the reconstruction. Then, the two systems were compared with each other, using these optimized geometries. The optimization and the comparison of the two systems was mainly performed by two analytical methods.

New idea about system comparison

Previously, the comparative studies between the PH and the RS collimator system were mostly based on the same collimator resolution, and the spatial resolutions in the reconstruction image were not the same for both systems [59,60,76,77,141, 157]. In our study, we imposed equal spatial resolution in the reconstruction for both systems. It was found that the variance in the reconstruction image is a function of collimator resolution, and a unique minimal variance can be found for each type of collimator at a predefined target resolution. The collimator resolution corresponding to this minimal variance is referred to as *optimal collimator aperture*, which was determined by the type of collimator (PH or RS) and the acquisition mode (planar or volume imaging). We proposed to compare different systems, each with its own optimal collimator aperture, in order to yield the fairest results. With the proposed analytical methods, it was found that the ratio between the optimal collimator aperture of a line integral system (PH) and that of a plane integral system (RS) is always $\sqrt{2}$. The idea about comparing different imaging systems using their optimized geometries is applicable to any system comparison task, as long as an optimal configuration exists for each system for the given figure of merit.

Mathematical derivations

Based on the theory of filtered back-projection (FBP) reconstruction, we have derived the concise expressions for the optimal collimator aperture at a given target resolution, the minimal variance in the center of a uniform object, as well as the gain (RS versus PH) in the minimal variance. The derivations were based on a simplified acquisition model for both planar imaging and volume imaging. With mathematical derivations, we got insight in the tradeoff between the collimator resolution and the geometric efficiency of each collimator system. With the expressions of the gain in the variance, it is straightforward to see that the relative performance of the two systems is determined by the object-to-detector distance and the size of the object with respect to that of the detector array. Although these results were derived with a series of approximations, they are generalized by the other well-validated analytical method, namely the Fisher information-based method (FIM). FIM proves that the basic results obtained from the FBP-based method are also approximately valid with non-uniform, non-symmetrical objects using more sophisticated system models.

Extension of Fisher information-based method

The Fisher information-based method is an efficient and reliable analytical method which can be used to evaluate the resolution and the noise properties in the reconstructions. In previous studies of our group [129], FIM was used to estimate the linearized local impulse response (LLIR) and the covariance image correlated to a pixel in the post-smoothed maximum likelihood expectation maximization (MLEM) reconstruction. In this PhD study, FIM has been extended to estimate the contrast-to-noise ratio (CNR) in regions of interest (ROIs) and the signal-to-noise ratio (SNR) for a channelized Hotelling observer (CHO). The latter is particularly interesting to evaluate the performance of a system in lesion detection tasks. The estimation of these figures of merit by FIM were verified by repeated numerical simulations. With the extended Fisher information-based method, we compared the PH and the RS systems using all these figures of merits. It was found that different figures of merit tend to give very similar rankings in the system comparison.

6.1.2 Multi-pinhole SPECT calibration

For multi-pinhole SPECT calibration, we investigated how the errors in the measured calibration data propagate during the fitting procedure and affect the estimated parameters, and how these inaccuracies are further propagated during the reconstruction and degrade the final image quality. The analysis was performed using an analytical linear model, which can be applied as an efficient and powerful tool for the optimization of the calibration configuration for multi-pinhole SPECT systems.

Use of new prior information

For geometrical calibration of a multi-pinhole SPECT system, the data used in the fitting procedure is normally acquired by measuring several radioactive point sources in the field of view. To stabilize the fitting solution, prior information is always applied during the calibration. Previously, we always used the distances between the point sources as prior knowledge, meaning that the inter-point distances are fixed to their true values during the fitting procedure. In this PhD work, we explored the use of another prior information, i.e., the distances between the pinhole apertures. Since pinholes are often drilled in a rigid plate or a rigid tube, their distances with respect to each other are constant. These distances can easily be implemented as prior information if they are accurately known. It was proven that the use of this new prior information yields a very similar estimation accuracy and reconstruction accuracy comparing to those obtained with the previously used prior information. In addition, applying the inter-pinhole distances as prior knowledge avoids the effort to position the point sources with exact distances with respect to each other, making it much easier to combine the animal scan and the calibration scan as one acquisition.

Influence of systematic deviations

In the literature [131, 142], it was proven mathematically that two point sources without distances between them are sufficient to yield a unique solution for the geometrical calibration of rotating multi-pinhole SPECT systems. However, this approach did not provide stable calibration results with our system. With further investigation, it was found that this instability is due to the small deviations between the expected camera orbit and the actual camera orbit, which we call *systematic deviations*. These systematic deviations yield non-negligible bias on the estimated parameters, which degrades the spatial resolution in the reconstruction, and may greatly scale the dimension of the reconstructions. The influence of systematic deviations on the reconstruction accuracies depends on the choice of the point configuration (the number and the locations of the point sources) and the use of prior information. A well-chosen point source configuration can reduce the loss of the spatial resolution, and applying prior information about the distances, which helps to constrain the magnification of the projection, can minimize the scaling effect in the reconstruction.

Extension of analytical evaluation method

In a previous work of our group [19], an analytical method was developed to investigate the noise propagation in single pinhole SPECT calibration. In this PhD work, this analytical method has been extended and fully validated to study the calibration procedure of rotating multi-pinhole SPECT systems. The extended method incorporates the choice of different prior information about the distances, and it can be used to estimate the variance and the bias on the estimated parameters (calibration accuracy), as well as the resolution loss and the image deformation (reconstruction accuracy) in the presence of random data noise and systematic deviations. These calibration/reconstruction accuracies can be fast estimated for a given point configuration, thus it can be considered as a helpful tool to optimize the point configuration for rotating multi-pinhole SPECT systems.

Simultaneous phantom/calibration acquisition

Routinely, a small animal experiment with our multi-pinhole SPECT consists of an animal scan and a subsequent calibration scan. It is because the calibration is always done using a 3-point calibration phantom (called *Bequé phantom*) which needs to be positioned in the center of field of view, making it difficult to be combined with the animal scan [21]. Due to the presence of potentially time dependent systematic deviations, it is preferable to acquire both animal data and calibration data within one acquisition, such that the estimated parameters are most representative to establish the system matrix for the reconstruction of animal data. In order to do simultaneous phantom/calibration, we selected a 2-point and a 3-point configuration from combinations of point source candidates which are only allowed to be attached to the animal carrier. The selection was done using the proposed analytical method. Two types of systematic deviations were used for point configuration selection. One is the deviations which are most relevant to the behavior of our camera, and the other is the deviations which yields the worst possible reconstruction errors (WPRE). The latter was considered to yield a generally good point configuration which gives adequate result regardless of the behavior of camera motion. The resultant 2-point configuration was applied to a real simultaneous phantom/calibration scan. The results confirmed that the selected point configuration yields very similar accuracy in the reconstructions compared to the typically used Bequé phantom, meaning that it is very promising to perform simultaneous animal/calibration acquisition in the near future.

6.2 Suggestions for future work

6.2.1 Improvement of Fisher information-based method

The Fisher information-based method is a very interesting tool for fast analysis of the resolution and the noise properties in the reconstruction. However, it has some limitations due to the approximations made during the derivations. One of the major limitations is that it was derived by linearizing the solution around the expectation value, meaning that it does not take into account the non-negativity constraint in the EM reconstructions. Therefore, the estimates made by FIM are less accurate in low-count regions. Improvement has been made in [108] to compensate this constraint, with assumptions that still affect the approximation accuracy. Another limitation is that FIM assumes that the estimate is acquired at the point of convergence. In practice, we only perform a finite number of iterations with the reconstruction algorithm, which cannot guarantee fully converged solutions. How to overcome these limitations is still an open question.

In emission tomography, the system response and the impulse response are shift-variant. Besides the commonly used pixel- or Fourier-basis function, one can apply the concept of wavelets for imaging analysis. The advantage of a wavelet basis is that it incorporates both spatial and frequency information, making it a perfect choice for the study of shift-variant systems. Previously, the wavelets have been applied to do image reconstruction with multi-resolution levels [22, 23, 31, 37, 47, 159], or to build the crosstalk matrix for the evaluation of the system performance [105]. One may explore the use of wavelets for calculating the approximate inverse of the Fisher information matrix, which could lead to a more accurate solution.

In addition, it might also be interesting to compare our Fisher information-based method with the "small ROI method" proposed in [32], which avoids the computation of the entire Fisher information matrix by evaluating the Fisher elements only for pixels within a neighborhood of a point of interest. This formulates invertible sub-matrices of the Fisher information matrix, which are used to estimate the best achievable variance with the Cramér-Rao bound.

Furthermore, one can explore the feasibility of using FIM to predict artifacts in the reconstruction. Artifacts are normally caused by the inaccuracy in the system modeling, or due to truncated or overlapped projections (for example the multiplexing effect with the multi-pinhole SPECT [134]). The presence of artifacts is expected to be reflected in the covariance images. However, there is no straightforward way to estimate or quantify the artifacts directly based on the covariance images. If one could find a way to make quantitative predictions of the artifacts with a fast analytical method, the severity of the artifact will become another figure of merit for the optimization and comparison of various tomographic imaging systems.

6.2.2 Further improvement of multi-pinhole calibration

Simultaneous animal/calibration scan

In chapter 5, we have shown the feasibility of simultaneous animal/calibration scan using the selected point configuration, provided that the inter-pinhole distances are used as prior information. The advantages of performing both scans at the same time are as follows. 1) The total acquisition time will be reduced, especially when the experiment is performed with multiple animals and the camera geometry needs to be adapted individually for each animal (for example a large FOV for a whole-body scan and a small FOV for a focused ROI scan). 2) The geometry and the camera motion are exactly the same for the calibration data and the animal data, thus the estimated parameters, especially the systematic deviations, are more representative to build the system matrix used for reconstruction. Therefore, it is our intention to apply this idea to real animal experiments. In order to distinguish the projections of the point sources and the projection of the animal, we would use gadolinium-153 (^{153}Gd) for the point sources. ^{153}Gd has different photonpeaks (97keV and 103keV) from the commonly used radionuclides ^{99m}Tc (140 kev) and ^{123}I (159 kev) with a half life of 242 days. These characteristics make ^{153}Gd a very good choice for our purpose. The calibration point sources attached to the animal carrier can also be considered as rigid markers used for the registration between the SPECT image and the image obtained from another imaging modality (for example the CT image). For registration purposes, 3 point sources are essentially needed. In that case, the selected 3-point configuration should be applied.

Adaptation of calibration procedure

The current calibration procedure consists of two steps, i.e., the conventional calibration and the refined calibration [99]. The former assumes that all the geometrical parameters are constant for each acquisition angle (i.e., no systematic deviations), and the latter uses the outputs of the first step as initial values and estimates the 6 degrees of freedom of the camera deviation individually for each projection angle. It was found that with systematic deviations, the parameters estimated by conventional calibration are biased, and this bias cannot be corrected for by refined calibration, leading to quality degradation in the reconstruction. It might be interesting to adapt the second step, such that all parameters are fitted individually for each acquisition angle with refined calibration. To that end, first, one needs to investigate theoretically the minimal number of point sources that can give a unique solution for the parameter estimation at each projection angle (similar as the work in [83] for cone-beam CT and [61] for C-arm systems), taking into account the truncation effects due to the limited field of view of the pinhole apertures and the limited size of the detector. Then, the accuracy and the stability of the calibration results need to studied. Since the projections of increasing number of point sources will be difficult to be distinguished from each other, it may introduce extra errors in the identification of the mass centers of the point projections. In addition, estimating parameters for each individual angle will be much more time consuming than the current calibration procedure. The advantages and the limitations of such a calibration procedure with respect to the current one need to be fully investigated before it is applied to real experiments.

Appendix A

Effective Detector Width

In this appendix, we calculate the effective detector width for the RS collimator (see (4.38) and (4.39)). As shown in Fig. A.1(a), we denote (α, γ) the coordinates of a point on a plane centered between two adjacent slat septa, with α measured along the axis lying in the detector plane along the slat septa, and γ measured along the axis orthogonal to the detector. The coordinate center is taken at the center of the detector strip, so that γ is the distance between the point and the detector surface. For this point, the effective detector width $\Omega_W(\alpha, \gamma)$ is defined as

$$\Omega_W(\alpha, \gamma) = \int_{-W/2}^{+W/2} \cos^3 \beta(\alpha - l, \gamma) dl \tag{A.1}$$

where W is the width of the detector along the slat septa, and $\beta(\alpha - l, \gamma)$ is the angle between the normal to the detector and the trajectory of the photon (emitted

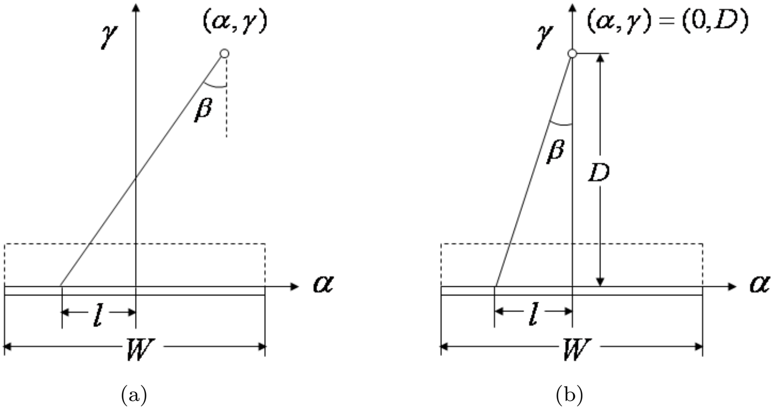

Figure A.1: Notations used to calculate the effective detector width a) in general case, b) with the FBP-based method.

from point (α, γ) and detected at location l along the slat septa):

$$\cos\beta(\alpha - l, \gamma) = \frac{\gamma}{\sqrt{(\alpha - l)^2 + \gamma^2}} \tag{A.2}$$

With the FBP-based method, we focus on the central point of the image space, for which $(\alpha, \gamma) = (0, D)$ (see Fig. A.1(b)). For convenience, we use Ω_W (without the arguments α and γ) to denote the effective detector width for that central point. (A.1) yields then

$$\Omega_W = \int_{-W/2}^{+W/2} \cos^3\beta(l, D)dl = \frac{DW}{\sqrt{D^2 + W^2/4}} \tag{A.3}$$

If $D >> W$, (A.3) becomes

$$\Omega_W \approx W \tag{A.4}$$

Appendix B

Geometric Efficiency

In this appendix, we calculate the geometric efficiencies E_p and E_r used in the data acquisition models of (4.5), (4.6), (4.9) and (4.11) for the PH and the RS collimator systems, respectively.

For the PH collimator (see Fig. B.1(a)), the geometric efficiency E_p is shift-invariant. For square holes, E_p is estimated as [73, 90, 145]

$$E_p = \frac{d_p^2}{4\pi h_p^2} = \frac{\mathrm{FWHM}_p^2}{4\pi D^2} = \frac{2\ln 2\, \sigma_p^2}{\pi D^2} \tag{B.1}$$

where d_p and h_p are the length and the height of the holes, respectively, and σ_p (or FWHM_p) represents the PH collimator aperture that corresponds to the center of the image space (see (4.4)).

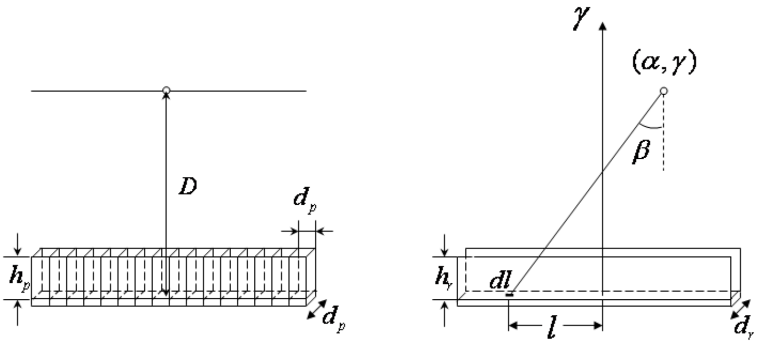

(a)

(b)

Figure B.1: Notations used to calculate the geometric efficiency a) with PH collimator and b) with RS collimator.

For the RS collimator (see Fig. B.1(b)), the geometric efficiency E_r is shift-variant. The geometric efficiency of a small detector element dl at location l along the slat for a point source located at (α, γ) in the plane defined by two adjacent slat septa is [126]

$$E_r(\alpha - l, \gamma)\, dl = \frac{d_r\, dl}{4\pi\gamma h_r} \cos^3\beta(\alpha - l, \gamma) \tag{B.2}$$

where d_r is the distance between two adjacent slat septa, h_r is the height of the septa, and α, β and γ are defined in appendix-A. (B.2) is used to defined the system matrix A for the FIM method, where the detector is modeled as an array of individual square detector elements of length $dl = d_r$.

For the FBP-based calculation, the position-dependence of E_r is ignored and a single value is used for the entire image space. This value is calculated as the geometric efficiency of the central point of the image space, integrated over the whole detector strip. We denote this value as E_r, without arguments. Substituting $(\alpha, \gamma) = (0, D)$ in (B.2) and integrating over the length of the detector strip, we obtain

$$E_r = \int_{-W/2}^{+W/2} E_r(l, D) dl = \frac{d_r}{4\pi D h_r} \Omega_W \tag{B.3}$$

with Ω_W given by (A.3). Using (4.2) and (4.4), this can also be written as

$$E_r = \frac{\mathrm{FWHM}_r}{4\pi D^2} \Omega_W = \frac{\sqrt{2 \ln 2}\sigma_r}{2\pi D^2} \Omega_W \tag{B.4}$$

where σ_r (or FWHM_r) is the RS collimator aperture corresponding to the center of the image space (see (4.4)).

Appendix C

FBP Calculation for Planar Imaging

In this appendix, we derive the optimal collimator aperture ((4.33) and (4.34)) and the optimized CNR gain ((4.38)) for the two collimator systems by simplifying the acquisition models ((4.5) and (4.6)) for planar imaging (Fig. C.1).

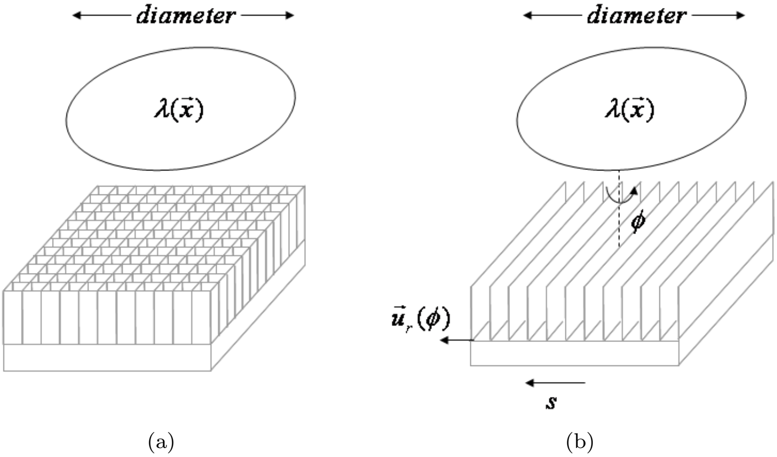

(a) (b)

Figure C.1: Planar imaging a) with the PH collimator, b) with the RS collimator.

C.1 Parallel hole collimator

For a 2-D tracer distribution $\lambda(\vec{x})$ in a plane parallel to the detector surface, we model the PH data (y_p) as a convolution between $\lambda(\vec{x})$ and a 2-D Gaussian PSF with standard deviation σ_p, which is used to model the aperture of the collimator holes. The data are scaled by the geometric efficiency E_p and the acquisition time T_p, i.e.,

$$\begin{aligned} y_p(\vec{x}) &= T_p \times E_p \times \big(\lambda(\vec{x}) \otimes G_2(\vec{x}, \sigma_p)\big) \\ &= T_p E_p \int_{\mathbb{R}^2} f(\vec{x}-\vec{y}) \frac{1}{2\pi\sigma_p^2} e^{-|\vec{y}|^2/2\sigma_p^2} d\vec{y} \end{aligned} \tag{C.1}$$

where $\otimes$ represents the convolution operation, and G_i denotes the ith-dimensional isotropic Gaussian function

$$G_i(x_1, x_2, \cdots, x_i, \sigma) = \frac{1}{(\sqrt{2\pi}\sigma)^i} e^{-(x_1^2+x_2^2+\cdots+x_i^2)/2\sigma^2} \tag{C.2}$$

Denoting the total acquisition time as T, we have

$$T_p = T \tag{C.3}$$

since PH is stationary.

We assume the noise on the data is Poisson noise. Hence, the covariance in the data is

$$\operatorname{Cov}(y_p(\vec{x}), y_p(\vec{y})) = y_p(\vec{x})\delta(\vec{x}-\vec{y}) \tag{C.4}$$

We aim to do the reconstructions with a fixed target resolution σ_t, with the constraints of $\sigma_t > \sigma_p$:

$$\lambda_{tp}(\vec{x}) = \int_{\mathbb{R}^2} \lambda(\vec{x}-\vec{y}) \frac{1}{2\pi\sigma_t^2} e^{-|\vec{y}|^2/2\sigma_t^2} d\vec{y} \tag{C.5}$$

In the Fourier space, (C.1) and (C.5) become:

$$\tilde{y}_p(\vec{\nu}) = T_p E_p \, \tilde{\lambda}(\vec{\nu}) e^{-2\pi^2\sigma_p^2|\vec{\nu}|^2} \tag{C.6}$$

$$\tilde{\lambda}_{tp}(\vec{\nu}) = \tilde{\lambda}(\vec{\nu}) e^{-2\pi^2\sigma_t^2|\vec{\nu}|^2} = \frac{1}{T_p E_p} \tilde{y}_p(\vec{\nu}) e^{-2\pi^2(\sigma_t^2-\sigma_p^2)|\vec{\nu}|^2} \tag{C.7}$$

The inverse 2-D Fourier transform of (C.7) is:

$$\begin{aligned} \lambda_{tp}(\vec{x}) &= \frac{1}{T_p E_p} \int_{\mathbb{R}^2} y_p(\vec{x}-\vec{y}) \frac{1}{2\pi(\sigma_t^2-\sigma_p^2)} e^{-|\vec{y}|^2/2(\sigma_t^2-\sigma_p^2)} d\vec{y} \\ &= \frac{1}{T_p E_p} \left(y_p(\vec{x}) \otimes G_2(\vec{x}, \sqrt{\sigma_t^2-\sigma_p^2}) \right) \end{aligned} \tag{C.8}$$

(C.8) can be interpreted as follows. To reconstruct the image for PH, we should apply a Gaussian filter with standard deviation of $\sqrt{\sigma_t^2-\sigma_p^2}$ to yield the target resolution σ_t in the reconstructed image.

The variance of the PH estimate $\lambda_{tp}(\vec{x})$ is

$$\begin{aligned}\mathrm{Var}(\lambda_{tp}(\vec{x})) &= \frac{1}{(T_pE_p)^2}\int_{\mathbb{R}^2} d\vec{y}\int_{\mathbb{R}^2} d\vec{z}\, G_2(\vec{y}, \sqrt{\sigma_t^2-\sigma_p^2}) \\ &\quad \times G_2(\vec{z}, \sqrt{\sigma_t^2-\sigma_p^2})\mathrm{Cov}(y_p(\vec{x}-\vec{y}), y_p(\vec{x}-\vec{z})) \\ &= \frac{1}{(T_pE_p)^2}\Big(G_2(\vec{x}, \sqrt{\sigma_t^2-\sigma_p^2})\Big)^2 \otimes y_p(\vec{x}) \qquad \text{(C.9)}\end{aligned}$$

The convolution kernels $\Big(G_2(\vec{x}, \sqrt{\sigma_t^2-\sigma_p^2})\Big)^2$ in (C.9) is sharply peaked around the origin, therefore we use the data acquired by the central detector to approximate the data acquired by all the other detectors [35]. Assuming the activity in $\lambda(\vec{x})$ is λ/sec, we have

$$y_p(\vec{x}) \approx \lambda \times T_p \times E_p \qquad \text{(C.10)}$$

We have the variance of the central point

$$\begin{aligned}\mathrm{Var}(\lambda_{tp}(\vec{x}))\Big|_{\vec{x}=0} &\approx \frac{\lambda \times T_p \times E_p}{(T_pE_p)^2}\int_{\mathbb{R}^2} d\vec{y}\Big(\frac{1}{2\pi(\sigma_t^2-\sigma_p^2)}\Big)^2 e^{-2|\vec{y}|^2/2(\sigma_t^2-\sigma_p^2)} \\ &= \frac{\lambda}{T_pE_p}\times\frac{1}{4\pi(\sigma_t^2-\sigma_p^2)} \\ &= \frac{4\pi D^2\lambda}{8\ln 2\sigma_p^2 T}\times\frac{1}{4\pi(\sigma_t^2-\sigma_p^2)} \\ &= \frac{D^2\lambda}{8\ln 2T\sigma_p^2(\sigma_t^2-\sigma_p^2)} \qquad \text{(C.11)}\end{aligned}$$

To find the minimum of this variance, we derive the denominator $\sigma_p^2(\sigma_t^2-\sigma_p^2)$ with respect to σ_p^2 and solve

$$\frac{d}{d\sigma_p^2}\sigma_p^2(\sigma_t^2-\sigma_p^2) = \sigma_t^2 - 2\sigma_p^2 = 0 \qquad \text{(C.12)}$$

The solution is $\sigma_p^2 = (1/2)\sigma_t^2$, which means the optimal collimator aperture should be equal to the target resolution divided by $\sqrt{2}$, i.e.,

$$\sigma_p^{opt} = \sigma_t/\sqrt{2} \qquad \text{(C.13)}$$

With the optimal aperture, the minimal variance of the central point in the reconstruction yields

$$\mathrm{Var}_p^{min} = \frac{D^2\lambda}{2\ln 2T\sigma_t^4} \qquad \text{(C.14)}$$

From (C.11), we can also write (C.14) as the function of E_p:

$$\mathrm{Var}_p^{min} = \frac{\lambda}{2\pi TE_p\sigma_t^2} \qquad \text{(C.15)}$$

C.2 Rotating slat collimator

For planar imaging, the data of RS is modeled as the plane integral of a 2-D tracer distribution. We use $y_r(s,\phi)$ to denote the RS data with the usual sinogram variables, where s is the distance between the slat interval and the spin axis on the gamma camera, and $\phi \in [0,\pi)$ denotes the angular position of the RS collimator as it spins on the fixed camera. Similarly, The data (y_r) is modeled as a convolution between the ideal 2-D Radon transform of $\lambda(\vec{x})$ (i.e., the line integral in s) and a 1-D Gaussian PSF with standard deviation σ_r.

$$\begin{aligned} y_r(s,\phi) &= T_r \times E_r \times \big(y_{r0}(s,\phi) \otimes G_1(s,\sigma_r)\big) \\ &= T_r E_r \int_{\mathbb{R}} y_{r0}(s-s',\phi) \frac{1}{\sqrt{2\pi}\sigma_r} e^{-s'^2/2\sigma_r^2} ds' \end{aligned} \tag{C.16}$$

with y_{r0} the ideal unblurred 2-D Radon transform of y_r:

$$y_{r0}(s,\phi) = \int_{\mathbb{R}^2} d\vec{x} \lambda(\vec{x}) \delta(\vec{x} \cdot \vec{u}_r(\phi) - s) \tag{C.17}$$

with $\vec{u}_r(\phi) = (-\sin\phi, \cos\phi)$ the unit vector orthogonal to the slats in the detector plane.

For fair comparison between PH and RS, the acquisition time for both collimator systems should be the same. For RS, T_r is the acquisition time per unit spinning angle. Integrating T_r over π results in the total acquisition time T:

$$T = \int_0^{\pi} T_r d\phi = \pi T_r \tag{C.18}$$

Therefore

$$T_r = T/\pi \tag{C.19}$$

With the assumption of Poisson noise in the data, the covariance matrix of the data is

$$\mathrm{Cov}(y_r(s,\phi), y_r(s',\phi')) = y_r(s,\phi)\delta(s-s')\delta(\phi-\phi') \tag{C.20}$$

In the Fourier space, (C.16) becomes

$$\tilde{y}_r(\nu,\phi) = T_r E_r \, \tilde{y}_{r0}(\nu,\phi) e^{-2\pi^2\sigma_r^2\nu^2} \tag{C.21}$$

where ν is the frequency conjugate to the sinogram variable s. The standard FBP algorithm reconstructs the image $\lambda(\vec{x})$ from the ideal data y_{r0} by applying the ramp filter to y_{r0} and then backprojecting. To reconstruct the blurred image $\lambda_{tr}(\vec{x})$ with a target resolution σ_t ($\sigma_t > \sigma_r$), on one hand, we should apodize the ramp filter by the window $e^{-2\pi^2\sigma_t^2\nu^2}$, on the other hand, based on (C.21), we need to deconvolve the slat blurring by applying a filter $e^{+2\pi^2\sigma_r^2\nu^2}$ to the data y_r for the recovery of y_{r0}

before the apodization. All this leads to the conclusion that λ_{tr} is reconstructed by applying to the data y_r the FBP algorithm with a convolution kernel $h_r(s)$ that is equal to the inverse 1-D Fourier transform of $|\nu|e^{-2\pi^2(\sigma_t^2-\sigma_r^2)\nu^2}$:

The reconstruction images $\lambda_{tr}(\vec{x})$ in the spatial domain is

$$\begin{aligned}\lambda_{tr}(\vec{x}) &= \frac{1}{T_r E_r}\int_0^{\pi} d\phi \int_{\mathbb{R}} ds y_r(\vec{x}\cdot\vec{u}_r(\phi)-s,\phi)h_r(s)\\ &= \frac{1}{T_r E_r}\int_0^{\pi} d\phi \, [y_r(s,\phi)\otimes h_r(s)]_{s=\vec{x}\cdot\vec{u}_r(\phi)}\end{aligned} \tag{C.22}$$

with

$$h_r(s) = \int_{\mathbb{R}} d\nu|\nu|e^{-2\pi^2(\sigma_t^2-\sigma_r^2)\nu^2}e^{+2\pi i\nu s} = \int_{\mathbb{R}} d\nu\tilde{h}_r(\nu)e^{2\pi i\nu s} \tag{C.23}$$

The variance of the RS estimate $\lambda_{tr}(\vec{x})$ is

$$\begin{aligned}\mathrm{Var}(\lambda_{tr}(\vec{x})) &= \frac{1}{(T_r E_r)^2}\int_0^{\pi} d\phi \int_{\mathbb{R}} ds \int_0^{\pi} d\phi' \int_{\mathbb{R}} ds' h_r(s)h_r(s')\\ &\quad\times \mathrm{Cov}(y_r(\vec{x}\cdot\vec{u}_r(\phi)-s,\phi), y_r(\vec{x}\cdot\vec{u}_r(\phi')-s',\phi'))\\ &= \frac{1}{(T_r E_r)^2}\int_0^{\pi} d\phi \int_{\mathbb{R}} ds|h_r(s)|^2 y_r(\vec{x}\cdot\vec{u}_r(\phi)-s,\phi)\\ &= \frac{1}{(T_r E_r)^2}\int_0^{\pi} d\phi \, [y_r(s,\phi)\otimes|h_r(s)|^2]_{s=\vec{x}\cdot\vec{u}_r(\phi)}\end{aligned} \tag{C.24}$$

For a 2-D uniform disc distribution, we can ignore ϕ since the object is symmetrical about the spinning axis. With the same approximation as in (C.10), the data $y_r(s,\phi)$ can be written as

$$y_r(s,\phi)\approx\lambda\times T_r\times E_r\times diameter \tag{C.25}$$

with *diameter* the diameter of object.

Based on the well-known Parseval's theorem, we have

$$\int_{\mathbb{R}} ds|h_r(s)|^2 = \int_{\mathbb{R}} d\nu|\tilde{h}_r(\nu)|^2 \tag{C.26}$$

With (C.26), the variance of the central point is calculated as

$$\begin{aligned}\mathrm{Var}(\lambda_{tr}(\vec{x}))\Big|_{\vec{x}=0} &\approx \frac{\lambda\times T_r\times E_r\times diameter}{(T_r E_r)^2}\int_0^{\pi} d\phi \int_{\mathbb{R}} ds|h_r(s)|^2\\ &= \frac{\lambda\times diameter}{T_r E_r}\int_0^{\pi} d\phi \int_{\mathbb{R}} d\nu|\tilde{h}_r(\nu)|^2\\ &= \frac{\lambda\times diameter}{T_r E_r}\times\pi\times\frac{\pi^{-5/2}}{16(\sigma_t^2-\sigma_r^2)^{3/2}}\\ &= \frac{\sqrt{\pi}D^2\lambda\times diameter}{8\sqrt{2\ln 2}\Omega_W T\sigma_r({\sigma_t}^2-\sigma_r^2)^{3/2}}\end{aligned} \tag{C.27}$$

To find the minimum of this variance, we derive the denominator $\sigma_r(\sigma_t^2 - \sigma_r^2)^{3/2}$ with respect to σ_r and solve

$$\frac{d}{d\sigma_r}\sigma_r(\sigma_t^2-\sigma_r^2)^{3/2} = (\sigma_t^2-\sigma_r^2)^{3/2} - 3\sigma_r^2(\sigma_t^2-\sigma_r^2)^{1/2} = (\sigma_t^2-\sigma_r^2)^{1/2}(\sigma_t^2-4\sigma_r^2) = 0 \tag{C.28}$$

The solution is $\sigma_r^2 = (1/4)\sigma_t^2$, which means that the slat aperture should be equal to the target resolution divided by 2, i.e.,

$$\sigma_r^{opt} = \sigma_t/2 \tag{C.29}$$

And the corresponding minimal variance is:

$$\text{Var}_r^{min} = \frac{2\sqrt{\pi}D^2\lambda\times diameter}{3\sqrt{6\ln 2}\Omega_W T\sigma_t^4} \tag{C.30}$$

From (C.27), We can also write (C.30) as the function of E_r:

$$\text{Var}_r^{min} = \frac{\lambda\times diameter}{6\sqrt{3\pi}TE_r\sigma_t^3} \tag{C.31}$$

C.3 Comparison between PH and RS

Since we image the same tracer distribution $\lambda(\vec{x})$ with the same target resolution σ_t and the same acquisition time for both PH and RS collimator, with the minimal variance (C.14) and (C.30), we can calculated the Gain (RS over PH) in variance:

$$\begin{aligned}
\text{Gain}^{opt} &= \sqrt{\frac{\text{Var}_p^{min}}{\text{Var}_r^{min}}} \\
&= \sqrt{\frac{D^2\lambda}{2\ln 2T\sigma_t^4} \times \frac{3\sqrt{6\ln 2}\Omega_W T\sigma_t^4}{2\sqrt{\pi}D^2\lambda\times diameter}} \\
&= \sqrt{\frac{3^{3/2}\Omega_W}{(8\pi\ln 2)^{1/2}\times diameter}} \\
&= \frac{3^{3/4}}{(8\pi\ln 2)^{1/4}} \times \sqrt{\frac{\Omega_W}{diameter}} \\
&= 1.116\sqrt{\frac{\Omega_W}{diameter}}
\end{aligned} \tag{C.32}$$

With the minimal variance (C.15) and (C.31), if we define the gain of geometric efficiency as $F = E_r/E_p$, we can also get the gain as the function of F:

$$\begin{aligned}
\text{Gain}^{opt} &= \sqrt{\frac{\text{Var}_p^{min}}{\text{Var}_r^{min}}} \\
&= \sqrt{\frac{\lambda}{2\pi T E_p \sigma_t^2} \times \frac{6\sqrt{3\pi} T E_r \sigma_t^3}{\lambda \times diameter}} \\
&= \sqrt{\frac{E_r}{E_p} \times \frac{3^{3/2}\sigma_t}{\pi^{1/2} \times diameter}} \\
&= \frac{3^{3/4}}{\pi^{1/4}} \sqrt{\frac{F\sigma_t}{diameter}} \\
&= 1.712 \sqrt{\frac{F\sigma_t}{diameter}} \qquad \text{(C.33)}
\end{aligned}$$

with

$$F = \frac{\sigma_r \sqrt{8\ln 2}\,\Omega_W / 4\pi D^2}{\sigma_p^2 8 \ln 2 / 4\pi D^2} = \frac{\Omega_W}{\sqrt{8\ln 2}} \times \frac{\sigma_r}{\sigma_p^2} = \frac{\Omega_W}{\sqrt{8\ln 2}\,\sigma_t} \qquad \text{(C.34)}$$

Appendix D

FBP Calculation for Volume Imaging

In this appendix, we derive the optimal collimator aperture ((4.35) and (4.36)) and the optimized CNR gain ((4.39)) by simplifying the acquisition models ((4.9) and (4.11)) for volume imaging (Fig. D.1).

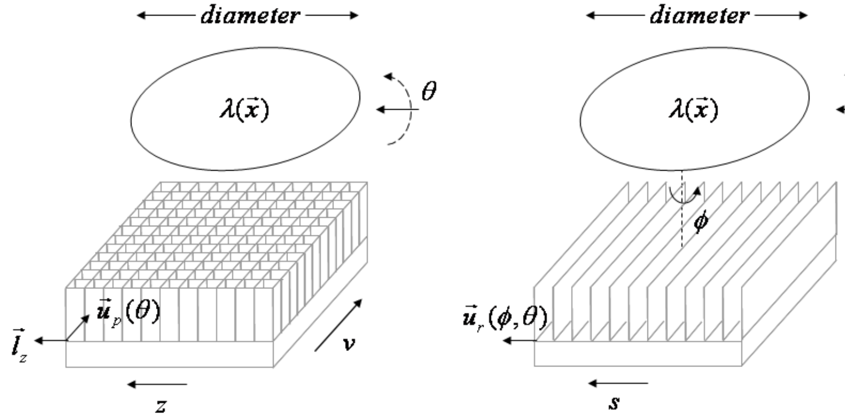
diameter
$\lambda(\vec{x})$
θ
$\vec{u}_p(\theta)$
$\vec{l}_z$
v
z
diameter
$\lambda(\vec{x})$
θ
ϕ
$\vec{u}_r(\phi,\theta)$
s

(a) (b)

Figure D.1: Volume imaging a) with the PH collimator, b) with the RS collimator.

D.1 Parallel hole collimator

For volume imaging, the collimator and the gamma camera rotate around the axis of rotation $\vec{l_z}$ to obtain complete tomographic data. For PH, the data is denoted as $y_p(v, \theta, z)$ where v and θ are the usual sinogram coordinates in a slice, and z is the axial coordinate of that slice. In the first approximation, we neglect the distance-dependence of the collimator blurring, and model the 2-D blurring of the detected projection image as a 2-D convolution of the line-integral image with a 2-D Gaussian PSF with standard deviation σ_p. The measurement is again scaled by the geometric efficiency E_p and the acquisition time T_p:

$$\begin{aligned} y_p(v,\theta,z) &= T_p \times E_p \times \big(y_{p0}(v,\theta,z) \otimes G_2(v,z,\sigma_p)\big) \\ &= T_p E_p \int_{\mathbb{R}^2} y_{p0}(v-v',\theta,z-z') \frac{1}{2\pi\sigma_p^2} e^{-(v'^2+z'^2)/2\sigma_p^2} dv'dz' \end{aligned} \tag{D.1}$$

where $y_{p0}(v, \theta, z)$ denotes the unblurred 2-D Radon transform of $\lambda(\vec{x}) = \lambda(x, y, z)$ in slice z

$$y_{p0}(v,\theta,z) = \int_{\mathbb{R}^3} d\vec{x} \lambda(\vec{x}) \delta(\vec{x} \cdot \vec{l}_z - z) \delta(\vec{x} \cdot \vec{u}_p(\theta) - v) \tag{D.2}$$

where $\vec{u}_p(\theta)$ is a unit vector orthogonal to the integration line in the slice:

$$\vec{u}_p(\theta) = (-\sin\theta, \cos\theta, 0) \tag{D.3}$$

With $\theta \in [0, 2\pi)$, the acquisition time per unit rotation angle is

$$T_p = T/2\pi \tag{D.4}$$

We assume Poisson noise on $y_p(v, \theta, z)$, the covariance in $y_p(v, \theta, z)$ is

$$\mathrm{Cov}(y_p(v,\theta,z), y_p(v',\theta',z')) = y_p(v,\theta,z)\delta(v-v')\delta(\theta-\theta')\delta(z-z') \tag{D.5}$$

We aim to have an estimate $\lambda_{tp}(\vec{x})$ of $\lambda(\vec{x})$ with a target resolution corresponding to a 3-D Gaussian PSF of standard deviation σ_t, for some fixed $\sigma_t > \sigma_p$:

$$\lambda_{tp}(\vec{x}) = \int_{\mathbb{R}^3} \lambda(\vec{x} - \vec{y}) \frac{1}{(2\pi\sigma_t)^{3/2}} e^{-|\vec{y}|^2/2\sigma_t^2} d\vec{y} \tag{D.6}$$

Note that in the Fourier space, (D.1) becomes

$$\tilde{y}_p(\nu,\theta,\nu_z) = T_p E_p \, \tilde{y}_{p0}(\nu,\theta,\nu_z) e^{-2\pi^2\sigma_p^2(\nu^2+\nu_z^2)} \tag{D.7}$$

where ν is the frequency conjugate to the radial sinogram variable v, and ν_z is the axial frequency conjugate to z. The filtered-backprojection algorithm reconstructs the image λ from the ideal data y_{p0} by ramp filtering y_{p0} and back-projecting. To reconstruct the target image λ_{tp}, the ramp filter must be multiplied by the low-pass window $e^{-2\pi^2\sigma_t^2(\nu^2+\nu_z^2)}$. This simple result is due to the separability of the multi-dimensional Gaussian and to the fact that the 1-D apodizing filter multiplying the ramp filter is converted into the target 2-D radial filter by the backprojection (the central section theorem). Meanwhile, in view of (D.7), we first need to deconvolve the collimator blurring by applying a filter $e^{+2\pi^2\sigma_p^2(\nu^2+\nu_z^2)}$ to the data y_p to recover

y_{p0} before adopting the low-pass window. All these lead to the conclusion that λ_{tp} is reconstructed by applying the FBP algorithm to the data y_p.

$$\begin{aligned}\lambda_{tp}(\vec{x}) &= \frac{1}{2T_pE_p}\int_0^{2\pi} d\theta \int_{\mathbb{R}} dv \int_{\mathbb{R}} dz y_p(\vec{x}\cdot\vec{u}_p(\theta)-v,\theta,\vec{x}\cdot\vec{l}_z-z)h_p(v,z)\\ &= \frac{1}{2T_pE_p}\int_0^{2\pi} d\theta \, [y_p(v,\theta,z)\otimes h_p(v,z)]_{v=\vec{x}\cdot\vec{u}_p(\theta),z=\vec{x}\cdot\vec{l}_z}\end{aligned} \tag{D.8}$$

where each projection measured at a camera position θ is convolved with a 2-D kernel $h_p(v,z)$ equal to the inverse 2-D Fourier transform of $|\nu|e^{-2\pi^2(\sigma_t^2-\sigma_p^2)(\nu^2+\nu_z^2)}$:

$$h_p(v,z) = \int_{\mathbb{R}} d\nu \int_{\mathbb{R}} d\nu_z |\nu| e^{-2\pi^2(\sigma_t^2-\sigma_p^2)(\nu^2+\nu_z^2)} e^{+2\pi i(\nu v+\nu_z z)} \tag{D.9}$$

The variance of this estimate $\lambda_{tp}(\vec{x})$ is:

$$\begin{aligned}&\mathrm{Var}(\lambda_{tp}(\vec{x}))\\ &= \frac{1}{4(T_pE_p)^2}\int_0^{2\pi} d\theta \int_{\mathbb{R}} dv \int_{\mathbb{R}} dz \int_0^{2\pi} d\theta' \int_{\mathbb{R}} dv' \int_{\mathbb{R}} dz' h_p(v,z)h_p(v',z')\\ &\times\ \mathrm{Cov}(y_p(\vec{x}\cdot\vec{u}_p(\theta)-v,\theta,\vec{x}\cdot\vec{l}_z-z), y_p(\vec{x}\cdot\vec{u}_p(\theta')-v',\theta',\vec{x}\cdot\vec{l}_z-z'))\\ &= \frac{1}{4(T_pE_p)^2}\int_0^{2\pi} d\theta \int_{\mathbb{R}} dv \int_{\mathbb{R}} dz |h_p(v,z)|^2 y_p(\vec{x}\cdot\vec{u}_p(\theta)-v,\theta,\vec{x}\cdot\vec{l}_z-z)\end{aligned} \tag{D.10}$$

For a 3-D homogeneous circular phantom, we can ignore θ since the phantom is symmetrical about the rotation axis. $m_p(\theta,s,z)$ is then approximated as

$$y_p(v,\theta,z) \approx \lambda \times T_p \times E_p \times diameter \tag{D.11}$$

Using Parseval's theorem (see (C.26)), the variance in the central point becomes:

$$\begin{aligned}&\mathrm{Var}(\lambda_{tp}(\vec{x}))\Big|_{\vec{x}=0}\\ &\approx \frac{\lambda \times T_p \times E_p \times diameter}{4(T_pE_p)^2} \times 2\pi \int_{\mathbb{R}} d\nu \int_{\mathbb{R}} d\nu_z |\nu|^2 e^{-4\pi^2(\sigma_t^2-\sigma_p^2)(\nu^2+\nu_z^2)}\\ &= \frac{\lambda \times diameter}{4T_pE_p} \times 2\pi \times \frac{1}{32\pi^3(\sigma_t^2-\sigma_p^2)^2}\\ &= \frac{4\pi D^2\lambda \times diameter}{8\ln 2\sigma_p^2 T} \times \frac{1}{32\pi(\sigma_t^2-\sigma_p^2)^2}\\ &= \frac{D^2\lambda \times diameter}{64\ln 2T\sigma_p^2(\sigma_t^2-\sigma_p^2)^2}\end{aligned} \tag{D.12}$$

To find the minimum of this variance, we derive the denominator $\sigma_p^2(\sigma_t^2-\sigma_p^2)^2$ with respect to σ_p^2 and solve:

$$\frac{d}{d\sigma_p^2}\sigma_p^2(\sigma_t^2-\sigma_p^2)^2 = (\sigma_t^2-\sigma_p^2)(\sigma_t^2-3\sigma_p^2) = 0 \tag{D.13}$$

The solution is $\sigma_p^2 = (1/3)\sigma_t^2$, which means that the collimator aperture should be equal to the target resolution divided by $\sqrt{3}$, i.e.,

$$\sigma_p^{opt} = \sigma_t/\sqrt{3} \tag{D.14}$$

The corresponding minimal variance is:

$$\mathrm{Var}_p^{min} = \frac{27D^2\lambda \times diameter}{256 \ln 2T\sigma_t^6} \tag{D.15}$$

From (D.12), we can also write (D.15) as the function of E_p:

$$\mathrm{Var}_p^{min} = \frac{9\lambda \times diameter}{128\pi T E_p \sigma_t^4} \tag{D.16}$$

D.2 Rotating slat collimator

For volume imaging with the RS collimator, we model the data as the plane integral of the 3-D tracer distribution on the plane orthogonal to the detector, defined by the aperture between two adjacent slats. The acquired data is parametrized as $y_r(s,\phi,\theta)$, where s is the distance between the slat interval and the collimator spinning axis, ϕ is the rotational position of the collimator as it spins on the fixed camera, and θ is the rotational position of the camera around the z axis.

Similar as before, the RS collimator resolution is modeled as a 1-D convolution in s with a Gaussian PSF with standard deviation σ_r. The measurement is scaled by the geometric efficiency E_r and the acquisition time T_r:

$$\begin{aligned} y_r(s,\phi,\theta) &= T_r \times E_r \times \big(y_{r0}(s,\phi,\theta) \otimes G_1(s,\sigma_r)\big) \\ &= T_r E_r \int_{\mathbb{R}} y_{r0}(s-s',\phi,\theta) \frac{1}{\sqrt{2\pi}\sigma_r} e^{-s'^2/2\sigma_r^2} ds' \end{aligned} \tag{D.17}$$

where $y_{r0}(s,\phi,\theta)$ denotes the ideal 3-D Radon transform of $\lambda(\vec{x})$ over the plane $\Pi(\vec{u}_r(\phi,\theta),s)$ that is located at a distance s from the origin of the 3-D coordinate system and orthogonal to a unit vector $\vec{u}_r(\phi,\theta)$

$$y_{r0}(s,\phi,\theta) = \int_{\mathbb{R}^3} d\vec{x}\lambda(\vec{x})\delta(\vec{x}\cdot\vec{u}_r(\phi,\theta) - s) \tag{D.18}$$

with

$$\vec{u}_r(\phi,\theta) = (-\sin\phi\cos\theta, -\sin\phi\sin\theta, \cos\phi) \tag{D.19}$$

Since the gamma camera spins over π and rotates over 2π during the data acquisition, the time T_r at each unit angular position should be

$$T_r = T/(2\pi \times \pi) = T/2\pi^2 \tag{D.20}$$

The covariance matrix on $y_{r0}(s,\phi,\theta)$ due to Poisson noise is

$$\mathrm{Cov}(y_r(s,\phi,\theta), y_r(s',\phi',\theta')) = y_r(s,\phi,\theta)\delta(s-s')\delta(\phi-\phi')\delta(\theta-\theta') \qquad \text{(D.21)}$$

In the Fourier space, (D.17) becomes:

$$\tilde{y}_r(\nu,\phi,\theta) = T_r E_r\, \tilde{y}_{r0}(\nu,\phi,\theta) e^{-2\pi^2\sigma_r^2\nu^2} \qquad \text{(D.22)}$$

The standard filtered-backprojection formula for the inverse 3-D Radon transform is:

$$\lambda(\vec{x}) = \frac{-1}{8\pi^2}\int_{S^2} d\vec{u}_r \Big(\frac{\partial^2 y_{r0}(s,\phi,\theta)}{\partial s^2}\Big)_{s=\vec{x}\cdot\vec{u}_r(\phi,\theta)} \qquad \text{(D.23)}$$

Recall that the second derivative corresponds to the filter $-4\pi^2\nu^2$. Also note that from (D.19) the spinning angle ϕ and the camera rotation angle θ are respectively the polar and the azimuthal angle of the plane normal $\vec{u}_r(\phi,\theta)$(with respect to the camera rotation axis z). Therefore, the surface integration elements on the unit sphere S^2 in (D.23) is $d\vec{u}_r(\phi,\theta) = d\cos\phi d\theta$ and:

$$\lambda(\vec{x}) = \frac{1}{2}\int_0^{2\pi} d\theta \int_{-1}^{1} d\cos\phi \int_{\mathbb{R}} ds\, h(s) y_{r0}(\vec{x}\cdot\vec{u}_r(\phi,\theta) - s,\phi,\theta) \qquad \text{(D.24)}$$

where $h(s)$ is the inverse 2-D Fourier transform of ν^2. Following the same lines as in the previous sections, to reconstruct λ_{tr} we need to apodize the filter by $e^{-2\pi^2\sigma_t^2\nu^2}$ (this is again due to the central section theorem for the 3-D Radon transform). The filter used to reconstruct the ideal data y_{r0} with the target resolution is thus

$$h_{tr}(s) = \int_{\mathbb{R}} d\nu\nu^2 e^{-2\pi^2\sigma_t^2\nu^2} e^{+2\pi i\nu s} \qquad \text{(D.25)}$$

To reconstruct from y_r, which is subject to the collimator blurring (see (D.17)), a factor $e^{+2\pi^2\sigma_r^2\nu^2}$ is needed to deconvolve the PSF of the slat aperture. The reconstruction with target resolution σ_t then becomes:

$$\begin{aligned}\lambda_{tr}(\vec{x}) &= \frac{1}{2}\int_0^{2\pi} d\theta \int_{-1}^{1} d\cos\phi \int_{\mathbb{R}} ds h_{tr}(s) y_{r0}(\vec{x}\cdot\vec{u}_r(\phi,\theta) - s,\phi,\theta) \\ &= \frac{1}{2T_rE_r}\int_0^{2\pi} d\theta \int_{-1}^{1} d\cos\phi \int_{\mathbb{R}} ds h_r(s) y_r(\vec{x}\cdot\vec{u}_r(\phi,\theta) - s,\phi,\theta)\end{aligned} \qquad \text{(D.26)}$$

with

$$h_r(s) = \int_{\mathbb{R}} d\nu\nu^2 e^{-2\pi^2(\sigma_t^2-\sigma_r^2)\nu^2} e^{+2\pi i\nu s} = \int_{\mathbb{R}} d\nu \tilde{h}_r(\nu) e^{+2\pi i\nu s} \qquad \text{(D.27)}$$

The variance of this estimate $f_{tr}(\vec{x})$ is:

$$\begin{aligned}
&\mathrm{Var}(\lambda_{tr}(\vec{x})) \\
&= \frac{1}{4(T_rE_r)^2}\int_0^{2\pi} d\theta \int_0^{\pi} d\phi \int_{\mathbb{R}} ds \int_0^{2\pi} d\theta' \int_0^{\pi} d\phi' \int_{\mathbb{R}} ds' \sin\phi \sin\phi' h_r(s)h_r(s') \\
&\times \mathrm{Cov}(y_r(\vec{x}\cdot\vec{u}_r(\phi,\theta)-s,\phi,\theta), y_r(\vec{x}\cdot\vec{u}_r(\phi,\theta)-s',\phi',\theta')) \\
&= \frac{1}{4(T_rE_r)^2}\int_0^{2\pi} d\theta \int_0^{\pi} d\phi(\sin\phi)^2 \int_{\mathbb{R}} ds|h_r(s)|^2 y_r(\vec{x}\cdot\vec{u}_r(\phi,\theta)-s,\phi,\theta) \qquad \text{(D.28)}
\end{aligned}$$

Due to the symmetry of the 3-D tracer distribution, $y_r(s,\phi,\theta)$ is approximated as

$$y_r(s,\phi,\theta) \approx \lambda \times T_r \times E_r \times \pi(diameter/2)^2 \qquad \text{(D.29)}$$

With Parseval's theorem (see (C.26)), (D.28) becomes:

$$\begin{aligned}
\mathrm{Var}(\lambda_{tr}(\vec{x}))\Big|_{\vec{x}=0} &\approx \frac{\lambda \times T_r \times E_r \times \pi(diameter/2)^2}{4(T_rE_r)^2}\int_0^{2\pi} d\theta \int_0^{\pi} d\phi(\sin\phi)^2 \int_{\mathbb{R}} ds|h_r(s)|^2 \\
&= \frac{\lambda \times \pi \times diameter^2}{16T_rE_r} \times \pi^2 \times \int_{\mathbb{R}} d\nu |\tilde{h}_r(\nu)|^2 \\
&= \frac{\pi^3\lambda \times diameter^2}{16T_rE_r}\int_{\mathbb{R}} d\nu\nu^4 e^{-4\pi^2(\sigma_t^2-\sigma_r^2)\nu^2} \\
&= \frac{4\pi D^2\pi^3\lambda \times diameter^2}{16\Omega_W\sqrt{8\ln 2}\sigma_r T_r} \times \frac{3}{128\pi^{9/2}(\sigma_t^2-\sigma_r^2)^{5/2}} \\
&= \frac{3\pi^{3/2}D^2\lambda \times diameter^2}{256\sqrt{8\ln 2}\Omega_W T\sigma_r(\sigma_t^2-\sigma_r^2)^{5/2}} \qquad \text{(D.30)}
\end{aligned}$$

To find the minimum of this variance, we derive the denominator $\sigma_r(\sigma_t^2-\sigma_r^2)^{5/2}$ with respect to σ_r and solve:

$$\frac{d}{d\sigma_r}\sigma_r(\sigma_t^2-\sigma_r^2)^{5/2} = (\sigma_t^2-\sigma_r^2)^{5/2} - 5\sigma_r^2(\sigma_t^2-\sigma_r^2)^{3/2} = (\sigma_t^2-\sigma_r^2)^{3/2}(\sigma_t^2-6\sigma_r^2) = 0 \qquad \text{(D.31)}$$

The solution is $\sigma_r^2 = (1/6)\sigma_t^2$, which means that the slat aperture should be equal to the target resolution divided by $\sqrt{6}$.

$$\sigma_r^{opt} = \sigma_t/\sqrt{6} \qquad \text{(D.32)}$$

And the minimal variance is:

$$\mathrm{Var}_r^{min} = \frac{81\pi^{3/2}D^2\lambda \times diameter^2}{1600\sqrt{10\ln 2}\Omega_W T\sigma_t^6} \qquad \text{(D.33)}$$

From (D.30), we can also write (D.33) as the function of E_r:

$$\mathrm{Var}_r^{min} = \frac{27\sqrt{3\pi}\lambda \times diameter^2}{3200\sqrt{10}TE_r\sigma_t^5} \qquad \text{(D.34)}$$

D.3 Comparison between PH and RS

Similar as planar imaging, for the same tracer distribution, the same acquisition time and the same target resolution, the gain in the variance is:

$$\begin{aligned}
\mathrm{Gain}^{\mathrm{opt}} &= \sqrt{\frac{\mathrm{Var}_p^{min}}{\mathrm{Var}_r^{min}}} \\
&= \sqrt{\frac{27D^2\lambda \times diameter}{256\ln 2T\sigma_t^6} \times \frac{1600\sqrt{10\ln 2}\Omega_W T\sigma_t^6}{81\pi^{3/2}D^2\lambda \times diameter^2}} \\
&= \sqrt{\frac{5^{5/2}\Omega_W}{6\sqrt{2\ln 2}\pi^{3/2} \times diameter}} \\
&= \frac{5^{5/4}}{\sqrt{6}\pi^{3/4}(2\ln 2)^{1/4}} \times \sqrt{\frac{\Omega_W}{diameter}} \\
&= 1.192\sqrt{\frac{\Omega_W}{diameter}} \qquad \text{(D.35)}
\end{aligned}$$

With the minimal variance (D.16) and (D.34), if we define the gain of geometric efficiency as $F = E_r/E_p$, we can also write the gain as the function of F:

$$\begin{aligned}
\mathrm{Gain}^{\mathrm{opt}} &= \sqrt{\frac{\mathrm{Var}_p^{min}}{\mathrm{Var}_r^{min}}} \\
&= \sqrt{\frac{9\lambda \times diameter}{128\pi T E_p\sigma_t^4} \times \frac{3200\sqrt{10}T E_r\sigma_t^5}{27\sqrt{3\pi}\lambda \times diameter^2}} \\
&= \sqrt{\frac{E_r}{E_p} \times \frac{2^{1/2}5^{5/2}\sigma_t}{(3\pi)^{3/2} \times diameter}} \\
&= \frac{2^{1/4}5^{5/4}}{(3\pi)^{3/4}}\sqrt{\frac{F\sigma_t}{diameter}} \\
&= 1.653\sqrt{\frac{F\sigma_t}{diameter}} \qquad \text{(D.36)}
\end{aligned}$$

with

$$F = \frac{\sigma_r\sqrt{8\ln 2}\Omega_W/4\pi D^2}{\sigma_p^2 8\ln 2/4\pi D^2} = \frac{\Omega_W}{\sqrt{8\ln 2}} \times \frac{\sigma_r}{\sigma_p^2} = \frac{\sqrt{6}\Omega_W}{2\sqrt{8\ln 2}\sigma_t} \qquad \text{(D.37)}$$

Appendix E

Point-to-line distance

In this appendix, we calculate the distance ($S_{iq}(k_\theta)$) between the reconstructed point $X_q^R = [x_q^R, y_q^R, z_q^R]^T$ and the back-projection ray which is the intersection of two planes described by (5.23) and (5.24):

$$\begin{aligned} a_{uiq}(k_\theta)x_q + b_{uiq}(k_\theta)y_q + c_{uiq}(k_\theta)z_q + d_{uiq}(k_\theta) = 0 \\ a_{viq}(k_\theta)x_q + b_{viq}(k_\theta)y_q + c_{viq}(k_\theta)z_q + d_{viq}(k_\theta) = 0 \end{aligned}$$

with i and k_θ the index of pinhole aperture and the index of the projection angle, respectively.

Step 1: calculate the vector of the line. The norm vectors of the two planes are $V_1 = [a_{uiq}, b_{uiq}, c_{uiq}]$ and $V_2 = [a_{viq}, b_{viq}, c_{viq}]$. The vector along the projection ray is the cross product of these two vectors:

$$V_p = V_1 \times V_2 \tag{E.1}$$

Step 2: find an arbitrary point X_r on the line. In order to calculate the point-to-line distance, first we need to find an arbitrary point $X_r = [x_r, y_r, z_r]^T$ on the line (= projection ray). To do that, we need to solve

$$a_u x_r + b_u y_r + c_u z_r + d_u = 0 \tag{E.2}$$

$$a_v x_r + b_v y_r + c_v z_r + d_v = 0 \tag{E.3}$$

Note that here we drop the indices of the pinhole aperture (i), the point source (q) and the projection angle (k_θ) for convenience.

To stabilize the solution, we first check $V_p = [v_p^x, v_p^y, v_p^z]$ to see along which dimension it has the largest component. That dimension is set to zero in (E.2) and (E.3). For example, if the largest component is v_p^x, we set $x_r = 0$ in (E.2) and (E.3) and solve for y_r and z_r to obtain

$$y_r = \frac{c_v d_u - c_u d_v}{c_u b_v - c_v b_u} \tag{E.4}$$

$$z_r = \frac{b_u d_v - b_v d_u}{c_u b_v - c_v b_u} \tag{E.5}$$

Step 3: calculate the point-to-line distance. We denote the projection of X_q^R on the line as X_c. As shown in Fig. E.1, we define

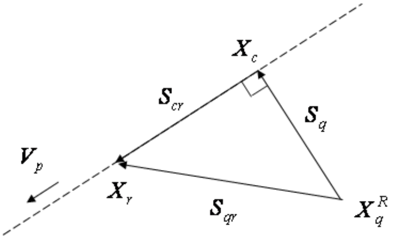

Figure E.1: Notations used to calculate the point-to-line distance.

$$S_{qr} = X_r - X_q^R \tag{E.6}$$

$$S_{cr} = X_r - X_c \tag{E.7}$$

S_{qr} can be directly calculated since we know X_q^R and X_r. S_{cr} is actually the projection of S_{qr} along V_p, i.e.,

$$S_{cr} = \left(S_{qr} \cdot \frac{V_p}{\|V_p\|} \right) \cdot \frac{V_p}{\|V_p\|} \tag{E.8}$$

With (E.6) and (E.8), we can calculate the point-to-line distance $S_q = [s_q^x, s_q^y, s_q^z]^T$:

$$S_q = S_{qr} - S_{cr} \tag{E.9}$$

Appendix F

Independent noise components

Assume the $K \times 1$ matrix ΔP is a sample from a distribution with zero mean and known covariance matrix $\mathrm{Cov}(P)$. We wish to compute the variance on the value $H^T \Delta P$, where H is a linear operator ($K \times 1$ matrix). Here we show how $\mathrm{Var}(H^T \Delta P) = H^T \mathrm{cov}(P) H$ can be computed as the sum of K independent contributions.

With the matrix decomposition described in [21], the covariance matrix of the parameters $\mathrm{Cov}(P)$ can be expressed as

$$\mathrm{cov}(P) = \Gamma\Gamma^T \tag{F.1}$$

The noise components in the $k-$th column can be extracted by $\Delta P_k = \Gamma e_k$, with e_k the $k-$th unit vector. The variation ΔP_k can be linked to the measure of the reconstruction error by the linear operator H. This measure is thus $H^T \Delta P_k$, with squared value

$$\begin{aligned} (H^T \Delta P_k)^2 &= H^T \Delta P_k \Delta P_k^T H \\ &= H^T \Gamma e_k e_k^T \Gamma^T H \end{aligned} \tag{F.2}$$

Adding all the distributions quadratically, it yields:

$$\begin{aligned} \sum_{k=1}^{K} (H^T \Delta P_k)^2 &= \sum_{k=1}^{K} (H^T \Gamma e_k e_k^T \Gamma^T H) \\ &= \sum_{k=1}^{K} H^T \Gamma (e_k e_k^T) \Gamma^T H \\ &= H^T \Gamma I \Gamma^T H \\ &= H^T \mathrm{cov}(P) H \end{aligned} \tag{F.3}$$

where I is the identity matrix.

Bibliography

[1] C. K. Abbey, H. H. Barrett, and D. W. Wilson. Observer signal-to-noise ratios for the ML-EM algorithm. In *Proc. Soc. Photo. Opt. Instrum. Eng.*, volume 2712, pages 47–58, 1996.

[2] R. Accorsi and S. D. Metzler. Analytic determination of the resolution-equivalent effective diameter of a pinhole collimator. *IEEE Trans. Med. Imag.*, 23(6):750–763, 2004.

[3] R. Accorsi, J. R. Novak, A. S. Ayan, and S. D. Metzler. Derivation and validation of a sensitivity formula for slit-slat collimation. *IEEE Trans. Med. Imag.*, 27(5):709–722, 2008.

[4] S. Alenius and U. Ruotsalainen. Bayesian image reconstruction for emission tomography based on median root prior. *Eur. J. Nucl. Med. Mol. Imaging*, 24(3):258–265, 1997.

[5] N. M. Alpert, D. A. Chesler, J. A. Correia, R. H. Ackerman, J. Y. Chang, S. Finklestein, S. M. Davis, G. L. Brownell, and J. M. Taveras. Estimation of the local statistical noise in emission computed tomography. *IEEE Trans. Med. Imag.*, MI-1(2):142–146, 1982.

[6] H. O. Anger. Scintillation camera with multichannel collimators. *J. Nucl. Med.*, 5(7):515–531, 1964.

[7] B. A. Ardekani, M. Braun, B. F. Hutton, I. Kanno, and H. Iida. Minimum cross-entropy reconstruction of PET images using prior anatomical information. *Phys. Med. Biol.*, 41:2497–2517, 1996.

[8] A. Atre, K. Vunckx, K. Baete, A. Reilhac, and J. Nuyts. Evaluation of different MRI-based anatomical priors for PET brain imaging. In *Conference Record of the IEEE Nucl. Sci. Symp. and Med. Imag. Conf.*, Orlando, Florida, USA, 2009.

[9] K. Baete, J. Nuyts, W. Van Paesschen, P. Suetens, and P. Dupont. Anatomical based FDG-PET reconstruction for the detection of hypo-metabolic regions in epilepsy. *IEEE Trans. Med. Imag.*, 23(4):510–519, 2004.

[10] G. Bal and P. D. Acton. Analytical derivation of the point spread function for pinhole collimators. *Phys. Med. Biol.*, 51:4923–4950, 2006.

[11] R. Bar-Shalom, N. Yefremov, L. Guralnik, Z. Keidar, A. Engel, S. Nitecki, and O. Israel. SPECT/CT using ^{67}Ga and ^{111}In-labeled leukocyte scintigraphy for diagnosis of infection. *J. Nucl. Med.*, 47(4):587–594, 2006.

[12] H. H. Barrett. Objective assessment of image quality: effects of quantum noise and object variability. *J. Opt. Soc. Am. A*, 7(7):1266–1278, 1990.

[13] H. H. Barrett, J. L. Denny, R. F. Wagner, and K. J. Myers. Objective assessment of image quality. II. Fisher information, Fourier crosstalk, and figures of merit for task performance. *J. Opt. Soc. Am. A*, 12(5):834–852, 1995.

[14] H. H. Barrett and K. Myers. *Foundations of image science.* John Wiley & Sons, 2003.

[15] H. H. Barrett, D. W. Wilson, and B. M. W. Tsui. Noise properties of the EM algorithm: I. Theory. *Phys. Med. Biol.*, 39(3):451–476, 1994.

[16] H. H. Barrett, J. Yao, J. P. Rolland, and K. J. Myers. Model observers for assessment of image quality. *Proc. Natl. Acad. Sci. USA*, 90(21):9758–9765, 1993.

[17] J. W. Beck, R. J. Jaszczak, R. E. Coleman, C. F. Starmer, and L. W. Nolte. Analysis of SPECT including scatter and attenuation using sophisticated Monte Carlo modeling methods. *IEEE Trans. Nucl. Sci.*, 29(1):506–511, 1982.

[18] F. J. Beekman and B. Vastenhouw. Design and simulation of a high-resolution stationary SPECT system for small animals. *Phys. Med. Biol.*, 49(19):4579–4592, 2004.

[19] D. Bequé. MicroSPECT imaging of small laboratory animals. In *Ph.D. thesis*, Katholieke Universiteit Leuven, Belgium, 2005.

[20] D. Bequé, J. Nuyts, G. Bormans, P. Suetens, and P. Dupont. Characterization of acquisition geometry of pinhole SPECT. *IEEE Trans. Med. Imag.*, 22(5):599–612, 2003.

[21] D. Bequé, J. Nuyts, P. Suetens, and G. Bormans. Optimization of geometrical calibration in pinhole SPECT. *IEEE Trans. Med. Imag.*, 24(2):180–190, 2005.

[22] M. Bhatia, W. C. Karl, and A. S. Willsky. A wavelet-based method for multiscale tomographic reconstruction. *IEEE Trans. Med. Imag.*, 15(1):92–101, 1996.

[23] N. Boussion, M. Hatt, F. Lamare, Y. Bizais, A. Turzo, C. Cheze-Le Rest, and D. Visvikis. A multiresolution image based approach for correction of partial volume effects in emission tomography. *Phys. Med. Biol.*, 51:1857–1876, 2006.

[24] J. E. Bowsher, V. E. Johnson, T. G. Turkington, R. J. Jaszczak, C. E. Floyd, and R. E. Coleman. Bayesian reconstruction and use of anatomical a priori information for emission tomography. *IEEE Trans. Med. Imag.*, 15(5):673–686, 1996.

[25] J. E. Bowsher, J. E. Yuan, L. W. Hedlund, T. G. Turkington, G. Akabani, A. Badea, W. C. Kruylo, C. T. Wheeler, G. P. Cofer, M. W. Dewhirst, and G. A. Johnson. Utilizing MRI information to estimate F18-FDG distributions in rat flank tumors. In *Conference Record of the IEEE Nucl. Sci. Symp. and Med. Imag. Conf.*, volume M2-157, Rome, Italy, 2004.

[26] J. F. Butler, C. L. Lingren, S. J. Friesenhahn, F. P. Doty, W. L. Ashburn, R. L. Conwell, F. L. Augustine, B. Apotovsky, B. Pi, T. Collins, S. Zhao, and C. Isaacson. CdZnTe solid-state gamma camera. *IEEE Trans. Nucl. Sci.*, 45(3):359–363, 1998.

[27] I. Buvat and I. Castiglioni. Monte Carlo simulations in SPET and PET. *Q. J. Nucl. Med*, 46(1):48–61, 2002.

[28] C. L. Byrne. Accelerating the EMML algorithm and related iterative algorithms by rescaled block-iterative methods. *IEEE Trans. Image Proc.*, 7(1):100–109, 1998.

[29] R. E. Carson, Y. Yan, B. Chodkowski, T. K. Yap, and M. E. Daube-Witherspoon. Precision and accuracy of regional radioactivity quantitation using the maximum likelihood EM reconstruction algorithm. *IEEE Trans. Med. Imag.*, 13(3):526–537, 1994.

[30] M. D. Cerqueira, D. Matsuoka, J. L. Ritchie, and G. D. Harp. The influence of collimators on spect center of rotation measurements: artifact generation and acceptance testing. *J. Nucl. Med.*, 29(8):1393–1397, 1988.

[31] Y. Choi, J. Y. Koo, and N. Y. Lee. Image reconstruction using the wavelet transform for positron emission tomography. *IEEE Trans. Med. Imag.*, 20(11):1188–1193, 2001.

[32] C. Cloquet, S. Goldman, and M. Defrise. Cramer-Rao bound for gated PET. In *Conference Record of the IEEE Nucl. Sci. Symp. and Med. Imag. Conf.*, Knoxville, Tennessee, USA, 2010.

[33] H. Cramér. *Mathematical methods of statistics.* Princeton University Press, 1946.

[34] M. Defrise and R. Clack. A cone-beam reconstruction algorithm using shift-variant filtering and cone-beam backprojection. *IEEE Trans. Med. Imag.*, 13(1):186–195, 1994.

[35] M. Defrise, D. W. Townsend, and F. Deconinck. Statistical noise in three-dimensional positron tomography. *Phys. Med. Biol.*, 35(1):131–138, 1990.

[36] M. Defrise, C. Vanhove, and J. Nuyts. Perturbative refinement of the geometric calibration in pinhole SPECT. *IEEE Trans. Med. Imag.*, 27(2):204–214, 2008.

[37] A. H. Delaney and Y. Bresler. Multiresolution tomographic reconstruction using wavelets. *IEEE Trans. Image Proc.*, 4(6):799–813, 1995.

[38] F. P. DiFilippo. Design and performance of a multi-pinhole collimation device for small animal imaging with clinical SPECT and SPECT-CT scanners. *Phys. Med. Biol.*, 53(15):4185–4201, 2008.

[39] F. P. DiFilippo. Geometric characterization of multi-axis multi-pinhole SPECT. *Med. Phys.*, 35(1):181–194, 2008.

[40] F. P. DiFilippo, M. J. Riffe, K. M. Harsch, N. P. McCabe, and W. D. Heston. Detached multipinhole small animal SPECT device with real-time calibration. *IEEE Trans. Nucl. Sci.*, 53(5):2605–2612, 2006.

[41] L. Elmbt and S. Walrand. Simultaneous correction of attenuation and distance-dependent resolution in SPECT: an analytical approach. *Phys. Med. Biol.*, 38:1207–1217, 1993.

[42] H. Erdoğan and J. A. Fessler. Ordered subsets algorithms for transmission tomography. *Phys. Med. Biol.*, 44:2835–2851, 1999.

[43] J. A. Fessler. Mean and variance of implicitly defined biased estimators (such as penalized maximum likelihood): Applications to tomography. *IEEE Trans. Image Proc.*, 5(3):493–506, 1996.

[44] J. A. Fessler. Spatial resolution and noise tradeoffs in pinhole imaging system design: a density estimation approach. *Optics Express*, 2(6):237–253, 1998.

[45] J. A. Fessler. Analytical approach to regularization design for isotropic spatial resolution. In *Conference Record of the IEEE Nucl. Sci. Symp. and Med. Imag. Conf.*, volume 3, pages 2022–2026, Portland, Oregon, USA, 2003.

[46] J. A. Fessler and W. L. Rogers. Spatial resolution properties of penalized-likelihood image reconstruction: space-invariant tomographs. *IEEE Trans. Image Proc.*, 5(9):1346–1358, 1996.

[47] T. Frese, C. A. Bouman, and K. Sauer. Adaptive wavelet graph model for Bayesian tomographic reconstruction. *IEEE Trans. Image Proc.*, 11(7):756–770, 2002.

[48] D. Gagnon, G. L. Zeng, J. M. Links, J. J. Griesmer, and F. C. Valentino. Design considerations for a new solid-state gamma-camera SOLSTICE. In *Conference Record of the IEEE Nucl. Sci. Symp. and Med. Imag. Conf.*, volume 2, pages 1156–1160, Norfolk, Virginia, USA, 2002.

[49] S. Geman and D. Geman. Stochastic relaxation, Gibbs distributions, and the Bayesian restoration of images. *IEEE Trans. Pattern Anal. Machine Intell.*, PAMI-6(6):721–741, 1984.

[50] H. C. Gifford, M. A. King, D. J. de Vries, and E. J. Soares. Channelized Hotelling and human observer correlation for lesion detection in hepatic SPECT imaging. *J. Nucl. Med.*, 41(3):514–521, 2000.

[51] G. Gindi, M. Lee, A. Rangarajan, and G. Zubal. Bayesian reconstruction of functional images using anatomical information as priors. *IEEE Trans. Med. Imag.*, 12(4):670–680, 1993.

[52] S. J. Glick, B. C. Penney, M. A. King, and C. L. Byrne. Noniterative compensation for the distance-dependent detector response and photon attenuation in SPECT imaging. *IEEE Trans. Med. Imag.*, 13(2):363–374, 1994.

[53] P. J. Green. Bayesian reconstructions from emission tomography data using a modified EM algorithm. *IEEE Trans. Med. Imag.*, 9(1):84–93, 1990.

[54] G. T. Gullberg, B. M. W. Tsui, C. R. Crawford, J. G. Ballard, and J. T. Hagius. Estimation of geometrical parameters and collimator evaluation for cone beam tomography. *Med. Phys.*, 17(2):264–272, 1990.

[55] G. T. Gullberg and G. L. Zeng. A cone-beam filtered backprojection reconstruction algorithm for cardiac single photon emission computed tomography. *IEEE Trans. Med. Imag.*, 11(1):91–101, 1992.

[56] R. G. Helmer, R. L. Heath, M. Putnam, and D. H. Gipson. Photopeak analysis program for photon energy and intensity determinations: Ge (Li) and NaI (Tl) spectrometers. *Nuclear Instruments and Methods*, 57:46–57, 1967.

[57] A. Hero and J. A. Fessler. A recursive algorithm for computing Cramer-Rao-type bounds on estimator covariance. *IEEE Trans. Information Theory*, 40(4):1205–1210, 1994.

[58] E. J. Hoffman, S. C. Huang, and M. E. Phelps. Quantitation in positron emission computed tomography: 1. effect of object size. *J. Comput. Assist. Tomogr.*, 3(3):299–308, 1979.

[59] R. Van Holen, S. Vandenberghe, S. Staelens, and I. Lemahieu. Comparing planar image quality of rotating slat and parallel hole collimation: influence of system modeling. *Phys. Med. Biol.*, 53:1989–2002, 2008.

[60] R. Van Holen, S. Vandenberghe, S. Staelens, and I. Lemahieu. Comparison of 3D SPECT imaging with a rotating slat collimator and a parallel hole collimator. In *Conference Record of the IEEE Nucl. Sci. Symp. and Med. Imag. Conf.*, pages 4592–4597, Dresden, Germany, 2008.

[61] S. Hoppe, F. Noo, F. Dennerlein, G. Lauritsch, and J. Hornegger. Geometric calibration of the circle-plus-arc trajectory. *Phys. Med. Biol.*, 52:6943–6960, 2007.

[62] I. T. Hsiao, A. Rangarajan, P. Khurd, and G. Gindi. An accelerated convergent ordered subsets algorithm for emission tomography. *Phys. Med. Biol.*, 49:2145–2156, 2004.

[63] T. Hsiao and G. Gindi. Noise propagation from attenuation correction into PET reconstructions. *IEEE Trans. Nucl. Sci.*, 49(1):90–97, 2002.

[64] H. M. Hudson and R. S. Larkin. Accelerated image reconstruction using ordered subsets of projection data. *IEEE Trans. Med. Imag.*, 13(4):601–609, 1994.

[65] R. J. Jaszczak, C. E. Floyd, and R. E. Coleman. Scatter compensation techniques for SPECT. *IEEE Trans. Nucl. Sci.*, 32(1):786–793, 1985.

[66] R. J. Jaszczak, C. E. Floyd Jr, S. H. Manglos, K. L. Greer, and R. E. Coleman. Cone beam collimation for single photon emission computed tomography: analysis, simulation, and image reconstruction using filtered backprojection. *Med. Phys.*, 13:484–489, 1986.

[67] R. M. Kessler, J. R. Ellis, and M. Eden. Analysis of emission tomographic scan data: limitations imposed by resolution and background. *J. Comput. Assist. Tomogr.*, 8(3):514–522, 1984.

[68] K. F. Koral, X. Wang, W. L. Rogers, N. H. Clinthorne, and X. Wang. SPECT Compton-scattering correction by analysis of energy spectra. *J. Nucl. Med.*, 29(2):195–202, 1988.

[69] S. Kulkarni, P. Khurd, T. Hsiao, L. Zhou, and G. Gindi. A channelized Hotelling observer study of lesion detection in SPECT MAP reconstruction using anatomical priors. *Phys. Med. Biol.*, 52:3601–3617, 2007.

[70] K. Lange and J. A. Fessler. Globally convergent algorithms for maximum a posteriori transmission tomography. *IEEE Trans. Image Proc.*, 4(10):1430–1438, 1995.

[71] J. Li, R. J. Jaszczak, K. L. Greer, and R. E. Coleman. A filtered backprojection algorithm for pinhole SPECT with a displaced centre of rotation. *Phys. Med. Biol.*, 39:165–176, 1994.

[72] J. Li, R. J. Jaszczak, H. Wang, K. L. Greer, and R. E. Coleman. Determination of both mechanical and electronic shifts in cone beam SPECT. *Phys. Med. Biol.*, 38:743–754, 1993.

[73] C. B. Lim, L. T. Chang, and R. J. Jaszczak. Performance analysis of three camera configurations for single photon emission computed tomography. *IEEE Trans. Nucl. Sci.*, 27(1):559–568, 1980.

[74] M. Ljungberg, M. A. King, G. J. Hademenos, and S. E. Strand. Comparison of four scatter correction methods using Monte Carlo simulated source distributions. *J. Nucl. Med.*, 35(1):143–151, 1994.

[75] M. Ljungberg and S. E. Strand. Scatter and attenuation correction in SPECT using density maps and Monte Carlo simulated scatter functions. *J. Nucl. Med.*, 31(9):1560–1567, 1990.

[76] M. A. Lodge, D. M. Binnie, M. A. Flower, and S. Webb. The experimental evaluation of a prototype rotating slat collimator for planar gamma camera imaging. *Phys. Med. Biol.*, 40:427–448, 1995.

[77] M. A. Lodge, S. Webb, M. A. Flower, and D. M. Binnie. A prototype rotating slat collimator for single photon emission computed tomography. *IEEE Trans. Med. Imag.*, 15(4):500–511, 1996.

[78] S. T. Mahmood, K. Erlandsson, I. Cullum, and B. F. Hutton. Design of a novel slit-slat collimator system for SPECT imaging of the human brain. *Phys. Med. Biol.*, 54:3433–3449, 2009.

[79] K. V. Mardia, J. T. Kent, and J. M. Bibby. *Multivariate analysis.* Academic press, 1979.

[80] S. R. Meikle, P. Kench, A. G. Weisenberger, R. Wojcik, M. F. Smith, S. Majewski, S. Eberl, R. R. Fulton, A. B. Rosenfeld, and M. J. Fulham. A prototype coded aperture detector for small animal SPECT. *IEEE Trans. Nucl. Sci.*, 49(5):2167–2171, 2002.

[81] J. L. Melsa and D. L. Cohn. *Decision and estimation theory.* McGraw-Hill New York, 1978.

[82] L. J. Meng and N. Li. A vector uniform Cramer-Rao bound for SPECT system design. *IEEE Trans. Nucl. Sci.*, 56(1):81–90, 2009.

[83] C. Mennessier, R. Clackdoyle, and F. Noo. Direct determination of geometric alignment parameters for cone-beam scanners. *Phys. Med. Biol.*, 54:1633–1660, 2009.

[84] C. E. Metz. ROC methodology in radiologic imaging. *Invest. Radiol.*, 21(9):720–733, 1986.

[85] S. D. Metzler, J. E. Bowsher, K. L. Greer, and R. J. Jaszczak. Analytic determination of the pinhole collimator's point-spread function and RMS resolution with penetration. *IEEE Trans. Med. Imag.*, 21(8):878–887, 2002.

[86] S. D. Metzler, J. E. Bowsher, M. F. Smith, and R. J. Jaszczak. Analytic determination of pinhole collimator sensitivity with penetration. *IEEE Trans. Med. Imag.*, 20(8):730–741, 2001.

[87] S. D. Metzler, K. L. Greer, and R. J. Jaszczak. Determination of mechanical and electronic shifts for pinhole SPECT using a single point source. *IEEE Trans. Med. Imag.*, 24(3):361–370, 2005.

[88] S. D. Metzler and N. H. Patil. Measuring the variation in radius of rotation as a function of gantry angle for ultra-high-resolution pinhole SPECT. *IEEE Trans. Nucl. Sci.*, 52(2):1236–1242, 2005.

[89] R. A. Moyer. A low-energy multihole converging collimator compared with a pinhole collimator. *J. Nucl. Med.*, 15(2):59–64, 1974.

[90] G. Muehllehner, J. Dudek, and R. Moyer. Influence of hole shape on collimator performance. *Phys. Med. Biol.*, 21:242, 1976.

[91] E. Ü. Mumcuoğlu, R. M. Leahy, and S. R. Cherry. Bayesian reconstruction of PET images: methodology and performance analysis. *Phys. Med. Biol.*, 41:1777–1807, 1996.

[92] K. J. Myers and H. H. Barrett. Addition of a channel mechanism to the ideal-observer model. *J. Opt. Soc. Am. A*, 4(12):2447–2457, 1987.

[93] T. K. Narayan and G. T. Herman. Prediction of human observer performance by numerical observers: an experimental study. *J. Opt. Soc. Am. A*, 16(3):679–693, 1999.

[94] F. Noo, R. Clackdoyle, C. Mennessier, T. A. White, and T. J. Roney. Analytic method based on identification of ellipse parameters for scanner calibration in cone-beam tomography. *Phys. Med. Biol.*, 45(11):3489–3508, 2000.

[95] J. R. Novak, A. S. Ayan, R. Accorsi, and S. D. Metzler. Verification of the sensitivity and resolution dependence on the incidence angle for slit–slat collimation. *Phys. Med. Biol.*, 53:953–966, 2008.

[96] J. Nuyts. The use of mutual information and joint entropy for anatomical priors in emission tomography. In *Conference Record of the IEEE Nucl. Sci. Symp. and Med. Imag. Conf.*, volume 6, pages 4149–4154, Honolulu, Hawaii, USA, 2007.

[97] J. Nuyts, D. Bequé, P. Dupont, and L. Mortelmans. A concave prior penalizing relative differences for maximum-a-posteriori reconstruction in emission tomography. *IEEE Trans. Nucl. Sci.*, 49(1):56–60, 2002.

[98] J. Nuyts and J. A. Fessler. A penalized-likelihood image reconstruction method for emission tomography, compared to postsmoothed maximum-likelihood with matched spatial resolution. *IEEE Trans. Med. Imag.*, 22(9):1042–1052, 2003.

[99] J. Nuyts, K. Vunckx, M. Defrise, and C. Vanhove. Small animal imaging with multi-pinhole SPECT. *Methods*, 42(2):83–91, 2009.

[100] K. Ogawa, Y. Harata, T. Ichihara, A. Kubo, and S. Hashimoto. A practical method for position-dependent Compton-scatter correction in single photon emission CT. *IEEE Trans. Med. Imag.*, 10(3):408–412, 1991.

[101] J. Qi. A unified noise analysis for iterative image estimation. *Phys. Med. Biol.*, 48:3505–3519, 2003.

[102] J. Qi. Analysis of lesion detectability in Bayesian emission reconstruction with nonstationary object variability. *IEEE Trans. Med. Imag.*, 23(3):321–329, 2004.

[103] J. Qi. Noise propagation in iterative reconstruction algorithms with line searches. *IEEE Trans. Nucl. Sci.*, 52(1):57–62, 2005.

[104] J. Qi and R. H. Huesman. Theoretical study of lesion detectability of MAP reconstruction using computer observers. *IEEE Trans. Med. Imag.*, 20(8):815–822, 2001.

[105] J. Qi and R. H. Huesman. Wavelet crosstalk matrix and its application to assessment of shift-variant imaging systems. *IEEE Trans. Nucl. Sci.*, 51(1):123–129, 2004.

[106] J. Qi and R. H. Huesman. Theoretical study of penalized-likelihood image reconstruction for region-of-interest quantification. *IEEE Trans. Med. Imag.*, 25(5):640–648, 2006.

[107] J. Qi and R. M. Leahy. A theoretical study of the contrast recovery and variance of MAP reconstructions from PET data. *IEEE Trans. Med. Imag.*, 18(4):293–305, 1999.

[108] J. Qi and R. M. Leahy. Resolution and noise properties of MAP reconstruction for fully 3-D PET. *IEEE Trans. Med. Imag.*, 19(5):493–506, 2000.

[109] P. Rizo, P. Grangeat, and R. Guillemaud. Geometric calibration method for multiple-head cone-beam SPECT system. *IEEE Trans. Nucl. Sci.*, 41(6):2748–2757, 1994.

[110] S. Sastry and R. E. Carson. Multimodality bayesian algorithm for image reconstruction in positron emission tomography: a tissue composition model. *IEEE Trans. Med. Imag.*, 16(6):750–761, 1997.

[111] O. Schillaci. Hybrid SPECT/CT: a new era for SPECT imaging? *Eur. J. Nucl. Med. Mol. Imaging*, 32(5):521–524, 2005.

[112] N. U. Schramm, G. Ebel, U. Engeland, T. Schurrat, M. Béhé, and T. M. Behr. High-resolution SPECT using multipinhole collimation. *IEEE Trans. Nucl. Sci.*, 50(3):315–320, 2003.

[113] L. A. Shepp and Y. Vardi. Maximum likelihood reconstruction for emission tomography. *IEEE Trans. Med. Imag.*, 1(2):113–122, 1982.

[114] M. F. Smith and R. J. Jaszczak. The effect of gamma ray penetration on angle-dependent sensitivity for pinhole collimation in nuclear medicine. *Med. Phys.*, 24(11):1701–1709, 1997.

[115] S. Somayajula, E. Asma, and R. Leahy. PET image reconstruction using anatomical information through mutual information based priors. In *Conference Record of the IEEE Nucl. Sci. Symp. and Med. Imag. Conf.*, volume M11-354, Puerto Rico, USA, 2005.

[116] S. Staelens, D. Strul, G. Santin, S. Vandenberghe, M. Koole, Y. D'Asseler, I. Lemahieu, and R. V. Walle. Monte Carlo simulations of a scintillation camera using GATE: validation and application modelling. *Phys. Med. Biol.*, 48:3021–3042, 2003.

[117] S. Staelens, K. Vunckx, J. De Beenhouwer, F. J. Beekman, Y. D'Asseler, J. Nuyts, and I. Lemahieu. GATE simulations for optimization of pinhole imaging. *Nucl. Inst. & Meth. A*, 569(2):359–363, 2006.

[118] J. W. Stayman and J. A. Fessler. Regularization for uniform spatial resolution properties in penalized-likelihood image reconstruction. *IEEE Trans. Med. Imag.*, 19(6):601–615, 2000.

[119] J. W. Stayman and J. A. Fessler. Compensation for nonuniform resolution using penalized-likelihood reconstruction in space-variant imaging systems. *IEEE Trans. Med. Imag.*, 23(3):269–284, 2004.

[120] J. A. Swets. Measuring the accuracy of diagnostic systems. *Science*, 240(4857):1285–1293, 1988.

[121] J. A. Swets and R. M. Pickett. *Evaluation of diagnostic systems: methods from signal detection theory.* Academic Press New York, 1982.

[122] T. Takahashi and S. Watanabe. Recent progress in CdTe and CdZnTe detectors. *IEEE Trans. Nucl. Sci.*, 48(4):950–959, 2001.

[123] H. L. Van Trees. *Detection, estimation, and modulation theory.* Wiley-Interscience, 2004.

[124] B. M. W. Tsui and G. T. Gullberg. The geometric transfer function for cone and fan beam collimators. *Phys. Med. Biol.*, 35:81–93, 1990.

[125] B. M. W. Tsui, G. T. Gullberg, E. R. Edgerton, D. R. Gilland, J. R. Perry, and W. H. McCartney. Design and clinical utility of a fan beam collimator for SPECT imaging of the head. *J. Nucl. Med.*, 27(6):810–819, 1986.

[126] S. Vandenberghe, R. Van Holen, S. Staelens, and I. Lemahieu. System characteristics of SPECT with a slat collimated strip detector. *Phys. Med. Biol.*, 51(2):391–405, 2006.

[127] C. Vanhove, A. Andreyev, M. Defrise, J. Nuyts, and A. Bossuyt. Resolution recovery in pinhole SPECT based on multi-ray projections: a phantom study. *Eur. J. Nucl. Med. Mol. Imaging*, 34(2):170–180, 2007.

[128] C. Vanhove, M. Defrise, T. Lahoute, and A. Bossuyt. Three-pinhole collimator to improve axial spatial resolution and sensitivity in pinhole SPECT. *Eur. J. Nucl. Med. Mol. Imaging*, 35(2):407–415, 2008.

[129] K. Vunckx. High quality image formation of small animals using emission tomography. In *Ph.D. thesis*, Katholieke Universiteit Leuven, Belgium, 2008.

[130] K. Vunckx, D. Bequé, M. Defrise, and J. Nuyts. Single and multipinhole collimator design evaluation method for small animal SPECT. *IEEE Trans. Med. Imag.*, 27(1):36–46, 2008.

[131] K. Vunckx, M. Defrise, D. Bequé, C. Vanhove, A. Andreyev, and J. Nuyts. Geometrical calibration and aperture configuration design in multi-pinhole SPECT. In *IEEE Internat. Symp. on Biomed. Imag.*, pages 1403–1406, Paris, France, 2008.

[132] K. Vunckx and J. Nuyts. Heuristic modification of an anatomical Markov prior improves its performance. In *Conference Record of the IEEE Nucl. Sci. Symp. and Med. Imag. Conf.*, Knoxville, Tennessee, USA, 2010.

[133] K. Vunckx, J. Nuyts, B. Vanbilloen, M. De Saint-Hubert, D. Vanderghinste, D. Rattat, F. M. Mottaghy, and M. Defrise. Optimized multipinhole design for mouse imaging. *IEEE Trans. Nucl. Sci.*, 56(5):2696–2705, 2009.

[134] K. Vunckx, P. Suetens, and J. Nuyts. Effect of overlapping projections on reconstruction image quality in multipinhole SPECT. *IEEE Trans. Med. Imag.*, 27(7):972–983, 2008.

[135] K. Vunckx, L. Zhou, S. Matej, M. Defrise, and J. Nuyts. Fisher information-based evaluation of image quality for time-of-flight PET. *IEEE Trans. Med. Imag.*, 29(2):311–321, 2010.

[136] K. Vunckx, L. Zhou, and J. Nuyts. Noise propagation in multipinhole SPECT calibration. In *Conference Record of the IEEE Nucl. Sci. Symp. and Med. Imag. Conf.*, pages 3166–3172, Orlando, Florida, USA, 2009.

[137] G. Wang, T. H. Lin, P. Cheng, and D. M. Shinozaki. A general cone-beam reconstruction algorithm. *IEEE Trans. Med. Imag.*, 12(3):486–496, 1993.

[138] G. Wang and J. Qi. Analysis of penalized likelihood image reconstruction for dynamic PET quantification. *IEEE Trans. Med. Imag.*, 28(4):608–620, 2009.

[139] H. Wang, M. F. Smith, C. D. Stone, and R. J. Jaszczak. Astigmatic single photon emission computed tomography imaging with a displaced center of rotation. *Med. Phys.*, 25:1493–1501, 1998.

[140] W. Wang and G. Gindi. Noise analysis of MAP-EM algorithms for emission tomography. *Phys. Med. Biol.*, 42:2215–2232, 1997.

[141] W. Wang, W. Hawkins, and D. Gagnon. 3D RBI-EM reconstruction with spherically-symmetric basis function for SPECT rotating slat collimator. *Phys. Med. Biol.*, 49:2273–2292, 2004.

[142] Y. C. Wang and B. M. W. Tsui. Pinhole SPECT with different data acquisition geometries: Usefulness of unified projection operators in homogeneous coordinates. *IEEE Trans. Med. Imag.*, 26(3):298–308, 2007.

[143] S. Webb, D. M. Binnie, M. A. Flower, and R. J. Ott. Monte Carlo modelling of the performance of a rotating slit-collimator for improved planar gamma camera imaging. *Phys. Med. Biol.*, 37, 1992.

[144] S. Webb, M. A. Flower, and R. J. Ott. Geometric efficiency of a rotating slit-collimator for improved planar gamma-camera imaging. *Phys. Med. Biol.*, 38:627–638, 1993.

[145] H. Wieczorek and A. Goedicke. Analytical model for SPECT detector concepts. *IEEE Trans. Nucl. Sci.*, 53(3):1102–1112, 2006.

[146] D. W. Wilson, B. M. W. Tsui, and H. H. Barrett. Noise properties of the EM algorithm. II. Monte Carlo simulations. *Phys. Med. Biol.*, 39(5):847–872, 1994.

[147] S. D. Wollenweber, B. M. W. Tsui, D. S. Lalush, E. C. Frey, K. J. LaCroix, and G. T. Gullberg. Comparison of Hotelling observer models and human observers in defect detection from myocardial SPECT imaging. *IEEE Trans. Nucl. Sci.*, 46(6):2098–2103, 1999.

[148] W. Xia, R. M. Lewitt, and P. R. Edholm. Fourier correction for spatially variant collimator blurring in SPECT. *IEEE Trans. Med. Imag.*, 14(1):100–115, 1995.

[149] Y. Xing, I.-T. Hsiao, and G. Gindi. Rapid calculation of detectability in Bayesian single photon emission computed tomography. *Phys. Med. Biol.*, 48(22):3755–3773, 2003.

[150] R. Yao, T. Ma, and Y. Shao. Derivation of system matrix from simulation data for an animal SPECT with slit-slat collimator. *IEEE Trans. Nucl. Sci.*, 56(5):2651–2658, 2009.

[151] A. Yendiki and J. A. Fessler. Analysis of observer performance in known-location tasks for tomographic image reconstruction. *IEEE Trans. Med. Imag.*, 25(1):28–41, 2006.

[152] A. Yendiki and J. A. Fessler. Analysis of observer performance in unknown-location tasks for tomographic image reconstruction. *J. Opt. Soc. Am. A*, 24(12):B99–B109, 2007.

[153] O. Ying-Lie. An ECAT reconstruction method which corrects for attenuation and detector response. *IEEE Trans. Nucl. Sci.*, 30(1):632–635, 1983.

[154] H. Zaidi. Relevance of accurate Monte Carlo modeling in nuclear medical imaging. *Med. Phys.*, 26:574–608, 1999.

[155] G. L. Zeng. Detector blurring and detector sensitivity compensation for a spinning slat collimator. *IEEE Trans. Nucl. Sci.*, 53(5):2628–2634, 2006.

[156] G. L. Zeng, D. Gagnon, C. G. Matthews, J. A. Kolthammer, J. D. Radachy, and W. G. Hawkins. Image reconstruction algorithm for a rotating slat collimator. *Med. Phys.*, 29:1406–1412, 2002.

[157] B. Zhang and G. L. Zeng. Study of noise propagation and the effects of insufficient numbers of projection angles and detector samplings for iterative reconstruction using planar-integral data. *Med. Phys.*, 33(9):3124–3134, 2006.

[158] Y. Zhang-O'Connor and J. A. Fessler. Fast predictions of variance images for fan-beam transmission tomography with quadratic regularization. *IEEE Trans. Med. Imag.*, 26(3):335–346, 2007.

[159] S. Zhao and G. Wang. Feldkamp-type cone-beam tomography in the wavelet framework. *IEEE Trans. Med. Imag.*, 19(9):922–929, 2000.

[160] L. Zhou, K. Vunckx, and J. Nuyts. Comparison between parallel hole and rotating slat collimation with a contrast phantom using an analytical method. In *Conference Record of the IEEE Nucl. Sci. Symp. and Med. Imag. Conf.*, pages 3678–3681, Orlando, Florida, USA, 2009.

[161] L. Zhou, K. Vunckx, and J. Nuyts. Comparison between rotating slat and parallel hole collimation: influence of projector models. In *Book of abstracts of the 5th International Conference on Imaging Technologies in Biomedical Sciences*, page 71, Milos Island, Greece, 2009.

List of publications

International Journals

1. **L. Zhou**, P. Dupont, K. Baete, W. Van Paesschen, K. Van Laere, and J. Nuyts. Detection of inter-hemispheric metabolic asymmetries in FDG-PET images using prior anatomical information, *NeuroImage*, 44(1): 35–42, 2009.

2. **L. Zhou**, M. Defrise, K. Vunckx, and J. Nuyts. Comparison between parallel hole and rotating slat collimation: analytical noise propagation models. *IEEE Transactions on Medical Imaging*, 29(12): 2038–2052, 2010.

3. **L. Zhou**, K. Vunckx, and J. Nuyts. Multi-pinhole SPECT calibration: influence of data noise and systematic orbit deviations. *IEEE Transactions on Medical Imaging*, 30(10): 1795–1807, 2011.

4. **L. Zhou**, K. Vunckx, and J. Nuyts. Selection of point source configuration for multi-pinhole SPECT. *In preparation.*

5. K. Vunckx, **L. Zhou**, S. Matej, M. Defrise, and J. Nuyts. Fisher information-based evaluation of image quality for time-of-flight PET. *IEEE Transactions on Medical Imaging*, 29(2): 311–321, 2010.

6. K. Prinsen, L. Jin, K. Vunckx, M. De Saint-Hubert, **L. Zhou**, J. Cleynhens, J. Nuyts, G. Bormans, Y. Ni, and A. Verbruggen. Radiolabeling and preliminary biological evaluation of a $^{99m}Tc(CO)_3$ labeled 3,3'-(benzylidene)-bis-(1H-indole-2-carbohydrazide) derivative as a potential SPECT tracer for in vivo visualization of necrosis. *Bioorganic & Medicinal Chemistry Letters*, 21(1): 502–505, 2011.

7. M. De Saint-Hubert, H. Wang, E. Devos, K. Vunckx, **L. Zhou**, C. Reutelingsperger, A. Verbruggen, L. Mortelmans, Y. Ni, and F. M. Mottaghy. Preclinical imaging of therapy response using metabolic and apoptosis molecular imaging. *Molecular Imaging & Biology*, 13(5): 995–1002, 2011.

International Conference Proceedings

1. K. Vunckx, **L. Zhou**, S. Matej, M. Defrise, and J. Nuyts. Fisher information-based evaluation of image quality for time-of-flight PET. In *Conference Record of the IEEE Nuclear Science Symposium and Medical Imaging Conference*, pages 4129–4136, Honolulu, Hawaii, USA, 2007.
2. **L. Zhou**, M. Defrise, K. Vunckx, and J. Nuyts. Comparison between parallel hole and rotating slat collimation. In *Conference Record of the IEEE Nuclear Science Symposium and Medical Imaging Conference*, pages 5530–5539, Dresden, Germany, 2008.
3. **L. Zhou**, K. Vunckx, and J. Nuyts. Comparison between parallel hole and rotating slat collimation with a contrast phantom using an analytical method, In *Conference Record of the IEEE Nuclear Science Symposium and Medical Imaging Conference*, pages 3678-3681, Orlando, Florida, USA, 2009.
4. K. Vunckx, **L. Zhou**, and J. Nuyts. Noise propagation in multipinhole SPECT calibration, In *Conference Record of the IEEE Nuclear Science Symposium and Medical Imaging Conference*, pages 3166–3172, Orlando, Florida, 2009.
5. **L. Zhou**, K. Vunckx, and J. Nuyts. Predicting the variance of ML reconstructions with body contour constraint for multi-pinhole SPECT, In *Conference Record of the IEEE Nuclear Science Symposium and Medical Imaging Conference*, pages 2376–2380, Knoxville, Tennessee, USA, 2010.
6. **L. Zhou**, K. Vunckx, and J. Nuyts. Multi-pinhole SPECT calibration: influence of data noise and systematic orbit deviations. *11th International Meeting on Fully 3D Image Reconstruction in Radiology and Nuclear Medicine*, pages 104–107, Potsdam, Germany, 2011.
7. **L. Zhou**, K. Vunckx, and J. Nuyts. Selection of point source configuration for multi-pinhole SPECT calibration, In *Conference Record of the IEEE Nuclear Science Symposium and Medical Imaging Conference*, Valencia, Spain, 2011.

International Conference Abstracts

1. K. Prinsen, Y. Ni, J. Zhang, M. De Saint-Hubert, K. Vunckx, C. Lemmens, **L. Zhou**, L. Mortelmans, J. Nuyts, G. Bormans, and A. Verbruggen. Radiosynthesis and preliminary evaluation in rats of a novel ^{99m}Tc-labelled necrosis avid imaging agent. In *European Symposium on Radiopharmacy and Radiopharmaceuticals*, Skopje, Macedonia, 2008.
2. **L. Zhou**, K. Vunckx, and J. Nuyts. Comparison between rotating slat and parallel hole collimation: influence of projector models. In *Book of abstracts of the 5th International Conference on Imaging Technologies in Biomedical Sciences*, page 71, Milos Island, Greece, 2009.

3. Y. Ni, J. Li, M. M. Cona, F. Chen, H. Wang, T. Marysael, P. De Witte, K. Prinsen, A. Verbruggen, G. Bormans, **L. Zhou**, J. Nuyts, G. Marchal, J. Zhang, and Z. Sun. Exploitation of Necrosis Avidity: from Diagnostics to Theragnostics in Oncology. *Contrast Media Research Meeting, Contrast Media & Molecular Imaging*, 4, page 280, Copenhagen, Denmark, 2009.

4. M. De Saint-Hubert, K. Prinsen, K. Vunckx, **L. Zhou**, H. Wang, J. Li, Y. Ni, J. Nuyts, C. P. Reutelingsperger, L. Mortelmans, A. Verbruggen, and F. M. Mottaghy. In vivo imaging of apoptosis with ^{99m}Tc$(CO)_3$-HIS-Annexin V. *Annual Congress of the European Association of Nuclear Medicine, European Journal of Nuclear Medicine and Molecular Imaging*, 36(Suppl.2), page S475, Barcelona, Spain, 2009.

5. M. De Saint-Hubert, K. Prinsen, J. Nuyts, K. Vunckx, **L. Zhou**, D. Rattat, L. Mortelmans, C. P. Reutelingsperger, A. Verbruggen, and F. M. Mottaghy. Site-specific labeling of second generation Annexin V with ^{99m}Tc$(CO)_3$ for improved imaging of apoptosis in vivo. In *Society of Nuclear Medicine's 56th Annual Meeting, Journal of Nuclear Medicine*, 50 (Suppl.2), page 567, Toronto, Canada, 2009.

6. J. Li, Z. Sun, H. Wang, F. Chen, K. Prinsen, A. Verbruggen, **L. Zhou**, J. Nuyts, G. Marchal, and Y. Ni. Targeting radiotherapy to cancer via small necrosis-avid molecules: a simpler approach to improve treatability and curability? In *Society of Nuclear Medicine's 57th Annual Meeting, Journal of Nuclear Medicine*, 51(Suppl.2), page 62, Salt Lake City, USA, 2010.

7. J. Li, Z. Sun, J. Zhang, K. Prinsen, H. Shao, T. Marysael, H. Wang, F. Chen, **L. Zhou**, M. M. Cona, P. De Witte, A. Verbruggen, J. Nuyts, G. Bormans, J. Yu, G. Marchal, Y. Li, K. Xu, and Y. Ni. Small molecular dual targeting chemo- and radiotherapy: an integrated approach to improve cancer treatability and curability. *8th International Symposium on Targeted Anticancer Therapies, Annals of Oncology*, 21(Suppl 2) page ii29, Bethesda, Maryland, USA, 2010.

Curriculum Vitae

- Date of birth: March 10th, 1982
- Place of birth: Shenyang, China

Educations

- 2007-2011: Ph.D in Engineering, Katholieke Universiteit Leuven, Belgium
- 2006-2007: M.Sc in Medical Imaging, Katholieke Universiteit Leuven, Belgium
- 2004-2006: M.Sc in Optical Engineering, Zhejiang University, Hangzhou, China
- 2000-2004: B.Sc in Optical Engineering, Zhejiang University, Hangzhou, China

Award

- Chinese government award for outstanding self-financed students aboard (2010)